Biochar production from pyrolysis and co–pyrolysis of biomass blends: analysis, characterization and applications

A Thesis

Submitted in the partial fulfilment of the requirements for the award of the degree of

DOCTOR OF PHILOSOPHY

By

Harrison Hihu Muigai

Centre of Energy
Indian Institute of Technology Guwahati
Guwahati – 781039
March 2021

This thesis is dedicated to my Dad

The late Peter V.M. Wainaina and Dad in Law The late Paul Mwangi Kangethe

DECLARATION

I hereby declare that this research work was written by me. It has not been presented in any previous application for the award of degree of PhD in renewable energy. Related work consulted on this project has duly been acknowledged and referenced.

03/07/2021

Signature *Date*

CERTIFICATE

It is certified that the work contained in this thesis entitled **“Biochar production from pyrolysis and co–pyrolysis of biomass blends: analysis, characterization and applications”** is submitted by **Mr. Harrison Hihu Muigai (Roll No. 176151012),** a student in the Centre for Energy, Indian Institute of Technology Guwahati for the award of degree of **Doctor of Philosophy** has been carried out under our supervision and this work has not been submitted for the award degree elsewhere.

Dr. Pankaj Kalita
Assistant Professor
Centre for Energy
Indian Institute of Technology Guwahati
Guwahati -781039, India

Prof. V.S. Moholkar
Professor
Department of chemical Engineering
Indian Institute of Technology Guwahati
Guwahati -781039, India

ABSTRACT

Co–pyrolysis of biomass is a promising technology capable of producing compatible substitutes for petroleum derived fuels and chemicals. To manufacture the renewable fuel precursors and chemicals on a large scale, the process needs to be cost–competitive. However, co–pyrolysis has not gained significant commercial success because of complex feedstock chemistry. Computational models help in efficient design of reactor, and understanding complex processes involved during pyrolysis and co-pyrolysis. However, all integral isoconversional methods are based on the assumption that activation energy remains constant over the whole interval of integration. In practice, such behaviour is not observed. Especially, for the biomass, the error can be as large as 20–30% in the case of strong variations of activation energy with conversion. The International Confederation for Thermal Analysis and Calorimetry (ICTAC) has recommended the use of more accurate equations and performing an iterative correction procedure for the value of activation energy. To correct these errors, ICTAC has recommended to use advanced methods that work with small conversion intervals such as Vyazovkin_advanced isoconversional model (AIC) and Distributed Activation Energy Model (DAEM).

In this the present study various aspects of biomass pyrolysis and co–pyrolysis processes were analyzed. Physico–chemical characterization and kinetic analyses of three biomass, viz. invasive species of water hyacinth (WH), *Thevetia peruviana* (TP), and industrial by–product of sugar cane bagasse (SCB) to assess their potential as feedstock for pyrolysis were investigated. Four isoconversional methods, viz. Kissinger–Akahira–Sunose (KAS), Friedman, Ozawa–Flynn–Wall (OFW), and advanced Vyazovkin_AIC were used to determine the kinetics triplets of thermal conversion at three different heating rates 10, 30 and 40 °C min^{-1}. The activation energies for raw biomass viz. WH, TP and SCB determined using the four isoconversional methods were found to be in the range of 188–330, 182–389, and 193–293kJ mol^{-1}, respectively. In the case of biomass blends the activation energies for binary blends of WHSCB, WHTP, TPSCB were observed to be in the range of 123–238, 128–273, and 125–236kJ mol^{-1}, respectively. For ternary blends of WH111, WH211 and WH311, activation energy varied in the range 120–194, 123–247, and 122–195kJ mol^{-1}, respectively. The characterization and kinetic analysis of all biomass essentially demonstrates their potential as feedstock for pyrolysis and co–pyrolysis.

Pyrolysis was carried out in a fixed batch reactor at 350°C and 550°C with a heating rate of 20°Cmin^{-1}. Biochars were characterized for proximate and ultimate (elemental) analysis, and also using standard techniques (SEM, EDX, TGA, BET, XRD, and FTIR). Biochars produced from three different biomass, viz. water hyacinth (whole plant and its components), yellow oleander and sugarcane bagasse, and their comparative assessment for potential application in agronomy and engineering were investigated. Biochar produced from sugarcane bagasse at 550ºC possessed best properties: fixed carbon (77.42 %), bulk density (0.13 kg/m^3), BET surface area (17.78 m^2/g), pore size (12.86 nm), total pore volume (0.025 cm^3/g), calorific value (30.18 MJkg^{-1}), ash content (1.16 %), and moisture content (2.03 %). Co–pyrolysis of ternary blend obtained from biomass viz. water hyacinth, *Thevetia peruviana* and sugarcane bagasse was carried out in a fixed bed reactor. The optimum process conditions were determined using response surface methodology (RSM). The optimum conditions for co–pyrolysis based on two responses viz. yield and higher heating value were obtained at the temperature of 368 C, heating rate of 16.33°C min^{-1} and residence time of 61min. The present study is useful for the understanding intensification of co–pyrolysis process and applications of biochar produced from noxious weeds and waste.

ACKNOWLEDGEMENT

Foremost, I take this opportunity to express my sincere gratitude to my supervisors, Dr. Pankaj Kalita and Professor V.S Moholkar for accepting and providing guidance to me as their PhD student. They have always given time, listened to my ideas patiently and constantly encouraged me to accomplish my research goals on time. During my studies I have learnt from them how to work with zeal, and how to precisely communicate my research findings. Words are not even enough to express how grateful I am to them. The best way to express gratitude to my supervisors is to put into practice what I have learnt from them and pass it to my students as I guide them in future.

I would like to thank my doctoral committee members, Professor P Muthukumar, Dr. Peela Nageswara Rao, and Dr. Singha Siddhartha for their valuable recommendations and encouragement in the entire journey of attaining my PhD.

I wish to thank to Mr. Dhiren Huzuri, Mr. Derbashi Baruah and Dr. Lerpakshi Barbora for their assistance during the experimental investigation in analytical laboratory.

I am grateful to all the staff members and teaching assistants of Central Instrumentation Facility, IIT Guwahati and the staff members of Guwahati Biotech Park for assisting me to carry out some of the experiments.

I would like to acknowledge Indian Institute of Technology Guwahati for providing the necessary infrastructure to carry out the research.

I would also like to acknowledge Indian Council for Cultural Relations (ICCR) for providing financial support extended to enable me pursue my studies in India.

I owe deep sense of gratitude to all my colleagues Dr. Dudul das, Mr. Samar Das, Mr. Shayaram Basumatary, Mr. Rabindra Kangsha Banik, Mr. Biraj Das, Mr. Akash Dilip Kamble, Ms.

Sudipta Bijoy Sarmah, Mr. Debangshu Kashyap, Ms. Urbashi Bordoloi and Mr. Dushyanta Madhav Sharma for their immense advice, support, ideas and encouragement which has enabled the completion of my present research work.

I appreciate the support from my dear wife, Mrs. Irene Njeri Mwangi Hihu for being part of my life giving me moral support and taking care of our children while I was away pursuing my studies. I am also grateful to my children, JabaliPeters, JayPaul and JewelNaomi who made my life easier with their encouraging questions and assurance that I'll soon be home with them after I have cleared my studies. I am immensely grateful to my parents in Molo and Nakuru for supporting me with prayers, finances and watching over my family while I was studying. Also I am grateful to my siblings and all the other family members and friends for their constant encouragement and moral support throughout my academic life.

I thank Saraighat community, Dr. Nelson Muthu and his family for their steady support and encouragement whenever I needed him to discuss my academic progress.

I thank all the anonymous referees of my manuscripts for their meticulous evaluation and constructive criticism, indeed their comments and suggestions have significantly contributed to the improvement of the manuscripts from their original version.

I am thankful to God for giving me good health and protection while pursuing my studies.

Finally, I would also like to thank Mr. Kamal Das and Mr. Dipankar Kalita for their continuous help during the experimental period especially setting up the pyrolysis experiments and collection of the feedstock.

Mr. Harrison Hihu Muigai

TABLE OF CONTENTS

Nomenclature

α	Conversion/reaction progress, dimensionless
β	Heating rate, °Cmin^{-1}
E_a	Apparent activation energy, kJ/mol
E_α	Activation energy at conversion α, kJ/mol
A	Pre-exponential factor, min^{-1}
R	Universal gas constant, J/mol-K
T	Temperature, °C
$f(\alpha)$	Differential form of reaction model, dimensionless
$f(E)$	Normalized distribution curve of activation energy
$g(\alpha)$	Integral form of reaction model, dimensionless
R^2	Correlation coefficient, dimensionless
T_{max}	Temperature at maximum peak in DTG curve, °C
T_{onset}	Intial temperature of the pyrolysis zone, °C
T_{offset}	Final temperature of the pyrolysis zone, °C
T_α	Temperature at α degree of conversion, °C
ΔH	Enthalpy (kJ mol^{-1})
ΔG	Gibbs free energy (kJ mol^{-1})
ΔS	Entropy (kJ mol^{-1})
k_B	Boltzmann constant= 1.381×10^{-23} J K^{-1}
h	Plank constant = 6.626×10^{-34} J s^{-1}
ρ	Bulk density (Kg/m^3)
vol	Volume (m^3)

Abbreviations

AC	Ash content
AAE	Alkali and alkaline earth metals
ANOVA	Analysis of variance
ASTM	American society for testing and materials
BET	Brannure Emmular Teller
BNTS	Biochar NPK treated soil
BS	Bare soil
BTS	Biochar treated soil
BVNTS	Biochar vermicompost NPK treated soil
BVTS	Biochar vermicompost treated soil
CCD	Central composite design
CEC	Cation exchange capacity
CHP	Combined heat and power
DAEM	Distributed activation energy model
DOE	Design of experiments
DP	Degree of polymerization
DTG	Differential thermogravimetric analysis
EC	Electrical conductivity
EC	Electrical conductivity
EDX	Energy dispersive X-Ray spectroscopy
FC	Fixed carbon
FESEM	Field emission scanning electron microscope
FTIR	Fourier transform infrared spectroscopy
F-value	Fischer test value
h	hour

HDPE	High–density polyethylene
HFO	Heavy fuel oil
HHV	High heating value
ICTAC	International Confederation for Thermal Analysis and Calorimetry
KAS	Kissinger–Akahira–Sunose
LDPE	Low–density polyethylene
LFO	Light fuel oil
MC	Moisture content
mm	Millimetre
NL	Number of leaves
NPK	Nitrogen phosphorus potassium
NTS	NPK treated soil
OFW	Ozawa – Flynn – Wall
PC	Polycarbonate
PCM	Phase change material
PET/PETE	Polyethylene terephthalate polyethylene
PH	Plant Height
PP	Polypropylene
PS	Polystyrene
PV	Photovoltaic
PV/T	Photovoltaic –Thermal
PV/T	Photovoltaic/Thermal system
P-value	Probability value
PVC	Polyvinyl chloride
RSM	Response surface methodology
SCB	Sugarcane bagasse
SCB350	Biochar pyrolyzed from sugar cane bagasse (at T= 350°C)

SCB550	Biochar pyrolyzed from sugar cane bagasse (at *T*= 550°C)
TES	Thermal energy storage
TGA	Thermogravimetric analysis/Thermogravimetry
TP	Thevetia Peruviana
TP SCB	Thevetia peruviana and sugarcane bagasse
TWh	Terawatt hour
VM	Volatile matter
VTS	Vermicompost treated soil
WH 111	Ternary blend from water hyacinth, sugarcane bagasse and Thevetia peruviana
WH 211	Ternary blend from water hyacinth, sugarcane bagasse and Thevetia peruviana
WH 311	Ternary blend from water hyacinth, sugarcane bagasse and Thevetia peruviana
WH SCB	water hyacinth and sugarcane bagasse
WH TP	water hyacinth and Thevetia peruviana
WH	Water hyacinth
WH350	Biochar pyrolyzed from Thevetia peruviana (at *T*= 350°C)
WH350	Biochar pyrolyzed from Thevetia peruviana (at *T*= 550°C)
WH350	Biochar pyrolyzed from water hyacinth whole plant (at *T*= 350 °C)
WH550	Biochar pyrolyzed from water hyacinth whole plant (at *T*= 550 °C)
WHL350	Biochar pyrolyzed from water hyacinth leaves (at *T*= 350°C)
WHL550	Biochar pyrolyzed from water hyacinth leaves (at *T*= 550°C)
WHR350	Biochar pyrolyzed from water hyacinth roots (at *T*= 350°C)
WHR550	Biochar pyrolyzed from water hyacinth roots (at *T*= 550°C)
WHS350	Biochar pyrolyzed from water hyacinth stem (at *T*= 350°C)
WHS350	Biochar pyrolyzed from water hyacinth stem (at *T*= 550°C)
XRD	X-Ray diffraction

List of figures

List of tables

CHAPTER 1-Introduction

1.0 Motivation

Global industrial development and increase of population (especially the urban sector) have led to an upsurge in energy demand. To satisfy the energy demand, most of the economies in the world rely on fossils fuels. Fossil fuels are depleting fast, resulting into energy insecurity all over the world. Climate change and global warming are also daunting global problems due to emissions from fossils fuels. Although in recent years, energy generation through renewable resources has shown a significant growth globally, about 54% of the global energy demand is met through non–renewable sources like fossil fuels [1]. Among all sources of renewable energies, biomass is the oldest form that has been used for decades. The main reasons why humankind has relied on biomass energy source are: (1) it is readily and abundantly available throughout year (approx. 220 billion tons per year worldwide); (2) energy can be derived from biomass with simple methods like combustion; (3) it is carbon–neutral and can produce multiple products with practically no SOx and NOx emissions; and (4) easy storage [2,3].

Recent decades have witnessed intensive research on novel technologies for deriving energy from biomass using thermochemical and biochemical methods. Pyrolysis is one of the thermochemical conversion routes that yields bio–oil and biochar thus making it one of the most preferred route. The use of edible crops for energy production has led to a great controversy in the world due to the upsurge in the price of human food and the food crisis being experienced in the world [4]. This has hindered the development of first generation biofuels (mainly biodiesel and ethanol) as expected. However, this is not the case for lignocellulosic biomass that yields second generation biofuel, since they cannot be consumed by human beings and they are composed of a wide range of materials, which are; wood, wood-derived products, energy crops, agricultural products, agricultural industry products, forest wastes, wood manufacturing wastes and noxious weeds. Therefore they provide the best substitute of feedstocks in first generation biofuel [4].

More recently, waste biomass such as grasses and invasive weeds have been explored as possible sources of bioenergy. Development of efficient technologies for thermal conversion of biomass to liquid and gaseous fuels requires comprehensive understanding and information on the kinetics of such processes.

Challenges encountered while managing the menace of water hyacinth and environmental concerns, as well as the on–going successful shifting of over reliance of non–conventional to conventionaltechnologies has given an impulse to focus on bio–oil and biochar production from noxious weeds. Effective control of these invasive species can be achieved through utilization as feedstock for value–added products. Another potential biomass feedstock is sugarcane bagasse (SCB), which is produced by sugar industries. With fast growing sugar production in developing economies like India (> 30 million tons annually), large quantities of sugarcane bagasse are available at cheap rates, and could be used as alternate feedstock for value-added products [5]. For decades most studies focused on utilizing water hyacinth for production of briquettes and biogas. Only few studies focused on using noxious weeds (water hyacinth and Thevetia peruviana) and SCB for production of bio char through co–pyrolysis to date. Research on briquette production by blending water hyacinth with other agricultural waste has been found to give good results especially in the increased calorific value in this case blending and co-processing of biomass is considered vital [6].

1.1 Problem statement

Fossil fuel is non–renewable form of energy which is a leading source of energy in the world. Its consumption is equivalent to 6287.28 Mtoe (67%) of the energy consumed in the world. Currently its usage as a major source for energy generation has appealed global concern, because of its high emission of greenhouse gases during combustion. These emissions are the major causes of environmental degradation due to global warming that has led: (1) increased temperature in the planet, (2) melting of the glacier, (3) increase of sea level, (4) drought and floods, (5) ozone layer depletion. Fossil fuels take millions of years to form and are depleting without an immediate replacement. Energy crisis, which includes uncertainties concerning fossil fuels availability and prices fluctuations have resulted to the need of developing sustainable forms energy. Utilization of edible feed stock for energy production has led to food crisis which is a global concern. All these contending issues are global concerns and have led to a shift in reliance of fossil fuel to a more environmentally friendly and sustainable source of energy in order to fulfil the increasing energy demand. It is necessary to focus on mitigating the use of first generation biomass by the use of readily available feed stock and non–edible plants to produce renewable forms of energies.

1.2 Background on biomass conversion routes and by–products

Various conversion technologies viz. thermochemical, biochemical and physical method could be used for valorization of biomass [2]. Since biomass exist in a heterogeneous nature any of conversion technologies could be adopted as shown in Figure 1.1. To intensify biomass utilization some factors have to be put into consideration while choosing which conversion route is appropriate to use: (1) physical and chemical characteristics of the biomass feedstock, (2) amount of biomass available, (3) desired form of energy, (4) final usage requirement of the form of energy produced, (5) environmental regulations and economic conditions [7]. Hybrid processing of biomass offers an opportunity for utilization and optimization of biomass for energy use which is capable of substituting fossil fuels and production of chemicals.

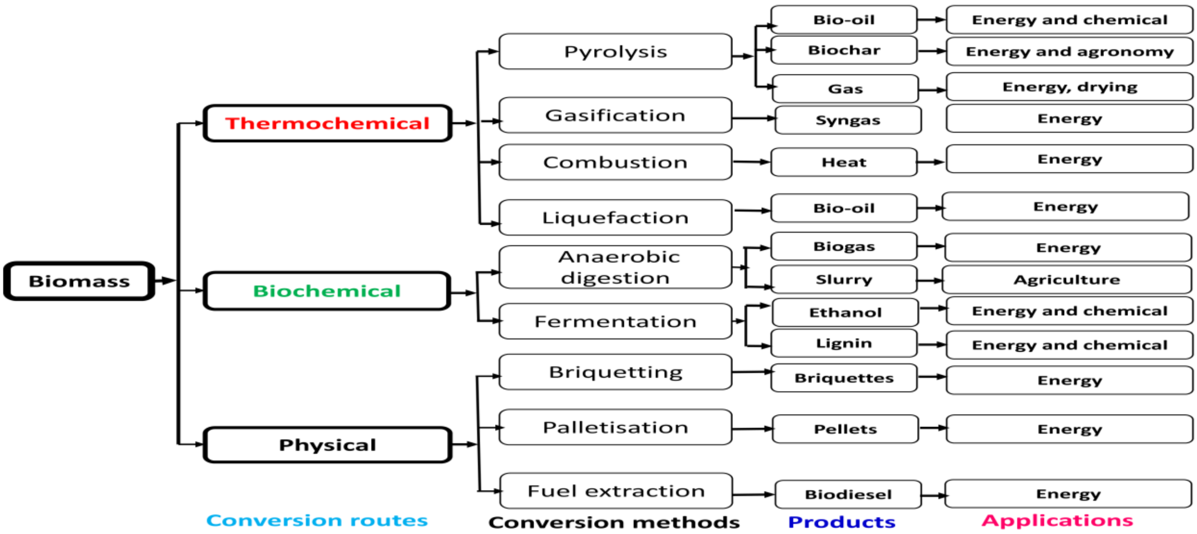

Figure 1.1 Biomass conversion routes

1.2.1 Thermochemical conversion

Thermochemical conversion technologies include; pyrolysis, combustion, liquefaction, and gasification. Thermochemical conversion methods have gained more attention because they have a shorter process time, can be used in the conversion of different feedstock that can't be broken down by micro–organisms [8]. Combustion is one of the oldest methods that have been used to produce heat that can be used directly as heat for drying and heating to produce electricity by incorporating a steam turbine. Gasification produces syngas that can be used directly in an engine or in a gas turbine to generate electricity [9,10]. Also the gas could be synthesised to produce chemicals. Among the thermochemical conversion technologies pyrolysis is more promising because it can produce three products viz. bio–oil, biochar and syngas. Other merits of pyrolysis include: (1) It is a self–dependent technology, since a wide variety of feedstocks can be utilized thus reducing emissions, waste heading to land fill. (2) pyrolysis can be performed in remote locations which enhance energy security in the rural area by utilizing readily available biomass resource hence reducing transport and handling cost of raw materials

1.2.1.1 Pyrolysis

Pyrolysis is one of the promising and effective process for valorizing various feedstocks. Pyrolysis of biomass in an inert atmosphere yields mainly two products, viz. bio–oil (comprising of high molecular weight hydrocarbons that condense at ambient conditions), and bio-char, which is a black porous solid residue rich in carbon. Bio-char can be used as a solid fuel for combustion/ gasification, and it can be blended with soil in agricultural land to enhance its fertility. Mixing of biochar with soil provides an additional carbon source for the plants. Biochar also acts as an adsorbent for the natural minerals as well as the nutrients/mineral added through fertilizers [11]. This prevents washing away of the minerals from soil – thus providing their better accessibility to the crops. Biochar can be utilized as an energy source for the production of briquettes and pellets, which could be used in gasifiers thus, substituting firewood [12]. The physico–chemical characteristics and surface properties of biochar essentially determine their suitability for application in energy and agriculture.

Bio-oil is multifaceted blend of extremely oxygenated compounds and water which is approximately 15–35% wt. [13,14]. Presence of the oxygenated compounds in the form of carbonyl and carboxylate leads to the storage instability, low calorific value and corrosion problems which confines its prompt acceptance as a transportation fuel [15]. Bio-oil can be used as fuel in boilers and engines in the form of heavy fuel oil (HFO) and light fuel oil (LFO). Moreover, valuable and useful chemicals can be obtained from pyrolytic oil. Bio–oil can be upgraded to liquid fuel through catalytic treatment [16].

1.3 Objectives

In the present study the major aim was to investigate sustainable methods of valorizing three biomass materials viz. water hyacinth, *Thevetia peruviana* and sugar cane bagasse.

The aim of this study was accomplished by completing the following objectives:

- Physico–chemical characterization and pyrolysis kinetics of water hyacinth, Thevetia Peruviana, and sugarcane bagasse.
- Synthesis and characterization of biochar derived from lignocellulosic biomass to determine their viability for application in agronomy and energy.
- Characterization, kinetic and thermodynamic analysis of biomass blends to determine the potential for bioenergy production.
- Co–pyrolysis of ternary biomass blend, optimization using response surface methodology and characterization of biochar.
- To determine the viability of applying biochar in engineering and agriculture.

1.4 Thesis outline

This thesis comprises of 8 chapters. **Chapter 1** discusses the motivation, and problem statement of the thesis. A brief summary on adverse impacts of fossil fuels, with the requisite for adopting biomass as an alternative energy source is discussed. The chapter then illustrates that among the thermochemical conversion technologies pyrolysis is a sustainable route for valorizing biomass feedstocks used in this work. The research aim and objectives are outlined in this chapter. The organization of the thesis is also presented in this chapter. **Chapter 2** provides a detailed literature review of related research works on co–pyrolysis which include co–pyrolysis of various feedstocks viz. plastics with biomass, sewage sludge with biomass, and biomass with biomass. A summary of the research findings based on the literature review was also presented. The chapter concludes by underlining the research gap that needs to be addressed based on the literature reviewed. **Chapter 3** presents the detailed physico–chemical properties and kinetics parameters of individual biomass such as water hyacinth, *Thevetia peruviana* and sugarcane bagasse. In **Chapter 4** results of the physico–chemical properties of biochar produced from three different biomass viz. whole water hyacinth plant, water hyacinth parts (roots, stem and leaves) *Thevetia peruviana* and sugarcane bagasse at 350°C and 550°C are presented. It further provides a detailed information on their potential utilization of biochar in agronomy and energy. **Chapter 5** presents the results of physico–chemical and kinetics and thermodynamics analysis of biomass blends viz. binary blends and ternary blends produced from water hyacinth, *Thevetia peruviana* and sugarcane bagasse. In **Chapter 6** results of co–pyrolysis of ternary biomass blend, optimization using response surface methodology and characterization of biochar synthesised at optimized conditions are discussed. **Chapter 7** presents the results of various applications of biochar in energy and agriculture. In **Chapter 8** main research outcomes of the study which are in line with the specific objectives are presented. The chapter concludes by proposing scope for future research.

1.5 Summary

In this chapter motivation, problem statement, background of the work, objectives and organization of the thesis are presented. In the next chapter literature review pertaining to the current research has been discussed.

CHAPTER 2 –Literature review

2.0 Introduction

This chapter includes the review of literature related to co–pyrolysis of different varieties of biomass. Influence of co–pyrolysis temperature, heating rate, time, type of feedstock, pyrolysis environment and significance of important parameters were also discussed and compared. Finally, scope of research were identified and objectives of the thesis are formulated.

2.1 Biomass resources

Biomass resources refer to all organic matter that could be utilized for energy generation [17]. Among all the other renewable energy sources biomass has a promising future since it can be used in all sectors. The global biomass power generation in the year 2000 was 132 TWh but in 2019 it increased to 589 TWh as shown in Figure 2.1. The increased growth of power generation from bioenergy could be attributed to the policies and market developments in emerging economies. It is estimated that by 2030, energy from biomass could account approx. 60% of total energy from renewable sources [1]. In most of the developing countries biomass is utilized using conventional forms viz. heating and cooking which have a lower efficiency and significantly contributes to indoor pollution [18,19]. Researchers are working towards mitigating these shortcomings by investigating sustainable ways of valorizing biomass [20]. At least a third of the available biomass resources could be consumed to produce power and value added products. In developed economies biomass could be used in combined heat and power (CHP) thus, raising its share in the energy sectors.

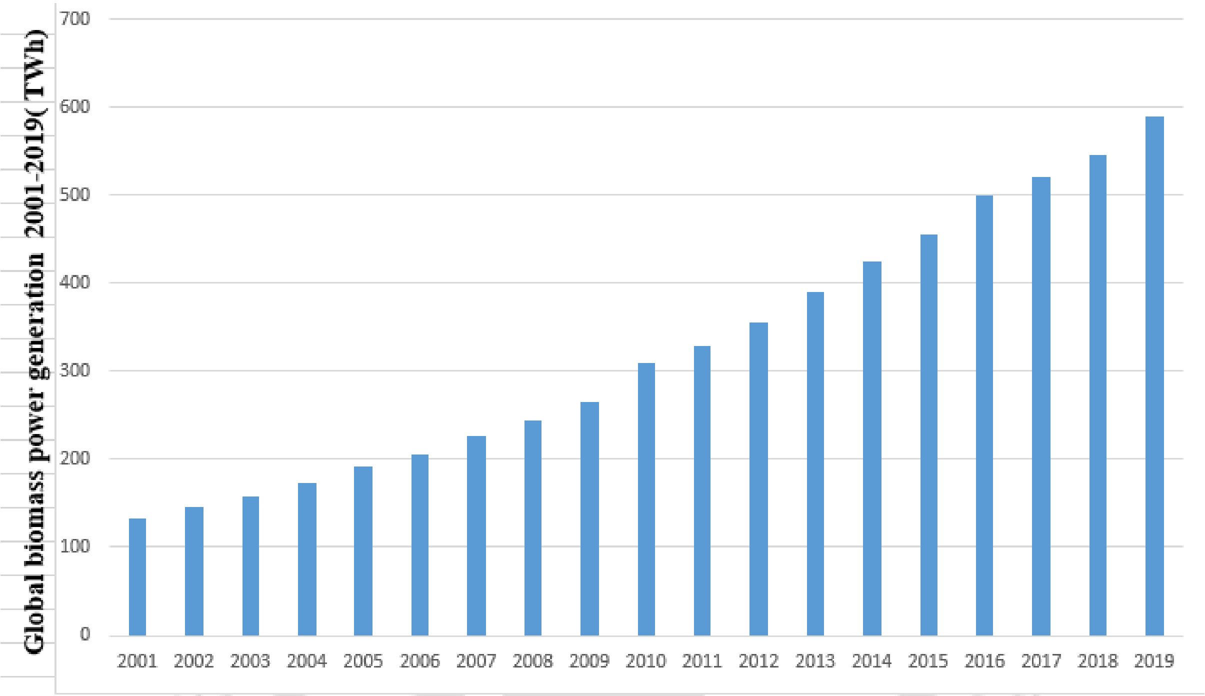

Figure 2.1 Power generation from bioenergy 2001–2019 (TWh) [1]

2.2 Structural composition of biomass

Biomass is considered as a bio polymer consisting of three major components viz. hemicellulose, cellulose and lignin with a small amount of inorganic matter in the form of extractives and ash as shown in Figure 2.2. The structural composition of lignocellulosic biomass depends on the following factors: (1) growing conditions, (2) species, (3) part and age of the plant, (4) geographic location, (5) climatic conditions and seasons, (6) soil type, (7) harvesting conditions of plants. The composition structure determines the kinetics parameters and quality and quantity of the by–products produced during pyrolysis. Although the structural composition of biomass is similar for all lignocellulosic biomass each biomass will exhibit a specific characteristic when they are converted into an energy source because of the percentage composition of the constituent elements and lignin. Low amount of lignin reduces the amount of oxygen in the bio–oil while higher hemicellulose contents of non–wood materials promotes the release of valuable materials during pyrolysis [21,22]. In order to fully utilize biomass for bioenergy and other valuable chemicals such as flavouring and resins, the chemical structure of lignocellulose must be well understood.

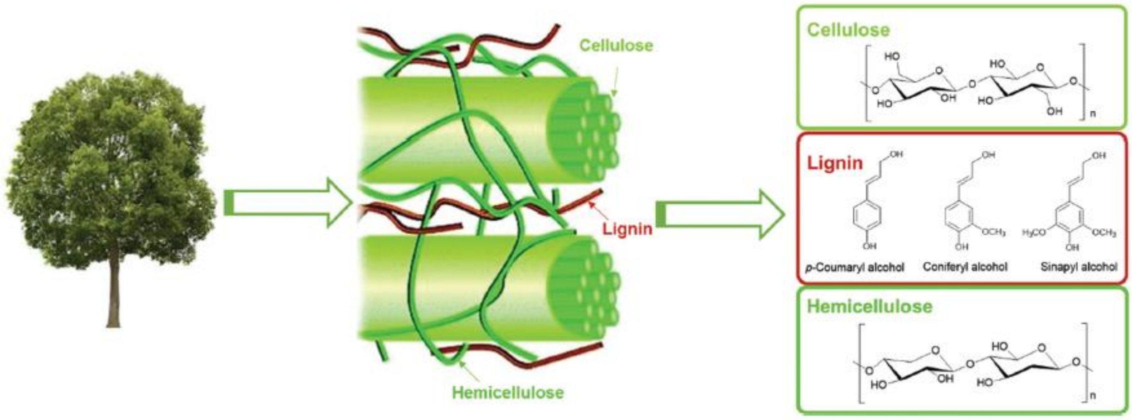

Figure 2.2 Structural composition of lignocellulosic biomass [23]

2.2.1 Cellulose

Cellulose is chemically represented as $(C_6H1OO_5)_n$ where n represents the degree of polymerization (DP) which ranges between 9,000–15,000. Cellulose forms the most abundant natural polymer in the cell wall of the plant It consists of long chains of glucose units linked by β–1,4–glycosidic bonds. The polymer contains three reactive hydroxyl groups at the C–2, C–3, and C–6 atoms, which are in general accessible to the typical conversions of primary and secondary alcoholic OH groups. The un–branched linkage results into linear chains that are stabilized by hydrogen bonds within the chain and between neighbouring chains. During fast pyrolysis the cellulose macrostructure degrades suddenly during the initial stage with a reduction of DP due to cleavage of relatively weak glycosidic bonds which are not strong [24].

The crystalline structure of cellulose is formed when three hydroxyl groups in each pyranose ring interact with one another to form an intra and intermolecular hydrogen bonds. Crystalline properties offer mechanical strength and chemical stability. Studies on lignocellulosic biomass by Shurong et al. (2017) [25], showed that the amount of cellulose in biomass determines the crystallinity indices and the maximum degradation temperature.

2.2.2 Hemicellulose

Hemicelluloses are the second major constituent and are heterogeneous highly branched chain polymers of carbohydrates consisting C5 pentose which include; xylose, arabinose hexoses mannose, glucose, galactose, and sugar acids. It is located beside cellulose and acts a connecting link between cellulose and lignin. In contrast with cellulose, hemicellulose primarily consists of xylose and other five–carbon monosaccharaides [26].

2.2.3 Lignin

Lignin is a complex high macromolecular weight polymer of coumaryl, conferyl and sinapyl alcohol. It is helical and contains ether and carbon– carbon (C–C) linkages. The concentration of these alcohols varies from plant to plant. This polymer is intimately associated with cellulose and hemicellulose and imparts physical strength to the plant. Furthermore, lignin forms a complex matrix in which cellulose micro fibrils are embedded [27].

2.3 Co–pyrolysis of different biomass

Utilisation of biomass with other feedstocks has offered a solution to the looming crisis of first generation biomass. Co–utilization is economically feasible since there is no need of investing in new infrastructures [28]. Also co–pyrolysis of biomass with other feedstock reduces the greenhouse gas emissions emitted by using individual feed stock like coal and polymers. In order to carry out co–pyrolysis in large scale, it is important to select the feedstock appropriately. Characterization of feedstock using standard techniques would provide all the physico–chemical properties thus, helping in choosing the appropriate feedstock. Blending ratio and operating parameters are also crucial since they determine the quality and quantity of products obtained. Diversity and availability of biomass feedstock has contributed to the increased adoption and commercialization of co–pyrolysis. The improved quality and quantity of the products is due to the synergistic effect among the feed stock. The biochar properties depend on type of feedstock and pyrolysis conditions. Previous authors have dealt with this matter, and a brief summary of literature on production and application of biochar and from various feedstock is shown in Table 2.1.

Co–pyrolysis process is similar to the normal slow pyrolysis process, both processes have similar vital features which are: (1) shorter residence times(5-40min) , (2) they take place in an inert atmosphere, (3) requires high heating rates and high heat transfer rates, (4) the feedstock should be finely ground of typically between 2–3 mm. and (5) reaction temperatures are within a range of 400–600°C [29]. The only difference is that co–pyrolysis involves pyrolyzing multiple feedstock together as shown in Figure 2.4. thus producing products with superior qualities that those produced from pyrolyzing individual biomass.

Co–pyrolysis process comprises three major steps: (1) feed preparation which encompasses washing, drying and grinding of the raw materials, (2) conversion of solid feedstock through co–pyrolysis to a more usable form of energy in an inert atmosphere, (3) upgrading of the primary liquid product by either processing, refining, cracking, or hydrogenation to produce a marketable end–product such as: chemicals and biofuels [30].

Table 2.1 Summary of literature review on the characterization of biochar and their applications

Author	**Feedstock**	**Operating temperatures (°C)**	**Reactor**	**Important findings**	**Applications of biochar**
	Cassia fistula	250	Muffle furnace	Higher tendency of adsorption of metal ions in the wastewater	Adsorption (Cu(II) ion for environmental management.
[31]	Pine sawdust Pea straw	350,500, 700	Fixed bed	Bulk density ranging between 0.12–0.17 g/cm^3.BET$_{SA}$ (16.2–397.4 m^2/g) pH (5.6–11.1),	Environmental applications
[32]	Rapeseed stem	200, 250, 300, 350, 400, 450, 500, 550, 600, 650, 700	Muffle furnace	Temperature is the greatest significant factor on biochar. Surface area and morphology were considerably determined by holding time	Soil quality enhancement in an agronomic surroundings
[24]	Apple tree branches	300, 400, 500, 600	Muffle furnace	Biochar consisting more functional groups and low pH values are more suitable for soil amendment in acidic soils	Soil amendment
[33]	Sawdust Eucalyptus, chicken manure Pine bark, coffee husk, sugarcane bagasse,	350, 450, 750	Muffle furnace	Higher ash content due to alkaline and alkali earth metals. Increase of temperature to 750°C reduces the adsorption ability of chicken manure and coffee husk. Biochar can be applied as a liming agents for acidic soils.	Agriculture and environmental applications
[34]	Water hyacinth	300, 500, 700	Tube furnace	Yield was in the range of 28.20–46.59% Mineral constituents permitted absorption Cd through precipitation or co–precipitation. Maximum absorption was 49.837, 36.899, and 25.826 mg g^{-1}	Elimination of cadmium from aqueous solutions
[35]	Rice husk Rice straw Apple tree	400, 500, 600, 700, 800	Fixed bed	High thermal stability at 600° C High biochar yields at low pyrolysis temperature. High yield in rice husk and straw	Carbon storage and soil fertility

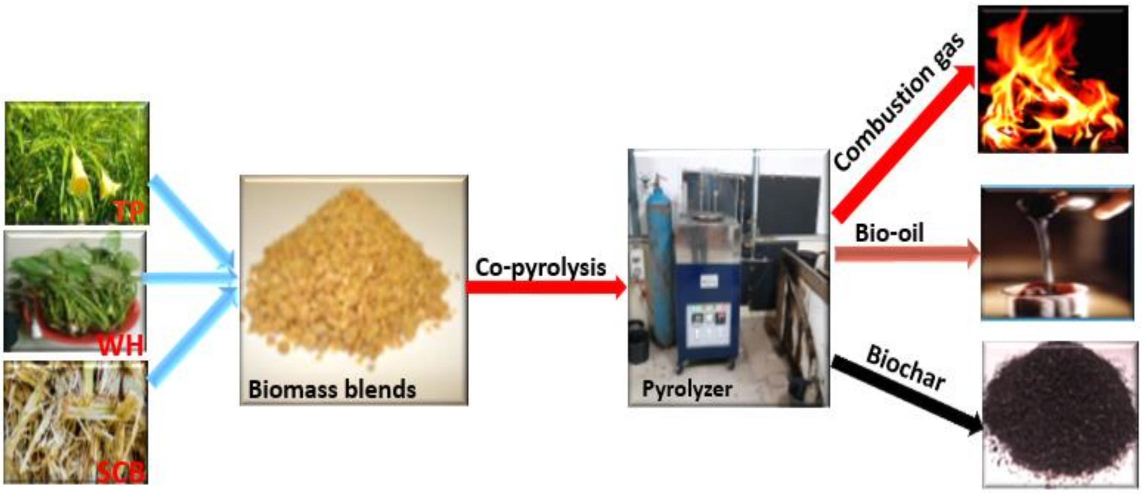

Figure 2.3 Schematic process of co–pyrolysis of lignocellulosic biomass

2.3.1 Co–pyrolysis of biomass with other feedstock

Researches have conducted a lot of experimental works to determine the feasibility of co–pyrolysis of biomass with different raw materials in laboratory and pilot scale set ups. These studies have shown the viability of co–pyrolysis using different feedstock since the quality and quantity of co–pyrolysis products obtained significantly changes as summarized in Table 2.2.

Table 2.2 Summary of the effect co–pyrolysis of biomass with other feedstock

Biomass	Important findings	Ref
Soybean straw+ Soapstock	✓ The amount of aromatics increased and the proportion of oxygen–containing compounds decreased in the bio–oil	[36]
Chlorella+ vulgaris Kitchen waste	✓ Co–pyrolysis enhanced the main pyrolysis stage since TGA–FTIR results showed that the degradation behaviour and the quality of thermal gas released improved after blending. ✓ Produced more hydrocarbons, hence making the bio–oil viable for purification and production chemicals	[37]
Waste tire + Cotton stalk	✓ Increased the bio–oil yield, carbon content of while oxygen reduced. ✓ The higher heating value of the co–pyrolysis bio–oil increased up to 41 MJ/kg which is comparable to diesel. ✓ The synergistic effects led to formation of significant amount of alkanes during co–pyrolysis.	[38]
Rice straw+ Polythene	✓ The yield of bio–oil increased whereas char and gases product decreased with the increase of polythene in the blends.	[39]
Bamboo wastes+ Micro *Chlorella vulgaris*	✓ Catalytic co–pyrolysis promoted the degradation of long–chain fatty acids and O–species thus decreasing the amount of bio–oil.	[40]
Sewage sludge+ Micro *Chlorella vulgaris*	✓ The co–pyrolysis kinetics showed a change in the reaction mechanism. ✓ The TGA showed that there was a slight change in the decomposition between individual pyrolysis of feedstock and co–pyrolysis below 550 ºC while obvious interaction was found from 550–700ºC during co–pyrolysis	[41]
Oil shale+ Wheat straw	✓ The presence of minerals such as calcite in oil shale make the oxygen in biomass move from oil to gas, thus enhancing the quality of bi–oil. ✓ Biomass offers H and other hydrocarbon free radicals during the reintegration process of kerogen, resulting in a lower energy obstruction, more saturated hydrocarbons, and a higher H/C ratio in shale oil.	[42]

2.3.1.1 Co–pyrolysis of biomass with polymers

Waste generation from plastic results to enormous build–up in the landfill and in the other natural habitats like rivers, lakes and oceans. The accumulation of these non–biodegradables wastes have an adverse impact in the surrounding flora and fauna. Thermal treatments like combustion and incineration are the most common methods being used to eradicate the plastic waste permanently but such processes result to generating toxic emissions to the environment. Reprocessing of the waste is another possible route for waste management of plastic. However, most of the recycling processes are energy demanding, expensive, and produces low–quality products. Plastics are synthetic polymers produced from petroleum products and their consumption and production is greater than before thus increasing the fossil fuel demand. Global production of plastics is approx. 380 Mtoe with a compounded growth of about 8.4% per year [43]. The global annual plastic production had surpassed approx. 360 million tonnes in 2018 and the consumption is progressively increasing to meet the high demand. Majority of the plastic remain as a pollutant to the environment since approx. 13% of plastic waste goes to recycling while the remaining end up in the landfill. Therefore, it is important to adopt some sustainable ways of handling these different types of plastics wastes available. Therefore, the co–pyrolysis of biomass and plastics have been found to be viable because plastics tend to have a higher H/C_{eff} hence a higher synergistic interaction exists between biomass and plastic. Therefore, the co–utilization of biomass and plastics with hydrogen rich is a real time solution that improves the overall H/C_{eff} of blends. Plastics with high H/C_{eff} ratio function as hydrogen donor for biomass conversion during co–pyrolysis. Co–pyrolysis is a very feasible and sustainable waste management process in the handling of municipal solid waste containing non–biodegradable materials like plastics.

Previous researchers have extensively studied co–pyrolysis of various biomass with different types of plastic viz. (1) polyvinyl chloride (PVC), (2) polypropylene (PP), (3) polycarbonate (PC), (4) polystyrene(PS), (5) polyethylene terephthalate polyethylene (PET/PETE), (6) high–density polyethylene (HDPE), and (7) low–density polyethylene (LDPE). Co–processing of biomass with polymers leads to the production of a high quality liquid fraction.

Many researchers have studied on co–pyrolysis of various types of plastics with different biomass to improve the yield, quality and quantity of bio–oil. When biomass pyrolyzed individually a lower yield of bio–oil is obtained which could be attributed to the relatively low amounts of hydrogen as shown in Table 2.2. It could be observed that the range of hydrogen in different types of biomass is in the range of 4–12% as shown in Table 2.3. Therefore, using feedstock with higher amount of hydrogen would help in improving bio–oil yield. This is why plastics are considered the most appropriate feedstock for co–pyrolysis. Many researchers have reported that co–pyrolysis of biomass and plastics resulted to increased bio–oil yields while the char significantly reduced.

Tang et al. [44] reported that the co–pyrolysis of microChlorella vulgaris and LDPE could promote production of small molecule olefins and high gas yield. This is attributed to the presence of O– and N– functional groups that promotes the depolymerisation of LDPE to procedure light molecular gases. Therefore, the results showed that co–pyrolysis allows the demethoxylation of carbohydrates present in biomass and the end–chain fission reactions of aliphatic acids, long– chain N–containing compounds, and long–chain hydrocarbons from plastics. In line with the results reported by Tang et al. [44] co–pyrolysis also depends on the operating conditions in the reactor. Dewangan et al. [45] studied the co– pyrolysis of sugarcane bagasse and LDPE and they reported that a blend consisting a ratio of 1:1 had a higher yield of bio–oil. The yield increased by 52.75% wt. The increase could be attributed to the presence of more hydrogen in the LDPE. Additionally, it was observed that the biochar yield decreased with an increase in LDPE ratio as a result of higher degree of conversion of LDPE and due to the secondary cracking of volatile matter present in char.

Hassan et al. [46] in their work reported that a positive synergistic effect existed in the feedstock and a higher yield on the bio–oil was observed, which could be ascribed to the interaction between the HDPE derived H radical and the SCB derived radical; further, the interface interaction repressed the production of low molecular product in form of gas and enhanced the establishment of bio–oil with high molecular weight organic compounds. Consequently, co–pyrolysis supressed acid formation by stimulating the transformation of carboxylic acid into aliphatic hydrocarbon through decarboxylation.

In their work Pinto et al. [47] demonstrated that structural composition of the biomass is an important factor. It significantly affects the degree of synergistic interaction between the blends during co–pyrolysis. It was observed that from the three biomass used a similar trend occurred with increase of PE up to 50% wt. there was a relatively high yield of bio–oil, and a decline in the gas yield. These results were attributed to the fact that PE degraded easily and had a higher conversion rate as shown by the TGA thus, a high mass and energy transfer was significantly favoured [47]. The pre– treated eucalyptus had a high yield than corn cob and miscanthus at 210°C. The bio–oil yield increased by 20% which corresponded to an increase of about 16% in total conversion in contrast to the other two feedstock which showed a slight increase in the bio–oil yield.

Izzatie et al. [48] co–pyrolyzed rubber wood sawdust and PP at a blending ratio of 1:1 and temperature 450–600°C. In their work they demonstrated better results in terms of high yield of 36.47 wt% at temperature 550°C compared to results reported by Hassan et al. [46]. The variation of the results could be attributed to the composition of the plastics. Some plastics tend to degrade at lower temperatures than others as shown by TG analysis. They further noted a fast reduction of bio–oil and char at 600°C and high production of syngas. These results were attributed to, at high temperature secondary cracking of blends and char occurred hence promoting further release of condensable vapour to syngas gas. Thermogravimetric studies on plastics and biomass shows that the decomposition of biomass takes three stages while that of plastics occurs in a single stage at higher temperatures within a very short range of temperature. Moreover, there was no residue left over at the final temperature in the case plastics.

Augustina et al.[49] showed that PVC had a high positive synergy on char yield, reporting a maximum value of 8 wt% when 30 wt% PVC was added in the pyrolyzer, whereas PS only showed a slightly positive synergy of 2.5 wt% at optimized levels. The reduced positive synergy was a result of PS promoting secondary reactions which formed secondary char. Whereas a high positive synergy was reported when PVC was co–pyrolyzed. This was as a result of emission of chlorine which form hydrochloric acid. The hydrochloric acid facilitated hydrolysis of the biomass which further contributed to the degradation of the cross–linking of cellulose in biomass, which in turn helps the carbonizing of cellulose. Similar results have been reported in other works by Matusuzawa et al. [50] where dehydration and charring of the cellulose was observed. It can be noted that co–feeding of different feedstock has contributed to high yield of char. Recent research on co–pyrolysis of biomass and PVC seem to differ with results reported with some researchers showing an insignificant effect of HCl on cellulose there the synergetic effect is relatively low. Therefore, more studies are needed to provide a better understanding of the mechanism that govern the interactions between HCl and biomass. Similarly, more attentions should be on the adverse effect of dioxins emitted when PVC is burnt and how they can be managed sustainably in the co–pyrolysis process. The co–pyrolysis of biomass and plastics have been found to be successful because of high yield and good quality bio–oil. However, the utilization of plastics as additive material is facing some challenges because of two major reasons. The first being its inadequate supply of waste plastic as majority of it is been recycled and secondly many countries have banned use of plastics for packaging which have tremendously reduced as PE and PP are the most common plastics used for producing packaging material. Plastics contains higher volatile matter hence co–pyrolysis of biomass with plastics will yield more bio–oil and syngas with less char. A summary of the most recent studies on co–pyrolysis of biomass and plastics are outlined in Table 2.4.

Table 2.3 Proximate and ultimate analysis of biomass and polymers

Feedstock	**Proximate analysis %wt**				**Ultimate analysis %wt**						**HHV MJ/kg**	**Ref**
	MC	**AC**	**VM**	**FC**	**C**	**H**	**O**	**N**	**S**	**Cl**		
					Biomass							
Wood chip	9.50	1.10	74.80	14.60	50.1	5.70	44.00	0.10		0.01	18.20	[51]
Kitchen waste	8.00	2.00	85.10	4.00	49.90	6.40	42.70	1.00		0.00	17.10	[52]
Rubber wood sawdust	4.30	1.80	79.80	14.10	44.20	7.20	48.30	0.30			18.90	[48]
Micractinium conductrix	10.55	23.28	58.97	7.20	33.87	3.97	57.75	4.41				[53]
SCB					55.06	4.71	39.56	0.56	0.11	0.00	20.26	[46]
Rice straw	7.61	8.80										[54]
Corn stove	3.18	4.44	73.83	18.56		5.13	50.03	0.61	0.08			[55]
Bamboo sawdust					48.88	7.59	43.14	0.39				[56]
Niger seed	5.97	6.6	86.13	1.3	50.96	7.13	37.58	4.05				[57]
Karanja seed	7.27	1.5	89.23	2.0	53.04	7.32	35.58	3.94	0.17			[57]
					Plastic Waste							
PP	0.00	0.00	100.00	0.00	85.40	14.60	0.00	0.00	0.0	0.00	49.40	[58]
PP	0.00	0.00	99.20	0.80	87.80	10.60	1.40	0.20			46.30	[48]
PS	0.00	0.00	99.60	0.40	92.40	7.80	0.00	0.00		0.00	39.80	[14]
PVC	0.00	0.00	95.80	4.20	38.70	4.80	0.00	0.00		56.60	19.30	[49]
HDPE					76.61	11.29	11.84	0.13	0.13	0.00	42.05	[46]
HDPE	1.02	4.10										[54]
PP					84.55	15.45						[56]
Waste polystyrene	0.5	99.50			91.5	8.5						[57]

Table 2.4 Summary of the effect co–pyrolysis of biomass with other feedstock

Biomass	**Plastic**	**Blending ratio**	**Type of reactor**	**HR (°C/Min)**	**Temp (°C)**	**HHV (MJ/kg)**			**Important findings**	**Ref**
						biomass	waste	Mixture		
Wood chip (WC)	PP	1:1	Fixed bed	20°C	600°C	18.2	49.4	45		[23]
Sugar cane bagasse	LDPE	9:1 3:1 1:1 1:3	semi–batch	20°C	500°C	35		40	High yield of bio–oil of 52.75%wt at ratio 1:1. Char decreased with addition of LDPE	[45]
Polar wood	PS & PVC			20°C	750°C					[14]
Nannochloropsis	LDPE	0:25 33:50 67:75 100	Fixed bed reactor		600°C				High gas yield at 75% LDPE. Polyaromatic hydrocarbons reduced in the bio–oil with increase of LDPE	[44]
Rice straw	HDPE	0:100 30:70 50:50 70:30 100:0	Batch reactor		550°C				Viscosity, density, and average molecular weight reduced with increasing HDPE ratio	[54]
Sugar cane bagasse	HDPE	0:100 20:80 40:60 60:40 100:0	Fixed–bed reactor	10°C	400–600°C	19.01	51.32		Co–pyrolysis supressed acid formation. There was high reduction of oxygenated compounds at 600°C with high yields of bio–oil	[46]
Eucalyptus forestry waste, Corn cobs Miscanthus	PE	0–100%	Autoclave		400°C		46.4		Pre–treatment of eucalyptus increased the bio–oil yield. Compositional structure of the biomass determines the extent of synergistic interactions	[47]
Rubber wood sawdust	PP	1:1	Fixed bed drop–type		450, 500,550,600,650				Hydrocarbons, alkyl acyclic olefin, and aromatic groups are the main functional groups in the bio–oil. 50% increase in CV of the co–pyrolyzed oil	[48]

2.3.1.2 Co–pyrolysis of biomass with sewage sludge

Management of sewage sludge (SS) is one of the greatest challenges been experienced by waste water treatment plants. It is only when SS is managed in a sustainable way then the wastewater treatment process is considered complete. Currently three methods are used to dispose SS: incineration, agricultural use and landfill. Both Incineration and landfill have been found to be uneconomical while agricultural use result to soil contamination due to presence of pathogens and toxic substances in SS [59–61]. Therefore, it is necessary to find a sustainable alternative of using the abundant SS waste generated by waste water plants. Co–pyrolysis of SS is one of the promising methods to manage the waste from water treatment plants. Thus SS has demonstrated to be a good a raw material for producing biochar, which can be used for soil amendment and as a solid fuel. Raw SS has a low heating value comparable to that of low–grade coal hence it important to find alternatives method of upgrading its quality. Though, SS is readily available in large amount the problem is that it contains high moisture content and biochar obtained from SS contains high amount of leachable heavy metal elements [62–64]. Therefore, to solve this problem many researchers have studied the effect of co–pyrolysis of SS with other biomass to investigate how blending can improve the quality co–pyrolysis products and enhance their application. Moreover, co–utilization of SS and biomass enables the reduction of the toxic substances in the bio char. The presence of alkali and alkali metals in SS provide the catalytic effect which improves on the yield of the co–pyrolysis products. This section reviews the most recent studies on the co–pyrolysis of different biomass feedstock with SS.

Regarding the synergistic interactions between sewage sludge and biomass have been widely investigated. Major interactions have been reported as a result of high ash content present in the sewage sludge, which catalyses the secondary reactions such as dehydrogenation, cracking, and dehydration. Alvarez et al. [65] carried out a comparative study on co–pyrolysis of pine saw dust and sewage sludge and the individual biomass. The authors concluded that major synergistic were detected the bio–oil yield decreased by 12% and gas yield increased by 48%. These results were attributed to the presence of some inorganic elements viz. Mg, K, and Ca in the SS that promotes the breaking down of holocellulose from biomass, preferring syngas formation.

Chlorella vulgaris is one of the promising feedstock for biofuels though the high cost has hindered its full utilization. Co–pyrolysis of *Chlorella vulgaris* with other feeds stocks is a feasible option to reduce feedstock cost and realize its application for fuel production. Wang et al. [41] studied the co–pyrolysis micro *Chlorella vulgaris* and SS at three different blending ratios and qualitatively assessed the composition of the bio–oil obtained. It could be observed that blending ratio is an important parameter during co–pyrolysis process. From the co–pyrolysis of blend SI21 the bio–oil had more ketones and aldehyde yield up to 11.32% than bio–oil from micro *Chlorella vulgaris* (5.54%) and sewage sludge (4.82%) while bio–oil from blend SI11 had a maximum alicyclic hydrocarbons content of 7.22%. Similar results were observed from the different heating value reported from the bio–oil obtained for the three blends. They concluded that an interaction existed among the feedstock since the yield of C4 and C7 increased while yield of C9 decreased in carbon distribution.

Many researchers have found that biochar is one of the promising product due to its multiple applications [11,66]. However, the properties of the biochar are highly dependent on the pyrolysis conditions considered and feedstock [24,67,68]. Therefore, to optimally produce biochar for different application the latter should be well selected. For the large scale production of the biochar availability of feedstock is a major factor that ought to be considered because biomass have been found to have several competing uses. Using SS as raw feedstock to produce biochar is sustainable method of ensuring continuous supply of raw material for the pyrolysis plant and reduce SS water treatment plants. Lately a lot of work have been done on pyrolysis SS to produce biochar for various applications [69–72]. Though, pyrolysis of SS results in biochar which has low surface area and pore structure due to the lower carbon quantity in SS. Also the pyrolysis of lignocellulosic biomass result into biochar that has lower bulk density hence not convenient to store and transport [11,32,66]. Co–pyrolysis of lignocellulosic biomass and SS would not only avert the shortcomings of biochar with low porosity and density but as well successfully uses the metal elements in the SS. Yin et al. [73] investigated the adsorption of $NH_4^+$and $PO_4^{3-}$from eutrophic water using biochar produced from co–pyrolysis of wall nut and sewage sludge. They concluded that biochar produced from the blend mixed from sewage sludge and walnut shell at a blending ration of 3:1 showed a high adsorption capacity for NH_4^-. This results could be attributed to the increase porosity in the biochar produced similar results were reported by [74].

2.3.1.3 Co–pyrolysis of multiple biomass

The growth of a bio–based economy is fast hence, most developing countries are in the process of implementing the concept of a bio refinery. The concept not only allows the reductions of greenhouse gases but allows energy security. It also enables the advancement of a regenerative loop economy by using various biomass. The concept has been realized through valorisation of the readily available biomass through co–pyrolysis of two or more biomass. Several studies have been done on pyrolysis of individual feedstock but due to competing uses and inadequate supply of biomass. Pyrolysis of a single biomass can't be fully relied on in a bio–refinery [75–79]. Therefore, researchers are studying the possibility of co–utilizing multiple biomass such as noxious weeds, agro–residues, and aquatic plants that have a short gestation period and readily available. Xu et al. [80] co–pyrolyzed water hyacinth and rice in a fixed bed reactor in different blending ratios and they observed that higher yield of 44.4 wt. %

for bio–oil with more aliphatic compounds. Hua et al. [81] have studied the co–pyrolysis of sugarcane bagasse and *E. prolifera* in 1:1 ratio. Blending of biomass in the same ratio reduced the acidity of the bio–oil produced while increasing its heating value.

The findings of various researchers have been summarized in Table 2.5. From the review of literature, it has been observed that there was an improvement in the of quality of produced bio–oil and biochar. These results were attributed to the synergistic interactions that occurred during co–pyrolysis due to variation of the compositional structure of various biomass.

Table 2.5 Summary of literature review on the co–pyrolysis of biomass blends

References	Feedstock	Blending ratio	Reactor type	Temperature	Important finding
[80]	Water hyacinth and rice	5:5, 7:3 and 3:7	Fixed bed reactor	300,350,400 and 450°C	Higher yield of 44.4 wt % for bio–oil More aliphatic compounds in bi–oil
[81]	Sugarcane bagasse and *E. prolifera*	50/50	Fixed bed reactor	550°C	Heating value for bio–oil was 26.4 MJ/kg. Acidity and density decreased
[82]	*Isochrysis* and *Chlorella vulgaris*:			400–500°C	
[83]	Enteromorpha and rice husk	–	Thermogravimetric coupled with mass spectrometry	–	Bio–oil yields reduced
[84]	*Chlorella vulgaris*, wood sawdust	100%CV, 70%CV:30%WS, 50%CV:50%WS, 30%CV:70%WS, 100%WS	Microwave–assisted pyrolysis	–	Higher bio–oil than biochar yield CV of bio–oil reduced by 30% in blend 50CV:50WS
[85]	Para grass and Phumdi	1:1	Laboratory scale glass reactor	300–500°C	High bio–oil yield of 37.80 wt%
	Rice husk and pine sawdust	30:70	Muffle furnace	200 and 500°C	

2.4 Significance of co–pyrolysis

Sustainability, cost effectives and efficiency are some of the parameters that determine the importance of developing a certain technology to produce the end products. Therefore, the idea of co–pyrolysis of various feedstock with biomass is a viable technology for improving the quality of the products as shown in Table 2. Co–pyrolysis has been found to be promising because of:

- ✓ It is carried out under an anaerobic condition with moderate operating temperature and pressure.
- ✓ Produces homogenous products which are more preferred because bio–oil have been found to be polar in nature and blending of different types of bio–oil would lead to phase separation [86–88].
- ✓ It allows interaction of radicals during co–pyrolysis which could contribute to improving the stability of pyrolysis oils, hence avoiding the phenomenon of instability. Addition of plastic waste in the blends considerably changes the composition of bio–oil obtained.
- ✓ The production of reactive oxygenated compounds such as aldehydes, acids, and ketones are inhibited, hence more stable hydrocarbons, esters, and alcohols are produced thus reducing the aging of the bio–oil [47].
- ✓ It is an alternative technique for waste management because it uses assorted waste as raw materials [89]. Co–pyrolysis allows the use of all waste materials having carbon both inorganic and organic as opposed to biochemical conversion technologies.
- ✓ Co–pyrolysis permits the use of the heterogeneous feedstock hence making it easy and economical since waste separation and sorting processes is not a perquisite. [23,90].

- ✓ Co–pyrolysis of biomass with polymers like plastics reduces the energy consumption needed for drying since plastics contain 0% moisture content as shown in Table 2.2.
- ✓ Co–pyrolysis process doesn't not require any solvent, hydrogen and catalysts which are required during the upgrading process of the bio–oil thus making co–pyrolysis more economical. Catalysts have been found to increase the operating heads since they are consumables, have short life span as a result of deactivation and poisoning thus affecting the life span of the bio–oil and they increases the solid waste in the process [91].
- ✓ Co–pyrolysis of coal and biomass leads to the reduction of emission of CO_2 in the downstream application of pyrolysis products not comparable with pyrolysis of coal individually.

Notwithstanding all the merits discussed above co–pyrolysis it is facing some challenges:

(1) instability of the bio–oil. (2) production of toxic gases during the thermal degradation of some plastics. Chlorinated aromatics and hydrochloric acid are some of the harmful toxics generated by degradation of PVC. It is not advisable to utilize such waste for co–pyrolysis without dechlorination process. Similarly, polystyrene has some poisonous elements styrene, benzene, and neurotoxins that are emitted when burnt at temperatures less than 900°C and they are harmful to human beings [92]. (3) Also availability of the PE and PP is an issue since many countries are either phasing out the use of light weight plastics commonly made of LDPE by either applying charges or banning their use. Globally as at 2019 62 countries had totally banned the use of plastic bags and 31 countries have imposed a charge per bag. This enforcement has greatly reduced the amount of plastic waste generated by many households [93,94].

2.5 Summary of literature review

In this chapter a critical literature review has been presented and summarized. Based on the literature review research gaps were identified. Most previous studies in this area of pyrolysis have focussed on individual feedstock from the same habitat – either terrestrial or aquatic. A comparative study is necessary to determine the potential of utilizing various biomass by characterizing various raw materials obtained from different habitants prior to kinetic analysis. From the open literature reviewed co–pyrolysis of biomass and other feedstock have shown a great potential of producing high quality products viz. bio–oil and biochar, hence there is a huge scope in future for commercialization of this technology. – However, the literature reporting on co–pyrolysis and kinetic analysis of blended feedstock of two or more biomass is quite limited. Previous authors have reported synergistic interactions (either supportive or opposing) between the individual biomass during process of co–pyrolysis, which results in significant changes in activation energies and kinetics of conversion. Many researches have studied the kinetics analysis of biomass blends with coal, plastics and sewage sludge using conventional methods viz. Ozawa–Flynn–Wall (OFW). The International Confederation for Thermal Analysis and Calorimetry (ICTAC) has recommended the use of more accurate equations and performing an iterative correction procedure for the value of activation energy. Furthermore, all integral isoconversional methods are based on assumption that activation energy remains constant over the whole interval of integration. In practice, such behaviour is not observed. More research using advanced isoconversional methods like Vyazovkin_AIC model and Distributed Activation Energy model (DAEM) on biomass blends is necessary to enable the utilization of abundantly available biomass. It is important that more research should be carried out to rationalize how co–pyrolysis could be used to produce quality biochar for various applications.

2.6 Scope for research

From the literatures reviewed in different sections of this chapter co–pyrolysis should be further studied and developed as a sustainable method for production of high quality products viz. biochar and bio–oil by investigating the eminent issues proposed below:

- Characterization and kinetic analysis of raw biomass prior to blending.
- Investigation of the physicochemical properties and kinetic parameters of the biomass blends at different ratios.
- Synthesize and characterization of biochar (under varying conditions) from various biomass from viewpoint of energy and agricultural applications.
- Optimization of the co–pyrolysis process by varying various pyrolysis conditions viz. heating rate, temperature, residence time, gas flow rate.
- Characterization of co–pyrolyzed products is limited therefore, there is a need to investigate bio–oil properties to determine its application in diesel engine setup

In the next chapter physico–chemical characterization and kinetics analysis of water hyacinth, *Thevetia peruviana*, and sugarcane bagasse are presented.

CHAPTER 3– Physico–chemical characterization and kinetics analysis of water hyacinth, Thevetia peruviana, and sugarcane bagasse

3.0 Introduction

More recently, waste biomass such as grasses and invasive weeds have been explored as possible sources of bioenergy. Development of efficient technologies for thermal conversion of biomass to liquid and gaseous fuels requires comprehensive understanding and information on the kinetics of such processes. Pyrolysis has been a popular technique of biomass treatment as it yields two products, viz. bio–oil, a precursor for liquid biofuels and chemicals, and biochar, which has potential applications in agronomy, geo–engineering and energy [95,96].

In this chapter, kinetic analysis of thermal conversion of two noxious weeds, viz. *Eichhornia Crassipes* (or water hyacinth, WH) and *Thevetia peruviana* (or yellow oleander, TP), which are abundantly found in Asia and Africa [97–102] have been discussed. In addition, studies on sugarcane bagasse (*Saccharum Officinarum*, SCB) is also carried looking into the importance of utilization of waste especially in India as well as developing economies in Africa (for example Kenya). With sugar production in India crossing 35 million tons per annum, tremendous quantities of bagasse are available at relatively cheaper price.

This chapter also discusses a comprehensive characterization with the help of standard techniques and kinetic analysis (i.e. determination of kinetic triplets) using conventional models, viz. KAS, OFW, and Friedman of WH, TP and SCB. Moreover, kinetics analysis with Vyazovkin_AIC model, which is an advanced integral isoconversional method that accounts for continuous variation in activation energy during the conversion has also been presented.

3.2 Materials and method

3.2.1 Feedstock selection and collection

Biomass of WH and TP were collected from IIT Guwahati campus (latitude 26.1879° N, longitude 91.6916° E), while SCB was obtained from a local market outside the campus. All biomass materials were washed under running water and sun–dried for 4 h to remove the excess water. Later, all biomass feedstock were oven–dried at 105 ± 2 °C for 12 h, followed by grinding and sieving through a 2 mm sieve. The samples were stored in airtight containers under ambient conditions.

3.2.2 Physical and chemical analysis

Proximate analyses of the three biomass were carried out as per the ASTM standards, viz. ASTM: E871–82 moisture content (MC), ASTM D1102–84 ash content (AC), ASTM: E872–82 volatile matter content (VM). The fixed carbon content (FC) was calculated by difference. The ultimate analyses were carried out to determine the elemental composition of the biomass using a CHNSO elemental analyzer (Make: Euro EA, Model: Eurovector EA3000) as per the ASTM standards E–777 (carbon and hydrogen content) and E–778 (nitrogen content). The oxygen content (or percentage) was determined by difference [22].

3.2.3 Calorific value

The calorific value or the higher heating value (HHV) of the three biomass was determined using an oxygen bomb calorimeter (Make: PARR, Model: 1341EB), according to standard ASTM D2015. HHV were calculated using Eq. (3.1).

$$HHV = \frac{\Delta \mathrm{T} \cdot W - \varepsilon_1 - \varepsilon_2 - \varepsilon_3}{m} \tag{3.1}$$

where, ΔT denotes the change in temperature (°C), W = energy equivalent of the calorimeter (cal $°C^{-1}$), m = quantity of the feedstock (g), ε_1 = correction factor in calories for the heat of formation of HNO_3 (cal), ε_2 = correction for the heat of formation of H_2SO_4 (cal), and ε_3 = correction for the heat of combustion of fused wire (cal).

3.2.4 Bulk density

The bulk densities of three raw biomass materials were determined using the mass per unit volume method, according to standard ASTM E 873–872 and calculated using Eq. (3.2) [103].

$$\text{Bulk density} = \frac{W_2 - W_1}{V} \tag{3.2}$$

where W_2 = weight of container + sample, W_1 = weight of empty container, V= volume of the container.

3.2.5 Compositional analysis

The structural composition contents of the feedstock, i.e., holocellulose and lignin, were determined following the procedure reported by Disco *et al.* [104] and Omoniyi *et al.* [105].

3.2.6 EDX analysis

Energy–dispersive X–ray spectroscopy (EDX) was used to approximate the presence of mineral matter in raw biomass and ash. The analysis was carried out using FESEM/EDX analyzer (Make: Zeiss, Germany, Model: Sigma 300).

3.2.7 X–Ray diffraction analysis

X–ray diffraction patterns of the three biomass were obtained using an XRD diffractometer (Make: Bruker, Netherlands, Model No: D8 Advance). The scanning range was $2\theta = 10^\circ$–50° with scan speed of $0.05^\circ\ s^{-1}$ and Cu–Kα radiation ($\lambda = 1.54056$ Å). The crystallinity index (*CrI*) of the feedstock was determined as [106]:

$$CrI\ (\%) = \frac{I_{002} - I_{amor}}{I_{002}} \times 100 \tag{3.3}$$

where I_{002} = crystalline plane intensity at $2\theta = 20^\circ$–22.8°, I_{amor} = amorphous plane intensity at $2\theta = 16^\circ$–18°.

3.2.8 FESEM Analysis

The surface morphology of biomass was assessed with FESEM micrographs (Make: Zeiss, Germany, Model: Sigma 300).

3.2.9 Fourier transform infrared spectroscopy

The functional groups present in WH, SCB TP were identified using solid–state Fourier transform infrared (FTIR) (Make: M/s Shimadzu, Japan Model: IRAffinity–1) in the wavelength range of 500–3500 cm^{-1} at a resolution of 4 cm^{-1}. The samples were mixed with potassium bromide in ratio 1:100 (w/w), and the mixture was compressed to form a pellet of 1 cm in diameter.

3.2.10 Thermogravimetry

The pyrolysis of WH, SCB, and TP was carried out in a thermogravimetric analyzer (TGA) (Make: M/s Netzsch, Germany, Model: TG 209 F1 Libra) to determine mass loss as a function of temperature. Sample amount of 5–10 mg was used in all experiments. Pyrolysis tests were carried out at three heating rates of 10°, 30°, and 40°C min^{-1} in the temperature range of 30°–700°C under nitrogen atmosphere. The data recorded were analyzed using STAR software. Data obtained from TGA experiments was used to determine kinetic parameters.

3.3 Kinetic analysis of biomass pyrolysis

The TGA data for pyrolysis was analysed using several models to get insight into the kinetics of the biomass under varying process conditions.

3.3.1 Determination of kinetic parameters

The rate of thermal decomposition of solid–state material to volatile products is described as:

$$\frac{d\alpha}{dt} = k(T)f(\alpha) \tag{3.4}$$

where, $\frac{d\alpha}{dt}$ is the rate of conversion, $k(T)$ is the rate constant as a function of temperature, and $f(\alpha)$ is the solid state reaction model. The degree of conversion of the sample is denoted by α, which is related to mass loss as:

$$\alpha = \frac{x_i - x_t}{x_i - x_f} \tag{3.5}$$

where, x_i = initial mass, x_t = mass of the feedstock at a time (t), x_f = residue mass at the end of degradation. The rate constant $k(T)$ is expressed by the Arrhenius equation as:

$$k(T) = A\exp\left(\frac{-E_\alpha}{RT}\right) \tag{3.6}$$

where, A is the pre–exponential factor (s^{-1}), E_α is the effective apparent activation energy (kJ mol^{-1}), T is absolute temperature (K), and R is the gas constant (8.314 J mol^{-1} K^{-1}).

Combining Eqs. 3.4 and 3.6, the rate of conversion can be expressed as:

$$\frac{d\alpha}{dt} = A\exp\left(\frac{-E}{RT}\right) f(\alpha) \tag{3.7}$$

3.4 Isoconversional methods

Thermal degradation of biomass during pyrolysis involves numerous chemical reactions as the structural components, viz. cellulose, hemicellulose, and lignin undergo decomposition. Thus, the degradation cannot be described based on a single or a well–defined set of chemical reactions [107]. Because of this limitation, isoconversional (or model–free) methods have been employed for the analysis. Isoconversional methods are aimed at determining the kinetics triplets of the thermal decomposition without a prior assumption of the reaction model. These methods follow the isoconversional principle, which states that "at a constant degree of conversion, the reaction rate is a function only of the temperature (given by Eq. (8)" [108]. Isoconversional methods are broadly classified into two broad categories, differential and integral. The classification depends on the computation of the main solid–state Eq. (3.6). The differential method uses the differentiation of solid–state Eq. (3.6). while integral is established on the integral form of the non–isothermal rate law defined by Eq. (3.8).

$$\left[\frac{d\ln\left(\frac{d\alpha}{dt}\right)}{dT^{-1}}\right]_{\alpha}=-\frac{E_{\alpha}}{R} \tag{3.8}$$

The isoconversional methods used for the kinetic analysis of the three biomass are described below.

3.4.1 Friedman method

Friedman is a differential isoconversional method and is used to determine the activation energy at any constant value of α independent of the solid–state reaction model $f(\alpha)$. Application of the isoconversional principle to Eq. (3.8) results in the Friedman equation given as:

$$\ln\left(\frac{d\alpha}{dt}\right)_{\alpha,i}=\ln\left[\beta_i\left(\frac{d\alpha}{dT}\right)_{\alpha,i}\right]=\ln\left[f(\alpha)A_{\alpha}\right]-\frac{E_{\alpha}}{RT_{\alpha,i}} \tag{3.9}$$

The slope of plot of $\ln\left[\beta\left(\frac{d\alpha}{dT}\right)\right]_{\alpha}$ versus $\frac{-1}{RT}$ for any constant value of α gives the activation energy. The conversion derivative, $\frac{d\alpha}{dT}$, of the data was calculated using the Eq. (3.10). The least–square regression technique was used to smoothen the fluctuations of the derivative conversion curve [109].

$$\left(\frac{d\alpha}{dT}\right)_i=\left\{\begin{array}{c}\left[\frac{\alpha_{i+1}-\alpha_i}{T_{i+1}-T_i}\right]_{\text{first point}}\\ \frac{1}{2}\left[\frac{\alpha_i-\alpha_{i-1}}{T_i-T_{i-1}}+\frac{\alpha_{i+1}-\alpha_i}{T_{i+1}-T_i}\right]_{\text{middle points}}\\ \left[\frac{\alpha_i-\alpha_{i-1}}{T_i-T_{i-1}}\right]_{\text{last point}}\end{array}\right\} \tag{3.10}$$

3.4.2 Kissinger–Akahira–Sunose (KAS) method

The KAS method is an integral isoconversional method and it has been widely used for kinetic studies in thermal conversion of biomass. The governing equation of KAS method is given below, and at any constant value of *α,* the activation energy can be calculated from the slope of the plot $\ln\left(\frac{\beta}{T^2}\right)$ versus $\frac{-1}{RT}$.

$$\ln\left(\frac{\beta_i}{T^2_{\alpha,i}}\right) = const - \frac{E_\alpha}{RT_{\alpha,i}} \tag{3.11}$$

3.4.3 Ozawa– Flynn –Wall (OFW)

The OFW method is also an integral isoconversional method and the governing equation is:

$$\ln(\beta)_{\alpha,i} = const - 1.052\left(\frac{E_\alpha}{RT_{\alpha,i}}\right) \tag{3.12}$$

The activation energy at a constant value of α is given by the slope of the linear plot between $\ln\beta$ versus $\frac{-1}{RT}$.

3.4.4 Vyazovkin_AIC model

This is a modification of the previous Vyazovkin integral isoconversional method expressed by following two equations [110].

$$\phi(E_\alpha) = \min\left(\sum_{i}^{n}\sum_{j\neq i}^{n}\frac{J[E_\alpha,\mathrm{T}_i(t_\alpha)]}{J[E_\alpha,\mathrm{T}_j(t_\alpha)]}\right) = n(n-1) \tag{3.13}$$

$$\text{Where, } J\left[\mathrm{E}_{\alpha}, \mathrm{T}_i(t_{\alpha})\right] = \int_{t_{\alpha}-\Delta\alpha}^{t_{\alpha}} \exp\left[\frac{-E_{\alpha}}{RT_i(t)}\right] dt \qquad (3.14)$$

wIn this method, E_α is considered constant only for a small segment $\Delta\alpha$ of total conversion, and the integral in Eq. (3.14) is evaluated numerically using the trapezoidal rule. The minimization of the function in Eq. (3.13) was carried out at each α value using Matlab 2019a by considering a step size of $\Delta\alpha = 0.025$.

3.5 Determination of solid state reaction mechanism (Criado method)

The isoconversional methods essentially determine values of apparent activation energy of solid state reactions without any prior assumption of the reaction mechanism. Once the activation energy values are calculated from the isoconversional methods, these values of the activation energy can be utilized to determine the prevalent reaction mechanism using $Z(\alpha)$ master plots [111]. $Z(\alpha)$ values used in the Criado method are calculated as:

$$Z(\alpha) = \frac{d\alpha/dt}{\beta}\pi(x)T \qquad (3.15)$$

where, $x = E_a/RT$ and $\pi(x)$ is a 4th order rational approximation given by the Eq. (16) [112].

$$\pi(x) = \left(\frac{x^3 + 18x^2 + 86x + 96}{x^4 + 20x^3 + 120x^2 + 240x + 120}\right) \qquad (3.16)$$

$Z(\alpha)$ plots obtained using the experimental data and the theoretical master plots are compared and the best–fit reaction model is obtained.

$$Z(\alpha) = f(\alpha)\cdot g(\alpha) \qquad (3.17)$$

The theoretical master plots are obtained from Eq. (3.17) using both differential and integral forms of solid–state reaction models outlined in appendix (Table A.1).

3.6 Determination of the pre–exponential factor

Kissinger developed a method for calculation of both activation energy and pre–exponential factor using following equation:

$$\ln\left(\frac{\beta}{T_{\max}^{2}}\right)=\ln\left(\frac{AR}{E_a}\right)-\left(\frac{E_a}{RT_{\max}}\right) \tag{3.18}$$

$T_{\max}$ is the temperature corresponding to the highest rate of degradation as seen on DTG curve. The pre–exponential factor at the corresponding α was determined using Eq. (3.19) with activation energies calculated with Vyazovkin_AIC model.

$$A=\frac{\beta E_a \exp(E_a / RT_{\max})}{RT_{\max}^{2}} \tag{3.19}$$

3.7 Results and discussion

3.7.1 Biomass characterization

Table 3.1 shows the proximate analyses, ultimate analyses, calorific values, and bulk densities for the biomass of WH, TP, and SCB. The ultimate analysis showed high carbon content for TP (44.7%), while SCB and WH had relatively lesser carbon content of 42.02% and 36.44%, respectively. This indicates that the biomass utilized in the current study is viable for energy production and they are consistent with other results reported in literature (Table 3. 1). Very small amount of nitrogen (< 4%) in biomass was detected in CHN analysis. HHVs of the biomass were calculated using Eq. (3.1) and they were in range of 10.04–19.19 MJ kg^{-1}, which are comparable with other biomass reported in the literature [106]. The amount of ash content was higher for WH (4.82%) and SCB (3.12%) while TP had the least ash content of 2.11%. The higher AC value for WH could be attributed to the presence of more silica content in WH feedstock. High ash content has a significant environmental effect due to the generation of dust, which leads to an increase in particulate matter in the atmosphere [113]. Moisture content depends on the type of feedstock, the method of pre–treatment, and origin. The moisture content was relatively small, in the range of 6.85–9.04% for WH, SCB, and TP, which is another merit as feedstock for pyrolysis due to rapid heat transfer and lesser by–products [104] .

Release of condensable and non–condensable vapour during thermal decomposition of biomass is related to its volatile matter (VM) content. All biomass had high VM content (74.02–79.07%). Bulk density of biomass is of relevance for transportation and storage. Bulk densities for WH, TP, and SCB were calculated using Eq. (3.2) and they were in the range of 275.41, 532.13, and 306.22 kg m^{-3}, respectively. The low bulk density in the WH could be attributed to its porous nature. Low bulk density has a significant influence on the handling and storage of the feedstock since more space is required. Structural composition of biomass (i.e. lignin/hemicellulose/cellulose) showed significant variation, as shown in Table 4.1. The XRD and TGA results could be correlated to the structural composition of biomass. SCB had the highest cellulose content (40.59 wt%) among the three biomass, while TP had the lowest content (28.90 wt%). The lignin contents of WH, TP, and SCB were 5.65, 15.76, and 19.89 wt%, respectively. The cellulose and hemicellulose content of the biomass samples were in the range of 28.90–40.59% and 34.79–21.45%, respectively. These features and properties of the biomass used in this study make them potential candidates for pyrolysis.

Table 3.1 Proximate and ultimate analyses and structural compositions of biomass

Analysis	**Present study**			**Rice husk** [114]	**Kenaf** [114]	**Castor residue** [115]	**Arundo donax** [116]	**Napier grass** [117]
	WH	**TP**	**SCB**					
Proximate analysis(% wt ad)								
Moisture content	9.04±0.04	6.85±0.05	7.83±0.05	4.36±0.007	4.54 ± 0.015	12	8.57	75.27 ± 0.21
Volatile matter	79.07±0.60	78.02±0.70	74.02±0.50	66.65±0.63	82.70 ± 0.17	76	74.36	81.51 ± 0.26
Ash content	4.82±0.10	2.11±0.40	3.12±0.05	18.82±2.00	5.73 ± 0.35	5.56	5.35	1.75 ± 0.04
Fixed carbon	7.07±0.20	13.02±0.20	15.03±0.30	10.17	7.03	6.44	11.72	16.74 ± 0.05
VM/FC	11.18±0.40	6.07±0.50	4.92±0.40	–	–	–	–	
Ultimate analysis (% wt daf)								
C	36.44	44.70	42.02	30.73	38.38	38.26	42.05	51.61 ± 0.24
H	5.02	5.84	5.77	6.58	8.84	1.25	6.24	6.01 ± 0.02
O(*)	54.68	48.09	49.91	42.89	46.31	55.7	36.37	41.07 ± 0.02
N	3.86	1.37	2.12	0.67	6.1	4.21	1.54	0.99 ± 0.01
S	–	–	–	0.31	0.44	0.58	–	0.32 ± 0.01
H/C	1.64	1.55	1.63	0.21	0.23		1.76	0.12
O/C	1.13	0.81	0.89	1.39	1.21		0.89	0.8
Calorific value (MJ kg^{-1})	15.45±0.30	20.41±0.70	18.77±0.10	14.37	16.66	17.09±0.2	17.14	18.05 ± 0.07
Bulk density (kg m^{-3})	275.41±1.00	532.13±0.70	306.22±0.70	328±7.60	170±8.13			
Composition analysis (%wt)								
Cellulose	30.56	28.90	40.59	–	–	42.07	29.2	38.75 ± 2.30
Hemicellulose	34.79	21.45	29.35	–	–	9.72	35.9	19.76 ± 1.68
Lignin	5.65	15.76	19.89	–	–	21.18	23.32	26.99 ± 1.29
Extractives and others(*)	29.0	33.89	10.17	–	–		11.58	12.07 ± 0.32

ad: air–dried; daf: dry ash–free basis *: calculated by the difference

3.7.2 XRD analysis

The X–ray diffractograms for WH, TP, and SCB are shown in Figure 3.1 and the crystallinity index was calculated using Eq (3.3). The crystallinity index is an indication of the structural uniformity of the biomass and is expressed as the mass ratio of the crystalline fraction of cellulose to the amorphous fraction. The crystalline structure is due to the presence of hydrogen bonds amid cellulose chains and van der Waal forces between the glucose molecules in hemicellulose and cellulose. Also, lignocellulosic biomass comprises of two types of glucans, viz. amorphous hemicellulose and crystalline cellulose. The X–ray diffractograms for WH, TP, and SCB showed the highest diffraction peak in the range of 2θ (I_{002}) 20.2°–22.4°, while the lowest peak in the range of 2θ (I_{amor}) 16.5°–18.7°. The peak intensity method, which uses the maximum and minimum peak height given by Eq. (3.3), was used to calculate the *CrI*. The biomass of SCB possessed the highest crystallinity of 42.25%, while WH and TP had relatively smaller crystallinity of 38.43% and 32.46%, respectively. Thus, it could be inferred that *CrI* depends on the compositional structure of the biomass. *CrI* varies proportionately with the cellulose content of biomass.

Similarly, crystallinity has a major effect on the pyrolytic behaviour of lignocellulosic biomass because biomass with high *CrI* are more stable, as reported by Wang et al. [119]. Further, these results can be confirmed by the TGA analysis in this study, which shows that the degradation of SCB started at a higher temperature. The high–temperature requirement is linked to the presence of glycosidic bonds, which require more energy to break down the high degree molecular structure [120].

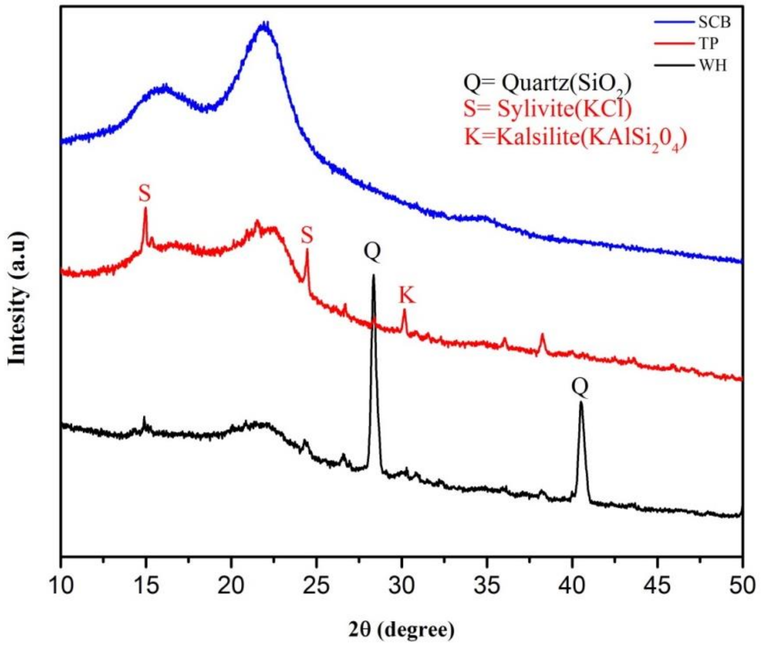

Figure 3.1. XRD results of WH, TP and SCB

3.7.3 FTIR analysis

The FTIR spectra of WH, SCB, and TP, and corresponding wavenumbers are shown in Figure 3.2. FTIR analysis indicated the presence of alkane, alcohol, ether, alkene, alkyne, and aromatics in the feedstocks. It was also observed that the existence of functional groups varies with the type of feedstock. The broad peaks observed for WH, SCB, and TP at wavelength 3280–3335 cm^{-1} were assigned to the O–H group, which could be due to the existence of alcohol and phenol [104]. The peaks in 2864–2914 cm^{-1} show the presence of an aliphatic C–H group which is a result of symmetrical and asymmetrical vibrations of alkane groups found in lignin and the extractives [117]. Weak peaks of 217–2300 cm^{-1} showed presence of C=C. This peak was not identified in WH, thus confirming that functional groups vary in the different feedstock. The peaks at 1602–1622 cm^{-1} are a result of C=C extending vibrations. This is a distinctive feature of the carbonyl band because of the presence of hemicellulose. Peaks 1402–1408 cm^{-1} illustrated the C–H group, which is a result of symmetric deformation CH_2 present in the cellulose. The peaks at 1022–1044 cm^{-1} correspond to C–O in hemicellulose, cellulose, and lignin [77]. The peaks between 501–549 cm^{-1} are attributed to C–H, which is part of the aromatic structures. The FTIR spectra of all the biomass were consistent with the results reported in the literature[106].

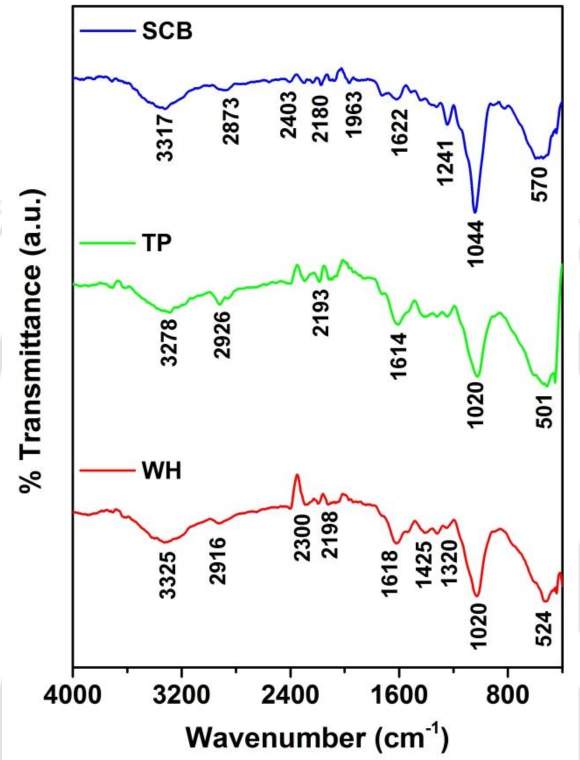

Figure 3.2 FTIR spectra for native (or raw) biomass of WH, TP and SCB

3.7.4 FESEM analysis

The morphologies of WH, TP, and SCB are shown in Figures. 3.3a–c. It could be seen from Figure 3.3a that WH primarily consisted of fibers that are closely packed together with some clear micropores which are uniformly distributed, while Figure 3.3b shows rod–type granules with irregular shapes of biomass for TP. Similarly, it was observed that Figure 3.3c illustrated the structure of pulverized SCB, which had solid, irregular, and has thick–walled fiber cells intertwined with the other part of the plant. The fiber is constituted of parallel stripes and is superficially covered with extractives. A comparative analysis of the surface morphologies of the three feedstock from the FESEM micrographs showed that the SCB had the most compact rod–like fibrous structure that has a circular surface area. In contrast, WH has slackened, and detached units and TP have fibrous fragments as well as clefts evenly distributed in the structure and some granular structures. The FESEM micrographs confirmed that these materials have different morphologies.

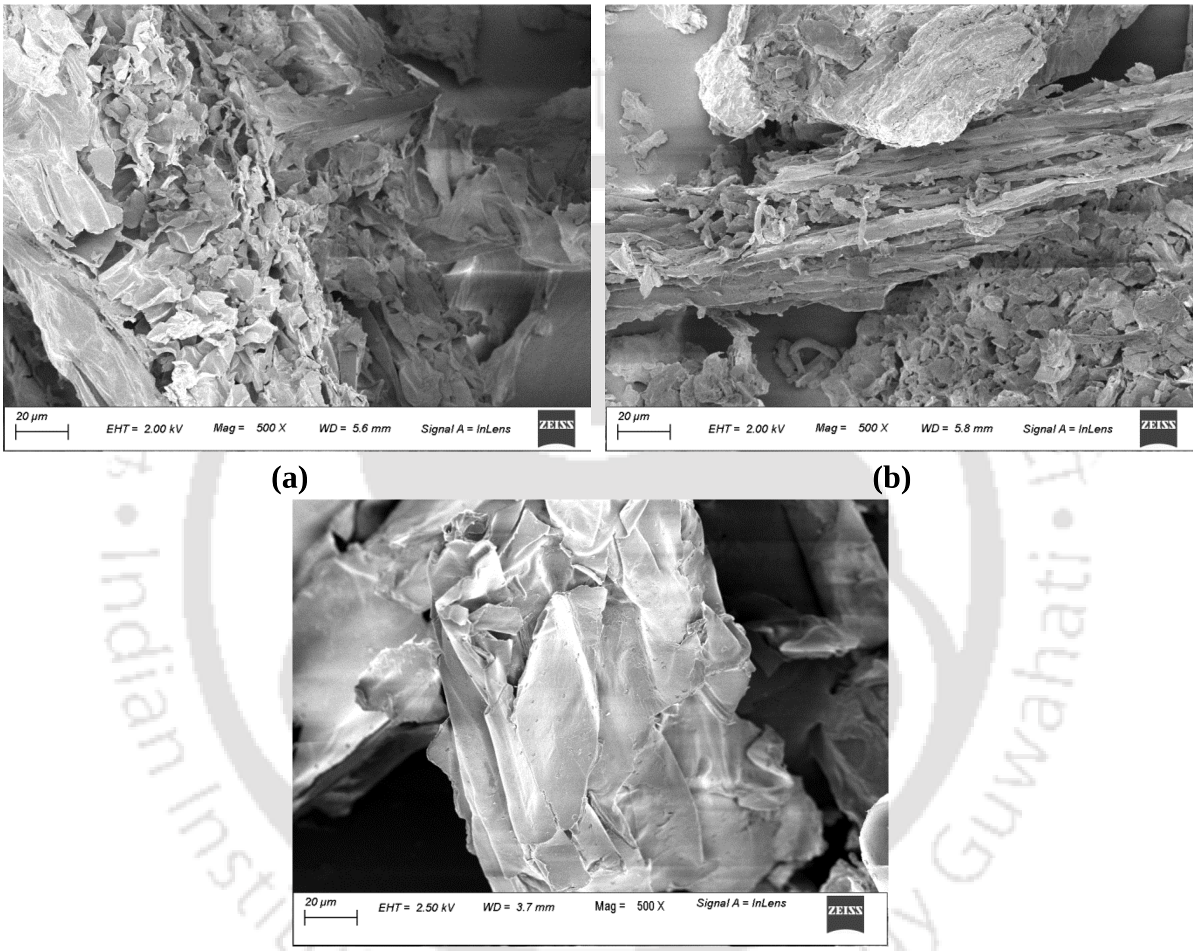

(a) **(b)**

(c)

Figure 3.3. FESEM micrographs (a) WH (b) TP and (c) SCB

3.7.5 Thermal analysis of biomass

The thermogravimetric (TG) and (DTG) curves of WH, SCB, and TP are shown in Figures 3.4a and b, respectively. It should be noted that the peak areas on the DTG curve are directly proportional to the corresponding sample weight loss on the TGA curve. As seen from

Figure 3.4a, the degradation of raw biomass is different from polymers, as it occurred in three stages, which is consistent with other biomass reported in the literature [121]. The three stages of degradation include stage 1 of drying/dehydration (30°–150°C), which was characterized by a slight loss of mass. This mass loss was mostly due to the release of inherently bound moisture and light volatiles. In stage 2 of degradation (150°–370°C) devolatilization of holocellulose occurred. Relatively high temperatures in this stage led to the degradation of high molecular weight compounds and holocellulose into smaller molecular weight pyrolysis products. The DTG curves shown in Figure 3.4b revealed significant difference in the temperatures corresponding to the maximum degradation rate for different biomass. The maximum temperature of decomposition ($T_{\max}$) for TP (309°C), was relatively low followed by WH (317°C), while SCB had the highest $T_{\max}$ of 335°C. Finally, the mass loss in stage 3 (370°–600°C) could be attributed to depolymerization of lignin. The third stage is characterized by slow rate of degradation with insignificant mass loss and yield of char. Although the TG and DTG curves of WH, TP and SCB showed some similarity of shape, each biomass showed a different TG profile, whereas the shift of $T_{\max}$ in the DTG curves could be attributed to the difference in structural composition of individual biomass.

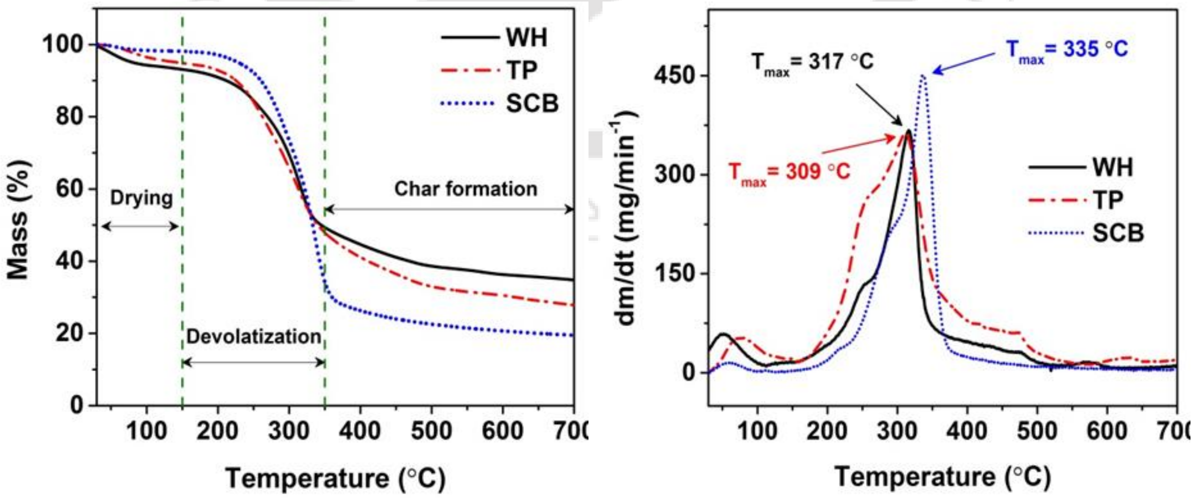

(a) (b)

Figure 3.4. (a) TG and (b) DTG curves for WH, TP and SCB at β = 10 °C min^{-1}

3.7.6 EDX analysis

It is essential to identify the alkali and alkaline earth metals (AAE) present in the biomass as they have significant catalytic influence on the kinetics of pyrolysis. These metals lead to a high rate of conversion, favouring the formation of low molecular weight hydrocarbon by assisting cleavage of the glycosidic bond. Other elements like P, S and Cl also contribute to formation of gaseous products during pyrolysis that contribute to GHG. The EDX results for the feedstock and their ashes are shown in Figure 3.5 and Appendix A–2. The mineral elements P, S, K, and Ca were present at various concentrations (wt %) because they are natural ingredients of proteins and act as osmotic agents. The presence of low amounts of AAE is a desirable property for the feedstock. The AAE are actively involved during the thermo–chemical conversion of biomass in the breakdown, corrosion, erosion, and reactors [122].

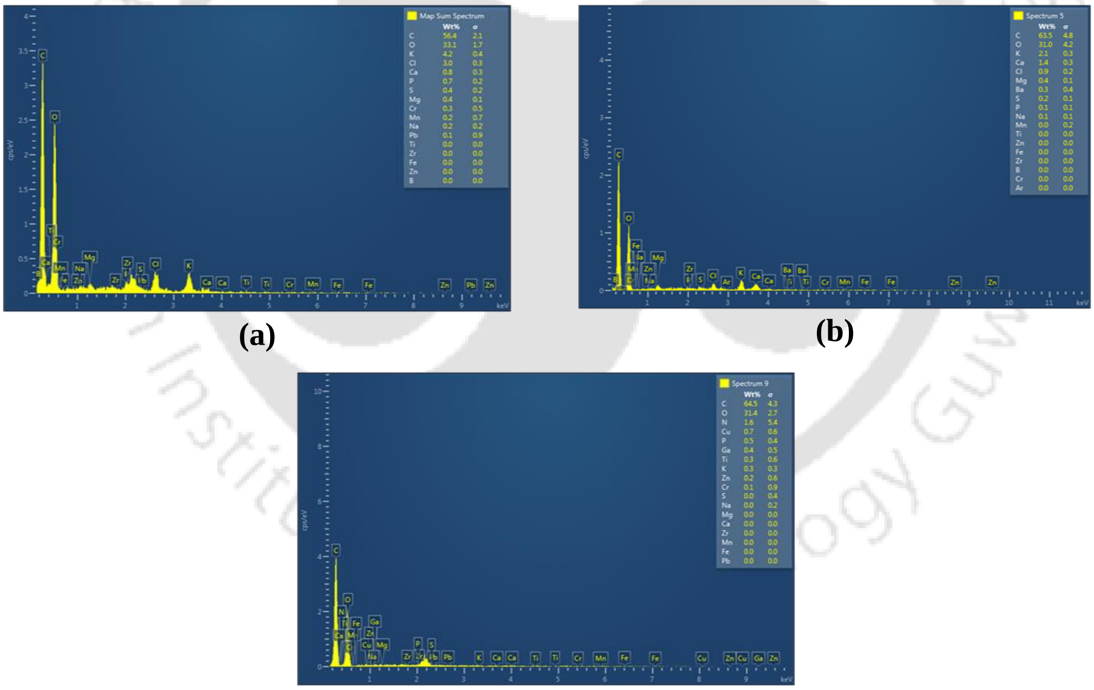

Map Sum Spectrum

	Wt%	σ
C	56.4	2.1
O	33.1	1.7
K	4.2	0.4
Cl	3.0	0.3
Ca	0.8	0.3
P	0.7	0.2
S	0.4	0.2
Mg	0.4	0.1
Cr	0.3	0.5
Mn	0.2	0.7
Na	0.2	0.2
Pb	0.1	0.9
Ti	0.0	0.0
Zr	0.0	0.0
Fe	0.0	0.0
Zn	0.0	0.0
B	0.0	0.0

(a)

Spectrum 5

	Wt%	σ
C	63.5	4.8
O	31.0	4.2
K	2.1	0.3
Ca	1.4	0.3
Cl	0.9	0.2
Mg	0.4	0.1
Ba	0.3	0.4
S	0.2	0.1
P	0.1	0.1
Na	0.1	0.1
Mn	0.0	0.2
Ti	0.0	0.0
Zn	0.0	0.0
Fe	0.0	0.0
Zr	0.0	0.0
B	0.0	0.0
Cr	0.0	0.0
Ar	0.0	0.0

(b)

Spectrum 9

	Wt%	σ
C	64.5	4.3
O	31.4	2.7
N	1.6	5.4
Cu	0.7	0.6
P	0.5	0.4
Ga	0.4	0.5
Ti	0.3	0.6
K	0.3	0.3
Zn	0.2	0.6
Cr	0.1	0.9
S	0.0	0.4
Na	0.0	0.2
Mg	0.0	0.0
Ca	0.0	0.0
Zr	0.0	0.0
Mn	0.0	0.0
Fe	0.0	0.0
Pb	0.0	0.0

(c)

Figure 3.5. EDX Micrographs of biomass (a) WH, (b)TP, (c) SCB

3.8 Kinetic parameter analysis

The TGA data obtained at three heating rates viz. 10, 30, and 40°C min^{-1} was used to determine the kinetic parameters. Four isoconversional methods viz. KAS, OFW, Friedman, and, Vyazovkin_AIC were used to determine the activation energy. A conversion range of 0.05–80% with an increment of 0.05% was used to obtain the kinetic parameters as recommended by the ICTAC [123]. Based on the DTG curve temperatures range of 150°–600°C was considered for the kinetic analysis. The temperature range was chosen by considering the degradation zone depicted by stage 2 of the DTG curve. The onset and offset of degradation temperatures were observed at 150°and 600°C, respectively. Also, the TG curve showed that at 150°C, there was a very insignificant amount of mass loss which could be attributed to the loss of moisture and some volatiles. Similarly, after 600°C, there is slight mass loss due to char formation. Thus, the degradation zone considered is fit for the kinetic analysis. The experimental data for Friedman, OFW, and KAS showed good linear fit for WH, TP, and SCB with regressions coefficients (R^2) $\geq$ 0.94 for the entire range of $\alpha = 0.05 - 0.80$. The details of the R^2 are provided in appendix Tables A3 – A5.

3.8.1 Activation energy

Figures. 3.6–3.8 show the linear regression graphs obtained using Friedman, KAS, and OFW kinetic models (i.e. the plots of Eqs. 3.9, 3.11, and 3.12) for WH, TP, and SCB, respectively. The activation energies calculated from the slope of the kinetic plots and those calculated using the Vyazovkin_AIC model are listed in Tables 3.2–3.4. It could be observed that the activation energies for WH, TP, and SCB were in the range of 187.74–329.71, 182.28–389.24, and 191.33–293.49 kJ mol^{-1}, respectively. The wide variation of activation energies of the feedstock implied occurrence of multiple reactions during pyrolysis. The change in activation energy with conversion could be attributed to the degradation of different structural components of biomass, viz. cellulose and hemicellulose and lignin. The variation in activation energies for WH, SCB, and TP could be attributed to variation in their compositional structure. These values of apparent activation energies in this study are consistent with other biomass reported in the literature[124–126].

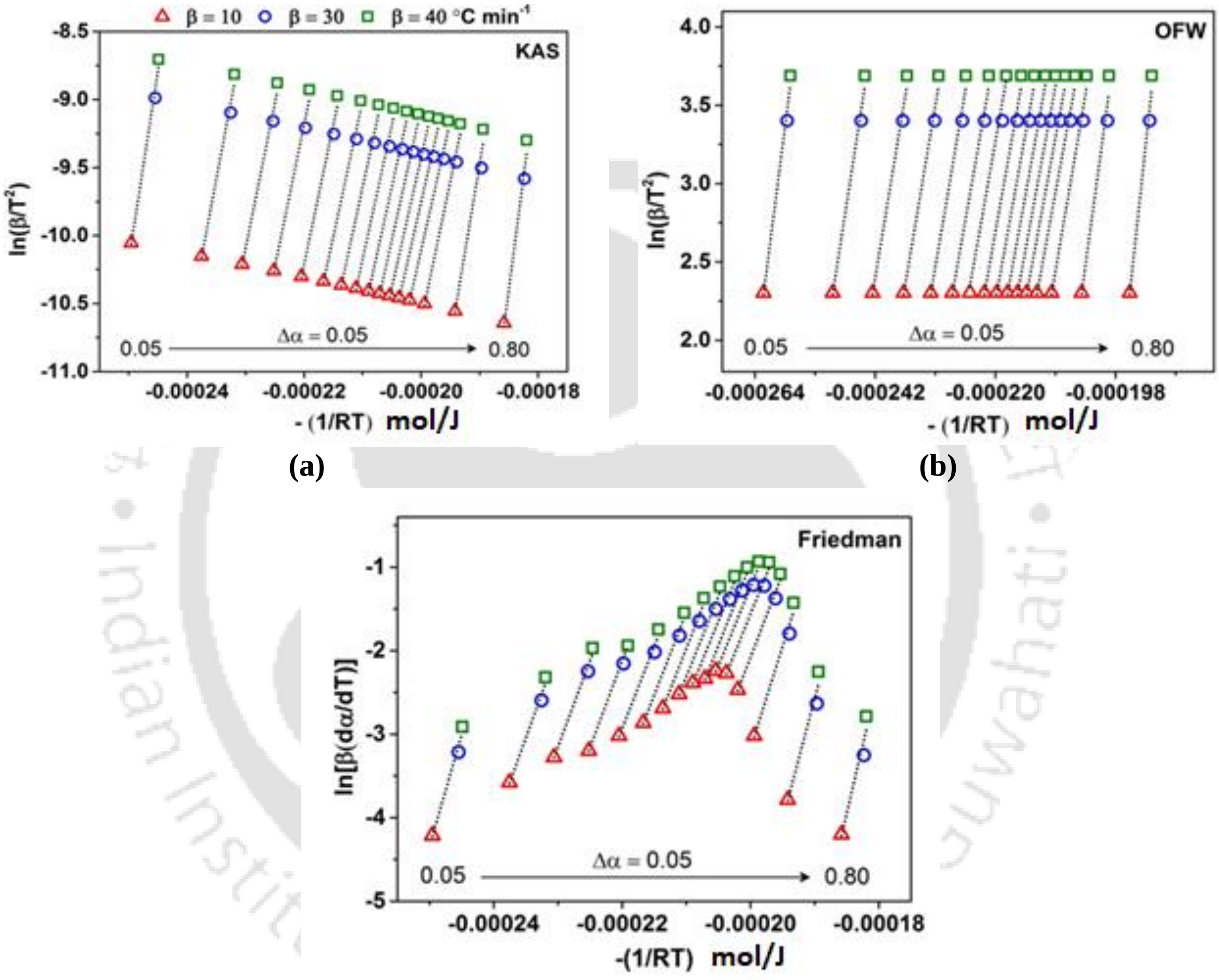

(a) **(b)**

(c)

Figure 3.6 Kinetic plots for WH using different isoconversional models.(a) KAS (b) FWO and (c) Friedman

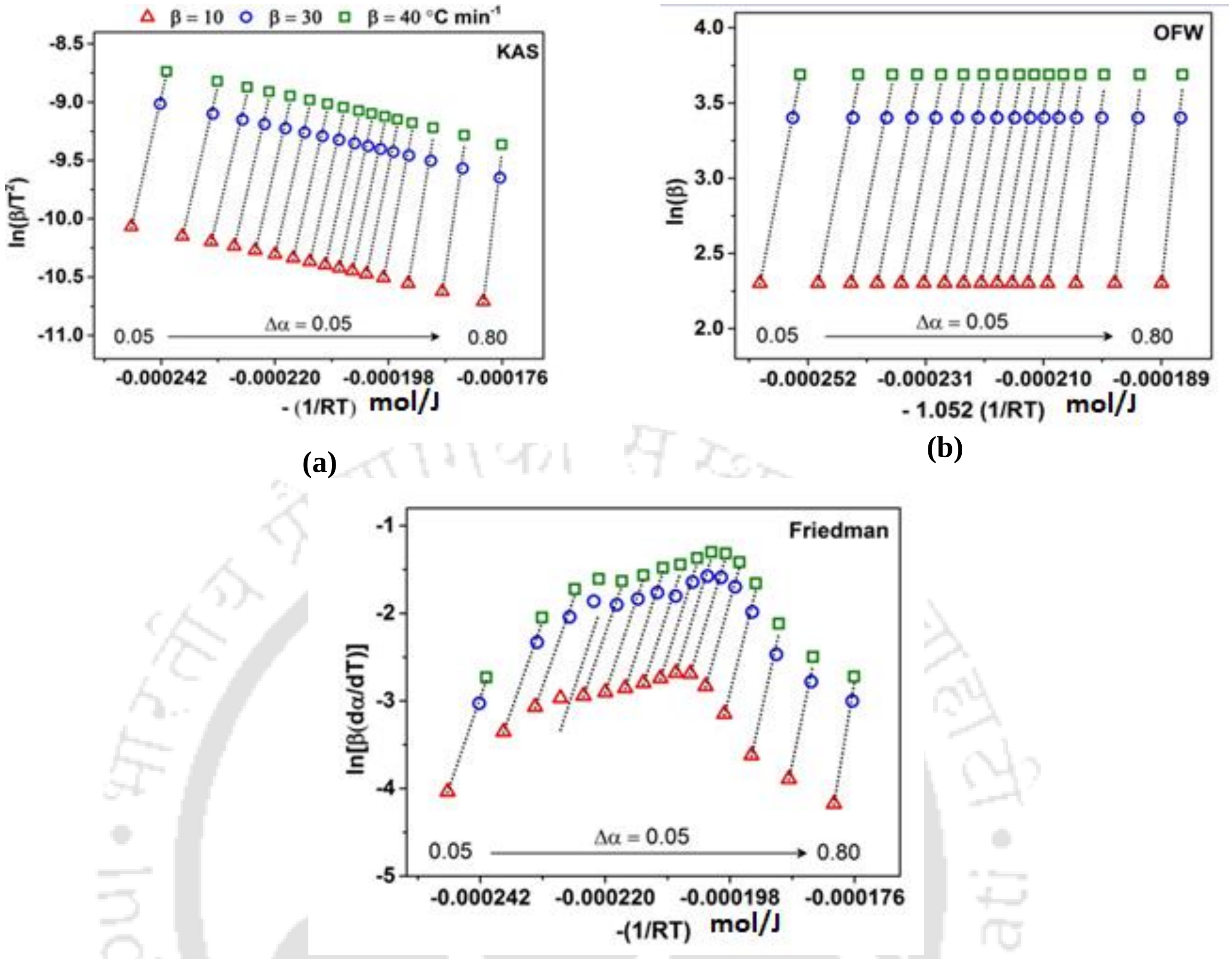

(a) **(b)**

(c)

Figure 3.7 Kinetic plots for TP using different isoconversional models.(a)KAS (b) FWO and (c) Friedman

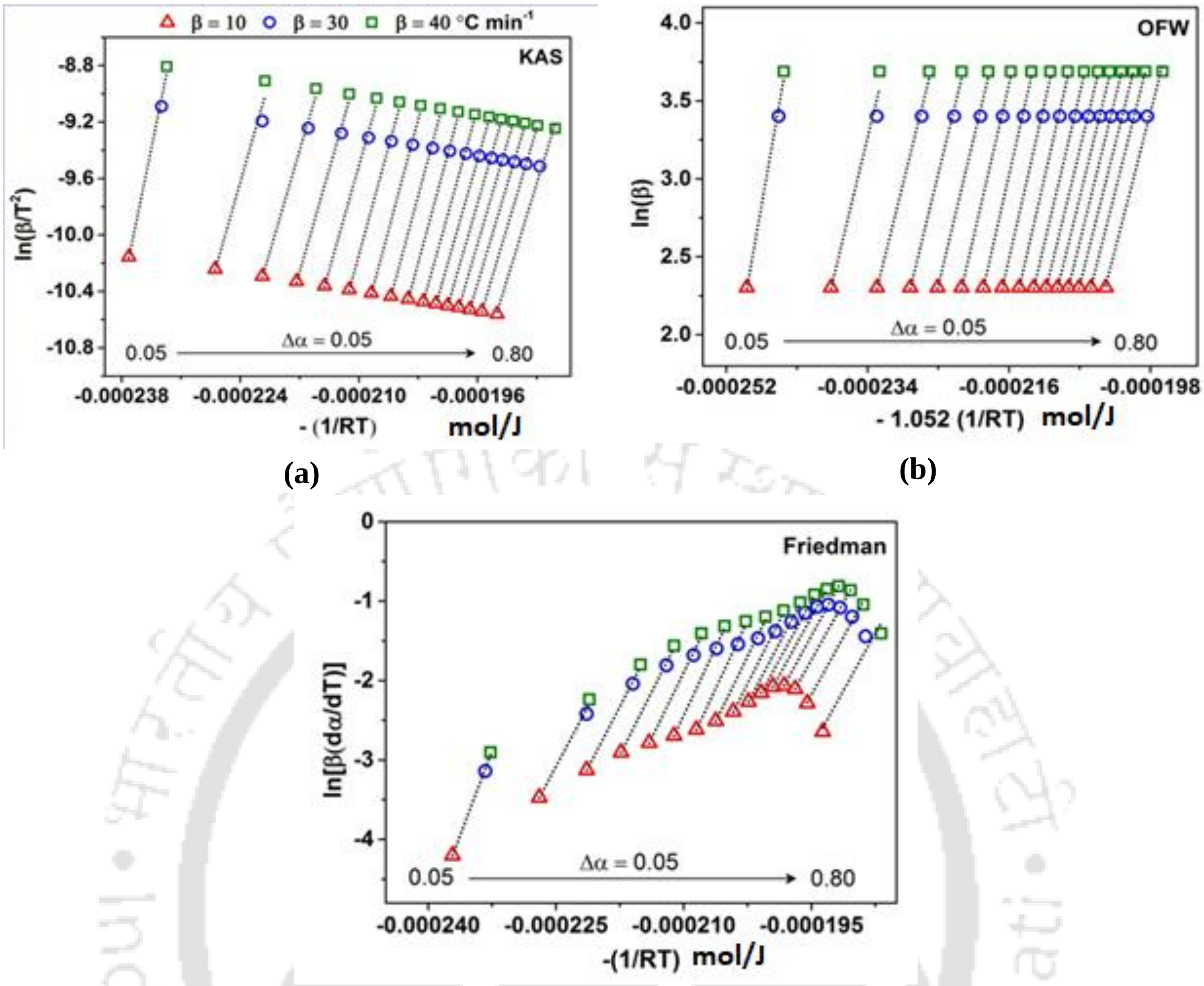

(a) (b)

(c)

Figure 3.8 Kinetic plots for SCB using different isoconversional models.(a)KAS (b) FWO and (c) Friedman

Table 3.2 Kinetic parameters of WH determined using various isoconversional methods

α	**WH**				
	KAS	**OFW**	**Friedman**	**Vyazovkin_AIC**	
	E_a (kJ mol^{-1})	E_a (kJ mol^{-1})	E_a (kJ mol^{-1})	E_a (kJ mol^{-1})	A (sec^{-1})
0.05	277.10	272.00	265.50	292.40	4.40×10^{33}
0.10	228.90	225.80	214.60	232.90	6.10×10^{25}
0.15	213.30	211.20	207.30	216.80	2.10×10^{23}
0.20	209.60	207.80	207.30	216.60	8.40×10^{22}
0.25	206.10	204.80	197.20	210.80	7.80×10^{21}
0.30	199.70	198.80	198.30	203.90	7.40×10^{20}
0.35	198.10	198.20	198.00	200.70	1.90×10^{20}
0.40	196.10	196.40	191.60	198.20	6.50×10^{19}
0.45	194.90	194.60	187.70	195.40	2.30×10^{19}
0.50	193.60	193.40	195.40	192.10	7.80×10^{18}
0.55	190.50	190.50	188.40	190.60	4.00×10^{18}
0.60	189.20	189.40	190.20	192.10	2.90×10^{18}
0.65	190.90	191.00	200.50	203.40	4.40×10^{19}
0.70	205.80	205.40	245.00	238.00	1.90×10^{22}
0.75	258.10	255.40	290.60	299.60	1.05×10^{27}
0.80	329.70	323.90	327.30	311.60	7.50×10^{26}

Table 3.3 Kinetic parameters of TP determined using various isoconversional methods

α	**TP**				
	KAS	**OFW**	**Friedman**	**Vyazovkin_AIC**	
	E_a (kJ mol^{-1})	E_a (kJ mol^{-1})	E_a (kJ mol^{-1})	E_a (kJ mol^{-1})	A (sec^{-1})
0.05	245.90	191.80	188.50	197.30	1.00×10^{23}
0.10	209.40	187.60	185.00	196.10	1.00×10^{22}
0.15	208.50	182.30	183.30	191.70	1.10×10^{21}
0.20	215.50	188.60	196.20	202.10	6.40×10^{21}
0.25	223.90	188.90	187.30	198.10	9.00×10^{20}
0.30	231.30	191.00	193.80	199.20	5.20×10^{20}
0.35	233.50	193.10	201.20	205.80	1.00×10^{21}
0.40	227.60	195.80	195.60	210.00	1.40×10^{21}
0.45	217.40	195.50	204.30	210.20	7.30×10^{20}
0.50	207.60	201.10	211.20	212.60	6.60×10^{20}
0.55	200.70	204.30	213.30	217.60	1.00×10^{21}
0.60	195.40	212.80	229.10	227.10	4.20×10^{21}
0.65	193.50	227.90	256.40	249.70	1.90×10^{23}
0.70	194.30	258.90	291.40	287.80	1.00×10^{26}
0.75	194.90	290.80	308.30	306.40	4.90×10^{26}
0.80	196.90	350.60	389.30	371.60	5.90×10^{30}

Table 3.4. Kinetic parameters of SCB determined using various isoconversional methods

α	**SCB**				
	KAS	**OFW**	**Friedman**	**Vyazovkin_AIC**	
	E_a (kJ mol^{-1})	E_a (kJ mol^{-1})	E_a (kJ mol^{-1})	E_a (kJ mol^{-1})	A (sec^{-1})
0.05	293.50	287.20	285.10	245.90	1.50×10^{27}
0.10	209.90	208.00	200.70	209.40	2.30×10^{22}
0.15	204.40	203.00	206.60	208.50	5.60×10^{21}
0.20	208.00	206.70	212.30	215.50	1.10×10^{22}
0.25	211.20	209.90	219.70	223.90	3.40×10^{22}
0.30	219.10	217.50	227.70	231.40	8.40×10^{22}
0.35	223.70	222.00	228.80	233.50	7.00×10^{22}
0.40	222.50	220.90	219.80	227.60	1.20×10^{22}
0.45	221.00	219.60	211.70	217.40	8.50×10^{20}
0.50	214.70	213.70	203.10	207.60	7.50×10^{19}
0.55	208.90	213.70	196.60	200.70	1.30×10^{19}
0.60	208.90	206.50	194.20	195.40	3.30×10^{18}
0.65	204.60	204.30	195.10	193.50	1.70×10^{18}
0.70	201.00	200.10	191.30	194.30	1.60×10^{18}
0.75	200.00	200.00	193.80	194.90	1.30×10^{18}
0.80	194.90	195.40	192.60	196.90	1.30×10^{18}

The variation of activation energies with the degree of conversion for WH, TP, and SCB determined using Friedman, KAS, OFW, and Vyazovkin_AIC models is depicted in Figures 3.9 a–c. It could be seen that the activation energy plots displayed a similar trend, and they are closely overlapping each other. However, the apparent activation energies determined using the Vyazovkin_AIC model were slightly higher at $\alpha \leq 0.4$ for WH, TP, and SCB. Also, a peculiar observation was noted that the values of activation energy obtained from the Friedman method and those of Vyazovkin_AIC were close to each other. The activation energies determined with the Friedman method and Vyazovkin_AIC model are likely to be more accurate, as the other two methods (KAS and OFW) involve empirical approximations [127]. Vyazovkin_AIC model is an advanced version of the Vyazovkin model and is more accurate since it considers smaller conversion intervals. The apparent activation energies fluctuate with the increase of conversion and as the degradation proceeds and these variations indicate the occurrence of complex multi–step reactions in the degradation process and via different reaction models [128]. It was observed that the apparent activation energies for WH and TP increased after α ≥ 0.6. The activation energy for SCB increased up to α = 0.35 and decreased thereafter which could be due to the lesser ash content in SCB.

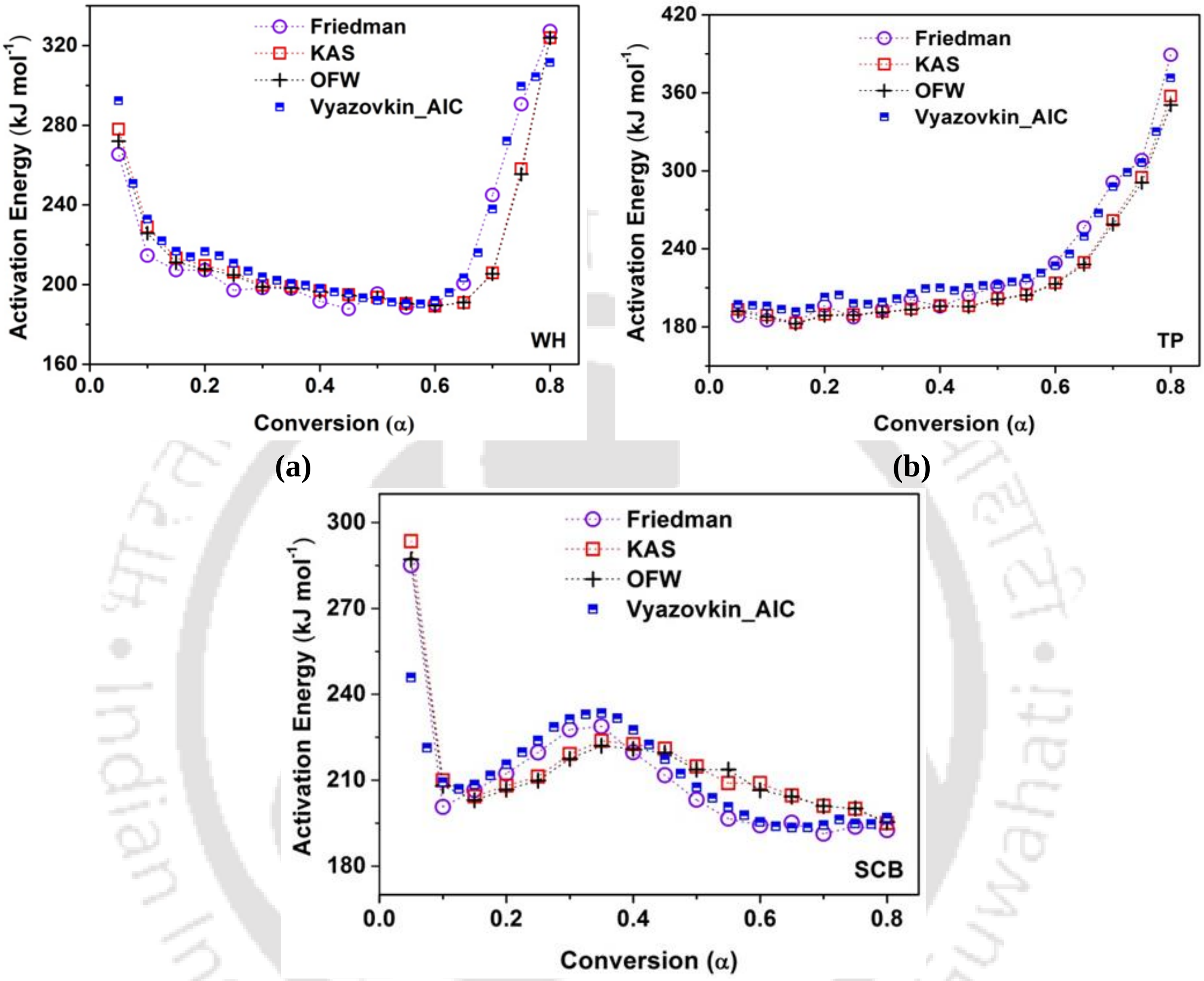

(a) (b)

(c)

Figure 3.9 Trends of activation energy with degree of conversion using different isoconversional methods. (a) WH, (b) TP and (c) SCB

3.8.2 Reaction model

The Criado method was used to determine the main reaction model for the three biomass, as shown in Figure 3.10. The theoretical and experimental master Z(*α*) master plots showed a close correspondence, and the best–fitted reaction models were identified for WH, TP, and SCB. From the Criado master plot, it could be observed that pyrolysis of each biomass involves two consecutive reactions. WH and TP indicated the pyrolysis mechanism of three–dimensional heat diffusion (D3) in the conversion range $\alpha \leq 0.6$, and 3rd–ordered reaction (F3) at $\alpha \geq 0.6$. SCB exhibited the mechanism of two–dimensional diffusion (D2) in the range $\alpha \leq 0.6$, and after $\alpha \geq 0.6$ showed better correlations were seen with both 2nd and 3rd–order (F2 and F3) reactions at as illustrated in Figure 3.10. The D3 reaction model could be attributed to the degradation of cellulose and hemicellulose at a lower temperature. It could be inferred that the thermal degradation commences from random points of feedstock and is transmitted in the entire sample through the diffusion of the hot gasses [129]. The propagation of the complex multistep reactions commences on the surface and propagates towards the centre of the feedstock as the thermal degradation takes place. This phenomenon could also be attributed to the different structural components of individual feedstock. The ordered reaction model F2 and F3 could be attributed to the degradation of cellulose [130].

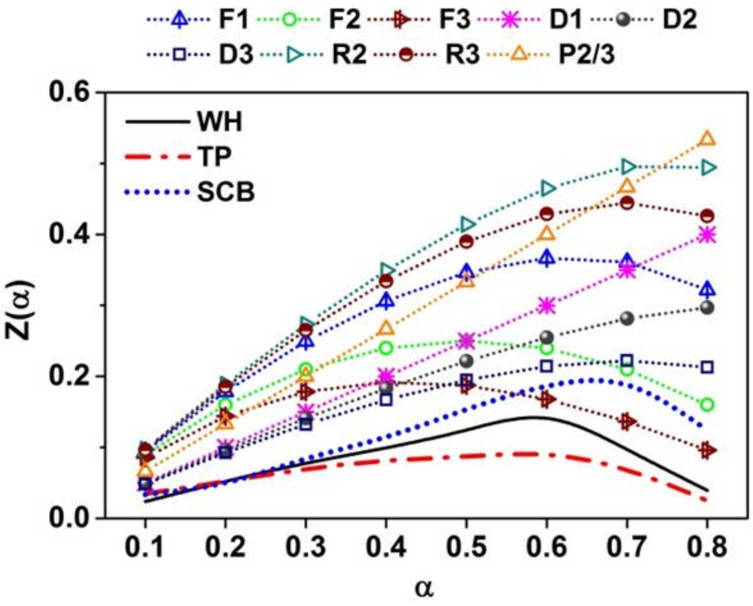

Figure 3.10 Criado master plots for WH, TP and SCB.

3.8.3 Pre–exponential factor

The pre–exponential factors (A) was determined by Kissinger’s equation (Eq. 18) using the activation energies obtained using Vyazovkin_AIC method. The pre–exponential factor for WH, SCB, and TP were in the range of $2.88 \times 10^{18} – 4.40 \times 10^{33}$ $s^{–1}$, $34 \times 10^{18} – 1.47 \times 10^{27}$ $s^{–1}$, and $2.88 \times 10^{18} – 4.40 \times 10^{33}$ $s^{–1}$, respectively as outlined in Table 3.2a–c. The wide variation of A values showed the complexity of reactions taking place during the pyrolysis of the biomass [54,55]. Also, it was observed that relatively high values of A occurred at $\alpha \leq 0.3$ for WH, SCB and TP, followed by a slight drop in values A at $\alpha = 0.30–0.45$. The high values of A observed at $\alpha \leq 0.3$ could be attributed to extra energy needed during the commencement of degradation for hemicellulose and cellulose, and after the energy barrier is broken, the biomass degradation occurs at relatively lower activation energy [124]. Towards $\alpha \geq 0.7$ there was a significant rise of A which could be attributed to the degradation of remaining lignin and char formation. Higher values of pre–exponential factor point at three distinct features of the reaction system: (1) high reactivity, (2) existence of an energy barrier that requires transfer of higher quantum of energy, and (3) formation of a relatively simple complex (or transition state) [126].

3.9 Summary

This chapter has presented a comprehensive physico–chemical characterization and pyrolysis kinetics of three biomass materials, viz. WH, SCB and TP. The TGA data was analysed using four isoconversional models, viz. Friedman, KAS, OFW, and Vyazovkin_AIC. Characterization showed that all biomass were potential candidates for pyrolysis due to high contents of volatile matter, low moisture and ash content. All biomass had high heating value in the range of 15.45–20.41 MJ $kg^{–1}$. A wide range of activation energies with conversion level showed that multiple reactions occurred during the pyrolysis. Variation in activation energy with conversion level could be attributed to degradation of different structural components, viz. cellulose, hemicellulose and lignin, with multiple reactions at different temperature levels. For each biomass Criado master plot revealed two distinct reaction mechanisms during thermal conversion. WH and TP indicated the mechanism of three–dimensional heat diffusion (D3) for conversion level $\alpha \leq 0.6$, and 3rd–order reaction (F3) for $\alpha \geq 0.6$. SCB exhibited the mechanism of two–dimensional diffusion (D2) for $\alpha \leq 0.6$, and after $\alpha \geq 0.6$ showed better correlations were seen with both 2nd and 3rd order reaction (F2 and F3). High values of pre–exponential factor A were observed for all biomass – which is an indication of their reactivity towards thermal conversion. In the next chapter, the synthesis and characterization of biochar (under varying conditions) from three different biomass (WH, TP and SCB) to determine their potential in energy and agricultural applications is presented.

CHAPTER 4– Synthesis and characterization of biochar derived from lignocellulosic biomass

4.0 Introduction

In the present chapter, the synthesis and characterization of biochar (under varying conditions) from three different biomass such as WH, TP and SCB from the viewpoint of determining their potential in energy and agricultural applications is presented. The physicochemical characteristics and surface properties of biochar essentially determine their suitability for wide applications. The biochar properties depend on type of feedstock and pyrolysis conditions. Therefore, a thorough study of the relation among pyrolysis conditions and characteristics/properties of biochar is necessary. Also variations in the properties of biochar produced from different components (leaves, stem, root) of a single plant of WH have been discussed in this chapter. As many as 12 biochar were produced from the three different feedstock at 350° and 550°C. These biochar were characterized for proximate and ultimate analysis, functional groups, thermal stability, higher heating value, surface area, surface morphology, crystallinity and elemental composition with standard techniques. A comparative assessment of the 12 biochar has been made to identify best feedstock and pyrolysis conditions for synthesizing biochar for a particular application.

4.1 Materials and method

4.1.1 Biomass sources and collection

Procedure for collection and processing of biomass is described in Chapter 3 under sub–section 3.2.1.

4.1.2 Synthesis of biochar

Pyrolysis experiments were conducted using a rotary fixed batch pyrolyzer (designed indigenously and fabricated by Dass & Co., India). A schematic diagram of the pyrolyzer is provided in supplementary material (Figure S1). The pyrolyzer consisted of an electrically heated rotary tube furnace (vol. 6.28 m^3), a microprocessor (PID, i.e. proportional–integral–derivative) operated digital temperature controller with thyristor power drive (accuracy of ±1 °C) and a 4 kW heater. The microprocessor (Make: FUJI, Model: PXF9, Japan) has a single program of 64 segments for programming heating, cooling and holding time. The pyrolysis temperature in the furnace was monitored using a thermocouple positioned at 90 mm from the central part of the quartz tube reactor. Argon gas was delivered from the top of the pyrolysis tube reactor at a constant flow rate of 100 mL min^{-1}. As the surface of the reactor was heated, the heat was further passed to the feedstock. The inert gas flowing over the feedstock swept away the syngas and volatiles into a cooling system comprising of a condenser and an ice–cold water bath for collection of bio–oil. In each experiment, 500 g of biomass was pyrolyzed at two temperatures, viz. 350° and 550°C, at a heating rate of 20°C min^{-1} for 1 h and a holding time of 30 min. For TP and SCB, the entire biomass was used for analysis. However, in case of WH, experiments were performed in two categories: (1) biomass of the whole plant, and (2) segregated biomass of three components of the plant, viz. root, stem and leaves. This was done in view of significant variation in structural composition of different components of the WH plant. The solid residue remaining after the completion of pyrolysis was biochar. Each experiment was repeated 3× to assess reproducibility. Biochar mass was pulverized, followed by sieving through a $\leq$ 210–micron sieve. The biochar particles were stored in airtight containers for subsequent analysis. The following nomenclature has been used for the biochar produced at two temperatures: (1) biochar from water hyacinth (WH) – whole water hyacinth plant (WH 350, WH550), roots (WH R350, WH R550), stem (WH S350, WH S550), leaves (WH L350, WH L550); (2) biochar from *Thevetia peruviana* (TP 350, TP 550); and (3) biochar from sugar cane bagasse (SCB 350, SCB 550). The yield of biochar obtained in the pyrolysis experiments was defined as:

$$\text{Yield}(\%) = \left(\text{Mass}_{Biochar} / \text{Mass}_{Biomass}\right) \times 100 \tag{4.1}$$

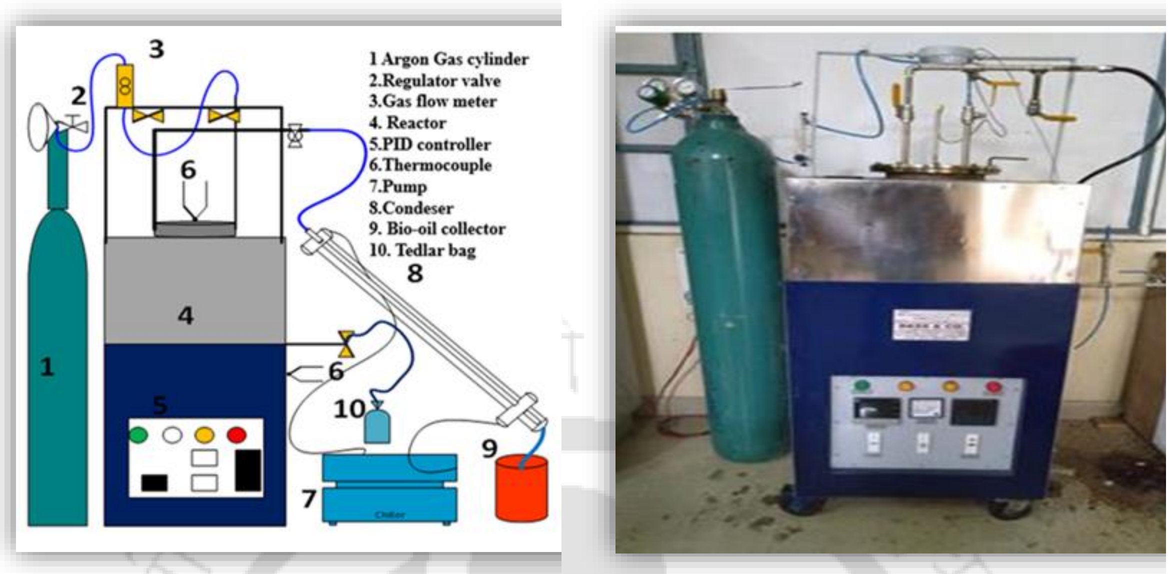

(a) **(b)**

Figure 4.1 Schematic diagram of the pyrolyzer

4.2 Biochar characterization

Extensive characterization of biochar was carried out using standard techniques as described below:

Both electrical conductivity (EC) and pH value were determined as per the procedure outlined by Yuang et al. [131]. The biochar samples were added to deionized water at a ratio of 1:20 (w/v). A pH Meter (Make: Mettler Toledo, Model: FEP20– Plus, India) was used for the measurement of pH value. An electrical conductivity meter (Make: Mettler Toledo, Model: FiveGo, India) was used to measure EC. The ultimate analysis (% of C, H and N) were done using an elemental analyzer (Make: Euro EA, Model: Eurovector EA3000, Italy), and oxygen (O) content was deduced by the difference in relation to the other elements [132,133]. The functional groups and moieties in original feedstock and biochar were analyzed using solid–state Fourier transform infrared (FTIR). (Make: Bruker, Model: VERTEX 70, Germany) in the wavelength range 500–3500 cm^{-1} at a resolution of 4 cm^{-1} by applying 32 scans. The samples were mixed with potassium bromide in ratios 1:100 (w/w), and the mixture was compressed to form a pellet of 1.00 cm of diameter. The biochar samples were analyzed for total pore volume (V_{tot}), pore size distribution (P_{size}) and surface area (S_{BET}), with adsorption of nitrogen at 77 K using surface area and pore size analyzer and high pressure analyzer (Make: Quanta chrome, Model: Autosorb–IQ–MP, USA). The biochar samples were degassed for 6 h at 160°C after drying them in a vacuum oven at 120°C overnight. The total pore volume of biochar was determined from N adsorption and desorption isotherms in pressure range of $P/P^0 = 0–1.0$. The minerals present in the biochar were identified with the help of a X–ray diffractometer (Make: Bruker, Model: D8 Advance, Netherlands). The scanning range for XRD analysis was $2\theta = 10–60^\circ$ with scan speed of $0.05^\circ\ s^{-1}$ using Cu–Kα radiation ($\lambda = 1.54$ Å). The mineral components were matched with the International centre for diffraction data (ICDD–PDF). The morphological structures and elemental distribution were detected using a scanning electron microscope (SEM) (Make: Zeiss, Model: Sigma 300, Germany) at different magnifications 150–20000×. Thermogravimetric analysis experiments (TGA) and differential thermogravimetric (DTG) were conducted using a thermogravimetric analyzer (Make: Netzsch, Model: STA449F3A00, Germany). Biomass and biochar samples (5–10 mg, dry weight) were weighed into an Al_2O_3 crucible, and the temperature was ramped from 30–700°C at a heating rate of 10 °C min^{-1} under inert environment (N_2). The calorific values (CV) were determined according as per ASTM D5865−13 standard using an oxygen bomb calorimeter (Make: PARR, Model: 1341EB, USA). Proximate analysis was performed as per different ASTM standards: D3173–11 for moisture content (MC) [134], D3175–11 for volatile matter (VM) [135], and D3174–12 for ash content (AC) [136]. The fixed carbon (FC) was deduced by the difference. Bulk density was calculated following the core method, as outlined by Han et al. [137].The cation exchangeable cations (CEC, i.e. Na, K, Ca and Mg) were extracted using the ammonium acetate (NH_4 OAC), and quantified using a flame photometer following the

ASTM standards and procedures outlined by Bhowmick et al. [138]

4.3 Results and discussion

4.3.1 Characterization of raw biomass

The physicochemical properties of each feedstock are shown in Table 4.1. From proximate analysis results, it could be inferred that all biomass had high content of VM (73.24–79.07 wt %), and thus, they were potential precursors for pyrolysis. The feedstock contained a moderate percentage of AC (2.11–9.16 wt %), and a small percentage of FC content (7.07–15.03 wt %). The MC of all the samples was < 10 % (in the range 6.85–9.36 wt %), which is consistent with other biomass [114]. Low MC of biomass was additional helpful feature for pyrolysis. N content of feedstock was quite low (~ 3.86 wt %). Thus, the content of NO_x species (which are environmental pollutants) in the pyrolysis gas is expected to be very low.

Table 4.1 Proximate and ultimate analysis of individual feedstock

Analysis	**WH**	**TP**	**SCB**	**WHR**	**WHL**	**WHS**
Proximate analysis(% wt ad)						
Moisture content (MC)	9.04±0.10	6.85±0.30	7.83±0.01	8.69±0.40	9.14±0.20	9.36±0.20
Volatile matter (VM)	79.07±0.60	78.02±0.70	74.02±0.50	73.24±0.30	79.63±0.20	78.25±0.40
Ash content (AC)	4.82±0.10	2.11±0.40	3.12±0.01	9.16±0.00	3.31±0.20	4.13±0.20
Fixed carbon* (FC)	7.07±0.20	13.02±0.20	15.03±0.20	8.91±0.10	7.92±0.30	8.26±0.10
Ultimate analysis (% wt daf)						
C	36.44±0.10	44.70±0.10	42.02±0.20	31.03±0.80	34.87±0.10	36.06±0.20
H	5.02±0.00	5.84±0.10	5.77±0.10	7.19±0.30	5.65±0.20	4.98±0.10
O$^{(*)}$	54.68±0.00	48.09±0.10	49.91±0.20	60.57±0.10	57.33±0.10	55.88±0.20
N	3.86±0.40	1.37±0.20	2.12±0.60	1.21±0.00	2.15±0.10	3.07±0.10
H/C	1.64	1.55	1.63	2.76	1.93	1.65
O/C	1.13	0.81	0.89	1.47	1.23	1.16
Calorific value (MJ/kg)	15.45±0.50	20.41±0.70	18.77±1.10	10.97±1.00	14.12±0.70	14.89±1.20

Notation: air–dried basis (adb), dry ash–free basis (daf), * by difference

4.3.2 Thermal analysis of feedstock

The thermogravimetric (TG) and (DTG) curves of raw biomass are shown in Figures 4.2a and b, respectively. It should be noted that the peak areas on the DTG curve are directly proportional to the corresponding sample weight loss on the TGA curve. As seen from Figure 4.2a, the decomposition of raw biomass occurred in three stages, which is consistent with other biomass reported in the literature[114,121]. The three stages of degradation include: stage (1) drying/dehydration (150–200°C), which was characterized by a slight loss of mass. The % weight loss was mostly due to release of inherently bound moisture and light volatiles; stage (2) devolatilization (200–390°C) where pyrolysis holocellulose occurred. Relatively high temperatures in this stage led to degradation of high molecular weight compounds and holocellulose into smaller molecular weight pyrolysis products. The DTG curves shown in Figure 4.2b reveal significant difference in the temperature corresponding to maximum degradation rate for different biomass. The maximum temperature of decomposition (T_{max}) for roots was relatively low (301°C), followed by TP (309°C), WH whole plant (317°C), WH stem (328°C), WH leaves (332°C), while SCB had the highest T_{max} of 335°C. Finally, in stage 3, the mass loss was due to depolymerisation of lignin and it ranged from 400°–600°C. The third stage is characterized by a slow rate of degradation with less mass loss and high yield of char. The total mass loss varied among the feedstock. SCB had the highest mass loss of 64.71 % while WH roots had the least mass loss of 38.13%. The mass loss for the biomass showed inverse relation with the AC

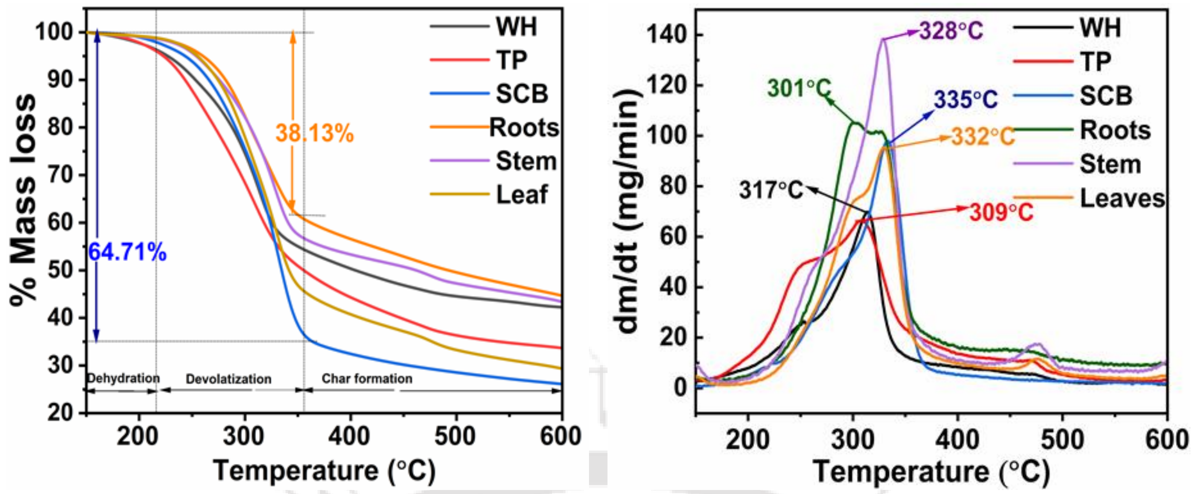

(a) (b)

Figure 4.2 (a) TGA and (b) DTG curves for WH, TP, SCB, roots, stem, and leaf at 10 °C/min

4.4 Characterization of biochar

4.4.1 Proximate and ultimate analysis

Proximate and ultimate results are outlined in Table 4.2a. The C content in all biochar increased with temperature. This is ascribed to the release of hydroxyl functional groups and evaporation of VM. Higher pyrolysis temperature triggered thermal degradation reactions, dehydration, decarboxylation and aromatization, which led to the enrichment of the C content in the resulting biochar. These results are further confirmed by the significant decline of the VM in biochar as the temperature rose from 350° to 550°C. The higher amount of VM at lower temperatures is ascribed to incomplete carbonization, which can be further correlated to the high atomic ratios and less amount of FC. The higher amount of VM in biochar obtained at low temperatures could be ascribed to the functional groups of C=O and C–H, which were identified in the FTIR analysis.

The calorific values (CV) of the biochar are also listed in Table 4.2. The biochar produced at higher pyrolysis temperature had higher CV. The CV of the biochar was in the range of 16.98–30.18 MJ kg^{-1}. SCB had the highest CV of 30.18 MJ kg^{-1} while WH R350 had the lowest CV of 16.98 MJ kg^{-1}. The CV of biochar can be correlated to their elemental composition, especially the C content. The atomic ratios decreased at higher pyrolysis temperature, which is attributed to the advanced decarboxylation and dehydration chemical reactions resulting in the formation of stable carbonaceous structures. The CV values of TP350, TP550, SCB350 and SCB550 are 24.82, 26.17, 29.46, and 30.18 MJ kg^{-1}, respectively. These CV values are higher than that of lignite and sub–bituminous coals (17–24 MJ kg^{-1}) [139]. Therefore, the biochar produced in this study have high potential as solid fuel.

The ash content of the biochar is also an important facet. Handling and processing feedstock with great AC is a contentious issue because they require more recurrent deposit removal, as well as maintenance on the boiler due to slagging [140,141]. The amount of AC in the biochar increased with rise in temperature. The increase was due to mineralization of the mineral matter, which is formed into ash during carbonization. AC varied in all the feedstock in the range of 2.11–9.16% as seen in Table 4.1. The AC in the biochar was in the range of 1.16–21.78 % as seen in Table 4.2. The AC of biochar produced from WH and TP were quite high, while SCB had the least quantities. The difference in AC is attributed to the varying amounts of alkali and alkali earth metals (AAEM) in the feedstock, which essentially appear in the form of ash [142]. The AAEM content of ash is highly conducive for plant nourishment and growth. Thus, biochar produced at higher temperatures would be more preferred for agronomy applications.

4.4.2 BET analysis

The results of BET analysis of the biochar are presented in Table 4.4. As the pyrolysis temperature increased from 350° to 550 °C, the S_{BET} values increased considerably. The highest

S_{BET} of 17.78 m^2/g was obtained for SCB 550**.** Similarly, it can be seen from Table 4.4 that V_{tot} and P_{size} values of the biochar also increased with pyrolysis temperature. These results were attributed to the elimination of VM through dehydration, softening, melting and carbonization that resulted in high pore volume and surface area of the biochar. A lower S_{BET} at 550°C was observed in WH L550 and WH S550 owing to the contraction of biochar due to the softening of the fibers. The reduction and closing of pores resulted in reduced pore volume. S_{BET} was a pointer of the adsorption capacity of biochar (which governs the uptake/retention of nutrients in the soil), and thus, an important facet for application in agronomy. Lower porosity in biochar produced at 350^{o}C could be a consequence of high VM in the biochar, which clogged the pores. The BET results showed potential of using biochar produced at 550^{o}C for soil amendment because it would markedly enhance soil adsorption capacity. The adsorption properties could help removal of the organic pollutants. Moreover, biochar could also remove heavy metal ions found in soil [143–147].

The P_{size} of biochar listed in Table 4.4 varied significantly in the range of 2.8–22.08 nm. Thus, the biochar are classified as mesoporous. The wide variation in the P_{size} is attributed to the structural composition of the native or raw feedstock [147]. Additionally, the permeable nature of biochar makes them potential precursors for production of organic C based form–stable composite phase change material (PCM). The bio–composite PCM synthesized from biochar could provide a solution to the leakages and low thermal conductivity problems associated with conventional PCM [148]. The biochar have a high tendency to adsorb metal ions and this enables addition of metal elements while producing the bio–composite. This can contribute to enhancing of thermal conductivity of PCMs, which can be used in the production of novel materials for heat storage [149].

Table 4.2 Physicochemical properties of biochar (Proximate and ultimate analysis

Analysis	WH R350	WH S350	WH L350	WH R550	WH S550	WH L550	WH 350	TP 350	SCB 350	WH 550	TP 550	SCB 550
Proximate analysis (% wt)												
MC^a	2.36±0.10	3.24±0.00	3.55±0.10	1.98±0.20	4.02±0.30	3.97±0.00	3.65±0.10	2.94±0.10	1.18±0.30	3.81±0.40	3.43±0.40	2.03±0.30
VM	27.40±0.20	35.29±0.20	36.41±0.20	32.36±0.40	31.25±0.20	31.33±0.50	33.47±0.20	19.53±0.10	23.72±0.10	19.61±0.30	13.64±0.40	19.39±0.20
AC	21.78±0.00	10.49±0.20	4.14±0.10	14.48±0.40	12.44±0.10	8.40±0.40	10.42±0.30	7.24±0.40	0.89±0.00	13.60±0.20	9.67±0.10	1.16±0.10
FC*	48.46±0.20	50.98±0.10	55.90±0.10	51.18±0.20	52.29±0.20	56.30±0.10	52.46±0.30	70.29±0.20	74.21±0.20	63.28±0.00	73.26±0.20	77.42±0.10
CV (MJ/kg)	16.98±0.00	17.19±0.20	18.03±0.20	17.56±0.00	17.97±0.10	18.74±0.10	17.90±0.00	24.82±0.10	29.46±0.20	18.93±0.90	26.17±0.20	30.18±1.30
BD (kg/m^3)	0.19±1.12	0.13±0.35	0.11±0.49	0.21±0.77	0.16±0.07	0.14±0.12	0.13±0.65	0.22±1.42	0.11±0.21	0.16±0.17	0.26±0.34	0.13±0.19
Yield (%)	39.84±1.03	36.54±0.65	31.28±0.42	32.46±0.26	26.94±0.15	24.68±0.33	34.25±0.56	29.63±0.75	26.41±0.67	28.39±0.27	25.69±0.39	21.15±1.23
Ultimate analysis (% wt daf)												
C	39.09±0.00	43.84±0.10	46.72±0.20	42.92±0.20	45.41±0.40	48.24±0.00	39.13±0.30	59.09±0.50	61.49±0.10	40.32±0.70	80.74±0.10	74.72±0.20
H	2.36±0.10	2.40±0.20	1.50±0.40	0.89±0.60	1.65±0.20	1.14±0.20	3.74±0.30	4.64±0.30	4.08±0.30	1.60±0.20	2.74±0.10	2.94±0.20
N	0.72±0.10	0.19±1.00	0.62±0.10	0.62±0.10	0.12±0.10	0.01±0.40	4.18±0.20	0.07±0.60	0.18±0.40	3.30±0.20	0.12±0.20	0.03±1.00
O*	57.83±0.00	53.57±0.60	51.17±0.10	55.57±0.80	52.82±0.70	50.61±0.30	52.95±0.20	36.20±0.10	34.25±0.10	54.78±0.40	16.35±0.20	22.32±0.70
H/C	0.72	0.65	0.38	0.25	0.43	0.28	1.14	0.94	0.79	0.47	0.40	0.47
O/C	1.11	0.92	0.82	0.97	0.87	0.79	1.02	0.46	0.42	1.02	0.15	0.22

Notation: ^{a} air–dried basis (adb), ^{b} dry basis (db), ^{c} dry ash–free basis (daf), * by difference

Table 4.3 Physicochemical properties of biochar (other analysis)

	Exchangeable bases											
	WH R350	WH S350	WH L350	WH R550	WH S550	WH L550	WH 350	TP 350	SCB 350	WH 550	TP 550	SCB 550
pH	9.14±0.25	7.71±0.09	8.82±0.03	10.02±0.04	10.20±0.06	10.42±0.11	7.66±0.05	8.46±0.07	7.36±0.10	10.05±0.08	10.01±0.06	10.06±0.15
EC (dS/m)	12.56±0.90	7.71±0.16	8.99±0.12	6.03±0.42	17.26±0.84	11.26±0.93	26.87±0.18	6.13±0.20	0.79±0.04	33.26±0.84	7.10±0.05	1.13±0.06
	Effective cation exchange capacity (ECEC) (cmol kg^{-1})											
Na$^+$	6.18±1.10	2.17±0.70	5.74±1.00	12.67±0.90	5.39±1.70	8.12±2.10	5.72±1.00	2.10±0.70	1.2±0.60	10.67±0.90	5.45±0.40	4.4±0.20
K$^+$	18.43±0.80	16.49±1.30	11.43±0.40	21.49±0.50	26.21±0.80	19.31±0.20	24.30±0.40	18.66±2.40	18.87±0.80	26.97±1.10	25.84±3.40	19.31±0.40
Mg^{2+}	4.11±0.50	8.56±0.90	8.97±0.60	10.23±1.00	13.24±0.50	14.25±1.20	9.61±0.60	5.62±0.90	9.3±0.10	12.62±0.10	9.30±0.90	16.45±1.00
Ca^{2+}	13.90±1.40	17.12±1.60	14.34±1.10	27.42±0.90	24.62±1.60	24.28±0.50	13.45±2.10	17.45±1.00	8.97±1.90	29.19±0.70	28.39±0.80	21.58±0.40
ECEC (cmol kg^{-1})	42.62	44.34	40.48	71.81	69.49	65.96	53.08	43.83	38.34	69.45	62.78	61.74

Table 4.4 BET properties of the biochar

	WH R350	WH S350	WH L350	WH R550	WH S550	WH L550	WH 350	TP 350	SCB 350	WH 550	TP 550	SCB 550
S_{BET} (m^2/g)	2.81	3.36	3.13	13.70	7.44	8.28	3.47	5.33	7.55	14.00	14.37	17.78
Pore volume (cm^3/g)	0.004	0.0052	0.0046	0.0047	0.0059	0.0196	0.02924	0.0075	0.0066	0.0417	0.0181	0.0250
Pore size (nm)	13.82	2.82	10.89	22.09	11.13	18.14	5.92	3.09	3.79	11.92	13.62	12.86

4.4.3 Crystalline structure

This section presents results on determination of crystalline structure of biochar from X–ray diffractogram (XRD) analysis. Moreover, identification of the major functional groups (or chemical composition) in the raw biomass and biochar using FTIR has also been discussed. The distinction between the functional groups of raw biomass and biochar gives an idea of the chemical effect of pyrolysis.

The XRD diffractograms of the biochar samples are presented in Figures 4.3a–f, which essentially show the mineral components identified in the biochar**.** The XRD patterns of SCB350 and SCB550 (depicted in Figure 4.3c) showed amorphous nature due to broad bumps and few peaks in the range 2θ = 10–33° [146,150]. The peaks in the XRD pattern for SCB 350 disappeared as temperature increased to 550°C. No detectable peaks were observed in the XRD pattern of SCB550. This indicated that the crystallinity reduced with the increasing pyrolysis temperature, and formation of C rich amorphous biochar [151]. These results are comparable to biochar obtained from corn straw at 300°C [131]. The peaks observed identified the dominance of tridymite (SiO_2) in the biochar produced from SCB. Also the XRD patterns of WHR350 and WHR550 biochar (Figure 4.3d) did not show well–defined peaks in the range 2θ =10–28° indicating presence of amorphous C. Biochar from whole WH plant and plant components (WHS and WHL) are crystalline in nature as seen from XRD patterns in Figures 4.3a, e and f. These XRD patterns reveal evenly–distributed sharp peaks. The peaks seen in Figure 4.3a (WH plant) at 2θ = 26.59°, 41.2°, 50° are assigned to quartz (SiO_2), and the peaks in Figures 4.3e and f (WHL350, WHL550, WHS350, and WHS550) were assigned to sylvite (KCl). For both TP350 and TP 550 biochar, the existence of kalisite ($KAlSiO_4$) was detected as illustrated in Figure 4.3b, where the high pitched peaks concentrated at 2θ = 29–40°. Thus, these biochar showed the presence of a crystalline structure.

The formation of $KAlSiO_4$ could be due to thereaction of K, Al, Si with O_2 present in raw biomass during pyrolysis. The other high peaks in the XRD pattern of TP 350 and TP 550 showed the existence of sylvite (KCl). These results are comparable to the X–ray spectra analysis of pine bark produced at three different temperature [152].

Relatively more intense peaks were noticed in biochar produced at 550°C, viz. WH 550, WH L550, WH S550 and TP 550. These results could be attributed to the shrinkage in the amorphous C based phase and structural alterations in both WH and TP. This also indicated rise in crystallinity of biochar with temperature. The strength of the peaks in XRD patterns of WH R350 and WH R550 (produced from WH roots) was relatively small. This could possibly be attributed to low holocellulose content of the feedstock. The XRD analysis essentially reveals that the biochar produced at 550°C, by virtue of their crystalline structure, could be excellent electrical conductors [153], and could be utilized for production of nanomaterials.

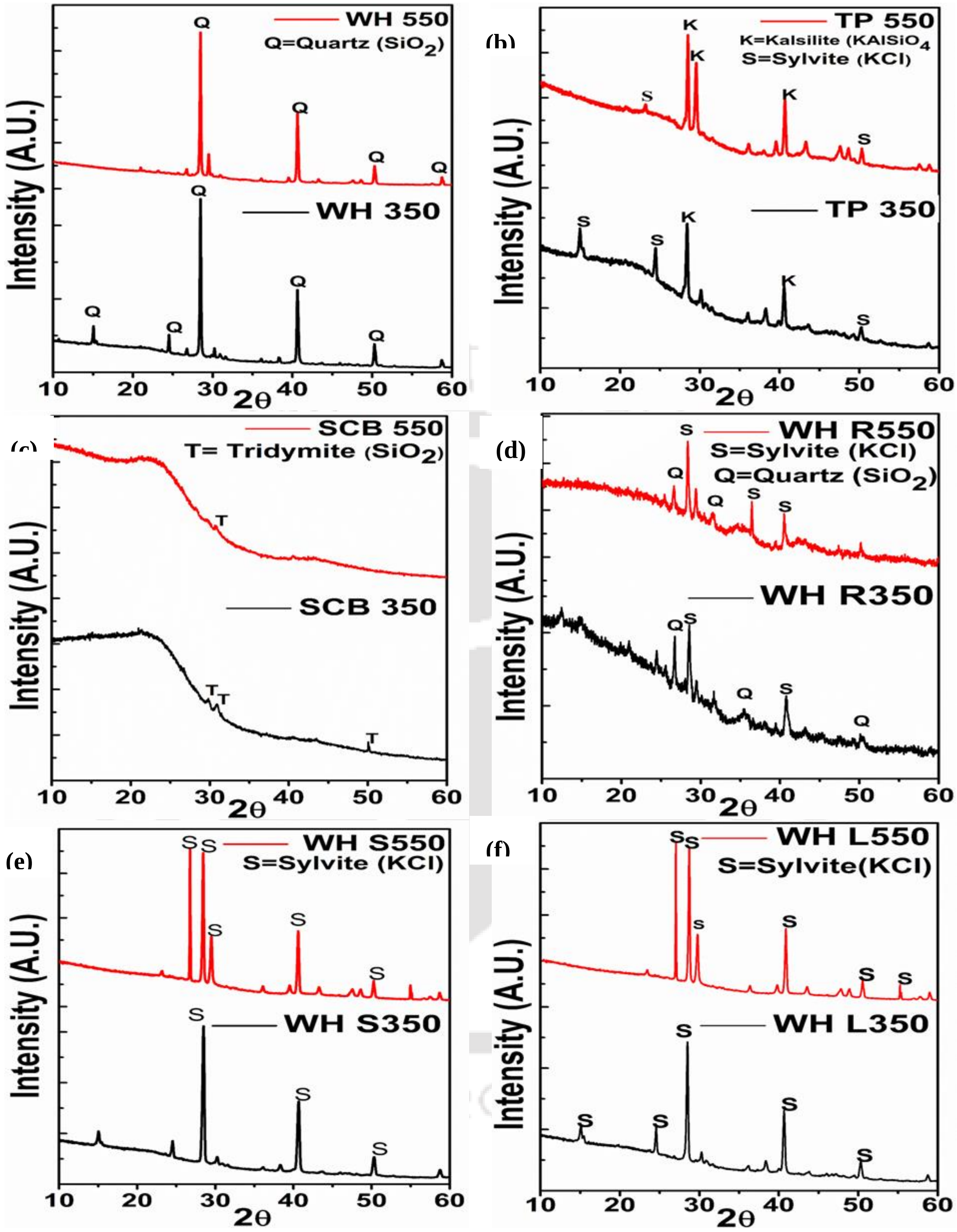

Figure 4.3 XRD diffractogram of biochar (a) WH 350, WH 550, (b) TP 350, TP550, (c) SCB 350, SCB 550, (d) WH R350, WH R550 (e) WH S350. WH S550, (f) WH L350, WH L 550

4.4.4 Functional groups analysis

Determination of the functional groups in the biochar was vital because they would affect the sorption properties of biochar. FTIR spectra of the biochar along with raw biomass, are shown in Figures 4.5a–f. The peaks in the spectra corresponding to different functional groups have been listed in Table 4.4. A comparative evaluation of FTIR spectra of the biochar with raw biomass clearly showed structural advancement of certain functional groups originally present in the feedstock after pyrolysis. The peak intensities in the range 1022–1064 cm^{-1} that corresponded to C–O, C=C and C–C–O increased after pyrolysis due to dehydration and degradation of the structural composition (decomposition of holocellulose, and breaking off their β–glycosidic bonds) of the raw biomass. However, the rise in intensity was more marked for pyrolysis at 550° than 350°C.

Intensification of the peak between 2500 and 2800 cm^{-1} showed the presence of aliphatic and aromatic C=C in SCB 550. It signified a greater extent of carbonization, which was also confirmed by high CV of the biochar. The transmittance of the band between 2700–3000 cm^{-1} (ascribed to C–H) in biochar is weak, which indicates presence of alcohol and carboxylic acid. The same band showed a lower intensity as the temperature rose to 550°C. Similarly, the intensities of the peaks in range 3100–3415 cm^{-1} (O–H) appeared to be weak in the biochar produced at 550°C, and in some of the biochar it could not be identified. This showed that an increase in temperature led to greater dehydration and decarboxylation [154]. Similar variations in functional groups of the biomass post pyrolysis have been reported in previous literature [6,145,152,155]. In summary, FTIR analysis shows loss of carboxyl, hydroxyl and, carbonyl groups in raw biomass during pyrolysis leaves behind a carbon–rich biochar with high CV. This could be used as solid fuel.

Table 4.5 Classification of functional groups of biochar and biomass from FTIR spectra

Wavenumber (cm^{-1})	Functional group	Class of compounds	Ref
781	C–H	Pyridine	[138]
885	C–H	Aromatics	[156]
1030–1100	C–O	Cellulose, hemicellulose, and lignin	[157]
1325	O–H	Phenols	[156]
1440	C=C	Lignin carbohydrates	[157]
1600	C=C, C=O	Ketones	[158]
2935	C–H	Aliphatic	[158]
3200–3500	O–H	Hydroxyl	[154]

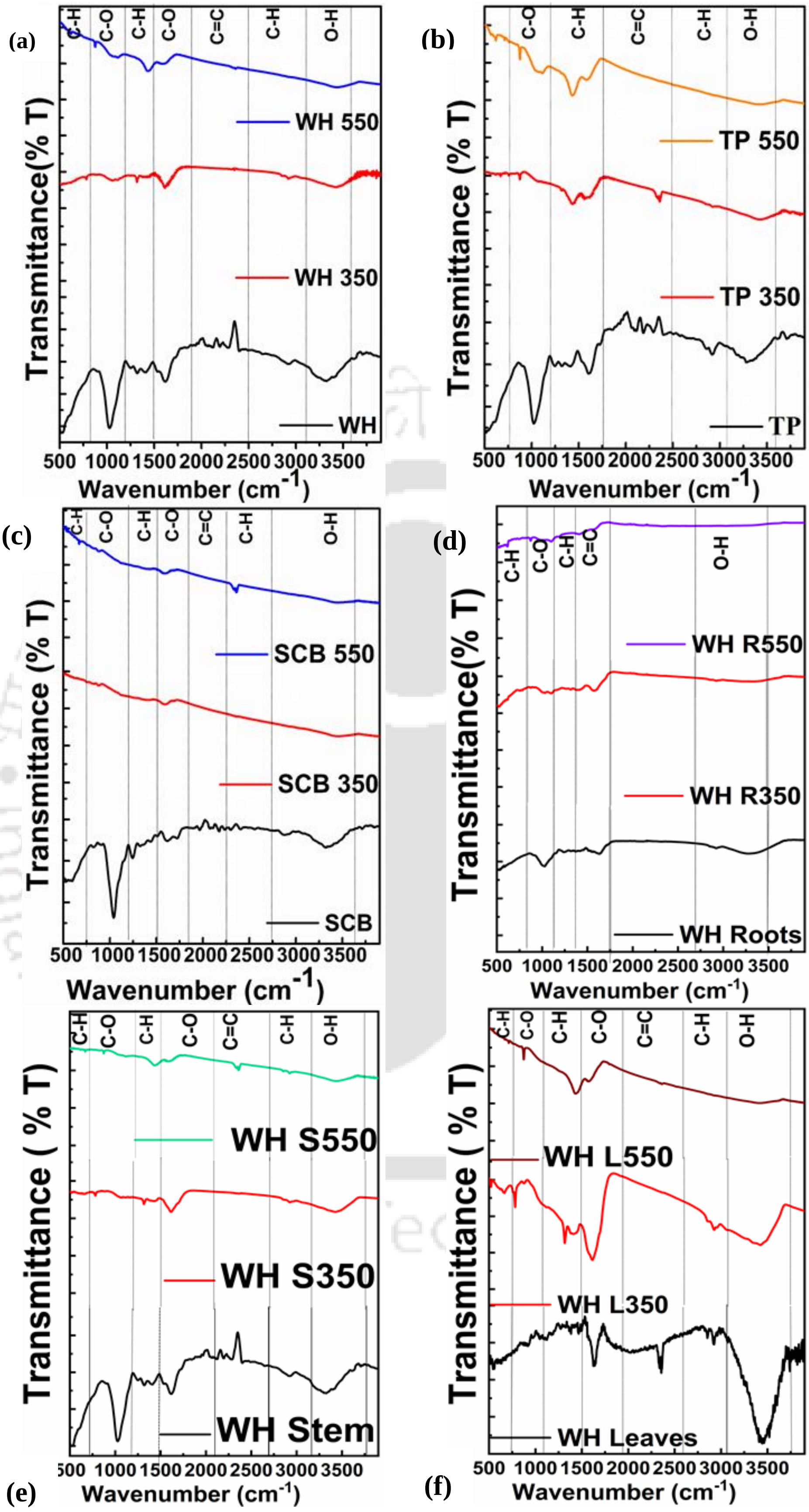

Figure 4.4 FTIR Spectra of biomass and biochar produced at 350°C and 550°C

4.4.5 Surface morphology analysis

Representative SEM micrographs of twelve biochar are shown in Figures 4.5a–f. The micrographs of biochar obtained from individual components of WH plant are given in Figures 4.6 g–l.

All micrographs exhibited porous facades on the biochar. With rising temperature, VM was released out of the feedstock in the form of H_2O, CH_4, CO_2, and CO creating pores on the façade [159]. Moreover, volatiles confined inside the feedstock inflated the surface due to expansion and thermal decomposition of holocellulose, which led to the porous nature of the biochar, as seen in Figures 4.5a–f.

It can be seen from the micrographs that biochar WH 350, WH R350, WH S350, WH L350, WH 550, WH R550, WH S550, and WH L550 had rough, withered, and solid coarse surfaces with many uneven pores. Surfaces of the biochar TP 350 and TP 550 were rough and had slight trails, as seen from Figures 4.5c and d. The biochar SCB 350 and SCB 550 (Figures 4.4e–f) had visible pores that were in good shape, similar to a honeycomb. The shape of all biochar produced at 550°C showed pores of smaller size, which is ascribed to dehydration of the cell structure at higher pyrolysis temperature. Permeable structure of biochar makes it suitable for soil amendment and as precursor for form–stable material for energy storage. Structural changes were further evident by the FTIR results, which shows a decrease of C–O, C=C, and O–H peaks and formation of alkyl bonds. At higher pyrolysis temperature, smoother and thinner lamellar structures prevailed with high surface area. Expansion of the VM enclosed in the stacks of the biochar contributed to opening of pores, as shown in the SEM micrographs in Figs.4.5a–l the difference in morphological structures of biochar produced from different biomass at a particular pyrolysis temperature is attributed to varying degree of mass conversion and devolatilization of organic materials in the feedstocks. The diverse structure and distribution of pores present in the biochar affirmed the heterogeneous nature of biomass, which is in agreement with previous literature [160,161].

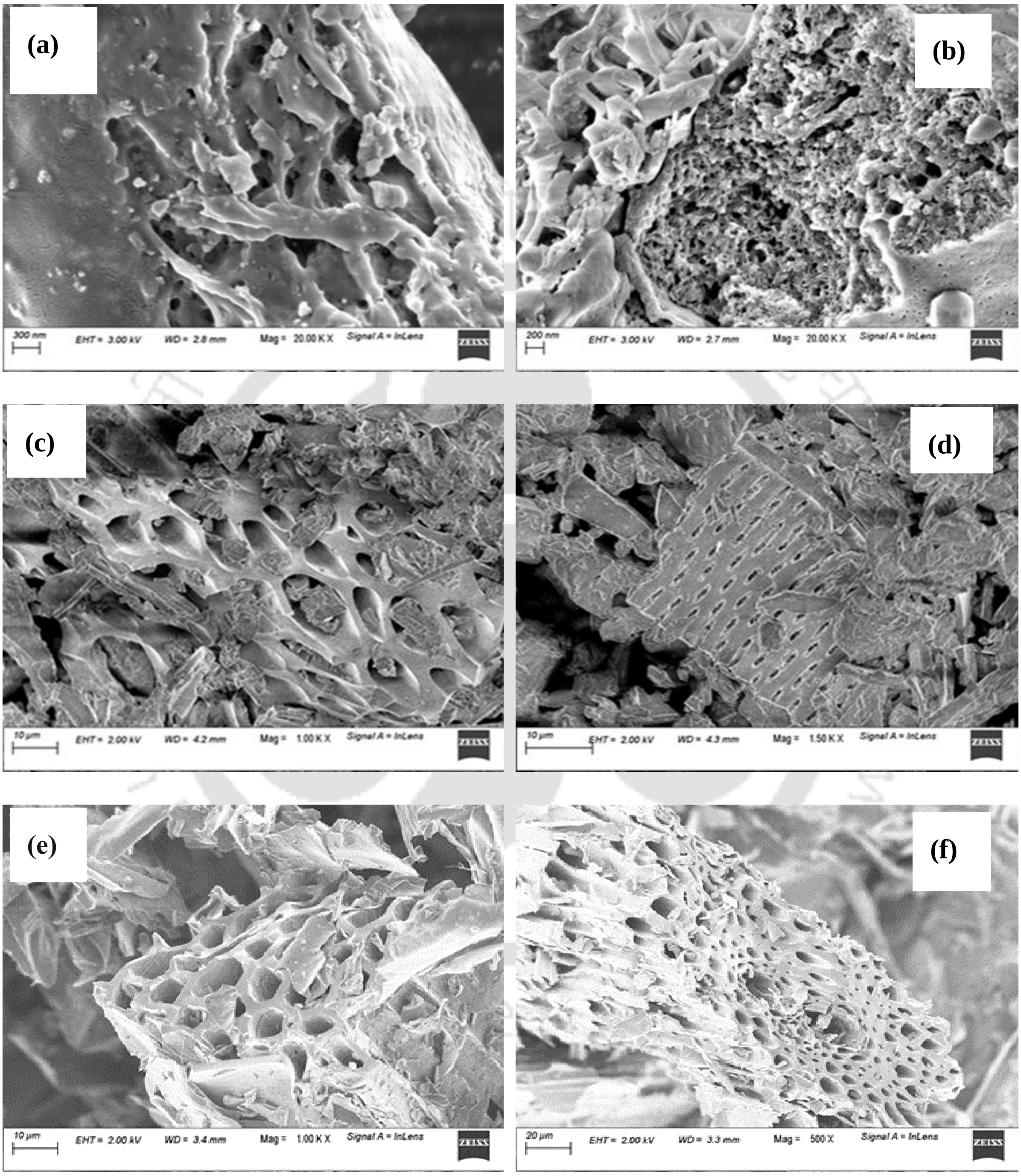

Figure 4.5 SEM micrographs of biochar (a) WH 350 (b) WH 550 (c) TP 350 (d) TP 550 (e) SCB 350 (f) SCB 550

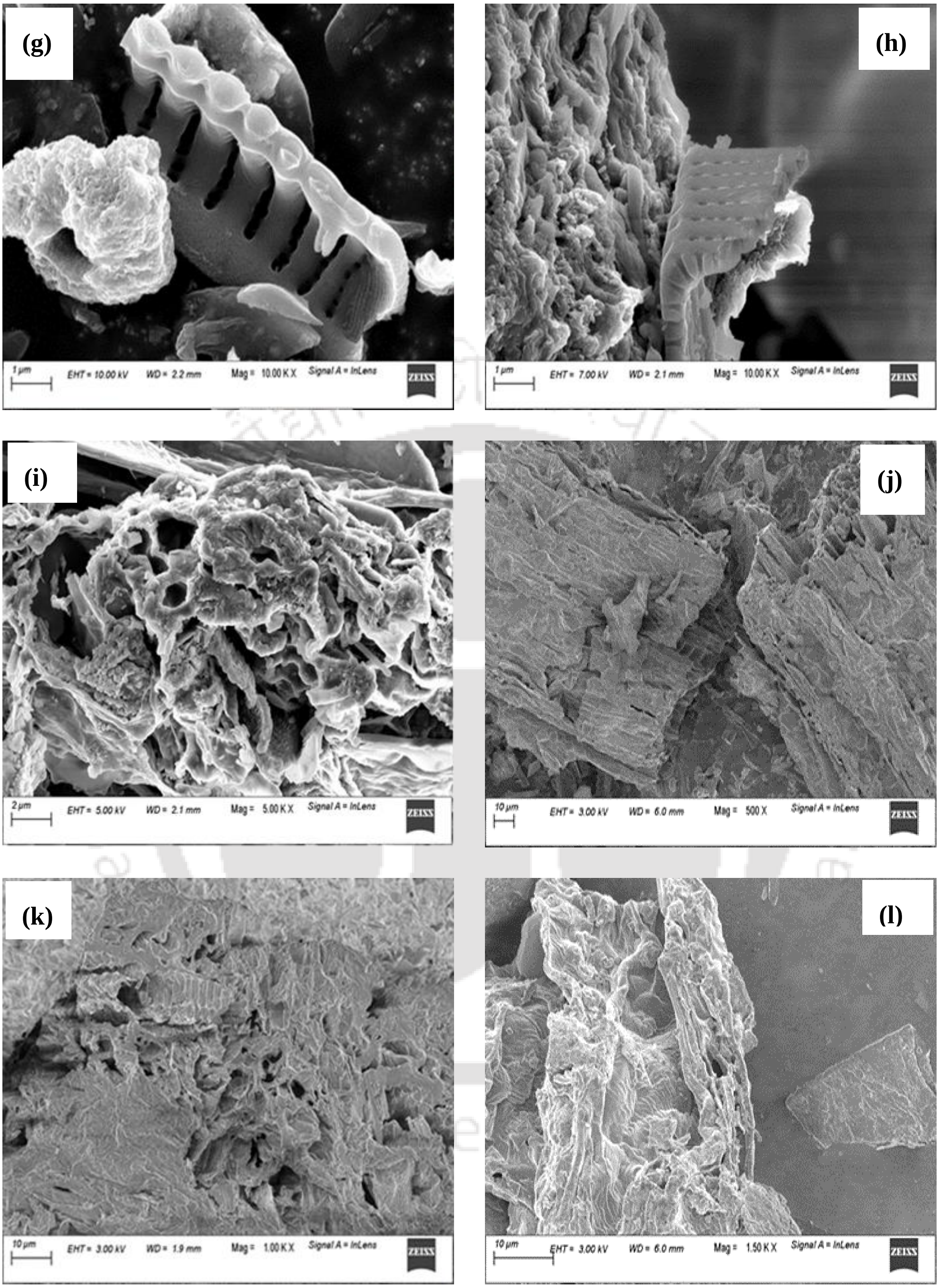

Figure 4.6 (g) WH R350, (h) WH R550, (i) WH S350, (j) WH S550, (k) WH L350, (l) WH L550

4.5.6 Thermal analysis

The TGA curves of the biochar and the corresponding raw biomass are shown in Figures 4.7. The biochar produced at 350°C were thermally less stable as the TGA curve showed the three zones of disintegration – as the original biomass. This was attributed to the fact that they were not fully carbonized with some inbound MC and VM – which is also confirmed by the proximate analysis given in Table 4.1a. Due to pyrolysis that takes off VM, the TGA curves of biochar showed relatively lesser weight loss. Both SCB 350 and SCB 550 clearly showed two sharp weight loss peaks, which overlapped each other with a slight difference in their intensity (which corresponds to actual mass loss). This could be a consequence of relatively low MC and high C content of biochar. The high stability is attributed to the formation of heat resistant carbon in the biochar due to aromatization and dehydrogenation at higher temperature. This also indicated higher thermal stability of the biochar produced at 550°C with % weight loss in the range of 2.76–10.56%. These biochar could be applied in agronomy for carbon sequestration due to their stability, and could also be utilized as fuel owing to the high C content and high CV. The high thermal stability of biochar also shows their potential in energy engineering for developing of a supporting matrix used in organic PCMs that are used in heat storage systems [162].

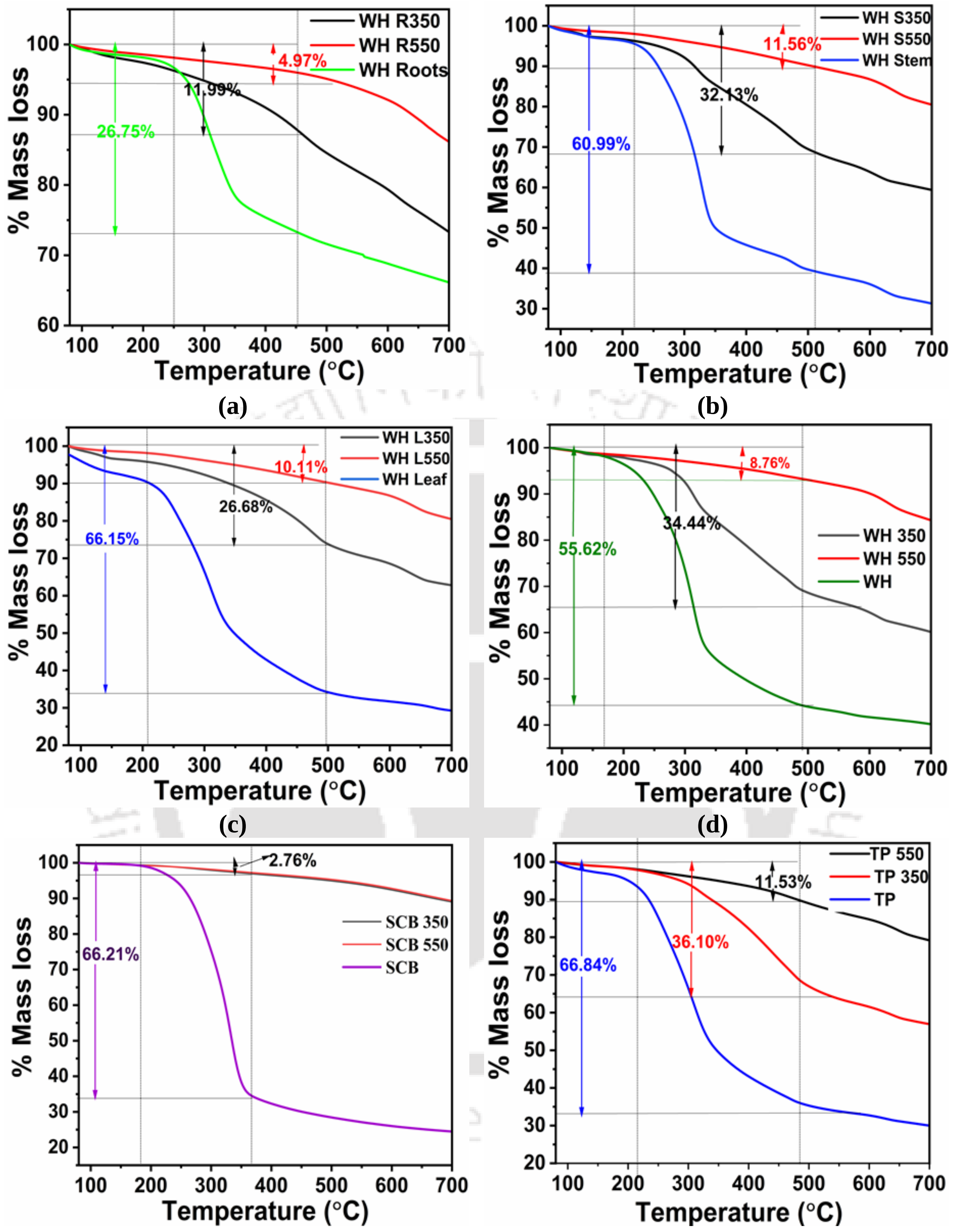

(a) (b)

(c) (d)

(e) (f)

Figure 4.7 TGA curves of feedstock and biochar. (a) WH Roots, (b) WH Stem, (c) WH Leaf, (d) WH whole plant, (e) SCB, (f) TP

.

4.5.7 EDX and atomic ratio analysis

The EDX spectra and summary of minerals present in the biochar are shown in Figures B1 and Table B1 (Appendices). The intense peak corresponding to C in EDX spectra of all biochar shows C–rich content of the biochar [163]. Moreover, the intensity of the peak increased with temperature, as confirmed by the ultimate analyses. The other prominent elements in biochar are alkali and alkaline earth metals like aluminium (Al), magnesium (Mg), calcium (Ca), and potassium (K). EDX spectra also indicated that biochar produced at lower temperatures had more O in their structures. The EDX results are further supported by the FTIR spectra of biochar produced at 350^{o}C (shown in Figure 4.3), which showed a dominant peak assigned to O–H group. These biochar had a tendency to be more hydrophilic. Higher temperature contributed to the removal of O, and hence, resulted in hydrophobic biochar.

The C content of biochar increased while both O and H content reduced considerably with increasing temperature due to decarboxylation and dehydration reactions during pyrolysis. A low H/C ratio in the range of 0.25–0.47 of biochar at high temperature reveals that there is a higher grade of aromatization and thermal change of biomass by means of major loss of H and increase of C in the biochar. A lower atomic ratio also indicates that there is an extremely condensed aromatic structure due to depolymerization of the feedstock after pyrolysis. For agronomy applications, biochar with lower H/C ratios are ideal because higher aromaticity levels would render them relatively stable in the soil – in contrast to the decomposition of carbon in raw biomass resulting in release of methane [6,155]. Higher O/C ratio of 0.42–1.11 in biochar produced at low temperatures indicated low aromatic content and higher oxygen content as indicated by EDX spectra.

They had more hydrophilic surfaces than biochar produced at high temperatures due to lower levels of carbonization and a large quantity of polar functional groups [164]. Due to removal of O and the O–H groups at higher temperature, as revealed by EDX analysis, the biochar produced at higher temperature had higher hydrophobic character. These biochar were not preferred for carbon sequestration because they have shorter durability and are less recalcitrant. From the Van Krevelen diagram (Figure 4.6), it can be observed that most biochar underwent dehydration, depolymerization and decarboxylation at higher temperature, and hence, improved their fuel quality – in contrast to raw biomass. The rate of depolymerization in WH R350 and WH R550 biochar was low as exhibited by the higher atomic ratios.

4.5.8 BIOCHAR YIELD

Maximum biochar yield of 39.84 % was obtained at 350°C from WH R350; even though the other feedstock also showed a high yield of biochar at low temperatures. The yield of biochar decreased because of the rise in temperature. This is accredited to more rapid devolatilization and removal of excess volatile compounds at 550°C. The lowest yields of 21.15 % and 26.94% were obtained for SCB 550 and WH S550, respectively. The low biochar yield from SCB, at low temperatures, could be attributed to the full degradation of holocellulose material. The higher yield of WH R550 (32.46%) at 550°C could be attributed to high AC of the roots. Similar results were reported for the biochar produced from sewage sludge and cow and pig manures [165,166].

The results in Table 4.2 indicated that bulk densities of biochar are in the range of 0.11–0.26 g cm^{-3}. This is consistent with previous literature [32]. TP 550 showed the highest bulk density of 0.26 g cm^{-3}, and bulk density increased with temperature due to decrease in VM. All biochar, by virtue of their low bulk density and porous structure, are found to be suitable for agricultural applications.

Mixing of biochar with soil could result in the reduction of soil bulk density. This would help increase the water content of the soil. The porous structure of biochar could also assist adsorption of minerals and the growth of nitrogen/carbon fixing bacteria in soil, which is highly conducive for crop growth and yield [32].

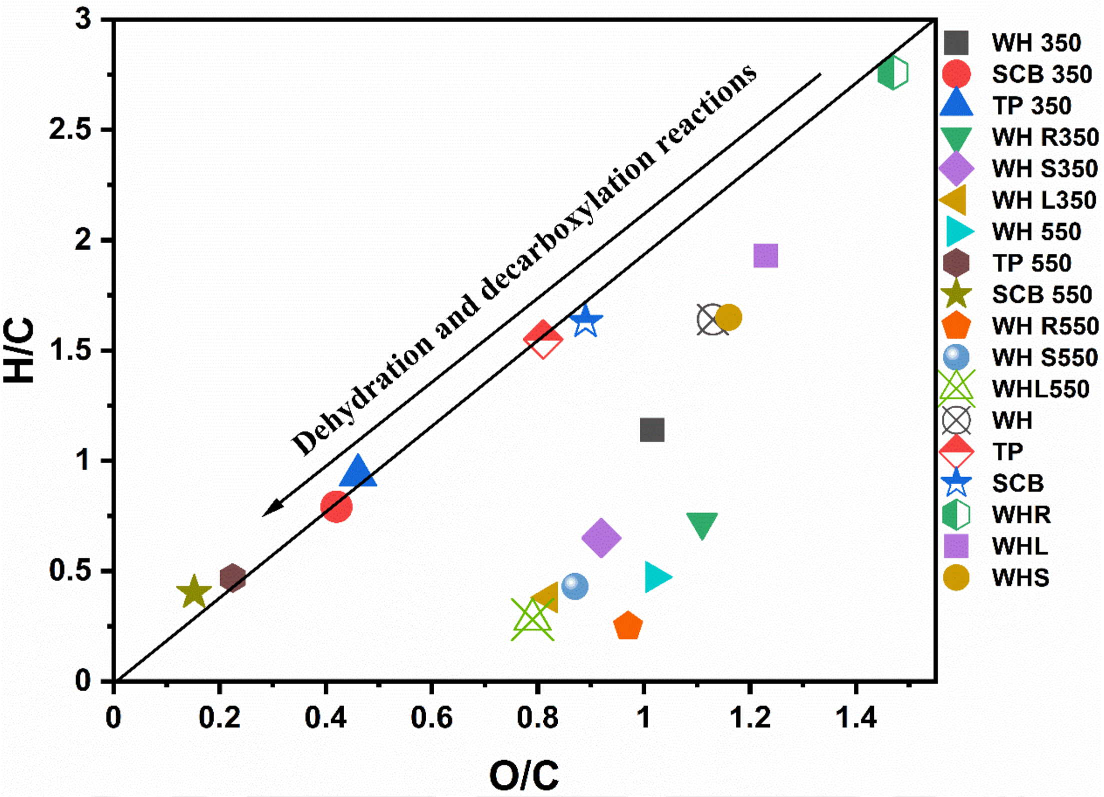

Figure 4.8 Van Krevelen plot of biochar and biomass

4.5.9 Exchangeable bases

The pH of biochar determines its application in agriculture. The alkalinity of biochar can efficiently decrease soil acidity and increase soil pH, as evident from the results shown in Table 4.3. High pH of biochar produced at 550°C could be a result of high contents of alkali and alkali earth metals present in ash. Also, the reorganization of functional groups because of decarboxylation, dehydration, and aromatization usually led to the increase in pH. Moreover, from FTIR analysis, it can be established that the presence of phenolic and carboxyl groups imparted negative surface charge to the biochar that resulted in rise in pH. As the pyrolysis temperature increased there was a rise in EC. The EC ranges were found to be within 0.79–33.26 dS m^{-1}. The rise in EC could be attributed to higher ion content of biochar due to high AC.

4.5.10 Effective cation exchange capacity (ECEC) analysis

From Table 4.2, it can be inferred that ECEC values of the biochar were in the range of 38.34–71.81 cmol kg^{-1}. WH R550 had the highest ECEC, which is attributed to the presence of clay minerals. ECEC values signify potential of biochar for both C storage and as a soil additive to increase the natural soil CEC. The ECEC results compare well with the atomic ratios of the biochar, which can be attributed to the high O content in the functional groups. ECEC essentially specifies the ability of biochar to absorb the cations. Addition of biochar to the soil with low ECEC (or mixing of biochar with fertilizers) could enable soil to hold nutrients like NH^{+4} and K^{+} for plant growth. Consequently addition of biochar could prevent the leakage of the nutrients from inorganic fertilizer that have a tendency to pollute the phreatic water [167]. ECEC values of biochar in this study were comparable to those reported in the literature (for example, biochar at 550°C from rice husk: 29.59–41.36 cmol kg^{-1}, pine sawdust: 39.22–56.13 cmol kg^{-1}) [138,151].

4.6 Summary

From the analysis it has been seen that properties of biochar are not only a function of composition of original feedstock but also the pyrolysis temperature. The porous surface morphology, higher AC, high BET surface area, high thermal stability and low bulk density, alkalinity and low atomic ratios are the crucial properties that determine the suitability of the biochar in agronomy and these properties enhanced with the temperature of pyrolysis. However, the yield of biochar reduced with temperature. Thus, optimization of the pyrolysis temperature is an important issue in biochar synthesis. Addition of biochar in agronomy increases the mineral content and pH value of soil. These biochar also prevent uptake of organic contaminants and heavy metals present in soil by the plant roots. High carbon content, and high CV, in addition to low MC makes the biochar a solid fuel at par with lignite coal. Porosity of the biochar provides supporting matrix for PCM, which assists manufacture of form–stable material for thermal energy storage. By virtue of enhanced surface area, WH derived biochar can also be used as supporting matrix for synthesis of form–stable bio–composites. In the next chapter kinetic and thermodynamic aspects of pyrolysis of biomass blends (ternary and binary) obtained from WH, TP and SCB, using thermogravimetric analysis have been discussed

CHAPTER 5– Characterization, kinetic and thermodynamic pyrolysis of biomass blends

5.0 Introduction

Kinetic and thermodynamic investigations of blends of three lignocellulosic biomass, viz. WH, TP and SCB, using thermogravimetric analysis have been discussed in this chapter. Prior to kinetic analysis physiochemical characterization of biomass blends was carried out using standard techniques. This chapter mainly focuses on the use of advanced isoconversional method of Vyazovkin, Vyazovkin_AIC model, Distributed Activation Energy model (DAEM) along with the conventionalmethod Ozawa–Flynn–Wall (OFW). Large scale processes for production of biofuels and value–added products from lignocellulosic biomass would require feedstock in large quantities, and would thus necessitate use of blends of biomass – instead of a single type of biomass [168]. Processing of biomass blends is a significant challenge due to significant variations in the structural compositions and physicochemical properties of the individual biomass [80]. There could be several synergistic interactions between the individual biomass as they undergo physical, chemical or biological changes during the process. Identification of these synergistic effects is also crucial for proper design and optimization of the processes based on biomass blends.

5.1 Materials and method

5.1.1 Collection and processing of biomass

Procedure for collection and processing of biomass is described in Chapter 3 under sub–section 3.2.1.

5.1.2 Preparation of biomass blends

Both binary and ternary blends of WH, TP and SCB were prepared on the basis of weight percent or fraction using an analytical precision balance (Make: Metter–Toledo, Model: ME802E, least count: 0.1 mg). Three binary blends were prepared by mixing the 3 biomass (WH, TP and SCB) in equal proportions (50 wt % each) abbreviated as: WH TP, WH SCB and TP SCB. Three ternary biomass blends were prepared by mixing 33.3, 50 and 60 wt % of WH, and the balance composition (i.e. 66.6, 50 and 40 wt %) equally distributed among other two biomass feedstock, viz. TP and SCB. These ternary blends were designated as WH111, WH211 and WH311, where the numbers 111, 211 and 311 represent relative proportions of the biomass in the blend, as shown in Table 1. The samples were mixed through repetitive scooping and homogenized in a rotating grinder for uniformity. Samples selected for co–pyrolysis experiments were further milled and sieved to pass through 2 mm sieve and stored in airtight packets.

Table 5.1 Sample code and % weight composition of noxious weeds with agro residue

Sample code	% Weight of each component blended		
	Water hyacinth	*Thevetia peruviana*	Sugar cane bagasse
Binary blends			
WH SCB	50	–	50
WH TP	50	50	–
TP SCB	–	50	50
Ternary blends			
WH 111	33.33	33.33	33.33
WH 211	50	25	25
WH 311	60	20	20

5.1.3 Characterization of blended feedstock

Proximate analysis of the raw biomass and the blends was done according to protocols outlined in ASTM standards (moisture content: ASTM E871–82, ash content: ASTM D1102–84, volatile matter content: ASTM E872–82), and fixed carbon content was calculated by mass difference. Ultimate analysis of raw biomass and the blends was done for determination of % content of C, H, N, S, and O using an elemental analyzer (Make: Euro EA, Model: Eurovector EA3000). Calorific value (CV) was determined using an oxygen bomb calorimeter (Make: PARR, Model: 1341EB). Surface morphology of the biomass blends was examined using field emission scanning electron microscope (FESEM) (Make: Zeiss, Germany, Model: Sigma 300). Thermal degradation of the blends were studied using a thermal gravimetric analyzer (TGA) (Make: M/s Netzsch, Germany, Model: TG 209 F1 Libra). The functional groups present were identified by Fourier transform infrared spectroscopy (FTIR) analysis (Make: Shimadzu, Japan, Model: IRAffinity–1). The compositional analyses were determined as per the procedure outlined by Singh et al. [169]. The bulk density was determined as per ASTM D873–82 [103] standard which involved measuring the weight of the sample and calculating the ratio of the sample to the volume of the container.

5.2 Kinetic analysis

The TGA data of each blend were obtained at four different heating rates, viz. 8, 10, 15 and 30 °C min^{-1}. The TGA data was analyzed with three models, viz. the conventional model of OFW, Vyazovkin_AIC [123] and DAEM [170] to determine the kinetic triplets (i.e. activation energy, pre–exponential factor and the solid state reaction mechanism representing co–pyrolysis) of the blends. A conversion range of 5–75 % was used for kinetic analysis. The co–pyrolysis process is a step–wise reaction mechanism, and hence, a step size of 0.05 was applied. The step size chosen for multistep kinetics is as per recommendations of ICTAC [123]. The thermogravimetric (TG) and differential thermogravimetric (DTG) curves for the biomass blends essentially revealed that the temperature ranges over which maximum mass loss occurred (corresponding to decomposition of organic matter) was 150°– 600°C. Prior to 150°C, the mass loss corresponded to loss of moisture and the volatiles, while beyond 600°C, the mass loss was negligible. Thus, 150° and 600°C could be considered as 'onset' and 'offset' temperatures of thermal degradation of biomass blends. Thus, the kinetic analysis was based on TGA data in this temperature range [125].

5.2.1 Kinetic model analysis

The rate of decomposition from solid–state to volatile products is described by Eq. (5.1) [171]

$$\frac{d\alpha}{dt} = k(T) f(\alpha) \tag{5.1}$$

where $\frac{d\alpha}{dt}$ is the rate of conversion; $k(T)$ is the temperature–dependent rate constant, and $f(\alpha)$ is the of the reaction model. The degree of conversion α represents the standardized form of mass loss of the decomposed sample and is expressed by Eq. (5.2) [172].

$$\alpha = \frac{x_i - x_t}{x_i - x_f} \tag{5.2}$$

where x_i = initial mass, x_t = instantaneous mass of the feedstock at any time t, x_f = residual mass at the end of degradation. The rate constant $k(T)$ is expressed by the following Arrhenius equation Eq. (5.3).

$$k(T) = A\exp\left(\frac{-E_\alpha}{RT}\right) \tag{5.3}$$

where A is the pre–exponential factor (s^{-1}), E_α is the apparent activation energy (kJ mol^{-1}), T is the absolute temperature (K), and R is the universal gas constant (8.314 J mol^{-1} K^{-1}). Combining Eq. (5.1) and Eq. (5.3) the rate of conversion can be expressed as Eq. (5.4).

$$\frac{d\alpha}{dt} = A\exp\left(\frac{-E}{RT}\right) f(\alpha) \tag{5.4}$$

For non–isothermal TGA experiments at constant (linear) heating rate $\beta = \frac{dT}{dt}$ Eq. (5.4) can be expressed using chain rule as [110].

$$\frac{d\alpha}{dT} = \left(\frac{A}{\beta}\right)\exp\left(\frac{-E_a}{RT}\right) f(\alpha) \tag{5.5}$$

5.2.2 Isoconversional methods

Thermal degradation of biomass involves numerous chemical reactions during decomposition of the three components, viz. cellulose, hemicellulose and lignin. Thus, the degradation cannot be described on basis a single or a well–defined sets of chemical reactions [173]. In view of this limitation, isoconversional (or model–free) methods have been employed for analysis. Isoconversional methods are aimed at determining the kinetics triplets of the thermal decomposition without a prior assumption of the reaction model [174]. The isoconversional methods are based on principle: at a constant extent of conversion, the reaction rate is a function only of the temperature as shown in Eq. (5.6) [108].

$$\left[\frac{d\ln\left(\frac{dx}{dt}\right)}{dT^{-1}}\right]_\alpha = -\frac{E_\alpha}{R} \tag{5.6}$$

As noted earlier, the kinetic analysis is based on three isoconversional methods, viz. OFW and Vyazovkin_AIC and DAEM.

5.2.3 Ozawa–Flynn–Wall (OFW)

This is an integral isoconversional model that uses Doyle's approximations of the temperature integrals. It is described by Eq. (5.7) [175]:

$$\ln(\beta_i) = const - 1.052\left(\frac{E_\alpha}{RT_\alpha}\right) \tag{5.7}$$

Considering any constant value of α and plotting $\ln\beta$ against $\frac{-1.052}{RT}$ results into a straight line. The apparent activation energy can be determined from the slope.

5.2.4 Vyazovkin_AIC model

Advanced isoconversional method of Vyazovkin_AIC model is given the following equations for determining activation energy (E_α) for any particular value of α:

$$\phi_{E_\alpha} = \min\left(\sum_{i}^{n}\sum_{j\neq i}^{n}\frac{J\left[E_\alpha, \mathrm{T}_i(t_\alpha)\right]}{J\left[E_\alpha, \mathrm{T}_j(t_\alpha)\right]}\right) \tag{5.8}$$

The activation energy for a given value of α is determined by minimization of the function given by Eq. (5.8). The integral $J\left[E_\alpha, T_i(t_\alpha)\right]$ is given as:

$$J\left[E_\alpha, T_i(t_\alpha)\right] = \int_{t_{\alpha-\Delta\alpha}}^{t_\alpha} \exp\left(\frac{-E_\alpha}{RT_i(t)}\right)dt \tag{5.9}$$

Eq. (5.9) assumes constant E_α only for a small segment (or fraction) $\Delta\alpha$ of total conversion and is evaluated numerically from non–isothermal data using trapezoidal rule. The minimization of Eq. (5.8) is repeated at different values of α to find the E_α dependence on α. The minimization of the function was carried out at each α value using Mat lab R2019a by considering a step of $\Delta\alpha = 0.025$.

5.2.5 Distributed activation energy method (DAEM)

This method has been frequently used to simulate the multifaceted reactions taking place during the pyrolysis of biomass and fossil fuels [176]. DAEM considers the thermal degradation of fuels as a large number of autonomous processes, which are characterized exclusively by their apparent activation energy. The DAEM procedure presumes that the entire biomass decomposition process occurs in the form of several parallel first–order reactions. The reactions share a similar pre–exponential factor and have a continuous Gaussian distribution of the apparent activation energies [177]. Therefore, the rate at which volatiles are released by a particular reaction can be expressed in the form of mass balance of the reactant species expressed by Eq. (5.10) [178].

$$1-\alpha = \int_0^\infty \exp\left(-A\int_0^t \exp\left(\frac{-E}{RT}\right)dt\right) f(E)dE \tag{5.10}$$

where $f(E)$ is the distribution of activation energy that fulfils the condition:

$$\int_0^\infty f(E)dE = 1 \tag{5.11}$$

It is not virtually possible to estimate the quantity of volatiles released and kinetic constraints from experimental data for all the first order reactions occurring. Therefore, Eq. (5.12) developed by Miura [179] was used to estimate the kinetic parameters.

$$1-\alpha = \int_{E_S}^\infty f(\mathrm{E})\,\mathrm{dE} \tag{5.12}$$

where E_s is the apparent activation energy at a specific temperature (T) that fulfils the condition expressed by Eq. (5.13)

$$\frac{0.545\beta E_S}{ART^2} = \exp\left(\frac{-E_S}{RT}\right) \tag{5.13}$$

Miura and Maki [180] have approximated Eq. (5.13) as:

$$\ln\frac{\beta}{T^2} = \ln\left(\frac{AR}{E}\right) + 0.6075 - \frac{E}{RT} \tag{5.14}$$

Using Eq. (5.14) the kinetic parameters can be found by plotting $\ln\frac{\beta}{T^2}$ versus $\frac{-1}{RT}$. E_α can be determined by slope at various mass conversion and pre–exponential factor A can be deduced from intercept.

5.2.6 Determination of reaction mechanism using Criado method

Eqn. (5.15) represents the reaction as a single–step reaction, which is dependent only on temperature (T) and mass conversion (α). The process of co–pyrolysis satisfies this condition, and thus, the prevalent solid state reaction mechanism can be predicted using the master plot method proposed by Criado [181]. If the temperature of the sample subjected to co–pyrolysis increases at a constant rate β, we can write:

$$\frac{d\alpha}{dT}\cdot\frac{dT}{dt} = A\cdot\exp\left(\frac{-E}{RT}\right)f(\alpha) \tag{5.16}$$

$$\int\frac{d\alpha}{dT}dT = \int\frac{A}{\beta}\exp\left(\frac{-E}{RT}\right)f(\alpha)dT \tag{5.17}$$

The integral on RHS of Eq. (5.17) can be approximated as:

$$g(\alpha)=\frac{ART^2}{E\beta}\exp\left(\frac{-E}{RT}\right) \tag{5.18}$$

Eliminating *A* between Eqs. (5.15) and (5.18) gives:

$$g(\alpha)=\frac{RT^2}{E\beta}\frac{d\alpha}{dt}\frac{1}{f(\alpha)} \tag{5.19}$$

which for $\alpha = 0.5$ becomes:

$$g(0.5)=\frac{RT_{0.5}^2}{E\beta}\left(\frac{d\alpha}{dt}\right)_{0.5}\frac{1}{f(0.5)} \tag{5.20}$$

where $T_{0.5}$ and $\left(\frac{d\alpha}{dt}\right)_{0.5}$ are, respectively, the temperature and the rate when $\alpha = 0.5$. Dividing Eqs. (5.19) and (5.20) yields:

$$\left(\frac{T}{T_{0.5}}\right)^2\left\{\frac{\left(\frac{d\alpha}{dt}\right)}{\left(\frac{d\alpha}{dt}\right)_{0.5}}\right\}=a\cdot f(\alpha)\cdot g(\alpha) \tag{5.21}$$

where $a=\frac{1}{f(0.5)\cdot g(0.5)}$ is a constant for a given mechanism. The point $\alpha = 0.5$ is considered as a reference point where the standard master plots of each considered kinetic mechanism intersect each other corresponding to value of $\frac{f(\alpha)\cdot g(\alpha)}{f(0.5)\cdot g(0.5)}=\frac{Z(\alpha)}{Z(0.5)}=1$. The theoretical curves of $f(\alpha)$ and $g(\alpha)$ corresponding to different standard solid–state reaction mechanisms are listed in Table A1 of appendix A.

5.2.7 Determination of the pre–exponential factor

The isoconversional approach can precisely predict the activation energy of solid–state reaction models, but they can't accurately calculate both the frequency factor and the reaction model [175,182,183]. Therefore, Kissinger proposed a non–isothermal isoconversional method for calculation of both activation energy and pre–exponential factor given by the equation:

$$\ln\left(\frac{\beta}{T_{\max}^{2}}\right)=\ln\left(\frac{AR}{E_a}\right)-\left(\frac{E_a}{RT_{\max}}\right) \tag{5.22}$$

where $T_{\max}$ is the temperature at conversion rate under consideration or the maximum temperature on the DTG curve. The Vyazovkin_AIC pre–exponential factor at the corresponding α can be calculated (using the apparent activation energy determined from Vyazovkin_AIC methods) as follows [125,182]:

$$A=\frac{\beta E_a \exp\left(\dfrac{E_a}{RT_{\max}}\right)}{RT_{\max}^{2}} \tag{5.23}$$

5.2.8 Determination of thermodynamic parameters

Thermodynamic parameters, viz. enthalpy (ΔH), Gibbs free energy (ΔG), and entropy (ΔS) were calculated as follows [126]:

$$\Delta H = E - RT \tag{5.24}$$

$$\Delta G = E + RT_{\max}\ln\left(\frac{k_B T_{\max}}{hA}\right) \qquad 5.25)$$

$$\Delta S = \frac{\Delta H - \Delta G}{T_{\max}} \tag{5.26}$$

where, Boltzmann constant (k_B) = 1.381 × 10^{-23} J K^{-1}, Plank constant (h) = 6.626 × 10^{-34} J s^{-1}, T_{max} = maximum peak temperature observed in the DTG curve.

5.3 Results and discussion

5.3.1 Proximate and ultimate analysis of biomass blends

The proximate and ultimate results of the raw biomass, binary and ternary blends are listed in Table 5.2. Several studies have suggested that the best feedstock for pyrolysis ought to have a moisture content (MC) less than 10 % to allow rapid heat transfer [77]. It could be observed that MC of the blends were in a range of 7.52–8.92 wt %, which made them suitable for co–pyrolysis. Low MC of biomass would yield bio–oil with less moisture. The volatile matter content of the binary and ternary blends was more than 75%, and thus, these blends were ideal feedstock for co–pyrolysis for obtaining bio–oil. Fixed carbon content (FC) is inversely related to the amount of VM in the feedstock. From Table 5.2 it could be seen that the feedstock with a higher amount of VM had low FC. The FC of the samples were in the range of 4.91–5.86 % ternary blends while that for binary blends was 8.35–9.48 wt %. Also, FC determines the heating value of the feedstock. The feedstock with higher FC content had a higher CV. Ash content (AC) infers the existence of inorganic components in the feedstock in the form of metal oxides. High amounts of AC in the fuel leads to corrosion, fouling, and slagging of reactors, in addition to reduction in calorific value (CV). The ash content in the blends was mainly contributed by WH, and thus, the ash content of the blend varied in proportion of WH in it. The binary blends of WH SCB and WH TP had ash contents of 4.02 and 6.02 wt %, respectively, while the blend of TP SCB had least ash content of 3.08 wt %. Similarly, the ternary blends WH 111, WH 211 and WH 311 had ash contents of 5.79, 6.13 and 5.97 wt %, respectively. The presence of AC directly dictates the quality of feedstock because ash is considered a contaminant. The CV of blends in the present work are in agreement with those of other biomass reported in the literature [77,117,171,175]. Among the ternary blends, WH 311 had the least CV of 16.12 MJ kg^{-1}, which is attributed to the highest water content of WH with the least individual CV among all biomass. The low nitrogen content (1.65–2.61 wt %) of the biomass blends is another merit, which would be manifested in terms of low nitrogen content of bio oil and reduced NO_x emissions during combustion. The structural composition of the individual biomass and their blends is shown in Table 5.2. The composition structure of feedstock influences the resultant co–pyrolysis product and their yields. Low lignin content of biomass reduces the amount of oxygen in the oil obtained from pyrolysis. Co–pyrolysis of biomass essentially transforms holocellulose into furans, organic acids, aldehyde ketones and non–condensable gases– all of which tend to increase the bio–oil yield [21,22]. Lignin is converted into organic oxygenates, phenolic compounds, acids, char, and non–condensable gases. High lignin content may also lead to higher yield of biochar due to presence of stable structures.

Table 5.2 Proximate, ultimate analysis and compositional results of blended feedstock

Analysis	Raw biomass			Binary blends			Ternary blends		
	WH	**SCB**	**TP**	**WH SCB**	**WH TP**	**TP SCB**	**WH 111**	**WH 211**	**WH 311**
Proximate analysis (a.d % wt)									
Moisture content (MC)	9.04±0.00	7.83±0.10	6.85±0.01	7.98±0.10	8.09±0.10	7.52±0.20	8.59±0.20	8.76±0.10	8.92±0.20
Volatile matter (VM)	79.07±0.60	74.02±0.50	78.02±0.70	78.56±0.20	77.54±0.40	79.92±0.20	80.76±0.10	79.04±0.00	79.98±0.20
Ash content (AC)	4.82±0.10	3.12±0.01	2.11±0.40	4.02±0.30	6.02±0.10	3.08±0.20	5.79±0.10	6.13±0.10	5.96±0.40
Fixed carbon (FC)	7.07±0.20	15.03±0.30	13.02±0.20	9.08±0.60	8.35±0.30	9.48±0.30	5.86±0.30	4.91±0.20	5.30±0.10
Ultimate analysis (daf. % wt)									
C	36.44	42.02	44.70	51.96	43.17	51.83	47.28	41.04	40.61
H	5.02	5.77	5.84	4.92	5.42	5.50	5.38	5.58	4.75
O$^{(*)}$	54.68	49.91	48.09	40.67	48.80	40.63	45.68	51.45	52.38
N	3.86	2.12	1.37	2.45	2.61	2.04	1.65	1.93	2.26
H/C	1.64	1.63	1.55	1.13	1.50	1.26	1.36	1.62	1.39
O/C	1.13	0.89	0.81	0.59	0.85	0.59	0.73	0.94	0.97
Calorific value (MJ kg^{-1})	15.45±0.30	18.77±0.10	20.41±0.70	18.42±0.50	17.07±0.10	18.97±0.10	17.79±0.10	17.08±0.30	16.12±0.10
Bulk density (kg m^{-3})	275.41±1.00	306.22±0.70	532.13±0.70	302.82±0.10	423.77±0.10	419.09±010	324.26±0.20	366.08±0.40	382.92±0.20
Composition analysis (% wt)									
Cellulose	30.56±0.30	40.59±1.10	28.90±0.80	37.15±1.20	38.19±2.70	35.34±1.10	34.86±1.30	33.27±0.86	32.07±1.30
Hemicellulose	34.79±1.30	29.35±0.20	21.45±0.20	28.76±0.10	29.24±1.10	30.28±1.50	31.29±2.50	31.82±1.20	30.80±1.00
Lignin	5.65±0.60	19.89±0.50	15.76±1.30	8.72±1.80	10.22±1.60	9.12±0.90	12.32±1.70	10.54±2.30	13.04±1.10
Extractives$^{(*)}$	29.0±0.90	10.17±1.00	33.89±0.70	25.37±1.40	21.85±1.00	25.26±1.20	21.53±1.30	24.37±0.90	24.09±0.50

ad: air–dried; daf: dry ash–free basis *: calculated by the difference

5.3.2 Scanning electron microscope analysis

Representative FESEM micrographs of biomass blends are shown in Figures 5.1(a)–(f). It could be seen from Figures 5.1(a)–(c) that binary blends primarily consisted of fibers that are closely packed together, and there are some loose strands that are linked with the other parts creating a web–like arrangement. Similarly, Figures. 5.1(d)–(f) show that the ternary blends had a variety of structures, which included long elongated fibers that were evenly distributed, coarse structures and irregular rod type granules. However, the micrograph of binary blend TP SCB (Figures 5.1(c)) showed detachment of some of the fibers from each other. In the micrographs of both binary and ternary blends, distinct contrasts of morphologies could be observed which could be peculiar of the individual morphologies of the components of the blends. All micrographs also show agglomeration of the biomass particles, which is indicative of thorough blending–which would help in uniform proceeding of co–pyrolysis. Agglomeration of the biomass particle could also assist and promote synergistic interactions during co–pyrolysis.

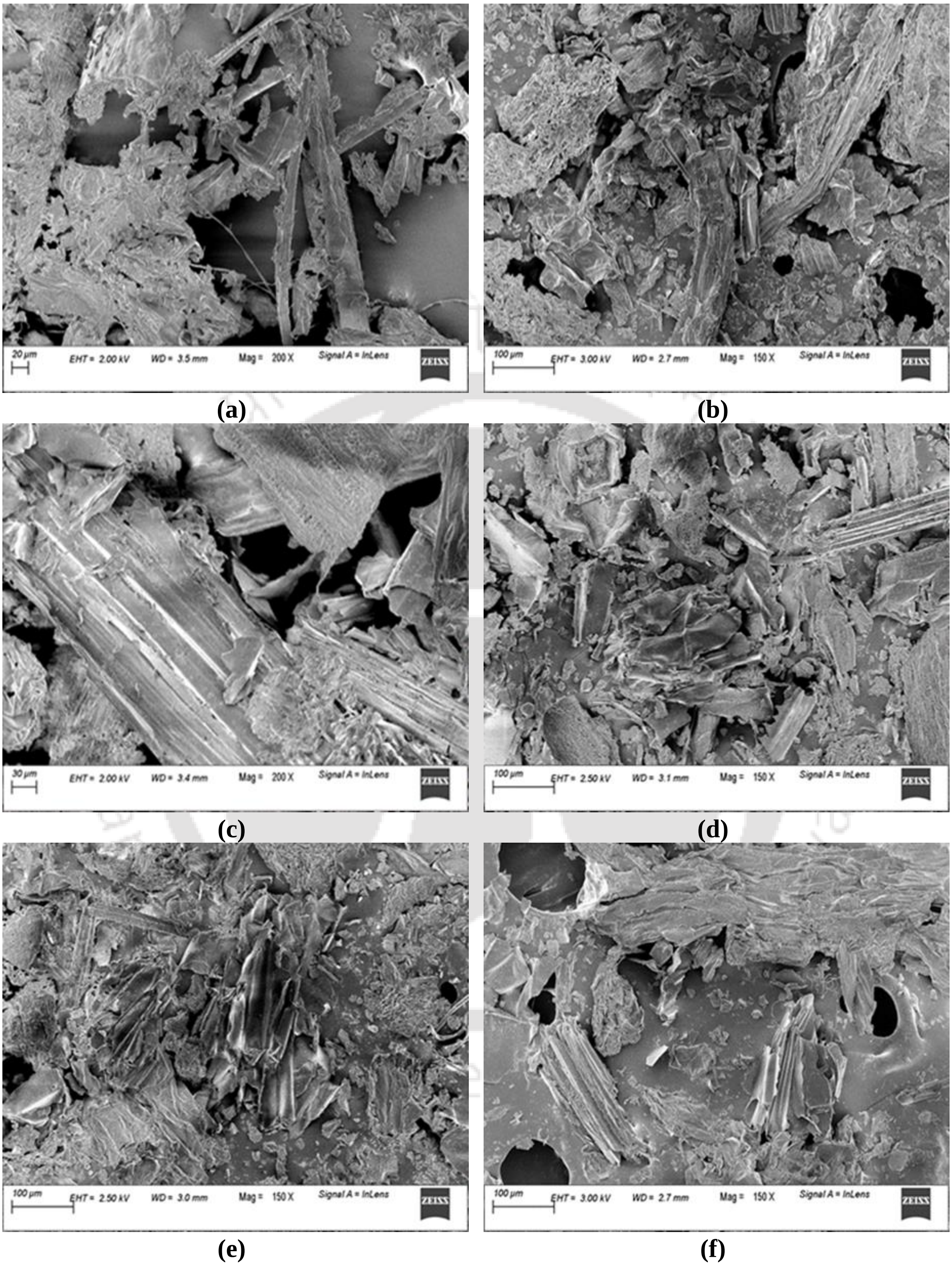

(a) **(b)**

(c) **(d)**

(e) **(f)**

Figures 5.1(a)–(f). FESEM micrographs of blended biomass (a)WH SCB (b) WH TP (c) TP SCB, (d) WH 111, (e) WH 211, (f) WH 311

5.3.3 Functional groups spectra analysis

The FTIR spectra of both binary and ternary blends are illustrated in Figures 2(a) and (b). The list of commonly observed peaks in spectra with corresponding wavelengths and functional groups are listed in Table 5.3 [114,184,185]. Figure 2(a) and (b) show distinct differences in the peaks for binary and ternary blends, in terms of both height and broadness. These peaks essentially point at different functional groups in the feedstock. The most prominent absorption peak observed in the FTIR spectra of two sets of blends is between 3000−3400 cm^{-1} band. This is attributed to O−H bond stretching. This peak confirms abundant presence of the hydroxyl group in macromolecular structure. The moisture content of biomass also contributes to this peak. Peaks corresponding to C−O stretch are also apparent in the two sets of blends. These bands are assigned wavenumber of 900−1300 cm^{-1}. These bands indicate that the biomass blends comprise of abundant phenolic groups, ether bonds, and hydroxyl groups in their structures. The comparatively weak stretching peaks located at 2700−3000cm^{-1} are attributed to aliphatic C–H, while the peaks corresponding to carbonyl (C=O) extending vibration appear in the bands 1600−1800 cm^{-1}. C=C stretching peaks located at 1200−1400 cm^{-1} essentially represent the aromatic structures. Relatively weak intensity of these peaks indicates relatively smaller content of carbonyl, aromatic structures and aliphatic chains in the biomass blends.

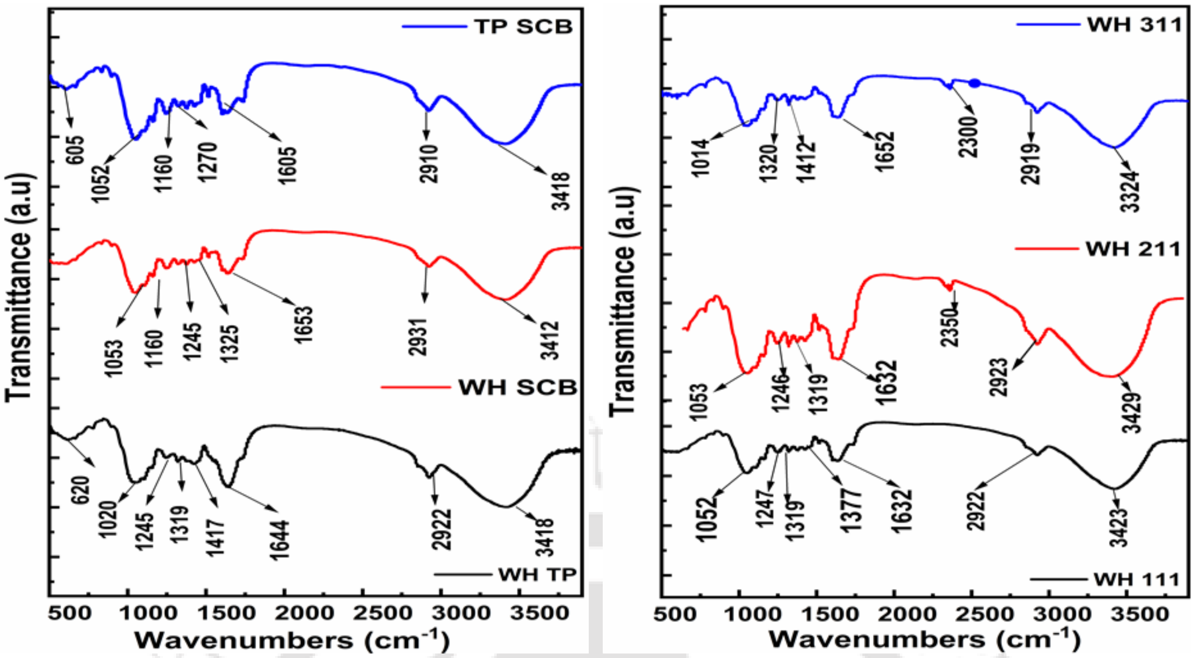

(a) **(b)**

Figure 5.2 FTIR spectra (a) binary blends, (b) ternary blends

Table 5.3 Functional groups detected by FTIR

Wavelength (cm^{-1})	Band assignment	Functional group
3000–3400	O–H	Hydroxyl
2700–2900	C–H	Aliphatic
1400–1700	C=O, C=C	Carbonyl
1200–1300	C–H	Phenols
1000–1200	C–O	Cellulose, hemicellulose and lignin
600–799	C–H	Pyridine

5.3.4 Thermal analysis

Figures 5.3(a) and (b), and Figures 5.4(a) and (b) show the TG and DTG curves for binary and ternary blends, respectively, for the heating rate of 10 °C min^{-1}. From Figure 5.3(a) and (b), it could be seen that all the curves followed a similar profile, depicting three different phases of mass loss in stepwise manner. The initial step (stage– 1) of mass loss occurs in temperature range of 150°–220°C. It is associated with dehydration of inbound moisture existing in structures of the fiber. Also, the breaking down of low molecular weight constituents occourred at this stage, which was characterized by a slight loss of mass of > 3%. This could also be a consequence of initial drying of the samples in a hot air oven for 24 h at 105 ±2°C. The onset degradation temperature (T_{onset}) for individual blends at which the thermal decomposition of the biomass components commences can be identified from DTG curves shown in Figs. 4(a) and (b). T_{onset} for binary blends were TP SCB = 180°C, WH SCB = 185°C and WH SCB = 196 #°C, while the T_{onset} for ternary blends were WH 311 = 170°C, WH 111 = 190°C and WH 211 = 192°C. The variations in T_{onset} for different biomass blends could be a consequence of differences in their structural compositions (viz. cellulose, hemicellulose and lignin) [25]. The rise or reduction in T_{onset} of an individual biomass after blending could also be a consequence of synergistic effects during thermal decomposition as reported by Mallick et al. [14]. The major mass loss occurred in the second stage of degradation. This stage essentially comprises of devolatilization, in which significant mass loss occurs due to degradation, decomposition and release of the volatile matters. The typical temperature range of second stage of degradation for both binary and ternary blends is 200° and 385°C. The highest stage 2 mass loss of 64.97% was observed for the binary blend TP SCB, followed by WH SCB (57.98 %) and WH TP (50.76 %). Variations in stage–2 mass loss for the three blends could be attributed to varying degrees of synergistic interactions during degradation. Similarly, the highest stage–2 mass loss of 56.93% occurred for the ternary blend WH 211, followed by WH 111 (53.45%) and WH 311 (48%). In this case too the variations in mass loss could be attributed to synergistic interactions as well as varying initial content of volatile matter. Two peaks were observed in the DTG curves corresponding to stage 2 decomposition (devolatilization). The initial peak is assigned to the decomposition of hemicellulose. Hemicellulose is made up of short–chain heteropolysaccharides, which can easily degrade at relatively low temperatures [187]. The second peak corresponds with the degradation of cellulose. Cellulose is a colinear polysaccharide consisting of the D–glucose units bonded with ether bonds. Due to crystalline structure, cellulose is more resistant to degradation than hemicellulose, which has significant amorphous character [188].

As seen from Figure. 5.4(a), the T_{max} for binary blends varied over much wider range (341°C for TP SCB and 325°C for WH TP) than ternary blends (329°C for WH 211 and 320°C for WH 111) [189]. The last stage of decomposition (i.e. stage 3) corresponded to the degradation of most recalcitrant part of biomass, i.e. lignin and other composite compounds that are more thermally stable. Lignin is a composite organic polymer that comprises of aromatic structures that crosslink the hollecellulose. Stage 3 also defines the offset degradation temperature T_{offset} that essentially corresponds to negligible mass loss with rising temperature or flattening of the DTG curve. As seen from Figures 5.4(a) and (b), the range of T_{offset} is similar for both binary and ternary blends (i.e. 400°–583.5°C). A peculiar feature of the TG curves is that they overlap closely in low temperature range (< 370°C), and then separate in higher temperature range. For the binary blends (Figure 5.3(b)), the blend of WH TP shows much larger mass loss than TP SCB. The structural component of biomass that degrades in high temperature range is cellulose and high molecular weight fraction of lignin. Significant difference in mass loss is an indication of dissimilar synergistic interactions during decomposition in the three binary blends [190]. TG curves of ternary blends (Figure 5.3(a)) are relatively closer indicating similar mass loss for all blend compositions. This could be a consequence of similar synergistic interactions among different biomass components irrespective of the composition of the blends. The similarity and dissimilarity of the interactions during thermal decomposition is also evident from the DTG curves. The DTG curves of binary blends shows significant variation in shapes as well as shifting of the peak temperatures. The binary blend of WH TP had least T_{max} (corresponding to maximum mass loss rate) of 325°C while TP SCB had the highest T_{max} of

341°C (i.e. difference of 16°C). On the other hand, DTG curves of ternary blends are quite similar in shape (cascading among themselves) and the $T_{\max}$ also shows minor variation. The highest $T_{\max}$ of 329°C is observed for WH 211 while the least $T_{\max}$ of 320°C seen for WH 111.

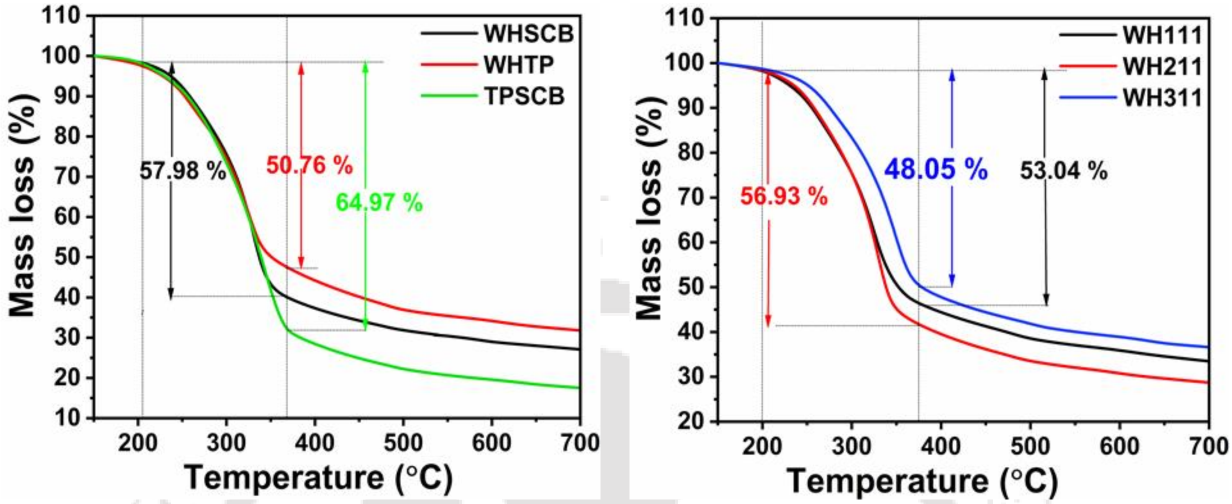

(a) (b)

Figure 5.3. TGA curves for (a) binary blends, (b) ternary blends

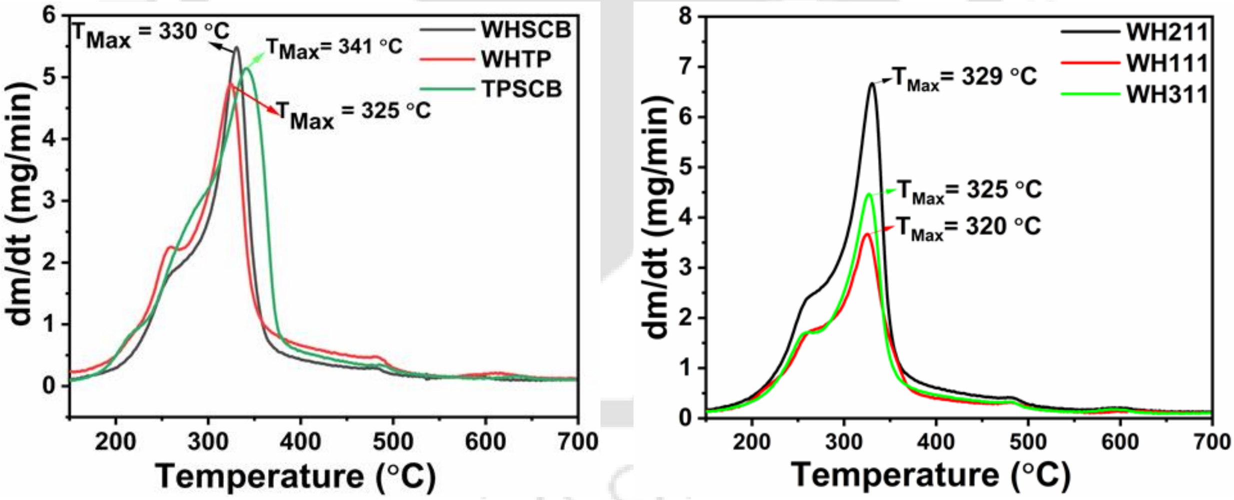

(a) (b)

Figure 5.4. DTG curves for (a) binary blends, (b) ternary blends

5.3.5 Kinetic parameters analysis

The TGA data for the binary and ternary blends at heating rates of 8, 10, 15, and 30°C min^{-1} were used to determine the kinetic parameters using OFW, Vyazovkin_AIC and DAEM.

methods On the basis of the DTG curve, the temperature range of 150°C–700°C was used for calculation of the kinetic parameters [191]. This temperature range corresponded to approx. 75% conversion for all blends. A step size of $\Delta\alpha = 0.05$ was used for calculations using both OFW and DAEM while $\Delta\alpha = 0.05$ was used for Vyazovkin_AIC model as per the ICTAC recommendations [123]. The experimental data for OFW and DAEM showed good linear fit for all biomass blends with regressions coefficients (R^2) higher than 0.85 for the entire range of α (0.05 to 0.75). The details are provided in Tables C1 and C2 in appendices C.

5.3.6 Activation energy

Figures 5.5(a) and (b) show the plots of E_α versus α for both binary and ternary blends. The variations of E_α versus α (or the E_α curves) calculated using all three models (OFW, DAEM and Vyazovkin_AIC) have similar shape. Moreover, for all blends, the E_α curves overlap very closely over entire range of α.

E_α values show significant and non–monotonous variations with α as the degradation proceeds. This is a clear indication of changing chemistry and reaction mechanism as the degradation of biomass blends proceeds through rising temperature. Three blends, viz. WH 311, WH TP and WH SCB, showed W–shaped profile in the α range of 0.1–0.75. This trend concurs with results reported in previous literature [188,192]. E_α values of binary and ternary varied slightly for $\alpha = 0.1–0.5$ and increased considerably after $\alpha \geq 0.75$. At higher α (i.e. higher temperature) the E_α values were significantly larger. For high conversion values ($\alpha \geq 0.6$), the biomass samples have lost most of the low molecular weight components (holocellulose) and the volatiles, and residual solids essentially comprise of high molecular weight (polyaromatic) components of lignin that are thermally recalcitrant and char, which also has low reactivity. This essentially is manifested in terms of rise in the activation energy [193]. More detailed discussion on thermal degradation of different structural components of biomass (hemicellulose, cellulose and lignin) and the underlying chemistry is given by Mallick et al. [175]. Tables 5.4(a) and (b) show the apparent activation (E_α) energies for the binary and ternary blends obtained using OFW, DAEM, Vyazovkin_AIC models. It was observed that E_α values determined using the Vyazovkin_AIC model were marginally higher than those obtained with the DAEM and OFW models. Among the three models, the Vyazovkin_AIC model is expected to give more accurate estimate of E_α by considering smaller segments of conversion for analysis. This technique effectively maps the variation in chemistry of thermal decomposition of different structural components of biomass at different stages of conversion [123]. Among the E_α values for ternary blends (as listed in Tables 5.4(a) and (b)) determined using the three isoconversional models, the E_α ranges of for binary blends were 122.90–237.53, 127.93–272.92, and 124.80–235.94 kJ mol^{-1} for WH SCB, WH TP, TP SCB, respectively. Similarly, the ranges of E_α for WH 111, WH 211 and WH 311 blends were 119.64–194.31, 123.40–246.80, and 121.65–194.75 kJ mol^{-1}, respectively.

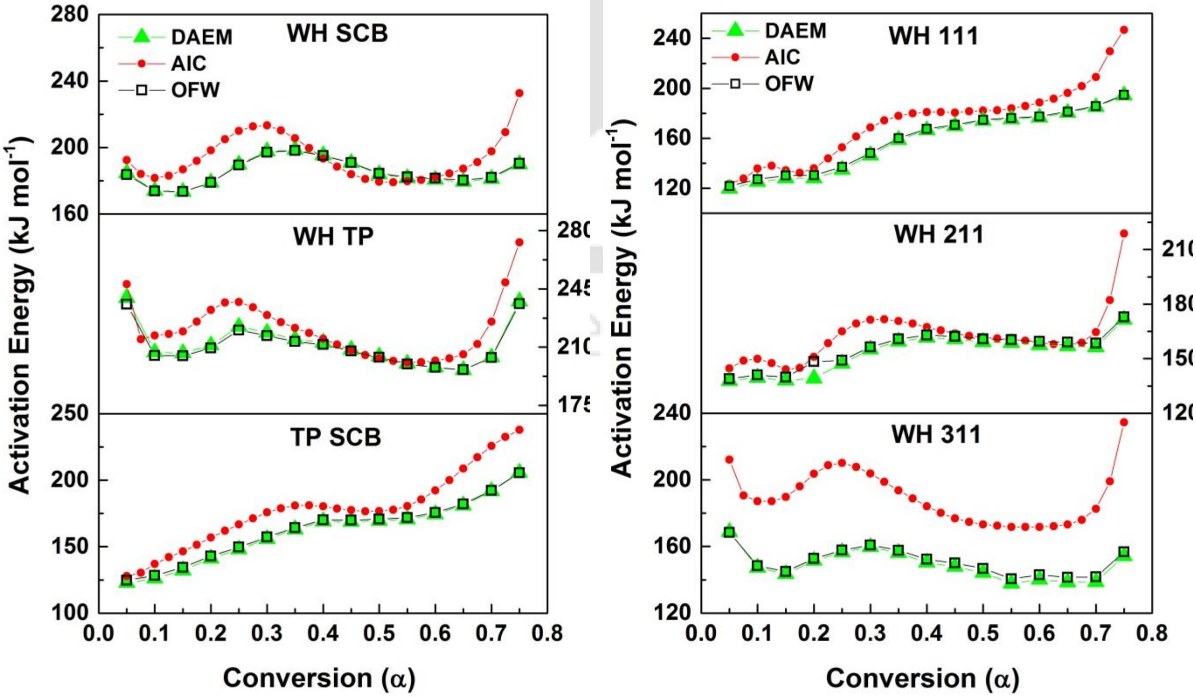

(a) (b)

Figure 5.5 Isoconversion plots of apparent activation versus conversion (a) binary blends, (b) ternary blends

Table 5.4 Estimated E_α (kJ mol^{-1}) values of binary blends

α	**WH SCB**			**WH TP**			**TP SCB**		
	DAEM	**Vyazovkin _AIC**	**OFW**	**DAEM**	**Vyazovkin _AIC**	**OFW**	**DAEM**	**Vyazovkin _AIC**	**OFW**
0.05	184.67	192.40	183.58	239.63	247.85	235.67	122.90	127.93	124.80
0.10	174.03	181.71	173.80	206.90	217.04	204.95	126.12	136.95	128.26
0.15	173.42	186.81	173.44	206.50	219.46	204.79	132.29	146.40	134.38
0.20	179.00	198.34	178.93	211.19	232.37	209.44	141.13	156.88	142.98
0.25	189.84	209.94	189.41	222.35	237.12	220.23	148.02	166.71	149.70
0.30	197.75	213.27	197.09	218.70	229.28	216.93	155.80	175.74	157.24
0.35	198.74	205.53	198.18	214.79	221.51	213.35	163.09	180.87	164.32
0.40	195.38	193.35	195.10	212.76	215.13	211.56	169.11	180.34	170.17
0.45	190.79	184.01	190.84	208.51	208.21	207.62	168.76	177.49	169.96
0.50	183.88	179.40	184.36	204.43	203.15	203.84	169.49	176.78	170.76
0.55	181.62	179.66	182.29	200.10	200.83	199.81	170.60	180.61	171.91
0.60	180.67	182.19	181.46	197.89	201.89	197.80	174.43	192.18	175.64
0.65	179.44	187.24	180.35	196.29	205.66	196.37	181.04	208.64	182.01
0.70	181.15	197.67	182.05	203.90	225.39	203.72	191.73	225.70	192.27
0.75	189.95	232.65	190.51	237.53	272.92	235.94	205.63	237.76	205.58
Variation in E_α (%)	14.60	29.49	14.26	22.07	34.34	20.15	67.31	85.85	64.72

Table 5.5 Estimated E_α (kJ mol^{-1}) values of ternary blends

α	**WH 111**			**WH 211**			**WH 311**		
	DAEM	**Vyazovkin _AIC**	**OFW**	**DAEM**	**Vyazovkin _AIC**	**OFW**	**DAEM**	**Vyazovkin _AIC**	**OFW**
0.05	119.64	123.40	121.65	137.84	144.6	139.03	168.70	212.19	168.34
0.10	125.10	135.76	127.21	139.62	149.87	141.08	147.33	187.19	148.40
0.15	127.95	134.33	130.14	138.00	144.1	139.76	143.49	189.72	144.96
0.20	127.98	135.96	130.36	139.21	151.05	148.37	151.46	203.62	152.73
0.25	134.84	152.79	137.05	147.42	165.02	149.07	156.52	210.22	157.73
0.30	146.36	168.64	148.16	155.06	171.46	156.49	159.66	203.77	160.88
0.35	158.72	178.00	160.06	159.50	170.76	160.85	156.13	193.72	180.35
0.40	166.48	180.87	167.56	161.64	167.35	163.01	150.39	184.15	152.32
0.45	169.70	180.54	170.74	160.81	163.98	162.33	147.86	176.93	150.02
0.50	173.98	182.10	174.90	159.21	161.83	160.90	144.32	173.23	146.75
0.55	175.29	183.96	176.24	158.67	160.54	160.47	137.77	171.79	140.61
0.60	176.55	188.56	177.52	157.55	158.91	159.47	140.13	171.79	142.92
0.65	180.44	196.25	181.30	156.99	157.55	159.02	138.52	173.27	141.46
0.70	185.05	209.06	185.78	156.36	164.64	158.51	138.66	182.66	141.69
0.75	194.31	246.8	194.75	171.45	218.82	172.99	154.31	234.5	156.71

Variation in E_α (%)	62.41	100	60.09	24.38	51.85	23.71	22.45	25.27	28.26

The linear regression graphs for binary and ternary blends obtained using OFW and DAEM models (i.e. the plots of Eqs. 7 and 14) are shown in Figures 5.6–5.7. The E_α and R^2 values were evaluated from the gradient of each plot. As seen from the result obtained from the regression plots, the E_α values for various conversion levels using OFW and DAEM methods match very closely. However, for any particular conversion level, significant variation in E_α values was seen among the binary and ternary blends. This variation is attributed the difference in structural composition of the blends. Comparing between binary and ternary blends, higher activation energy was observed for the binary blends, which indicates the relatively higher recalcitrant or resistant nature of these blends towards thermal decomposition [194]. The E_α values for binary and ternary blends in this study are in similar range as reported in previous literature [175,195].

The variation in E_α over entire conversion range from $\alpha = 0.05$ to 0.75 is representative of the uniformity of chemical mechanism of thermal degradation. Large variations in E_α values essentially point at complex chemical mechanism of thermal decomposition with diverge chemical reactions occurring at different stages of conversion [196]. The variation in E_α is listed in Table 3(a) for ternary and 3(b) for binary blends. The E_α values obtained using Vyazovkin_AIC model showed the highest variation for all blends. Among the ternary blends, the highest variation in E_α with conversion levels was seen for WH 111 (in the range of 60.09 to 100 % for the three isoconversional methods). On the other hand, the least variation in E_α was seen for WH 311, i.e. 22.45 to 28.26 %. Among the binary blends, the blend of WH SCB showed least variation in E_α (in the range of 14.26 to 29.49 %), while the blend of TP SCB has the highest variation (in the range 64.72 to 85.85 %).

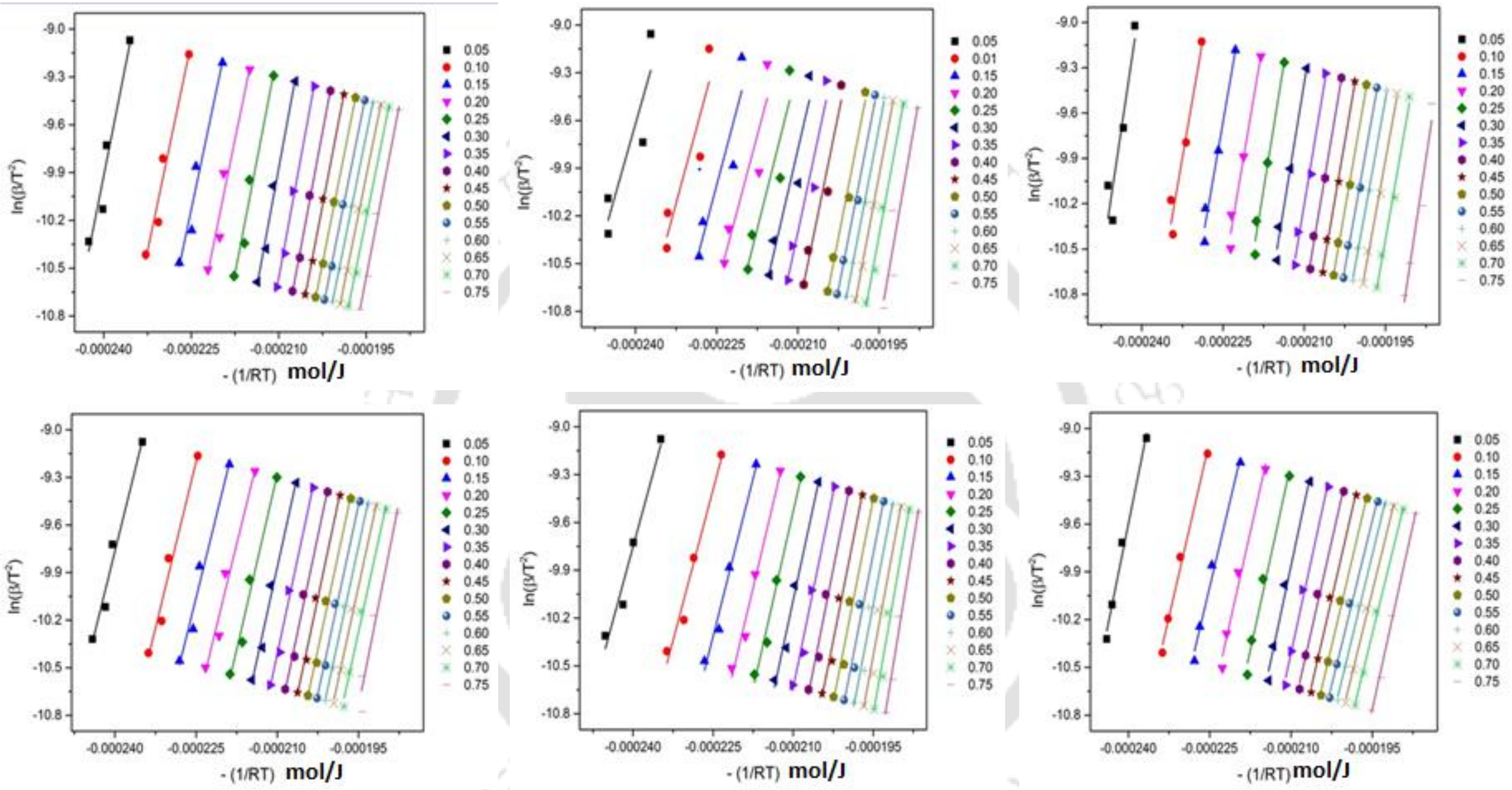

Figure 5.6 (a) DAEM plots of (a) WH SCB, (b) WH 111, (c) WH TP, (d) WH 211, (e) TP SCB and (f) WH 3111

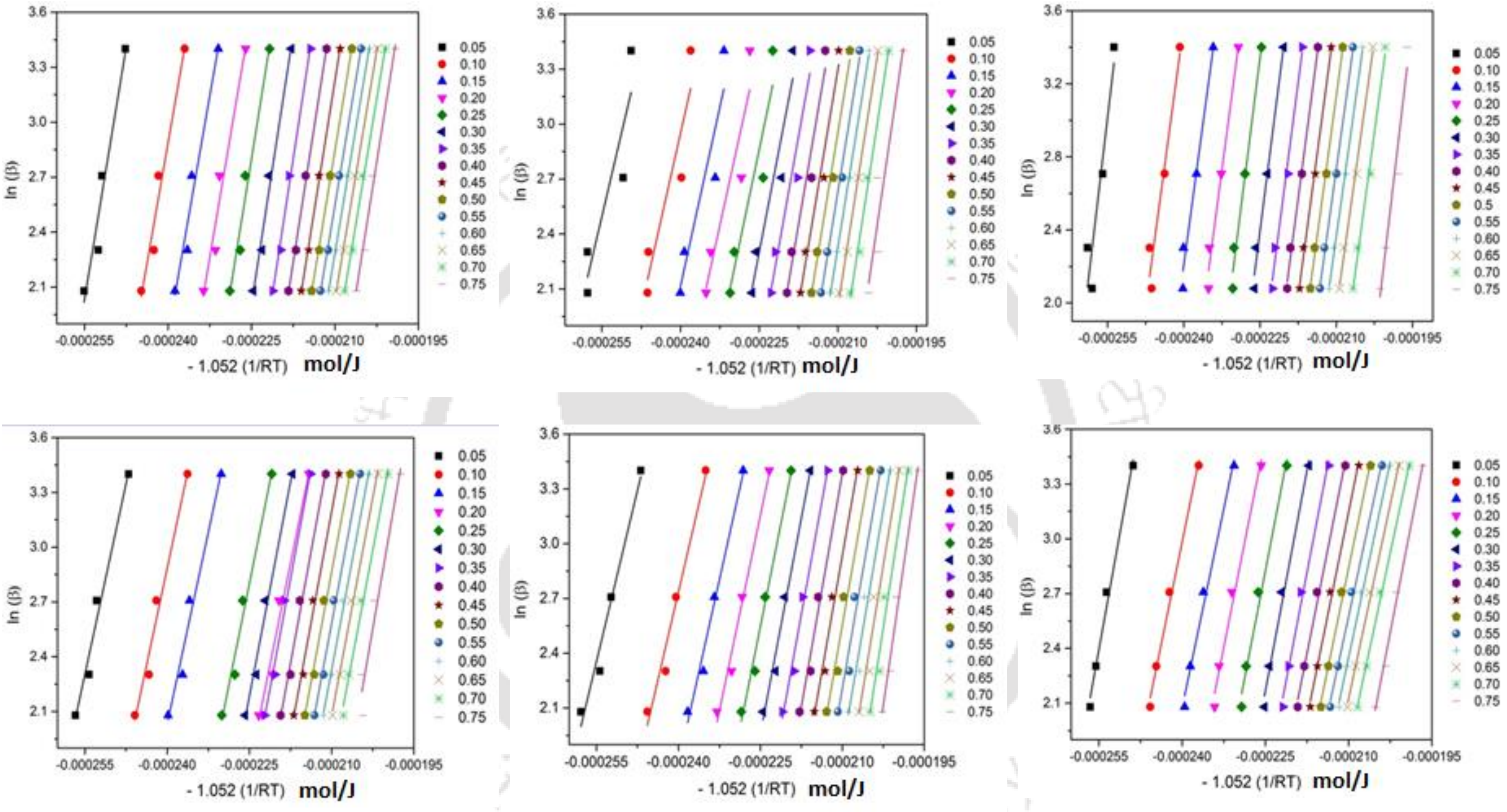

Figure5.7 OFW plots (a) WH SCB, (b) WH 111, (c) WH TP, (d) WH 211, (e) TP SCB and (f) WH 311

5.3.7 Pre–exponential factor

The pre–exponential factors (A_α) for both binary and ternary blends in the conversion range of $\alpha = 0.05$ to 0.75 were determined using the E_α obtained from Vyazovkin_AIC method. These values are listed in Table C3 in the appendices C. It is observed that the A_α varied in the range of 1.03×10^{15}–1.86×10^{24} s^{-1} and 5.03×10^{14}–1.89×10^{22} $s^{-1}$for the binary blends (WHSCB, WHTP, and TPSCB), and ternary (WH111, WH211 and WH311), respectively. The variation of pre–exponential factor with conversion is also an indication that degradation of the blends during co–pyrolysis is multifaceted. High values of A_α (~ 10^{14} – 10^{24} s^{-1}) indicated the presence of highly reactive system with complex and interactive (or synergistic) reactions occurring during the degradation of biomass blends. Although the two structural components of cellulose and hemicellulose have polymeric nature (polysaccharides), large variation in A_α values essentially indicates the heterogeneity of the structural composition of biomass.

5.3.8 Reaction mechanism

Figures 5.8(a) and (b) show the Criado master plots generated using Eq. (5.21) and different expressions of $f(\alpha)$ and $g(\alpha)$ (listed in supplementary material) that correspond to different solid state reaction mechanism. It could be observed that the experimental reduced plot overlapped with one or more master plots in different ranges of conversion (α). The predominant reaction mechanism in most binary and ternary blends at various levels of conversion was either diffusion limited process, viz. D1, D2, D3 (corresponding to 1– or 2– or 3–dimensional heat diffusion) and ordered reaction (mostly first order F1). The ternary blends WH 111 followed first order reaction mechanism (F1) in lower range of conversion (for $\alpha \leq$ 0.25) and 2–D heat diffusion mechanism D2 in the conversion range of α 0.25–0.55. The blend WH 211 followed 2–D heat diffusion mechanism (D2) in lower conversion range ($\alpha \leq 0.25$)

and 1–D heat diffusion (D1) mechanism in conversion range $\alpha = 0.25–0.55$. The blend WH 311 followed 1–D heat diffusion mechanism (D1) for smaller conversions, $\alpha \leq 0.15$. In the middle conversion range, viz. $\alpha = 0.15$ to 0.55 no particular and predominant reaction mechanism was seen. Thereafter, the D1 mechanism was again observed for a small conversion range, i.e. $\alpha = 0.5–0.6$. It is observed that with increasing WH content in blend, the practical degradation path deviated from the pre–defined models, which could be attributed to the occurrence of complex parallel reactions. These complex parallel chemical reactions are also correlated to high activation energy, as seen in the TGA data analysis. A similar thermal decomposition behaviour was also observed for binary blends comprising WH. The reduced degradation profiles of both WH SCB and WH TP didn't match with any of the pre–defined reaction models. The binary blend WH SCB followed D1 mechanism for smaller conversion levels ($\alpha \leq 0.25$), and thereafter, D3 mechanism for the small conversion segment ($\alpha = 0.5–0.6$). The degradation of WH TP followed D3 mechanism till $\alpha \leq 0.25$ and D1 mechanism in the range $\alpha = 0.25–0.55$. The TP SCB blend followed F1 mechanism for relatively large conversion range of $\alpha = 0.15–0.6$. The diffusion mechanism is attributed to heat transfer from an external source to solids (prior or concurrently with reaction). This mechanism also includes outward diffusive transport of the hot gases formed during decomposition of biomass.

Most noteworthy aspect of Criado analysis of binary and ternary blends was that for high conversion range of $\alpha > 0.6$, the experimental curve did not match with any of the pre–defined model. It may be noted that at higher conversion range, significant char formation occurs – which has limited reactivity. The higher conversion range also encompasses conversion of heavy and complex aromatic components of lignin [197]. These components have rather complex chemistry of conversion, which does not match with any of the simple pre–defined models.

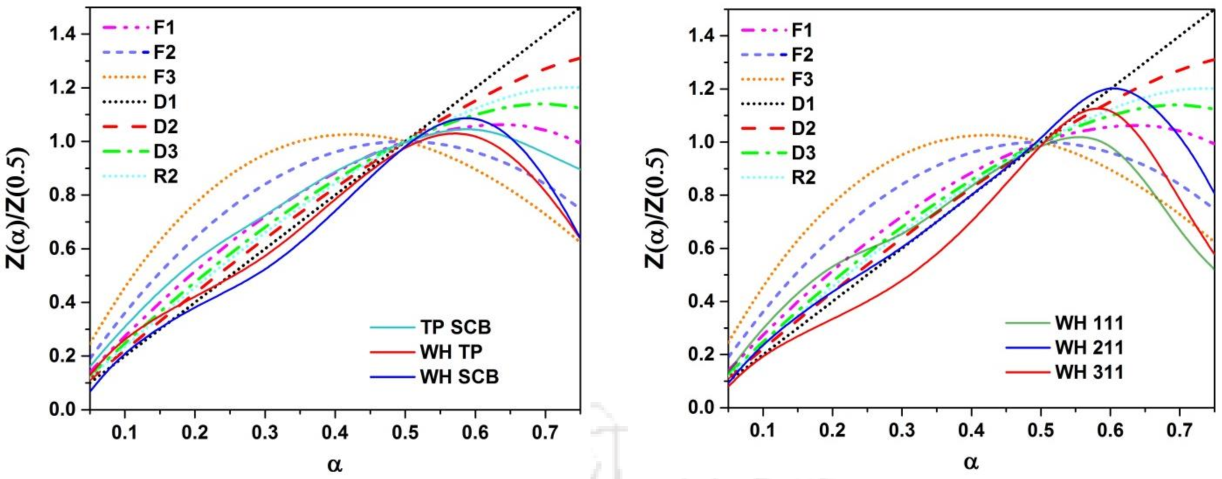

(a) **(b)**

Figure 5.8 Criado master plots for the (a) binary blends, (b) ternary blends

5.3.9 Thermodynamic parameters

Tables 5.5(a) and (b) show the thermodynamic parameters for the thermal degradation of ternary and binary blends, respectively. The enthalpies of thermal decomposition (ΔH) in all blends increased with conversion (α), which is in concurrence with trends of E_α. Positive ΔH for all blends essentially indicate that thermal decomposition or co–pyrolysis of biomass blend is an endothermic process. This essentially involves breaking of the recalcitrant structure of lignocellulosic biomass into biochar and bio–oil (with breakage of chemical bonds between moieties). Similar trends of ΔH for biomass conversion have been reported in literature [175,198]. Binary blends had the highest ΔH values, which indicated higher thermal resistance of the structural components, which may also be due to lesser extent of (positive) synergistic interactions, as noted earlier.

Gibbs free energies (ΔG) for the blends were in the range of 105.84–142.51 kJ mol^{-1}, and 72.80–144.97 kJ mol^{-1} for ternary and binary blends, respectively. Values of ΔG listed in Tables 4(a) and (b) depict rising trend in ΔG with biomass conversion – although the rise is relatively marginal. Positive ΔG values for thermal conversion of all biomass blends essentially indicates that this process is of non–spontaneous nature, and requires an external heat supply. Similarly, all the values of entropy (ΔS) were positive for both blends. It could be seen from Tables 4(a) and (b) that different blends showed dissimilar trends in ΔS with conversion. However, a common feature of ΔS values among all blends is that these values increased sharply in the α range of 0.20–0.35. This range of α essentially corresponds to decomposition of the polymetric structures (i.e. hemicellulose and some components of cellulose) in the biomass. This leads to increase in “randomness” or “disorder” of the system. Interestingly, ΔS values show reduction for $\alpha \geq 0.35$. This range corresponds to decomposition of major components of lignin, which has amorphous character. Finally, for the highest conversion of $\alpha > 0.75$, ΔS values again show sharp rise. This corresponds to almost complete breakdown of the biomass structure with formation of char (carbon rich solid) which is highly amorphous in nature [195].

Table 5.6 Thermodynamic parameter for binary blends

α	**WH SCB**			**WH TP**			**TP SCB**		
	ΔH kJ mol^{-1}	ΔG kJ mol^{-1}	ΔS kJ mol^{-1} K^{-1}	ΔH kJ mol^{-1}	ΔG kJ mol^{-1}	ΔS kJ mol^{-1} K^{-1}	ΔH kJ mol^{-1}	ΔG kJ mol^{-1}	ΔS kJ mol^{-1} K^{-1}
0.05	188.20	91.80	161.20	243.79	72.80	285.90	123.80	105.50	30.60
0.10	177.40	103.40	123.70	212.78	93.40	199.60	132.60	111.60	35.20
0.15	182.40	108.00	124.30	215.08	100.20	192.10	141.90	114.80	45.40
0.20	193.80	111.30	137.10	227.89	103.90	207.30	152.30	117.01	58.90
0.25	205.30	114.40	151.10	232.55	108.90	206.70	162.00	119.20	71.60
0.30	208.60	118.20	151.00	224.62	114.70	183.80	171.00	121.50	82.80
0.35	200.70	122.30	131.10	216.78	119.40	162.80	176.10	124.01	86.90
0.40	188.50	125.90	104.70	210.33	123.20	145.70	175.50	126.90	81.20
0.45	179.10	128.60	84.48	203.35	126.20	128.90	172.60	129.60	71.90
0.50	174.50	130.50	73.46	198.24	128.70	116.30	171.80	131.70	67.01
0.55	174.70	131.10	71.42	195.88	130.70	108.10	175.60	133.40	70.50
0.60	177.20	133.20	73.51	196.89	132.50	107.70	187.10	134.90	87.30
0.65	182.20	134.40	79.86	200.62	134.40	110.70	203.50	136.30	112.30
0.70	192.60	135.80	95.00	220.28	137.30	138.80	220.50	138.10	137.70
0.75	227.50	137.90	149.89	267.67	144.10	205.10	232.50	140.40	154.05

Table 5.7 Thermodynamic parameter for ternary blends

α	**WH 111**			**WH 211**			**WH 311**		
	ΔH kJ mol^{-1}	**ΔG** kJ mol^{-1}	**ΔS** kJ mol^{-1} K^{-1}	**ΔH** kJ mol^{-1}	**ΔG** kJ mol^{-1}	**ΔS** kJ mol^{-1} K^{-1}	**ΔH** kJ mol^{-1}	**ΔG** kJ mol^{-1}	**ΔS** kJ mol^{-1} K^{-1}
0.05	119.30	105.10	23.70	140.50	101.80	64.60	208.01	85.20	205.50
0.10	131.50	109.90	36.01	145.60	108.80	61.40	182.90	101.01	136.80
0.15	129.90	114.80	25.40	139.70	114.35	42.30	185.30	106.30	132.00
0.20	131.50	117.90	22.70	146.50	117.05	49.30	199.10	109.40	149.90
0.25	148.20	119.10	48.60	160.40	118.88	69.40	205.60	113.70	153.80
0.30	163.10	120.90	72.10	166.80	121.51	75.70	199.01	118.50	134.70
0.35	173.30	123.30	83.60	165.10	124.47	69.40	188.10	122.70	110.70
0.40	176.01	125.90	83.90	162.50	127.16	59.10	179.30	125.10	89.20
0.45	175.70	128.20	79.30	159.01	129.33	49.80	172.10	128.50	72.80
0.50	177.20	130.20	78.60	156.90	131.05	43.20	168.30	130.40	63.40
0.55	179.00	131.90	78.80	155.60	132.50	38.60	166.80	131.90	58.30
0.60	183.60	133.50	83.70	153.90	133.78	33.60	166.80	133.30	55.10
0.65	191.20	135.30	93.50	152.50	135.01	29.30	168.20	134.70	56.10
0.70	203.10	137.80	110.60	159.60	136.19	39.06	177.60	136.30	68.10
0.75	241.60	142.50	165.70	213.70	138.17	126.20	229.30	140.20	149.00

5.4 Summary

This chapter presents a comprehensive characterization, kinetic and thermodynamic analysis of biomass blends. Binary and ternary blends of three biomass, viz. WH, SCB and TP, were studied using thermogravimetric analysis. The TGA data was analysed using three models, viz. OFW and advanced isoconversional methods of DAEM and Vyazovkin AIC. The kinetic parameters obtained with Vyazovkin AIC are expected to be more realistic, as this method considered smaller conversional intervals for determination of kinetic triplets. Significant variations in activation energies and pre–exponential factors were seen with conversion levels. This clearly represents complex chemistry of thermal conversion with reactions of widely varying kinetic character occurring at different stages of conversion.

Substantial variation in kinetic parameters was also seen among binary and ternary blends – indicative of synergistic interactions among components of the blends. Despite these variations, the reaction mechanism of thermal conversion for all blends was rather consistent: in the lower conversion range ($\alpha \leq 0.25$), the reaction mechanism was ordered reaction (F1), while in higher conversion range ($\alpha = 0.35$–0.55), all blends followed diffusion (D1 or D2 or D3) mechanism. ΔH, ΔS and ΔG values for all blends were positive, indicating endothermic and non–spontaneous nature of co–pyrolysis. ΔH and ΔS showed significant variation with conversion levels. In the next chapter co–pyrolysis of biomass blends obtained from noxious weeds and industrial waste to produce biochar at optimized conditions is presented.

CHAPTER 6–Co–pyrolysis of ternary biomass blend, optimization using response surface methodology and characterization of biochar

6.0 Introduction

This chapter discusses co–pyrolysis of biomass blends obtained from noxious weeds and industrial waste to produce biochar in non–catalytic conditions. The issue was addressed systematically by investigating the interactions effects of three factors viz. temperature, heating rate and residence time on the yield and higher heating value of biochar from a ternary blend of biomass viz. WH, TP and SCB. The pyrolysis factors that influence the yield of products when ternary blends were co–pyrolyzed in fixed bed reactor were studied using the response surface methodology (RSM). The analysis of variance (ANOVA) and regression analysis were used to study the appropriateness of developed model using central composite design (CCD) technique. RSM is a multivariate statistical tool that has been widely used to investigate and optimize process parameters and their interactions with a least number of experiments [199]. Yield and HHV shows drift in opposite directions, when pyrolysis parameters are altered. Hence, optimizing the process parameters and realizing an equilibrium between the two responses becomes quite important factor that determines the viability of application of co–pyrolysis products for energy. The physicochemical properties of biochar at optimized conditions were investigated using standard characterization techniques viz. ultimate and proximate analysis BET, FTIR, EDX, pH, EC and SEM. The co–pyrolysis products of ternary blends obtained at the optimum condition have been compared with the pyrolysis products obtained after pyrolysis of WH, TP and SCB individually.

6.1 Materials and method

6.1.1 Collection and processing of biomass

Procedure for collection and processing of biomass is described in Chapter 3 under sub–section 3.2.1.

6.1.2 Preparation of ternary blends

The ternary blend of WH, TP and SCB was prepared as described in Chapter 5 under sub–section 5.1.2.

6.1.3 Experimental setup and co–pyrolysis procedure

Co–pyrolysis experiments were conducted using a rotary fixed batch pyrolyzer (designed indigenously and fabricated by Dass & Co., India). The description of the pyrolyzer and schematic diagram of the pyrolyzer is provided in Chapter 4 under sub–section 4.1.2. In each experiment, 500 g of biomass was pyrolyzed according to the CCD experimental design. The solid residue remaining after the completion of pyrolysis was biochar. Each experiment was repeated 3 times to assess reproducibility. Biochar mass was pulverized, followed by sieving through a ≤ 210–micron sieve. The biochar particles were stored in airtight containers for subsequent analysis.

6.1.4 Characterization of biochar

The proximate analysis of the biomass blends and biochar was done according to protocols outlined in ASTM standards moisture content (MC): ASTM E871–82, ash content (AC): ASTM D1102–84, volatile matter content (VM): ASTM E872–82), and fixed carbon (FC) content was calculated by mass difference. Ultimate analysis of raw biomass and the blends was done for determination of % content of C, H, N, S, and O using an elemental analyzer (Make: Euro EA, Model: Eurovector EA3000). Calorific value (CV) was determined using an oxygen bomb calorimeter (Make: PARR, Model: 1341EB). Surface morphology of the both biomass blends and biochar was examined using Field Emission Scanning Electron Microscope (FESEM) (Make: Zeiss, Germany, Model: Sigma 300). The functional groups present were identified by Fourier Transform Infrared Spectroscopy (FTIR) analysis (Make: Shimadzu, Japan, Model: IRAffinity–1). The bulk density was determined as per ASTM D873–82 [18] standard which involved measuring the weight of the sample and calculating the ratio of the sample to the volume of the container.

6.1.5 Design of experiments using RSM

RSM was used for experimental design to optimize the parameters that influence co–pyrolysis parameters. Central composite design (CCD) with the aid of Design–Expert Version 12, Stat–Ease Inc, MN,USA) was used by considering three influential factors (temperature, heating rate and residence time) to optimize two responses viz. yield and higher heating value on biochar. The CCD comprised of 20 experiments viz. cube 8 factorial points, 6 axial points and 6 central replicate experiments determined according to Eq. 6.1. The experimental design showing variables are presented in Table 6.1. In the present study 4 central replicates were consider thus 18 experiments were performed. A second– degree order polynomial given by Eq 6.2 was used to fit the experimental data. To determine the statistical significance and the fitness of regression models developed the data was analysed using analysis of variance (ANOVA)

Table 6.1 Experimental levels and range of independent variables

Variables		Experimental levels		
		–1	**0**	**+1**
Temperature °C	A	350	450	550
Heating rate °C/min	B	10	20	30
Residence time (min)	C	30	60	90

$$N = 2^n + 2n + n_c = 2^2 + 2 \times 3 + 6 = 20 \qquad (6.1)$$

where N = number of experiments, n = number of factors n_c = number of central replicates at the centre point.

$$Y=\beta_o+\sum_{j=1}^{k}\beta_j X_j+\sum_{j=1}^{k}\beta_{jj} X_j^2+\sum_{i<j}\beta_{ij} X_i X_j \qquad (6.2)$$

where Y = expected response, n is the number of experiments, β_o, β_i, β_{ii} and β_{ij} is regression coefficients for the constant, linear, quadratic and interaction terms, respectively. X_i and X_j are the coded independent factors.

6.2 Results and discussion

6.2.1 Properties of raw biomass and blend

Proximate and ultimate analysis for WH, TP, SCB and blend (WH111) used are summarized in Table 6.2. The proximate analysis results showed that there was a significant change in properties of the biomass after blending. Higher volatile matter (VM) and lower ash contents (AC), fixed carbon (FC) and (MC) were noted compared to the values observed for individual raw biomass. The high value of VM (80.76%) showed that the WH111 could utilized as a raw material for co–pyrolysis. The significant variation of the proximate analysis could be attributed to the effect of amount of the individual biomass added in the blend. For example, the AC WH 111 of (5.79%) increased due to more WH in the blend which had more AC of (4.82%) compared SCB and TP which had 3.12% and 2.11%, respectively. Higher heating value (HHV) of 18.05 MJ/kg for WH111 relative to 15. 45 MJ/kg for WH and 18.77 MJ/kg and 20.41 MJ/kg for TP. The CHN analysis indicated that the carbon content is 47.28 % for WH111. It was observed that carbon content was relatively high for WH 3111 compared to the individual raw biomass this supports the high calorific value thus suggesting a high a potential for bioenergy application. The results of proximate analysis and ultimate are within the range of other biomass reported in the open literature [104,200–202].

Table 6.2 Physicochemical properties of raw biomass and ternary blends

Analysis	**Raw biomass** [203]			**Ternary blend** [204]
	WH	**SCB**	**TP**	**WH 111**
Proximate analysis (ad% wt)				
Moisture content (MC)	9.04±0.00	7.83±0.10	6.85±0.05	8.59±0.20
Volatile matter (VM)	79.07±0.60	74.02±0.50	78.02±0.70	80.76±0.10
Ash content (AC)	4.82±0.10	3.12±0.10	2.11±0.45	5.79±0.10
Fixed carbon (FC)	7.07±0.20	15.03±0.30	13.02±0.20	5.86±0.30
Ultimate analysis (daf % wt)				
C	36.44	42.02	44.70	47.28
H	5.02	5.77	5.84	5.38
O$^{(*)}$	54.68	49.91	48.09	45.68
N	3.86	2.12	1.37	1.65
H/C	1.64	1.63	1.55	1.36
O/C	1.13	0.89	0.81	0.73
Calorific value (MJ kg^{-1})	15.45±0.30	18.77±0.10	20.41±0.70	17.79±0.10
Bulk density (kg m^{-3})	275.41±1.00	306.22±0.70	532.13±0.70	324.26±0.20
Composition analysis (% wt)				
Cellulose	30.56±0.30	40.59±1.10	28.90±0.80	34.86±1.30
Hemicellulose	34.79±1.30	29.35±0.20	21.45±0.20	31.29±2.50
Lignin	5.65±0.60	19.89±0.50	15.76±1.30	12.32±1.70
Extractives$^{(*)}$	29.0±0.90	10.17±1.00	33.89±0.70	21.53±1.30

ad: air–dried; daf: dry ash–free basis *: calculated by the difference

6.2.2 Central composite design (CCD) analysis

The design and statistical analysis of the co–pyrolysis process was executed with the help of State–Ease Design Expert 12 software. To develop the experimental matrix 3 levels were considered as shown in Table 6.1. The CCD design was employed to the experimental results with three variables (temperature, heating rate and residence time) as indicated in Table 6.3 for biochar yield and HHV. As per experimental conditions given by the software, a total of 18 experiments (including 4 central runs) were executed to optimize the biochar yield and HHV.

Table 6.3 Experimental responses for biochar yield and HHV

	Variables			**Responses**	
Run	Temp ° C/ (A)	HR° C/min (B)	RT min (C)	Yield (%)	HHV(MJ/kg)
1	618.18	20	60	24.30	29.46
2	450	36.82	60	26.41	24.23
3	450	20	60	33.36	25.25
4	550	10	90	24.60	28.23
5	450	20	60	34.02	24.97
6	450	20	60	33.40	25.88
7	550	30	90	23.40	26.09
8	550	30	30	26.07	25.88
9	550	10	30	21.35	26.17
10	350	10	90	33.46	21.02
11	450	3.18	60	26.27	25.32
12	450	20	60	33.68	25.17
13	350	10	30	31.28	18.42
14	350	30	90	29.63	19.98
15	281.82	20	60	37.84	19.42
16	350	30	30	32.35	19.48
17	450	20	9.54	29	18.42
18	450	20	110.45	29.61	22.10

6.2.3 ANOVA analysis

A second–degree polynomial model was used fit the experimental results for biochar. ANOVA was performed to investigate the interactions of variables (temperature, heating rate and residence time) on yield and higher heating value of biochar using the quadratic model in CCD. The reliability of the model depends on the Fischer test value (F–value) and probability value (p–value). A higher F–value shows a reliable model while a lower p–value indicates that the model is more significant. The ANOVA obtained for yield and higher heating value for biochar are shown in Table 6.4 and 6.5. The F–value for yield and HHV model were 269.97 and 153.69, respectively, with p–values <0.0001, suggesting that the regression models were highly significant. The F–value being so high suggests that that the model is reliable [205,206].

Table 6.4 ANOVA for biochar yield

Source	Sum of square	DF	Mean of square	F–value	P–Value	Remark
Biochar Yield						
Model	401.47	9	44.61	269.97	< 0.0001	significant
A– Temperature	214.08	1	214.08	815.73	< 0.0001	significant
B–Heating rate	0.0907	1	0.0907	505.24	0.0057	significant
C–Residence time	0.0832	1	0.0832	0.3170	0.0068	significant
AB	4.93	1	4.93	18.78	0.0025	significant
AC	0.1568	1	0.1568	0.5975	0.0046	significant
BC	14.63	1	14.63	55.76	< 0.0001	significant
A^2	30.51	1	30.51	116.25	< 0.0001	
B^2	132.60	1	132.60	0.3457	< 0.0001	
C^2	59.95	1	59.95	228.43	< 0.0001	
Residual	2.10	8	0.2624			
Lack of fit	2.10	5	0.4199		0.1020	not significant
Pure error	0.0000	3	0.0000			
Cor Total	403.57	17				

Std .dev= 0.51, **mean**=29.75, **C.V.** =1.72%, **R**^{2}=0.99, **R**$^{2}_{\mathrm{Adj}}$=0.98, **R**$^{2}_{\mathrm{pred}}$=0.96, **Adeq precision** =40.93

Table 6.5 ANOVA for HHV

Source	Sum of square	DF	Mean of square	F–value	P–Value	Remark
Biochar HHV						
Model	194.55	9	21.62	153.69	< 0.0001	significant
A– Temperature	144.06	1	144.06	357.79	< 0.0001	significant
B–Heating rate	1.32	1	1.32	3.27	0.0080	significant
C–Residence time	9.78	1	9.78	24.30	0.0012	significant
AB	0.7503	1	0.7505	1.86	0.2094	not significant
AC	0.0861	1	0.0861	0.2139	0.6561	not significant
BC	1.95	1	1.95	4.84	0.0589	
A^2	0.4894	1	0.0774	1.22	0.3023	not significant
B^2	0.0774	1	35.47	0.1924	0.6726	not significant
C^2	35.47	1	0.4026	88.09	< 0.0001	
Residual	3.22	8	0.26.25			
Lack of fit	1.31	5	0.6362	0.4127	0.8185	not significant
Pure error	1.91	3				
Cor Total	197.77	17				

dev= 0.63, **mean** =23.58, **C.V.** =2.69 %, **R**^{2}=0.98, **R**$^{2}_{\mathrm{Adj}}$= 0.97, **R**$^{2}_{\mathrm{pred}}$=0.93, **Adeq precision** =24.40

ANOVA summaries for quadratic models for biochar are shown in Table 6.6. It could be observed that the standard deviations for biochar yield and HHV were 0.51 and 0.63, respectively. The Standard deviations obtained were <1 therefore the models developed are considered to be adequate and fit for optimization. Also, the insignificant difference in standard deviation indicated that the models were acceptable. The mean responses for biochar yield and HHV were 29.75 and 23.58, respectively. A low coefficient of variation (CV) of < 3 % was observed for biochar yield=1.72 and HHV=2.69 this indicated reproducibility of the models considered [207]. The models fitness was also evaluated using R^2 test. The values of R^2 were in the range of 0.97–0.99 for biochar, which was close to 1 thus, indicating that they were suitable for the models. It could be observed that the individual models had high and comparable values of R^2 and adjusted R^2, it could be inferred that the selected quadratic response surface models for biochar are adequately described by the experimental data within the operating conditions selected. The adequate precision of 40.93 and 24.40 for biochar yield and HHV, indicated sufficient signal since the values obtained were > 4. Hence, models selected were capable to optimizing the co–pyrolysis process within the design space [208].

Table 6.6 Summary of ANOVA for quadratic model for biochar responses

Responses	**SD**[a]	**Mean**	**CV(%)**[b]	**R^2**	**Adj R^2**	**Pred R^2**	**Adeq Precision**[c]
Yield	0.51	29.75	1.72	0.99	0.98	0.96	40.93
HHV	0.63	23.58	2.69	0.98	0.97	0.93	24.40

The models obtained for the predicting yield and HHV for biochar are presented by Eqs. (6.3) and (6.4). after removing the insignificant terms. The positive and negative signs in model equations indicates the synergic effects and antagonistic effects on biochar yield and HHV, respectively [209]. In Eqs. (6.3) and (6.4), the terms A, B, and C represent the coded values of temperature, heating rate, residence time, respectively. To obtain the reduced terms in the equation P–values < 0.05 were consider since they are said to be significant. It could be observed from Eqs. (6.3) and (6.4) that all the significant terms had a positive synergic effect on yield and HHV. From F–values obtained it could be seen that for biochar yield the most significant terms had this sequence $A>B>C^2>A^2>BC>AB>AC>B^2>C$. In the case of HHV model the significant terms observed the following sequence $A>C^2>C>BC>B$ while the quadratic terms A^2, B^2 and the interaction AC does not have any significant impact on the biochar HHV.

$$\text{Biochar}_{\text{yield}} = 2.341 + 0.082A + 1.220B + 0.362C + 0.001AB - 0.004BC - 0.032B^2 \tag{6.3}$$

$$\text{Biochar}_{\text{HHV}} = -7.284 + 0.058A + 0.237B + 0.300C - 0.002BC \tag{6.4}$$

6.2.4 Optimization surface analysis (contours and 3D plots)

To investigate the effects of the process parameters on the responses with their interactions 3D plots and contours were used. The aim was to identify the best optimum conditions that would maximize yield and HHV of biochar individually by maintaining the process parameters within the experimental range shown in Table 6.1. The interactive effect of three variables on yield and HHV for biochar and couldn't be presented in a single three–dimensional (3D) plots thus, the variation of two variables maintaining one constant was presented separately for biochar as shown by Figures 6.1a–f and 6.2a–f. By considering the highest desirability obtained, the optimized conditions were found. The optimum conditions obtained for a high yield and HHV were temperature 368°C, residence time 37min, and heating rate of 16.33 °C/min with desirability of 1. The actual experimental results for biochar yield and HHV obtained from ternary blend at optimum condition are 35.84% and 23.47 MJ/kg, respectively.

6.2.5 Optimization of temperature and heating rate on biochar yield

The contours and 3D plots on optimization of temperature and heating rate for biochar is shown in Figures 6.1a–b. The biochar yield were significantly influenced by operating parameters (temperature and heating rate). It could be seen that maximum yield of biochar was obtained at lower temperature and heating rate, respectively. This could be attributed to an increase in temperature during co–pyrolysis that results in degradation of lignin hence, an increase in production of non–condensable gases. Increase in temperature resulted to a high yield of bio–oil and reached to a maximum at moderate temperature whereas heating rate showed opposite profile since yield of biochar decreased with high heating rate. This trends could be attribute to more volatiles were produced with an increase in temperature but beyond the optimum temperature degradation of lignin and secondary reactions occurs which leads to production of more non–condensable gases hence, decreasing the biochar yield.

6.2.6 Effect of optimization of temperature and residence time on biochar yield

The interaction amongst these two factors at constant heating rate are shown in Figure 6.1c–d. It was observed that temperature had a significant effect on biochar. Longer residence time increased, and decreased biochar yield. At higher temperature and longer residence time, biomass is subjected to longer period of degradation, hence, biochar the yield decreases. Also, higher residence time favors the occurrence of secondary reactions, which further reduces biochar yields.

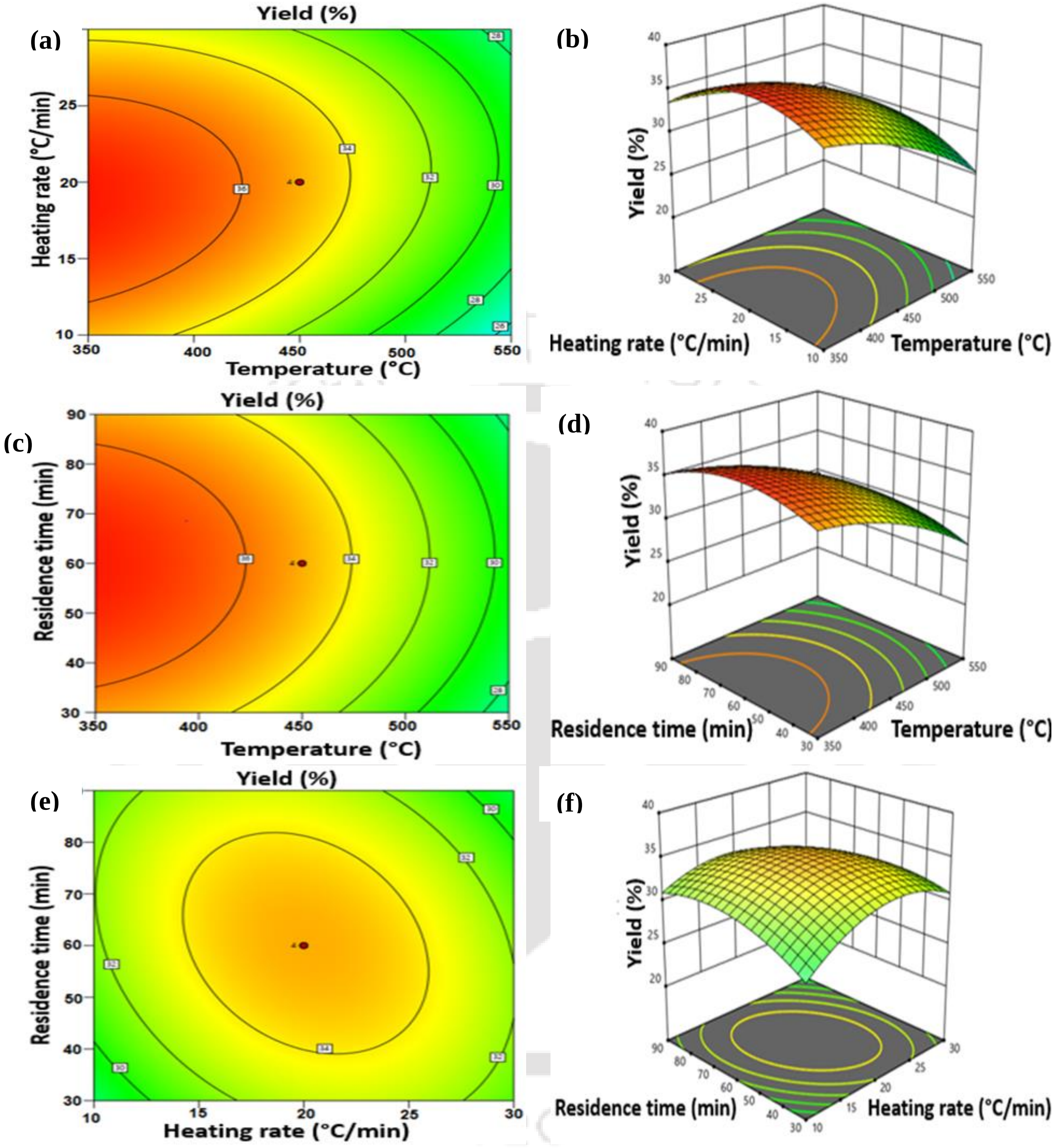

Figure 6.1 Contours and 3D plots for biochar yield biochar (a) and (b) temperature and heating rate, (c) and (d) temperature and residence time, (e) and (f) residence time and heating rate.

6.3 Response surface analysis for HHV

The contours and 3D plots showing interactive effect of variables on co–pyrolysis for HHV value on biochar are shown in Figures 6.2a–e. It could be seen that when heating rate and temperature changed there was a significant effect on HHV as depicted by Figure 6.2a and b However, when only heating rate was varied a relatively less effect was noted on HHV. The contour and 3D plots for HHV due to variation of residence and heating rate at a constant temperature were in Figure 6.2e and f. Significant variation in HHV was observed as heating rate and residence time increased. This results could be attributed to the formation of carbon rich solid and due to rapid devolatilization of volatiles. It is important to note that from Figures 6.1a–b and 6.2a–b the interaction among residence time and temperature at a constant heating rate showed that temperature had a significant effect on yield and HHV for biochar. This results confirms that both yield and HHV have opposite response towards the operating parameters. The optimum conditions based on maximum yield and HHV were obtained at a temperature of 368 ºC and residence time 61min at a constant heating rate of 16.33ºC/ min.

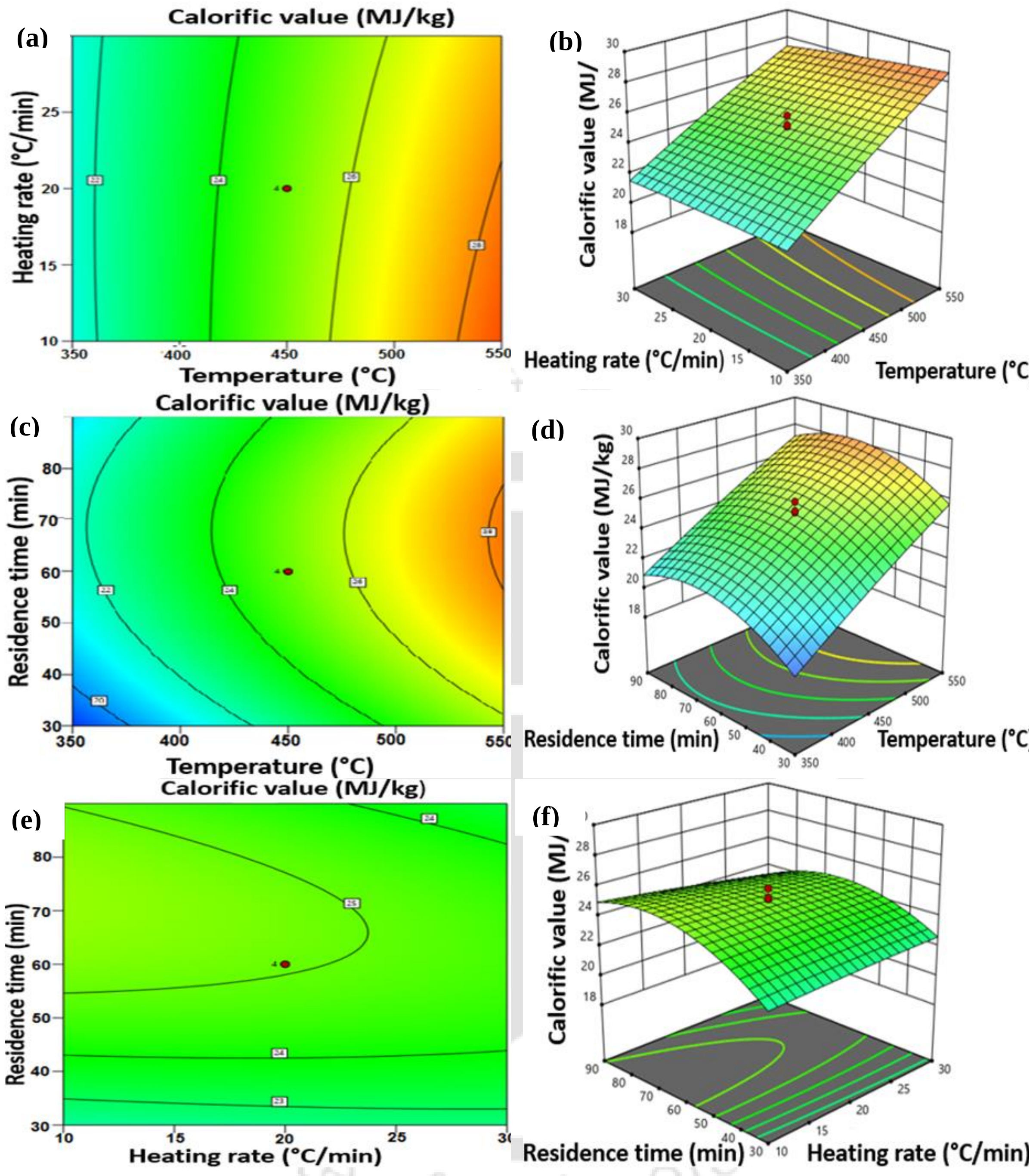

Figure 6.2 Contours and 3D plots for HHV of biochar (a) and (b) temperature and heating rate, (c) and (d) temperature and residence time, (e) and (f) residence time and heating rate.

6.4 Characterization of biochar

6.4.1 Physicochemical properties of biochar

In order to determine the synergistic interactions, the physicochemical properties of biochar produced at optimized conditions were compared with the biochar produced from raw biomass at the same optimum conditions. Table 6.7 shows the proximate and ultimate analysis of biochar produced from raw biomass and ternary blends at optimized parameters viz. temperature 367.68ºC, residence time 60.91min, and heating rate 16.33ºCmin^{-1}. It could be observed that feedstock is an important variable for the co–pyrolysis process. The physicochemical properties of the biochar varied significantly amongst the four biomass. A relatively high yield was obtained from the ternary blend which could be attributed to the structural variation of the biomass reported in Table 6.7. Other notable differences that could be observed were the decrease of moisture content, ash content and increase of fixed carbon when biochar obtained from the blend is compared with that produced from raw biomass. The FC content was found to be in the range of 5.86–15.03 wt.% in the parent biomass. Subsequently after co–pyrolysis the FC content increased significantly in the range of 52.94–75.54 wt.%. The change could be attributed to removal of volatile from the biomass. Proximate analysis results showed a significant advancement of the qualities of the biochar produced from the ternary blend thus suggesting that the biochar could be used as solid fuels.

The ultimate analysis results showed that the content of carbon increased while hydrogen and oxygen decreased after co–pyrolysis. Initially the carbon contents for raw biomass were in the range of 36.44–47.28 wt.%. while for biochar were in the range of 41.03–64.46 wt%. The increase of carbon and decrease of hydrogen and oxygen could be attributed to decarboxylation and dehydration reactions, respectively. Decarboxylation reactions converts the biomass into a highly carbonaceous solid material that can be used as solid fuel and for soil amendment. The molar atomic ratios are key indicators of the degree of carbonization as shown in Figure 6.3. Biochar with a lower H/C and O/C lower ratios experienced greater thermal degradation due to the greater loss of H and O resulting in a relatively high C content [210]. It could be observed there was a significant shift for biochar produced from ternary blend on the Van Krevelen plot. This suggest that a greater degree of carbonization happened in this biochar making it more superior than biochar produced from water hyacinth. The calorific values of the biochar increased significantly compared with raw biomass. The calorific value for biochar produced from ternary blend was relatively low compared to that of TP and SCB this could be attributed to the effect of WH which had a lower calorific value. It is worth noting that the properties of bio–char obtained from ternary blend improved significantly hence suggesting that co–pyrolysis of biomass had a unique effect on the end products.

Table 6.7 Physicochemical properties of biochar optimized conditions

Analysis	Sample code			
	WH	**TP**	**SCB**	**WH 111**
Proximate analysis^a (% wt ad)				
Moisture content	3.14±0.10	2.37±0.70	1.02±0.50	2.07±0.40
Volatile matter	32.89±0.01	18.19±0.80	22.46±0.40	26.51±0.10
Ash content	11.05±0.20	7.85±0.80	0.98±0.90	6.12±0.50
Fixed carbon	52.92±0.40	71.59±0.40	75.54±0.30	65.3±0.20
Ultimate analysis^b(% wt daf)				
C	41.03	61.96	64.46	58.74
H	3.65	4.17	3.97	3.98
N	4.38	0.07	0.19	1.89
O*	50.94	33.8	31.38	35.39
H/C	1.06	0.80	0.73	0.81
O/C	0.93	0.41	0.37	0.45
Other properties				
Higher heating value (MJ/kg)	18.43±0.20	25.17±0.70	29.82±0.60	23.47±0.30
Bulk density (kg/m^3)	0.14±0.30	0.23±0.60	0.12±0.80	0.17±0.20
pH	8.04±0.20	8.98±0.30	7.83±0.50	8.79±0.50
EC (dS/m)	28.42±0.20	7.92±0.01	6.65±0.30	11.09±0.70
Yield (%)	33.26±1.10	30.07±0.10	28.70±0.40	35.84±0.90

Notation: ^{a} air–dried basis (ad), ^{b}dry ash–free basis (daf), * calculated by difference

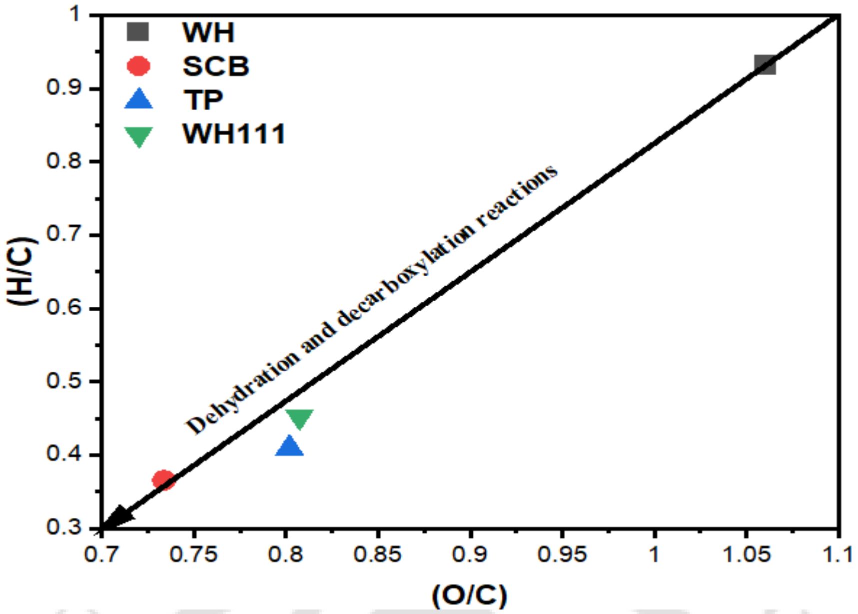

Figure 6.3 Van Krevelen plot of biochar produced at optimized conditions

6.4.2 Scanning electron microscope and EDX analysis

Figure 6.4a and b shows the SEM micrograph of the raw biomass at 500× and biochar synthesized at optimized conditions for ternary blend, respectively. The figures clearly showed that the morphology of raw biomass and that of biochar significantly varied. It could be observed from the SEM image Figure 6. 4a raw biomass consisted of long and rough elongated morphology which consisted of sheet–like structures, lacking any visible porous surfaces. Whereas in Figure 6.4b some evenly disturbed pores were observed on the surface of biochar. The pores are due to degradation of holocellulose during co–pyrolysis and dehydration and evaporation of volatiles. As the heating rate increased a significant disruption of the structure of biochar occurred which resulted to formation of well–defined pores. The presence of porosities on biochar are appropriate to allow them to be applied for various applications viz. soil amendment, water purification and manufacture of fabrication of form stable material for energy storage [145,211]. Figure 6.4 (c) and (d) shows the EDX micrographs which represents the element present in the raw biomass and biochar respectively. From the EDX images it could be observed that in the case of biochar the quantity of some of the elements were higher than that of raw biomass. Elements like carbon (C) showed higher peak intensity this could be attributed to aromatization due to co–pyrolysis. Similarly, the oxygen peaks were weak due to dehydration. These results are supported by the ultimate analysis results which shows increase in carbon content and decrease of oxygen content of the biochar listed in Table 6.6. The FTIR results further confirms the dehydration and depolymerisation reactions due to weaker O–H bond in the biochar compared to the raw biomass [159].

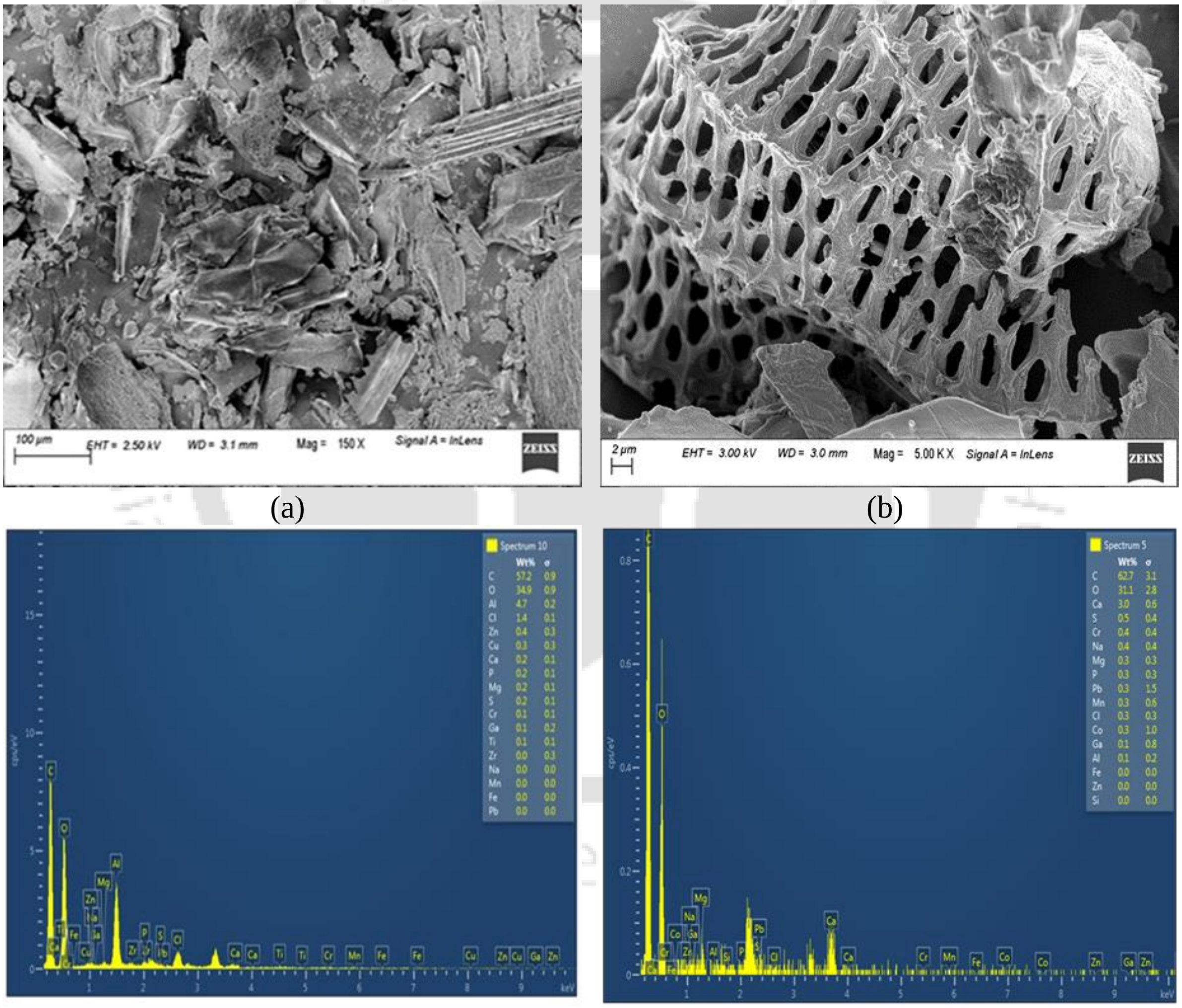

(a) (b)

Spectrum 10

	Wt%	σ
C	57.2	0.9
O	34.9	0.9
Al	4.7	0.2
Cl	1.4	0.1
Zn	0.4	0.3
Cu	0.3	0.3
Ca	0.2	0.1
P	0.2	0.1
Mg	0.2	0.1
S	0.2	0.1
Cr	0.1	0.1
Ga	0.1	0.2
Ti	0.1	0.1
Zr	0.0	0.3
Na	0.0	0.0
Mn	0.0	0.0
Fe	0.0	0.0
Pb	0.0	0.0

Spectrum 5

	Wt%	σ
C	62.7	3.1
O	31.1	2.8
Ca	3.0	0.6
S	0.5	0.4
Cr	0.4	0.4
Na	0.4	0.4
Mg	0.3	0.3
P	0.3	0.3
Pb	0.3	1.5
Mn	0.3	0.6
Cl	0.3	0.3
Co	0.3	1.0
Ga	0.1	0.8
Al	0.1	0.2
Fe	0.0	0.0
Zn	0.0	0.0
Si	0.0	0.0

(C) (d)

Figure 6.4. SEM and EDX micrograph (a) Raw biomass (b) biochar

6.4.3 FTIR analysis

The FTIR spectra for native biomass (WH111) and biochar (WH111 biochar) obtained at optimun conditions are illustrated in Figure 6.5. For the raw biomass the peaks observed at 1052 corresponded to C–O and were assigned holocellulose. The peaks found at 2921cm^{-1} are attributed to aliphatic C–H, while the peaks corresponding to carbonyl (C=O) extending vibration appear in the bands 1600−1800 cm^{-1}. The peaks corresponding to C=C are located at 1200−1430 cm^{-1} and essentially represent the aromatic structures.

It could be seen that the most prominent absorption peak observed in the FTIR spectra of raw biomass is between 3100−3450 cm^{-1} band. This is attributed to O−H bond stretching. This peak confirmed presence of the hydroxyl group in the macromolecular structure which is further confirmed by proximate analysis results which shows high moisture content in biomass blends than biochar. For the biochar peaks at 749 cm^{-1} are assigned to aromatic hydrocarbon C–H, while at 1372 cm^{-1} were corresponding to phenols O–H, and 2502 cm^{-1} showed the presence of aliphatic and aromatic C=C. The presence of aromatics indicated a significant extent of carbonization, which was also confirmed by ultimate analysis which showed more C content in the biochar that the raw biomass. It is worth noting that O–H group present in the raw biomass is not present in the biochar which could be as a result of dehydration during co–pyrolysis [79]. It could be observed that the spectra the intesity of FTIR spectra for biochar was relatively weaker which might be attributed to the associate dehydration of various functional groups and carbonization of biochar.

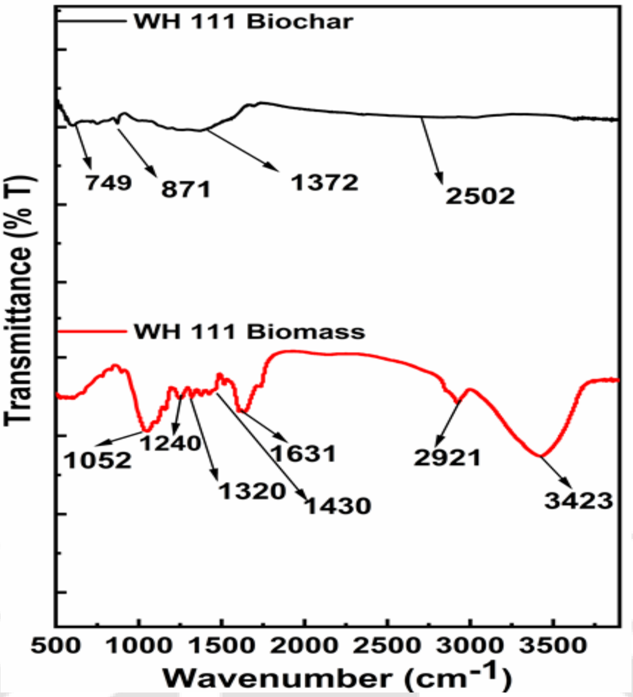

Figure 6.5 FTIR spectra for raw biomass and biochar

6.4.4 BET analysis

The BET surface analysis of biochar produced at the optimum conditions are shown on Table 6.8. The Pore size of biochar are listed in Table 6.8 and were in the range of 3.25–5.95 nm. Thus, the synthesized biochar are classified as mesoporous. The amount of gas adsorbed increased showing a hysteresis curve in a wide range of relative pressure. The highest volume of gas adsorbed could be observed at (P/P^O=0.97) as illustrated by the adsorption isotherm Figure 6.6. This showed the presence of large pores in the macrostructure of the biochar. It could be observed that BET surface area, pore volume and pore size have significantly improved for the biochar produced from ternary blends. The improvement of the BET properties could be attributed to the variation of the compositional structure after blending the raw materials [204]. BET surface area is an important factor is one of the most important factors that determines ability of biochar to be used for adsorption purposes. Biochar with larger surface area are considered to be more porous and could be used for agronomy and energy applications [96].

Table 6.8 BET analysis for biochar.

Properties	**WH**	**TP**	**SCB**	**WH111**
BET Surface area (m^2/g)	3.650	4.800	6.940	5.680
Pore volume (cm^3/g)	0.030	0.010	0.060	0.060
Pore size (nm)	4.210	3.250	3.980	4.950

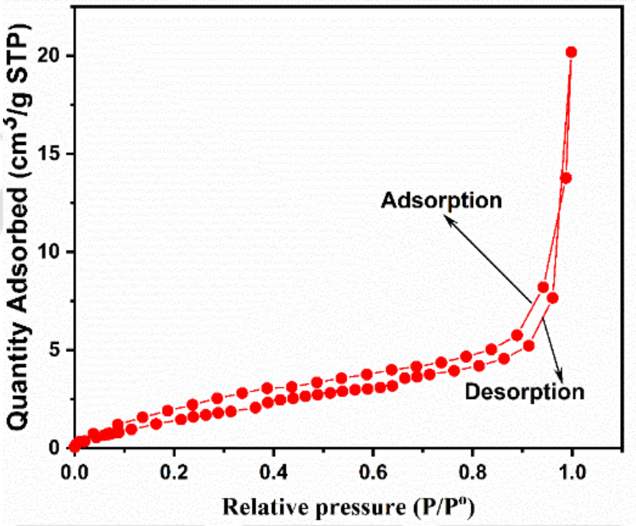

Figure 6.6 Nitrogen adsorption–desorption isotherms for biochar WH111

6.4.5 pH value, and electrical conductivity

The pH and electrical conductivity (EC) for the biochar produced at optimum conditions from WH, TP, SCB AND WH111 are shown in Table 6.6. The pH values ranged from 7.83–8.98. It could be observed that co–pyrolysis resulted to an increase in pH thus making the biochar. Biochar with a high pH could be used for soil amendment of acidic soils [212]. The EC varied from 6.65–28.42.

6.5 Summary

The optimum pyrolysis conditions to maximize biochar yield viz. heating rate, residence time and, temperature, were determined using CCD design with the help of RSM. The higher yield of biochar having a high heating value was produced successfully from co–pyrolysis of ternary blend of water hyacinth, Thevetia peruviana and sugarcane bagasse. The yield for WH111 was 35.84%, and HHV=23.47MJ/kg while using the ideal parameters viz. temperature=368°C, residence time=61min, and heating rate=16.33°C/min The experimental yields and heating value for biochar at optimum conditions were consistent with the ones predicted from RSM. The synthesized biochar was characterized using standard techniques to determine its inherent properties. These results showed the biochar produced from co–pyrolysis had better properties compared to the individual biochar obtained from raw biomass therefore, they could be used for energy, as solid fuels and soil amendment for agriculture. The BET and SEM analysis showed the porous nature of biochar produced. Therefore, it can be used as bio composite and biocatalyst which could be used in a manufacturing form stable materials for energy storage. In the next chapter applications of biochar in agriculture and engineering is discussed.

CHAPTER 7–Application of biochar in agronomy and engineering

7.0 Introduction

This chapter presents the applications of biochar in agriculture and engineering. Biochar promotes sustainable agriculture since its utilization as a soil amendment is an innovative and promising option for replenishment of soil fertility. All over the world many farmers have opted to use chemical or inorganic fertilizers to improve the agricultural yields and soil fertility. This approach is not sustainable, uneconomical and excessive use of inorganic fertilizers mainly nitrogen, has the ability to deteriorate soil environment and can also lead to the mineralization of organic matter [213]. Continuous cultivation to satisfy the high demand for food has highly contributed to the decrease of soil fertility due to soil acidification. Researchers have shown there are several benefits of using biochar in agronomy as illustrated in Figure 7.1. Biochar improves soil fertility through adjustment of soil pH, improved nutrient and water retention through cation adsorption, reduction in nitrous oxide (NO_x) and methane (CH_4), along with CO_2 emissions and sorption of organic contaminants. Further it provides habitat for soil microorganisms, improves soil structure. [214]

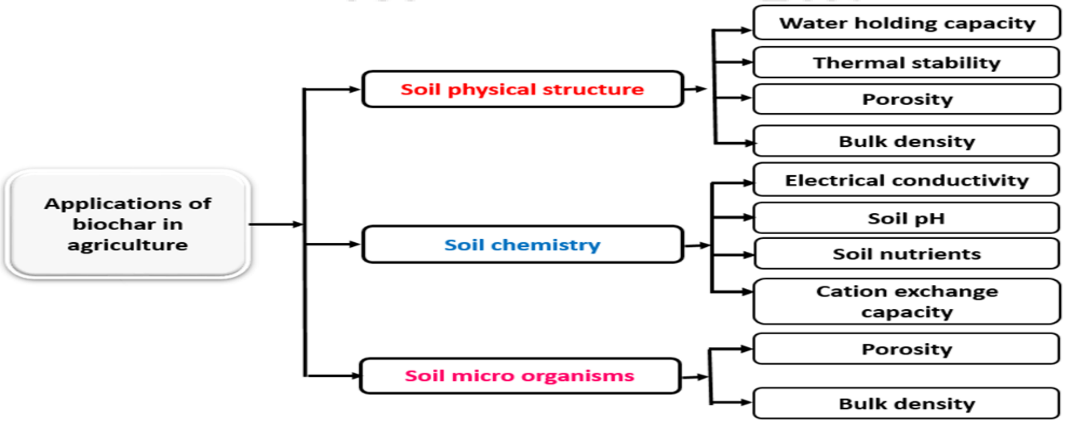

Figure 7.1 Summary of effects applications of biochar in agronomy

Researchers have devoted to study the application of phase change materials (PCMs), which have demonstrated significant capacities to store and discharge abundant thermal energy during the course of phase change. However, low heat conductivity, as well as the problem of liquid leakage during phase transitions, are the major shortcomings [215]. There are two ways to deal with pure PCMs to improve their stability and performance. The first one is to make form–stable PCMs, which is a network on micro or macroscale where PCMs are trapped. Whereas encapsulation is applied in the second case. The additional use of encapsulation may incur additional cost on the system and add up heat resistance caused by the capsule shell, thus reducing the effectiveness of heat transfer during utility mode. The low thermal conductivity of commonly used PCMs is another technological problem to be addressed. This leads to poor life stability of PCM containers and heat exchanger tubing, and also decrease the number of effective cycles they can undergo without any deterioration in their properties.

Researchers have tried to address these issues in the recent past around the globe to develop a suitable latent energy storage material. Inaba and Tu [216] blended paraffin and high–density polyethylene to develop a form–stable PCM. In an attempt to decrease the oozing rate of the new material, the authors added a small amount of the resin (ethylene– α olein). Hong and Ge [217] prepared a low–temperature heat storage compound consisting of paraffin as a dispersing medium with high–density polyethylene (HDPE) for improvement of the stability. Wan et al. [218] manufactured one form stable phase change material by using pinecone biochar as a supporting matrix for Palmitic Acid. They conducted various characterization tests and concluded that Palmitic Acid was bonded with biochar due to capillary force and surface tension. No chemical reactions happened between the two materials and so the chemical properties have not changed from the original biochar.

7.2 Materials and method

The soil used for the pot experiment was be obtained from a field at IIT Guwahati campus 26.1879° N, 91.6916° E). The soil was obtained from 0–20 cm depth and was uniformly mixed by repetitive scooping. The paraffin wax was purchased from Merck Chemicals, which has a melting temperature of 58–60°C. The organic PCM used in the PV/T (savE® OM 35) was purchased from Pluss Advanced Technologies, which has a melting temperature range of 35–39ºC. Pots and maize seedlings were purchased from a local market outside IIT Guwahati campus.

7.2.1 Synthesis of biochar for agriculture and engineering applications

Biochar used in for the application experiments was synthesized as discussed in chapter 4 subsection 4.1.2 of this thesis. For the agriculture applications three biochar were used which were abbreviated as WH550, SCB550 and TP550, while for engineering applications only biochar obtained from water hyacinth i.e. WH550 was used.

7.2.2 Pot experiment

Pot experiments were conducted to investigate the growth response of maize plant as a result of addition three different biochar produced from waste sugarcane bagasse and two noxious weeds viz. water hyacinth and *Thevetia peruviana*. The pot trial was conducted for a period of 7 weeks between October–November 2019 in a greenhouse located in IIT Guwahati as shown in Figure 7.2. Pots of (upper, middle and lower diameter: 20 cm, 19 cm, and 12 cm were filled with 3 kg of air–dried soil biochar, vermicompost and fertilizers mixtures. Three control experiments comprising of (1) Bare soil (BS) (2) Vermicompost treated soil (VTS) (3)

NPK treated soil (NTS), and four experiments for the three biochar (SCB,WH,TP) were prepared as follows: (1) biochar and vermicompost treated and NPK treated soil (BVNTS) (2) biochar and NPK treated soil (BNTS), (3) biochar vermicompost treated soil (BVTS), (4) biochar treated soil (BTS), Table 7.1 shows the treatment, abbreviations and amount of biochar, vermicompost and NPK added on individual pots.

Table 7.1 Treatment of biochar with alluvial soil

Treatment	**Abbreviation**	**Application rate (% w/w)**
Bare soil (control)	BS	0
Vermicompost treated soil (control)	VTS	2g
NPK treated soil (control)	NTS	1.17g
Biochar + vermicompost soil	BVTS	1g+1g
Biochar + NPK treated soil treated soil	BNTS	2g+1.17g
Biochar + vermicompost + NPK	BVNTS	1g+1g+1.17g
Biochar treated soil	BTS	2g

Figure 7.2 Pot experiment

7.2.3 Soil analysis

The soil was air dried at 105°C and sieved using a 2 mm sieve prior to the experiment. Soil properties cation exchange capacity (CEC), Electrical conductivity (EC), bulk density, particle size distribution, aggregate stability, water holding capacity and pH were determined.

7.2.4 Planting and data collection

Three seeds were planted at 2 cm maximum depth, and it was observed that germination occurred between 5 and 9 days after sowing. After germination, one strong plant was selected and allowed to grow in each pot. Plants were watered at the rate of 200 mL/pot after every 4 days. The amount of water was determined by physic impact method (citation). On weekly basis the following growth response parameters were evaluated after germination up to 56 days after planting, plant height (PH) was measured in cm from the soil base of stem to the arch of the uppermost whose tip is pointing down using a graduated ruler; number of leaves per plant were determined by counting the leaves. Two physical growth responses viz. plant height and number of leaves shown Figure 7.3 were recorded for the 7 wks.

Figure 7.3 Maize growth response

7.2.5 Preparation of the biochar PCM hybrid material

The PCM biochar composite material was manufactured via direct impregnation method as shown in Figure 7.4. Four different mass ratios of PCM and biochar were selected to optimize which would give better results in terms of stability, leakage test and conductivity. The PCM: biochar mixture ratio was taken as 5:5,6:4,7:3, 8:2 and 8:1 (w/w%) respectively. The PCM and biochar were put in a glass beaker with mouth covered in aluminium foil and put inside a hot air oven for 16 h at a set temperature of 80°C [215-216]. The mixture is stirred at an interval of 4 h to achieve the desired homogeneity. After 16 h, the samples were taken out from the oven and cooled to room temperature by natural air cooling.

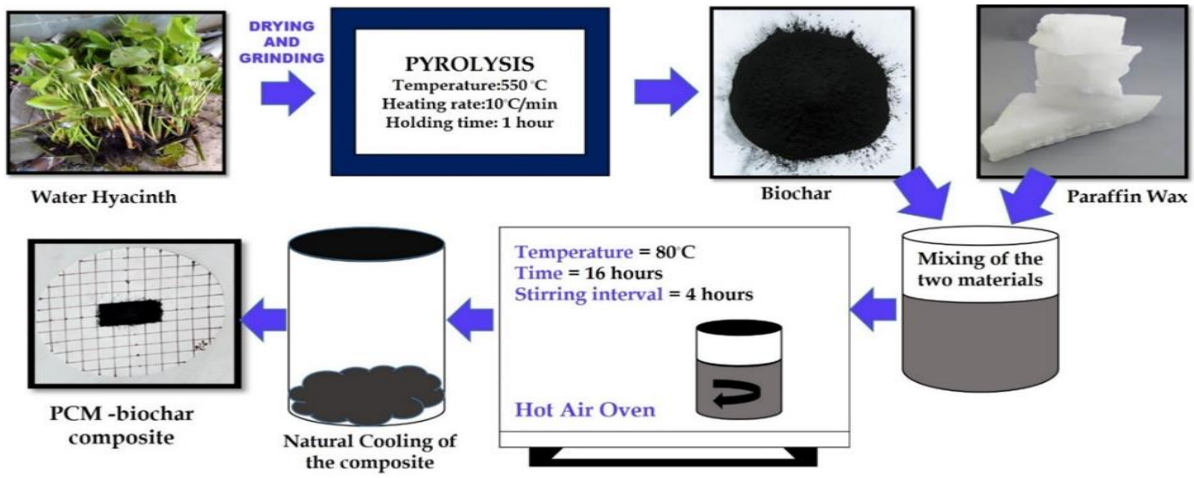

Figure 7.4 Steps of biochar PCM hybrid material

7.2.6 Characterization of the novel PCM–biochar thermal storage material

The surface morphologies of the biochar and bio composite were analysed using Field Emission Scanning Electron Microscope (FESEM) (Make: Zeiss, Model:–Sigma). Crystallinity and phase change identification was analysed using X–ray powder diffraction (XRD) (Model No: D8 Advance, Make: Bruker, Netherlands). The XRD measurements were done using Cu Kα (λ = 0.05°/s,1.54,056 nm) radiation a step size of 0.05° in the two theta degree range of 10°–50°. Functional groups were identified by a Fourier transform infrared spectrometry (FTIR, Nicolet iS10, Thermo Scientific, USA) the scanning scan range was from 4000cm^{-1} to 500cm^{-1}. The thermal conductivity of the composite material was tested using thermal conductivity meter. The device used in the work is KD2 Pro, which has a needle of length 10 cm long and 2.4 mm diameter with a measurement range of 0.02 to 2.00 W/mK. Thermal stability was determined using high–temperature differential scanning calorimetry (DSC)/ thermo gravimetric (TG) (Make: Netzsch, Model: STA449F3A00) a heating rate of 10

°C/ min from 50–500°C using Nitrogen. The DSC experiments were performed using the same equipment under similar conditions. The characteristic temperatures and heat of fusion were determined from the DSC peaks using a standard tangent method.

7.3 Results and discussion

7.3.1 Soil properties and vermicompost

Soil and vermicompost properties are shown in Table 7.2. It could be observed that vermicompost had a relative high EC, which could as a result of the activity of earthworms causing decomposition of organic matter, solubility and mineralization of compounds in the substrate and hence leading to increased EC of the substrate material due to the vermicomposting process [219]. The lower pH in the vermicompost could be attributed to the production of CO_2 and organic acids by microbial metabolism in the course of decomposition of the substrate during vermicomposting process [220].

Table 7.2 Properties of soil and vermicompost

Parameters	Soil parameters	Vermicompost parameters
pH	6.56±0.30	6.48±0.10
EC (dS/m)	0.02±1.30	1.59±2.30
Soil texture	Clay sandy	–
Bulk density (kg/m^3)	1480±0.00	537.5±0.90

7.3.2 Effect of addition of biochar with vermicompost and NPK on growth

7.3.2.1 Plant height

The effect of applying biochar with vermicompost and NPK fertilizer on plant height of maize on weekly basis is shown in Tables 7.3–7.5 Comparing the control experiments with the other treated soils it could be observed that the plant height significantly increased with addition of biochar with vermicompost and NPK fertilizer treatment (BVNTS). The highest value of plant height of 53.91cm was observed in the pots where SCB biochar was added in the eighth week. It was observed that application of biochar and vermicompost showed better results compared to the individual addition of biochar, vermicompost and NPK. These results could be attributed to the fact that vermicompost is easily degradable while biochar has an aromatic structure and it is recalcitrant in nature hence, very resistant to decomposition and it only enhance the adsorption of nutrients [221].

The results showed that application of biochar with additives viz. vermicompost and NPK on soil had a more significant effect on the growth performance of maize than those grown on soils without addition of biochar. The results could be attributed to fact that biochar helps in retaining of most applied nutrients by reducing leaching from vermicompost and NPK fertilizer hence making them available to growing plants [222]. Comparing the treatments where biochar was added with additives viz. vermicompost (VTS), NPK fertilizer (NTS) and biochar (BTS). A slight difference in terms of PH could be observed in these pots. From these results it could be inferred that biochar cannot be used as a substitute of other additives viz. inorganic fertilizer, compost or manures and vermicompost. The higher porous nature and surface area of biochar only enabled holding of higher amount of soil moisture available for crop uptake hence, all pots that were treated with biochar had a significant difference in terms of PH between them and control. Also the high growth in biochar treated soils could be attributed to the increased biological activity due to proper aeration as result of porous nature of the biochar.

Comparing the results in pots where NPK and vermicompost was used it could be observed that, an increase in PH in maize plants in pots treated with biochar and vermicompost than in soil that were treated with biochar and NPK alone as shown in Figure 7.5. It was inferred that addition of biochar with inorganic fertilizers is effective for maize crop as compared to conventional inorganic fertilizer.

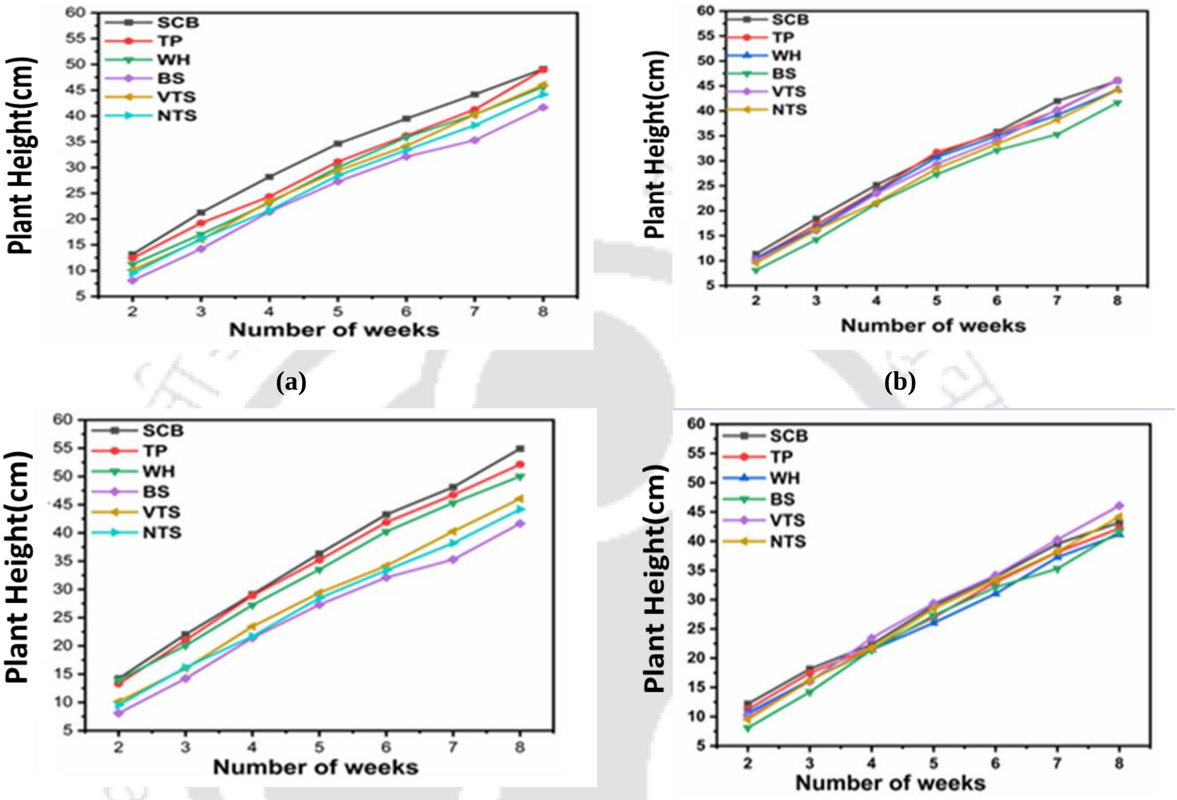

(a)

(b)

(c)

(d)

Figure 7.5 Effect of addition of biochar on maize plant height (a) BVNTS, (b) BNTS (c) BVTS (d) BTS

7.3.2.2 Number of leaves

The growth response in terms of number of leaves on maize plants are shown in Figure 7.6 and Tables 7.3-7.5. It could be observed from Figure 7.8 that after adding the three different types of biochar obtained from WH, SCB and TP, with vermicompost and NPK on weekly basis the was a significant difference in the number of leaves compared to the controls. From the Table 7.3–7.5.it could be observed that control treatments had the lowest number of leaves viz. BS=9.33, VTS=10.33 and NTS=10.33 compared to other treatments where the three types of biochar were added. It could be observed that there were no significant differences in number of leaves amongst the treatments viz. BVNTS, BNTS, BVTS and BTS in the first four weeks, but a significant difference was observed after five weeks and especially in the eighth week. Comparing the controls BS, VTS and NTS with the soils that contained biochar with additives. It could be observed that the number of leaves per plant increased in all the treatments where biochar was added. A significant difference was noted in the treatment BVNTS for all the three types of biochar viz. WH, TP SCB. The increase in number of leaves could be attributed to the superior growth of maize plants which was evident from the increased PH with the application biochar with additives. This is due to the increased availability of nutrients as a result of addition of biochar which has allowed nitrogen fixation, reduced nutrient leaching and combined nutrient supply compared to addition of vermicompost, NPK and biochar individually.

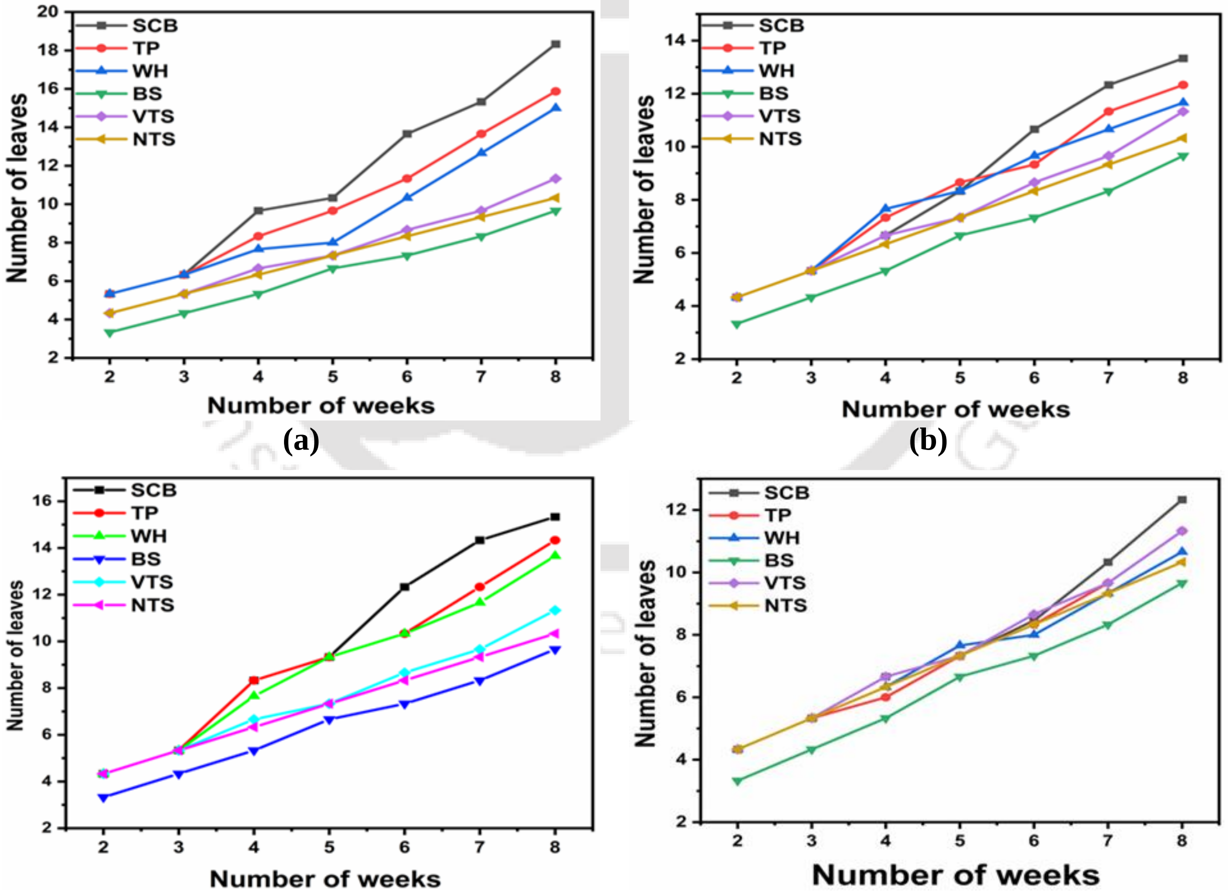

(a) (b)

(c) (d)

Figure 7.6 Effect of addition of biochar on number of leaves of maize plant (a) BVNTS, (b) BNTS (c) BVTS (d) BTS

Table 7.3 Effect of addition of SCB biochar on maize physical growth attributes

Treatment	Sampling time lines on plant height, and number of leaves													
	wk 2		wk 3		wk 4		wk 5		wk 6		wk 7		wk 8	
	PH*	NL#	PH*	NL#	PH*	NL#	PH*	NL#	PH*	NL#	PH*	NL#	PH*	NL#
BS	8.08 ± 0.90	3 ± 0.30	14.21 ± 0.30	4 ± 0.30	21.41 ± 0.30	5 ± 0.30	27.29 ±0.20	6 ± 0.33	32.11 ± 0.20	7 ± 0.30	35.28 ± 0.21	8 ± 0.30	41.65 ± 0.00	9 ± 0.30
VTS	10.13±0.20	4 ± 0.30	16.01± 0.10	5 ± 0.30	23.42± 0.20	6 ± 0.30	29.38± 0.20	7 ± 0.33	34.16± 0.50	8 ± 0.30	40.26± 0.78	9 ± 0.30	45.05± 0.50	10 ± 0.30
NTS	9.51± 0.40	4 ± 0.30	16.17± 0.80	5 ± 0.30	21.69± 0.80	6 ± 0.30	28.46± 0.20	7 ± 0.33	33.39± 0.10	8 ± 0.30	38.20± 0.07	9 ± 0.30	44.18± 0.70	10 ± 0.30
BVNTS	14.91± 0.60	5.± 0.30	22.03± 0.01	6 ± 0.30	29.13± 0.20	7 ± 0.30	36.33± 0.01	10 ± 0.33	43.10± 0.60	13 ± 0.30	48.09± 0.10	15 ± 0.30	53.91± 0.70	18 ± 0.60
BNTS	11.36± 0.40	4.± 0.30	18.43± 0.10	5 ± 0.30	25.17± 0.60	7 ± 0.30	31.15± 0.10	8 ± 0.33	35.81± 0.40	11 ± 0.30	41.96± 0.33	12 ± 0.30	46.03± 0.10	13 ± 0.30
BVTS	11.17± 0.20	4.± 0.30	21.26± 0.20	5 ± 0.30	28.19± 0.90	8 ± 0.30	34.63± 0.30	9 ± 0.33	39.47± 0.20	12 ± 0.30	44.18± 0.12	14 ± 0.30	49.11± 0.70	15 ± 1.20
BTS	12.18± 0.30	4 ± 0.30	18.14± 0.10	5 ± 0.30	22.32± 0.20	6 ± 0.30	28.96± 0.60	7 ± 0.33	33.89± 0.50	8 ± 0.30	39.53± 0.91	10 ± 0.30	43.19± 0.20	12 ± 0.30

*PH= Plant height in (cm), #NL= Number of leaves

Table 7.4 Effect of addition of TP biochar on maize physical growth attributes

Treatment	Sampling time lines on plant height, and number of leaves													
	wk 2		wk 3		wk 4		wk 5		wk 6		wk 7		wk 8	
	PH*	NL#	PH*	NL#	PH*	NL#	PH*	NL#	PH*	NL#	PH*	NL#	PH*	NL#
BS	8.01 ± 0.90	3 ± 0.30	14.20 ± 0.30	4 ± 0.30	21.40 ± 0.30	5 ± 0.30	27.30 ±0.20	6 ± 0.30	32.10 ± 0.20	7 ± 0.30	35.30 ± 0.20	8 ± 0.30	41.70 ± 0.00	9 ± 0.30
VTS	10.10± 0.22	4± 0.30	16.00± 0.10	5± 0.30	23.40± 0.20	6 ± 0.30	29.40± 0.20	7 ± 0.30	34.20± 0.50	8 ± 0.30	40.30± 0.80	9 ± 0.30	45.00± 0.50	10 ± 0.30
NTS	9.50± 0.41	4± 0.30	16.20± 0.80	5± 0.30	21.70± 0.80	6 ± 0.30	28.50± 0.20	7 ± 0.30	33.40± 0.10	8 ± 0.30	38.20± 0.07	9 ± 0.30	44.20± 0.70	10 ± 0.90
BVNTS	13.30± 1.14	5± 0.30	20.20± 0.60	6± 0.30	27.20± 1.40	7 ± 0.30	35.20± 0.60	9 ± 1.20	41.90± 1.00	11 ± 0.30	46.60± 0.10	12 ± 0.30	52.01± 0.20	15 ± 0.90
BNTS	10.50± 0.22	4± 0.30	17.20± 0.60	5± 0.30	24.01± 0.30	7 ± 0.30	31.80± 0.20	8 ± 0.30	35.40± 0.20	9 ± 0.30	40.01± 0.00	10 ± 0.30	46.20± 0.20	12 ± 0.30
BVTS	12.40± 0.13	4± 0.30	19.20± 0.01	5± 0.30	24.40± 0.20	8 ± 0.30	31.10± 0.50	9 ± 0.30	36.20± 0.90	10 ± 0.30	41.20± 0.60	12 ± 0.30	48.10± 0.70	13 ± 1.20
BTS	11.30± 0.16	4± 0.30	17.50± 0.40	5± 0.30	21.80± 0.01	6 ± 0.60	26.10± 0.10	7 ± 0.30	33.00± 0.20	8 ± 0.30	38.10± 0.00	9 ± 0.30	42.01± 0.70	11 ± 0.30

*PH= Plant height in (cm), #NL= Number of leaves

Table 7.5 Effect of addition of TP biochar on maize physical growth attributes

Treatment	**Sampling time lines on plant height, and number of leaves**													
	wk 2		**wk 3**		**wk 4**		**wk 5**		**wk 6**		**wk 7**		**wk 8**	
	PH*	**NL$^{\#}$**	**PH***	**NL$^{\#}$**	**PH***	**NL$^{\#}$**	**PH***	**NL$^{\#}$**	**PH***	**NL$^{\#}$**	**PH***	**NL$^{\#}$**	**PH***	**NL$^{\#}$**
BS	8.10 ± 0.90	3 ± 0.30	14.20 ± 0.30	4 ± 0.30	21.40 ± 0.30	5 ± 0.30	27.30±0.20	6 ± 0.30	32.10 ± 0.20	7 ± 0.30	35.30 ± 0.20	8 ± 0.30	41.70 ± 0.00	9 ± 0.30
VTS	10.10± 0.20	4 ± 0.30	16.00± 0.10	5 ± 0.30	23.40± 0.20	6 ± 0.30	29.40± 0.20	7 ± 0.30	34.20± 0.50	8 ± 0.30	40.30± 0.80	9 ± 0.30	45.00± 0.50	10 ± 0.30
NTS	9.50± 0.40	4 ± 0.30	16.20± 0.80	5 ± 0.30	21.70± 0.80	6 ± 0.30	28.50± 0.20	7 ± 0.30	33.40± 0.10	8 ± 0.30	38.20± 0.07	9 ± 0.30	44.20± 0.70	10 ± 0.30
BVNTS	14.00± 0.70	5 ± 0.30	21.00± 0.08	6 ± 0.30	26.90± 0.90	7 ± 0.30	33.50± 0.01	8 ± 0.60	40.20± 0.50	10 ± 0.30	45.30± 0.90	12 ± 0.30	49.10± 0.10	15 ± 0.60
BNTS	10.50± 0.05	4 ± 0.30	16.50± 0.70	5 ± 0.30	23.80± 0.20	7 ± 0.30	30.70± 0.90	8 ± 0.30	34.10± 0.80	9 ± 0.30	39.20± 0.20	11 ± 0.30	44.20± 0.20	13 ± 0.30
BVTS	11.20± 0.20	4 ± 0.30	17.00± 0.10	5 ± 0.30	23.20± 0.60	8 ± 0.30	30.00± 0.20	9 ± 0.30	35.90± 0.10	10± 0.30	40.30± 0.20	12 ± 0.30	45.60± 0.20	14 ± 1.20
BTS	10.70± 0.10	4 ± 0.30	16.20± 0.10	5 ± 1.20	21.40± 0.70	6 ± 0.30	26.00± 0.60	7 ± 0.30	31.00± 0.20	8 ± 0.30	37.30± 0.60	9 ± 0.30	41.10± 0.30	11 ± 0.30

*PH= Plant height in (cm), $^{\#}$NL= Number of leaves

7.4 Characterization of novel form–stable PCM–biochar composite

7.4.1 Surface morphology and BET analysis of the composite

The surface morphology structure of WH550 and WH–PCM biomaterial are shown in Figure 7.7. The average pore size of WH550 is 11.92 nm (BET analysis discussed in chapter three of this thesis, which confirms that WH550 has a mesoporous (2–50 nm) surface structure. The BET analysis results of various biochar used in the other reported literature are mentioned in Table E2 in appendix E. The small pores on biochar surface are obtained because of dehydration from the cell structure at a temperature of 550°C. The abundance of wide pore size distribution, i.e., the mesoporous structure, is suitable for the absorption of melting PCM during the phase change cycle. Figure 7.7(b) shows that the PCM is almost homogeneously dispersed on the honeycomb–like surface of biochar. After solidification of the composite, the shape remains. After solidification of the composite, the shape remains stable without any seepage of melted paraffin because the dispersion provides mechanical strength to the whole bio composite.

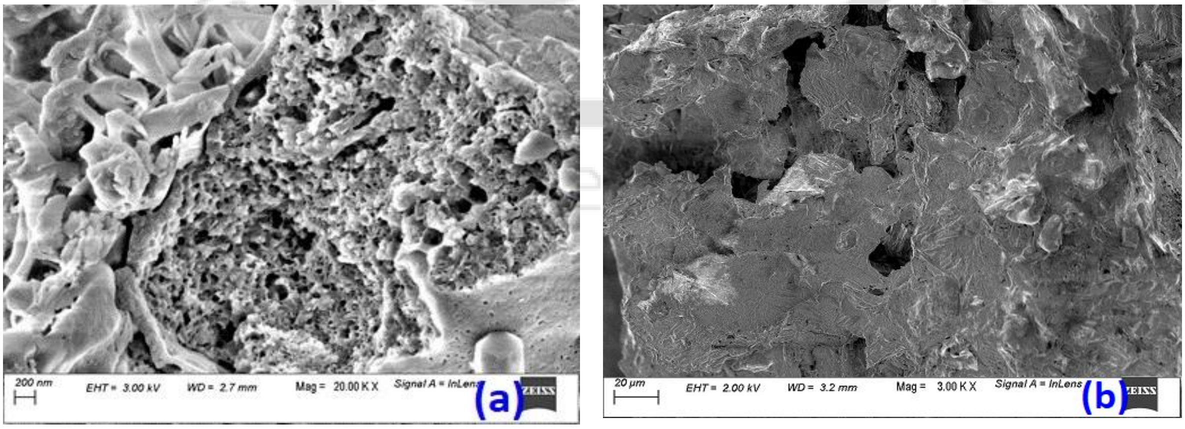

Figure 7.7 SEM images (a)WH550 (b) PCM–WH composite

A comprehensive BET analyses of adsorption–desorption isotherms using N_2 were conducted to determine the textural properties of biochar. The quantity of the adsorbed gas increased exhibiting a hysteresis curve in a wide range of relative pressure. The highest gas volume adsorbed was observed at ($P/P^O = 0.96$) from the adsorption isotherm Figure 7.8 therefore, showing the existence of large pores in the structure of the biochar.

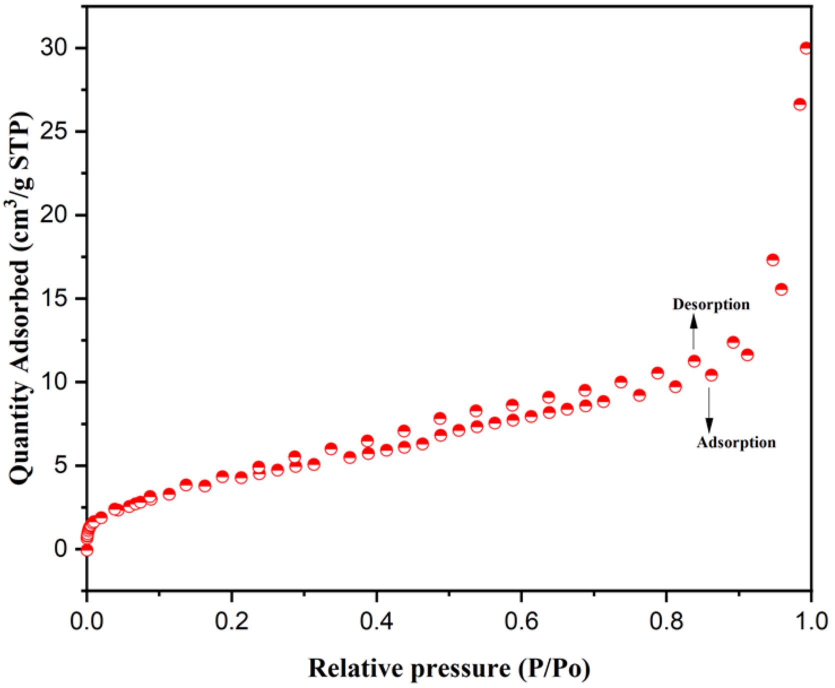

Figure 7.8 Nitrogen Adsorption – Desorption Isotherms of WH– 550 biochar

7.4.2 FTIR analysis

The FTIR spectral analysis of biochar, PCM and novel composite are shown in Figure 7.9. The FTIR spectra of the composite material comprise all characteristic transmittance bands of its pure constituents, which lie within the same range. It was observed from Figure some slight shift in the wavenumbers of the spectra for the composite material compared to pure PCM. For example, asymmetric stretching vibration of bending vibration bands detected at 2848 cm^{-1} shifted to 2859 cm^{-1}. This shift might be attributed to the weak physical attractions caused by surface tension and capillary forces present in the material. Comparing the three spectral, no new bands were identified in the spectral of the composite material. This showed that no chemical interactions happened amongst the constituents during preparation and after the formation of the composite. From the FTIR results, it can be inferred that there is a good physicochemical affinity among the raw materials used for the preparation of the composite [223].

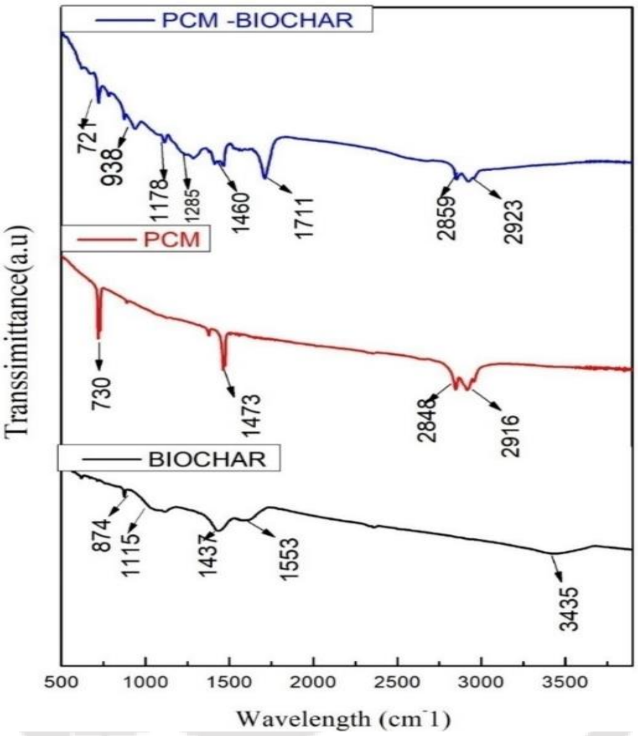

Figure 7.9 FTIR comparison curve for biochar, PCM and composite

7.4.3 XRD analysis

The XRD diffractogram of the PCM and composite are shown in Figure 7.10. It was observed that the sharp peaks were between 20–25^o in Figure 11 for PCM pointing out that PCM has a good crystallization. The only visible difference is that the intensities of the composite material at the peak points are lower than that of the PCM. The justification for this result can be stated as the influence of biochar pores, which limits some crystal formation in the composite. A similar trend in the XRD pattern confirms that the crystal structure of PCM can be held by the biochar matrix, and no chemical reaction happens during the composite formation [224].

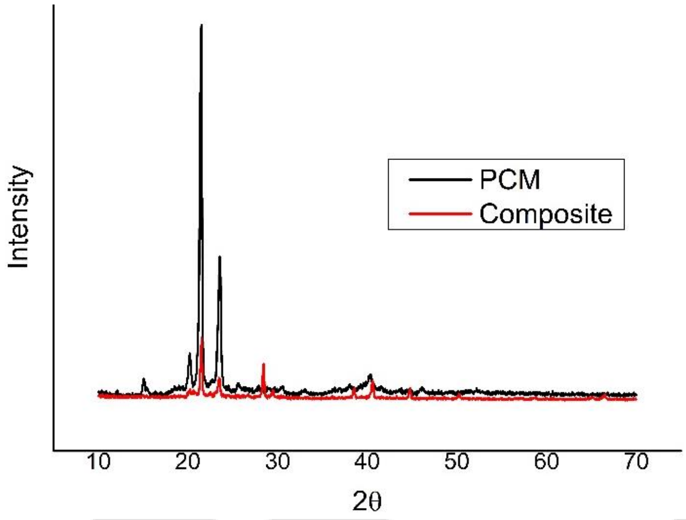

Figure 7.10 XRD comparison curve for PCM and composite

7.4.4. Thermal stability of the composite

Figure 7.11 (a) and (b) shows the TGA and DTG curves of the PCM and composite material. The thermal stability of PCMs is one of the important criteria to determine its applications in thermal energy storage (TES). It could be observed that PCM had a single step degradation that starts approximately at 128°C and full degradation of the sample took place at 252°C. The maximum degradation temperature required for the PCM is 240°C, which was depicted by the sharp peak on the DTG curve. The TGA curve showed that the mass of the prepared composite did not decrease until the temperature exceeded 128°C; this indicates that the composite has a good thermal stability. Additionally, PCM had approximately 99.1% of the weight of loss, whereas the composite had 63.84%. The values obtained are less are lower than PCM because of the existence of surface tension and capillary and forces in the materials used to prepare the composite. The presence of these forces not only assists in shaping the composite but also increases the thermal stability of the material [225,226].

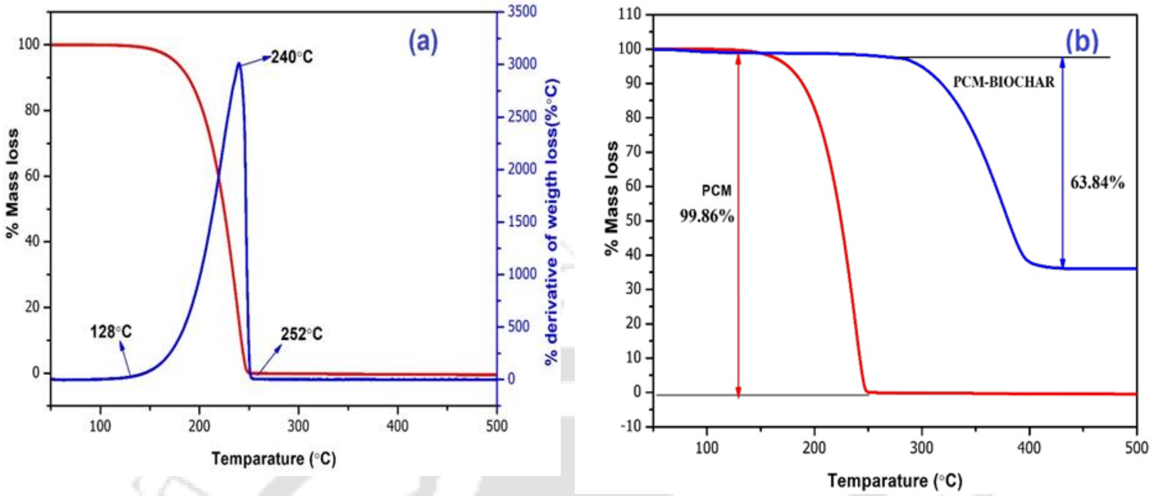

Figure 7.11(a) TGA; (b) DTG curves for the composite

7.4.5. Melting point and heat of fusion

The DSC results of the PCM–biochar composite is shown in Figure 7.12. The melting temperature of the composite is found to be 31.49°C, which is slightly lower than that of pure PCM. This is due to the reduction in the crystal nucleus with the addition of biochar. The heat of fusion calculated from the Figure 7.12 was found to be 78.12 J/g. This is lower than that of pure PCM. This is due to the difference in the specific heat of PCM, and biochar is high; thus, the overall thermal absorbance of the composite decreases. The other reason attributed to the lower heat of fusion is the homogeneity of the distribution of biochar in the composite [227].

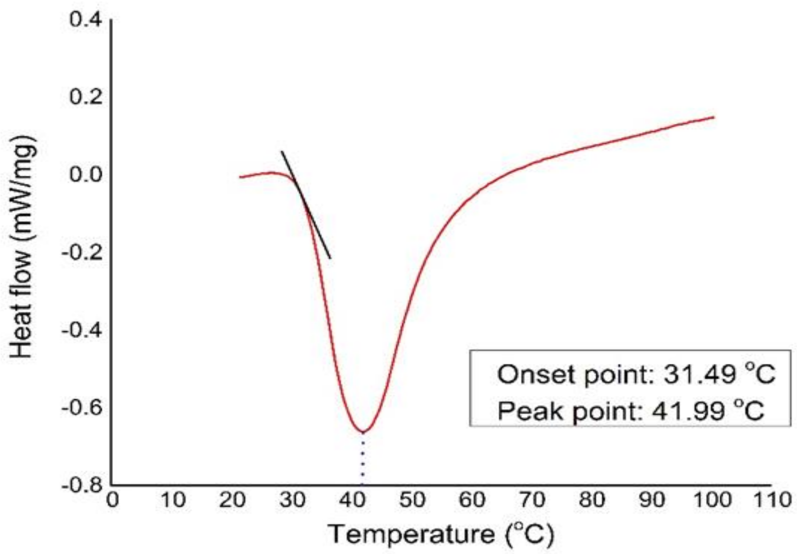

Figure 7.12 DSC curve for the composite

7.4.5 Thermal conductivity

The thermal conductivity of PCM, novel composite material and the composite material with metal powder are shown in Table 7.6. The thermal conductivity of the PCM is enhanced up to 1.5 times with the addition of water hyacinth biochar as a supporting matrix. The reason behind this enhancement is because of the filling of PCM material into the pores of water hyacinth. Thus the resistance offered by air pores has been reduced, and the thermal conductivity increases. Also, the addition of biochar increases the amount of carbon in the composite material. The addition of Aluminum metal powder (5% by weight) to the composite. further increases the thermal conductivity by 1.66 times higher than that of PCM alone. The microscopic view of metal powder is shown in Figure 7.13.

It could be observed that particles are not of any regular shape, but the size is in the micrometer range. This is because of the high thermal conductivity range of metal powder. The metal powder acts as the bridge for thermal flow between adjacent biochar particles. Thermal effusivity is a property of PCM material to exchange heat with its surroundings. Higher the thermal effusivity of PCM more is the rate of absorbance and release of thermal energy. The reason is that as the thermal effusivity increases, the material can store more thermal load during a dynamic thermal process [228].

Table 7.6 Thermal conductivity result of PCM and composite material

Material	Thermal conductivity (W/mK)
Pure PCM (Paraffin Wax)	0.18 ±0.0109
New composite material	0.271 ±0.009
Composite material with metal powder	0.302 ±0.009

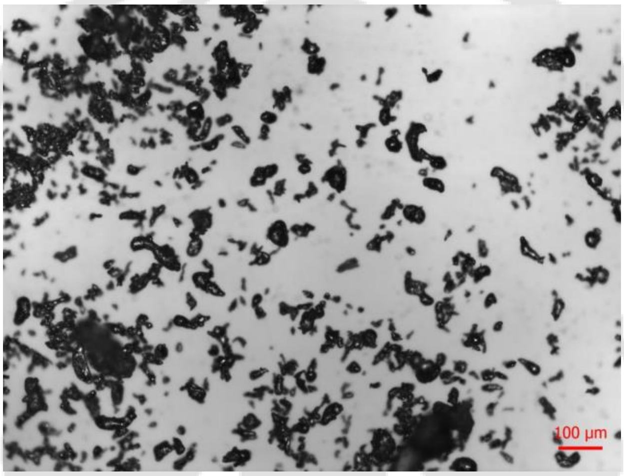

Figure 7. 13 Microscopic view of the metal powder added to the biocomposite

7.5 Application of the novel composite material

7.5.1 Estimation of surface temperature

The surface temperature of the PV/T system and the PV system at 12:00 hr, 12:30 hr and 13:00 hr, respectively are shown in Table 7.7. It could be observed from Figure 7.14 that the surface temperature of PV/T was significantly lower than that of PV. The average surface temperature of the PV is found to be 43.1°C at 12:00 hr, whereas, in the case of the PV/T system, the temperature is 30.6°C (a reduction of 12.5°C) under the same conditions. The reduction in the surface temperature at 12:30 hr and 13:00 hr is calculated to be 12.2°C and 8°C, respectively. A maximum reduction of 29% in the surface temperature of the PV/T as compared to PV has been observed using the form stable PCM–biochar composite. This reduction results in an 18.4% improvement in electrical output.

The average temperature of the modules found to decrease with the decrease in solar irradiance. One of the important heat sources in the PV is the Ohmic heat generation [229], the intensity of this source is directly dependent on the solar radiation; thus the intensity of the solar radiation is the key parameter which influences the PV temperature. An interesting observation that can be drawn from all the figures is that the use of PCM–biochar composite successfully maintained the surface temperature of PV/T below its melting point. The insertion of the PCM–biochar composite to the PV/T is useful to check the maximum working temperatures within a safe limit, thus acting as a protection for the PV module from overheating and helps to enhance the lifespan of the system.

Table 7.7 Temperature of the collectors

Time	PV			PV/T		
	Maximum (°C)	Minimum(°C)	Average(°C)	Maximum(°C)	Minimum(°C)	Average(°C)
12:00 hr	44.9	35.8	43.1	35	28.1	30.6
12:30 hr	43.4	37.3	41.2	31.9	27.2	29
13:00 hr	39.2	32.8	36.8	31.4	26.8	28.8

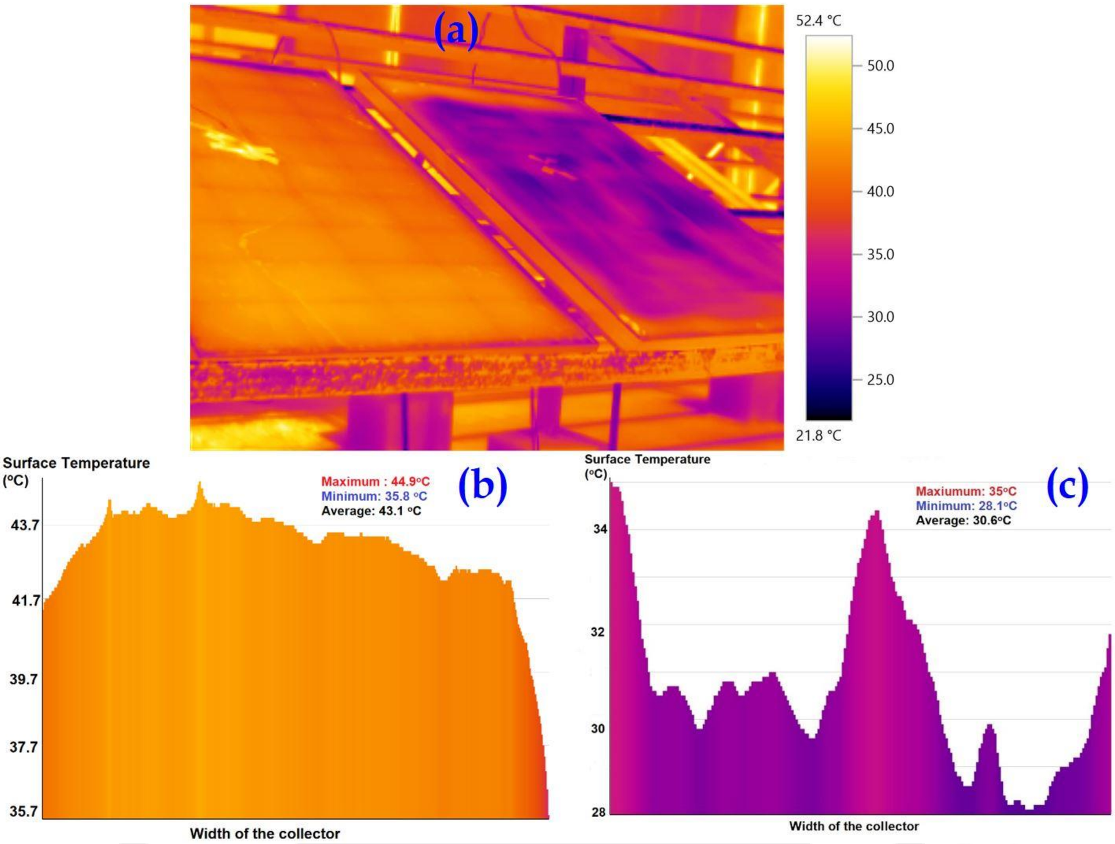

Figure 7.14 At 12:00 hr: (a)Temperature profile of the collectors ;(b) Temperature variation across the width of the PV; (c) Temperature variation across the width of the PV/T

7.5.2 Electrical output evaluation

The most important parameter to study in PV/T system is the electrical output since this is high–grade energy as compared to low–temperature heat that is collected from solar collectors. The variation of electrical power output throughout the day is illustrated in Figure 7.15. It could be observed that electrical output followed a similar trend like that of solar irradiance. It initially keeps on increasing till the solar noon and then start descending. The electrical output is found to be higher for the PV/T system as compared to the PV throughout the day. It could be observed that the difference in electrical output between PV/T and PV is more during the peak hours of the day. This difference is found to be a maximum of 18 W at 13:00 hr. The difference in the electrical output between the two collectors decreases as the irradiance reduces. This is due to a reduction in the intensity of solar radiation towards the latter half of the day; the temperature difference between the surfaces of the PV in the two collectors keeps on decreasing. The electrical output varies from 46.6 W at 10:00 hr and reaches the maximum of 86.2 W at 11:30 hr when the corresponding solar irradiance is 954.9 W/m^2.

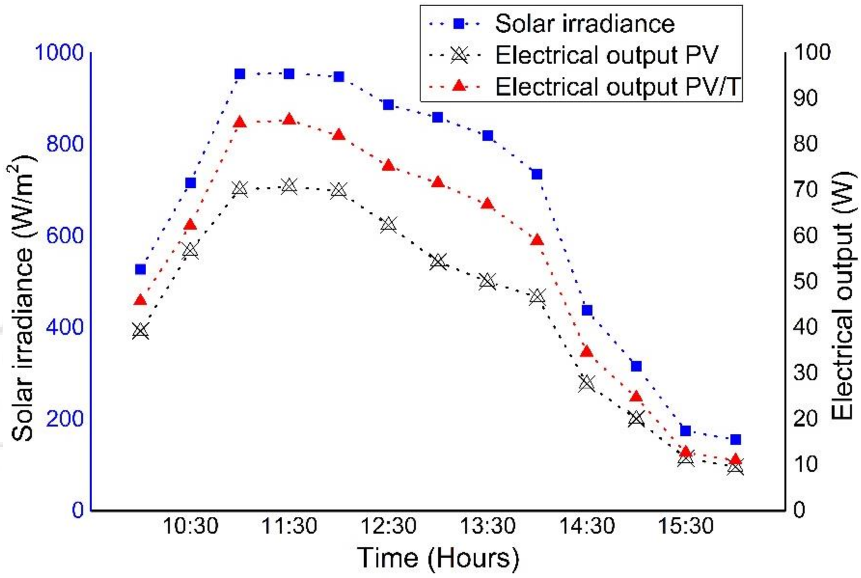

Figure 7.15 Electrical output for PV/T with PCM–biochar composite and PV

The variation of electrical efficiency for PV and PV/T system is shown in Figure 7.16. The electrical efficiency is mainly dependent on the solar irradiance and operating temperature. A decrease in the electrical efficiency of the PV module without cooling is observed between 11:30 hr to 13:30 hr; during this period, the solar irradiance is higher in the day and the PV surface temperature remains above 50°C, the temperature has been reported to affect the electrical conversion efficiency negatively. The electrical efficiency for the PV/T with thermal regulation through the use of PCM–biochar composite observed to be unaffected during peak sunshine hours. Even during the peak hours of the day temperature of the PV surface in the PV/T system remains between 42.6 and 45.4°C. The electrical efficiency for PV/T at 10:00 hr is 13.1%, which increases to 13.47% at 11:30 hr and slowly decreases and reaches a minimum value of 11.3%.

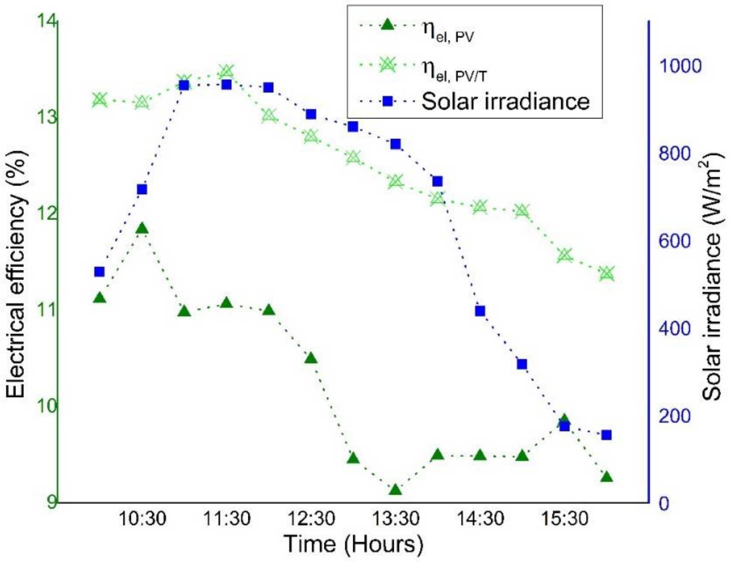

Figure 7.16 Electrical efficiency variation

7.5.3 Thermal output evaluation

The application of the form–stable PCM–biochar composite has successfully regulated the thermal output of the PV/T system as shown in Figure 7.17. After the solar radiation drops, the thermal efficiency drops and remains closer to 50%, whereas, without PCM, it drops to 38 %. The slight decrease could be attributed to the release of stored energy in the PCM layer once the thermal energy supplies reduced. The thermal efficiency for the PV/T with PCM found varying from 60.3% to a maximum of 71.2%, as shown in Figure 7.18. Though the addition of PCM did not affect the thermal efficiency significantly in the peak hours, it caused improvements in a better distribution of the heat produced during the day, thus increasing the average thermal efficiency over the day [230]. Most of the households remain unoccupied during daytime working hours when the water temperature was at its highest. The PV/T system with energy storage material has the potential to shift the time of availability of thermal energy. The thermal energy during peak sunlight hours can be stored and discharged to the water at a later time.

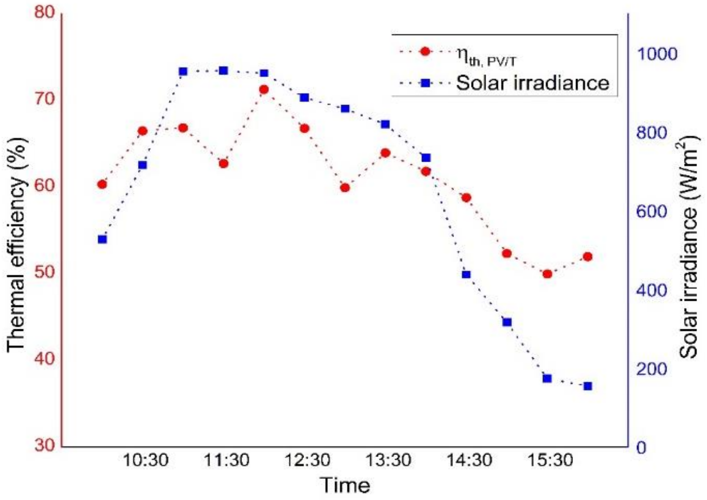

Figure 7.17 Thermal efficiency variation

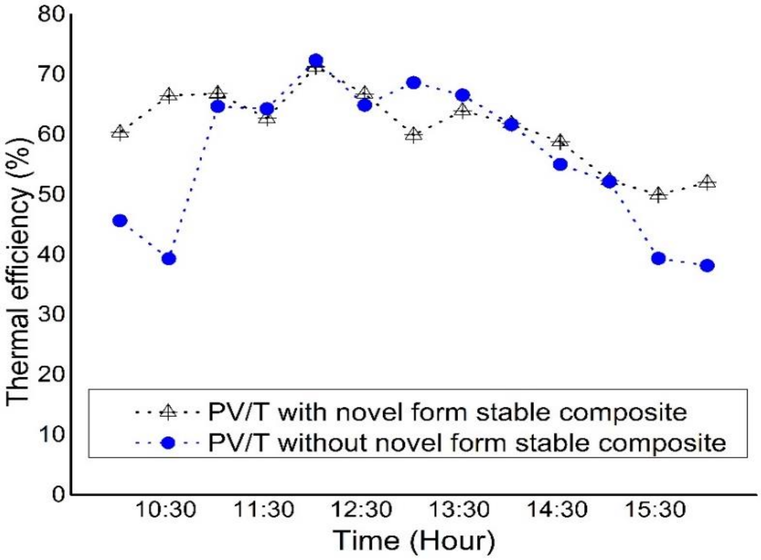

Figure 7.18 The thermal efficiency of PV/T with and without PCM

7.6 Summary

This chapter presented applications of biochar in agronomy and engineering. The pot experiments showed that application of biochar with vermicompost and fertilizers yielded better growth response on maize plant as compared to controls where NPK fertilizers and vermicompost were added individually. Higher porosity and surface area of the biochar enhances the uptake of minerals through roots hence increasing the availability of nutrients for the plant hence improving the growth of plants. The chemical properties of the composite remain the same as the pure PCM; this confirms no chemical interaction between the PCM and biochar. The heat of fusion is calculated to be 78 J/g. The thermal conductivity of the PCM is enhanced up to 1.55 times with the addition of water hyacinth biochar as a supporting matrix. The addition of aluminium metal powder further increases the thermal conductivity by 1.66 times higher than that of PCM alone. The charging–discharging time is also evaluated experimentally and results are found to be satisfactory. The use of PCM–biochar found to provide a satisfactory cooling effect. A reduction of 29% in the surface temperature of the PV/T is observed as compared to PV when composite material is applied. This reduction in temperature results in an 18.4% improvement in electrical output. This confirms the application of the PCM–biochar composite in the PV/T is useful to control the maximum working temperatures of PV cells within a safe limit, thus acting as a protection for the PV module from overheating, which leads to an augmentation of the lifespan of the system. Furthermore, the use of the composite material results in a reduction of hotspots by providing uniform distribution of the heat below the PV surface. The average electrical and thermal efficiency of the PV/T is found to be 12.6 ± 5.04% and 60.3 ± 5.48%, respectively.

CHAPTER 8–Conclusions and scope for future work

In the present study characterization and kinetic analysis of three biomass viz. water hyacinth, Thevetia peruviana and sugarcane bagasse and their blends (binary and ternary) have been carried out. TGA data was analysed using conventional methods viz. OFW, KAS and Friedman and advanced methods DAEM and Vyazovyzkin_AIC to determine kinetics parameters of raw biomass and their blends. The dominant reaction mechanism of pyrolysis and co–pyrolysis at different stages of conversions was deduced using Criado master plots. Pot experiments were carried out in a greenhouse to investigate the growth response of maize after adding various biochar produced from WH, SCB and TP with vermicompost and urea. For energy applications a novel PCM–water hyacinth biochar composite was produced and embedded on photovoltaic/Thermal (PV/T) collector to investigate its influence on the surface temperature of the solar collector. Biomass blends (WH111) and raw biomass of (WH, SCB and TP) were co–pyrolyzed in a fixed bed reactor at optimum conditions. RSM was used for experimental design to optimize the parameters that influence co–pyrolysis parameters by investigating the interactions of three factors viz. temperature, heating rate and residence time on the yield and higher heating value of biochar from a ternary blend of biomass (WH111).

8.1 Contributions of present work

Co–pyrolysis has emerged as a promising technology to utilize various biomass in a bio–refinery for production of fuel and chemicals for developing economies like India, Kenya etc. Given its potential for decentralised power plants where biomass is readily available there an urgent need to investigate biomass such as grasses and invasive weeds that have not been explored as possible sources of bioenergy. Processing of biomass blends is a significant challenge due to significant variations in the structural compositions and physicochemical properties of the individual biomass. There could be several synergistic interactions between the individual biomass as they undergo physical, chemical or biological changes during the process. Identification of these synergistic effects is also crucial for proper design and optimization of the processes based on biomass blends. In this essence this thesis work was undertaken. The key findings are summarized in the following subsections.

In **Chapter 3** we have reported the physico–chemical characterization and pyrolysis kinetics of three biomass materials, viz. WH, SCB and TP. The TGA data was analysed using four isoconversional models, viz. Friedman, KAS, OFW, and Vyazovkin_AIC at three heating rates 10, 15 and 30 ºC/min. Characterization showed that all biomass were potential candidates for pyrolysis due to high contents of volatile matter (74.02–79.07%), low moisture and ash content in the range of 6.85–9.04% and 2.11–4.82% respectively. The features and properties of the biomass used in this study are comparable with other biomass reported in open literature thus making them potential candidates for pyrolysis All biomass had high heating value in the range of 15.45–20.41 MJ kg^{-1}. From the thermal analysis the maximum temperature of decomposition (T_{max}) for TP (309°C), was relatively low followed by WH (317°C), while SCB had the highest T_{max} of 335°C. The shift of T_{max} in the DTG curves could be attributed to the difference in structural composition of individual biomass. The activation energies calculated from the slope of the kinetic plots and those calculated using the Vyazovkin_AIC model for WH, TP, and SCB were in the range of 187.74–329.71, 182.28–389.24, and 191.33–293.49 kJ mol^{-1}, respectively. From the Criado master plot, it could be observed that pyrolysis of each biomass involves two consecutive reactions. WH and TP indicated the pyrolysis mechanism of three–dimensional heat diffusion (D3) in the conversion range $\alpha \leq 0.6$, and 3rd–ordered reaction (F3) at $\alpha \geq 0.6$. SCB exhibited the mechanism of two–dimensional diffusion (D2) in the range $\alpha \leq 0.6$, and after $\alpha \geq 0.6$ showed better correlations were seen with both 2nd and 3rd–order (F2 and F3). The high values of pre–exponential factor for WH, SCB, and TP were in the range of

$2.88 \times 10^{18} - 4.40 \times 10^{33}$ s^{-1}, $34 \times 10^{18} - 1.47 \times 10^{27}$ s^{-1}, and $2.88 \times 10^{18} - 4.40 \times 10^{33}$ s^{-1}, respectively.

In **chapter 4** we have addressed the matter of synthesis of biochar from various biomass with the aim of assessing the effect of process parameters on pyrolysis. Biochar properties were investigated as function of temperature and type of feedstock for their application in agronomy and energy. Results of the physico–chemical characterization of biochar produced showed that properties of biochar are not only a function of composition of original feedstock but also the pyrolysis temperature. The porous surface morphology, higher AC, high BET surface area, high thermal stability and low bulk density, alkalinity and low atomic ratios are the crucial properties that determine the suitability of the biochar in agronomy. The above properties enhanced with the temperature of pyrolysis. However, the yield of biochar reduced with temperature. Thus, optimization of the pyrolysis temperature is an important issue in biochar synthesis. All biochar can be used as an additive in agronomy as additional carbon source, increasing the mineral content of soil and the pH. These biochar also prevent uptake of organic contaminants and heavy metals present in soil by the plant roots. High carbon content, and high CV, in addition to low MC makes the biochar a solid fuel at par with lignite coal. Porosity of the biochar provides supporting matrix for PCM, which assists manufacture of form–stable material for thermal energy storage – especially in solar thermal energy. By virtue of enhanced surface area, WH derived biochar can be used as supporting matrix for synthesis of form–stable bio–composites.

Chapter 5 presented the potential of utilizing biomass blends by carrying a comprehensive characterization, kinetic and thermodynamic analysis of binary and ternary blends. The study revealed that biomass blends are potential feedstock for bioenergy. It was observed that MC of the blends were in a range of 7.52–8.92 wt %, which made them suitable for co–pyrolysis. The volatile matter content of the binary and ternary blends was more than 75%, and thus, these blends were ideal feedstock for co–pyrolysis for obtaining bio–oil. Significant variations in activation energies and pre–exponential factors were seen with conversion levels. This clearly represents complex chemistry of thermal conversion with reactions of widely varying kinetic character occurring at different stages of conversion. Despite these variations, the reaction mechanism of thermal conversion for all blends was rather consistent: in the lower conversion range ($\alpha \leq 0.25$), the reaction mechanism was ordered reaction (F1), while in higher conversion range ($\alpha = 0.35$–0.55), all blends followed diffusion (D1 or D2 or D3) mechanism. ΔH, ΔS and ΔG values for all blends were positive, indicating endothermic and non–spontaneous nature of co–pyrolysis. ΔH and ΔS showed significant variation with conversion levels.

In **chapter 6** the co–pyrolysis of ternary blend obtained from biomass viz. water hyacinth, Thevetia peruviana and sugarcane bagasse was carried out in a fixed bed reactor. The optimum process conditions were determined using response surface methodology (RSM). The analysis of variance showed that temperature and heating rate had the significant effect on biochar yield than residence time while temperature and residence time significantly affected the HHV than heating rate. The optimum conditions for co–pyrolysis based on two responses viz. yield and higher heating value were obtained at temperature 368°C, heating rate 16.33°C/min and residence time 61min. The synthesized biochar obtained at optimum conditions was characterized using standard techniques to determine synergistic interactions. Biochar obtained from co–pyrolysis at optimum conditions had improved properties viz. high carbon content 58.74%, high heating value 23.47 MJ/kg, high BET surface area 5.681m^2/g and low moisture content and ash content of 2.07% and 6.12% respectively compared to biochar produced from native biomass. Optimization and characterization demonstrated that co–pyrolysis of biomass blends presents a possible method to produce biochar that can be applied in energy and agronomy.

Chapter 7 has shown the viability of using biochar in agronomy and engineering applications. The pot experiments showed that application of biochar with vermicompost and fertilizers yielded better growth response on maize plant as compared to control where NPK fertilizers and vermicompost were added individually. Higher porosity and surface area of the biochar enhances the uptake of minerals through roots hence increasing the availability of nutrients for the plant hence improving the growth of plants. The chemical properties of the composite remain the same as the pure PCM; this confirms no chemical interaction between the PCM and biochar. The heat of fusion is calculated to be 78 J/g. The thermal conductivity of the PCM is enhanced up to 1.55 times with the addition of water hyacinth biochar as a supporting matrix. The addition of aluminium metal powder further increases the thermal conductivity by 1.66 times higher than that of PCM alone. The charging–discharging time is also evaluated experimentally and results are found to be satisfactory. The use of PCM–biochar found to provide a satisfactory cooling effect. A reduction of 29% in the surface temperature of the PV/T is observed as compared to PV when composite material is applied. This reduction in temperature results in an 18.4% improvement in electrical output. This confirms the application of the PCM–biochar composite in the PV/T is useful to control the maximum working temperatures of PV cells within a safe limit, thus acting as a protection for the PV module from overheating, which leads to an augmentation of the lifespan of the system. Furthermore, the use of the composite material results in a reduction of hotspots by providing uniform distribution of the heat below the PV surface. The average electrical and thermal efficiency of the PV/T is found to be 12.6 ± 5.04% and 60.3 ± 5.48%, respectively.

8.2 Scope of future work

In this study pyrolysis and co–pyrolysis on raw and biomass blends were carried out in a fixed bed reactor at different conditions to determine the effect of pyrolysis conditions viz.

temperature heating rate and residence mainly on biochar. The research findings have been discussed in the preceding chapters of this thesis. However, there is a lot of scopes for further research which are listed below:

- ✓ The co–pyrolysis of biomass blends using catalyst could be investigated to enhance the bio–oil quality by reducing the oxygenic compounds.
- ✓ In the present study the pyrolysis and co–pyrolysis experiments were carried out in a lab scale experimental set up. These experiments could be scaled up by developing small scale portable setups for rural areas where various biomass are readily available.
- ✓ Investigate various agricultural applications on biochar produced from co–pyrolysis of different feedstock
- ✓ Explore on using microwave assisted co–pyrolysis on different feedstock owing to selective heating, effective heat transfer, its ability to handle high moisture feedstocks, and lower energy required.
- ✓ Further studies are also required to investigate the stability of bio–oil produced from co–pyrolysis to show it viability of being utilized for biofuel production in future.

References

[1] U.S. Energy Information Administration. Annual Energy Outlook 2019 with projections to 2050. 2019.

[2] Kumar, A., Kumar, N., Baredar, P., & Shukla, A. (2015). A review on biomass energy resources, potential, conversion and policy in India. Renew Sustain Energy Rev 2015;45:530–9. https://doi.org/10.1016/j.rser.2015.02.007.

[3] Kan, T., Strezov, V., & Evans, T. J. (2016). Lignocellulosic biomass pyrolysis: A review of product properties and effects of pyrolysis parameters. Renew Sustain Energy Rev, 57, 1126-1140. https://doi.org/10.1016/j.rser.2015.12.185.

[4] Saldarriaga, J. F., Aguado, R., Pablos, A., Amutio, M., Olazar, M., & Bilbao, J. (2015). Fast characterization of biomass fuels by thermogravimetric analysis (TGA). Fuel, 140, 744-751. https://doi.org/10.1016/j.fuel.2014.10.024.

[5] Mane, S. D. (2016). Cogeneration in Indian sugar industry: a review. Int. J. Sci. Eng. Appl. Sci, 2, 30-40.

[6] De Bhowmick, G., Sarmah, A. K., & Sen, R. (2018). Production and characterization of a value added biochar mix using seaweed, rice husk and pine sawdust: a parametric study. J Clean Prod 2018;200:641–656. https://doi.org/10.1016/j.jclepro.2018.08.002.

[7] Corton, J., Donnison, I.S., Patel, M., Bühle, L., Hodgson, E., Wachendorf, M., Bridgwater, A., Allison, G. and Fraser, M.D., (2016). Expanding the biomass resource: sustainable oil production via fast pyrolysis of low input high diversity biomass and the potential integration of thermochemical and biological conversion routes. Appl Energy 2016:852–862. https://doi.org/10.1016/j.apenergy.2016.05.088.

[8] Cai, J., He, Y., Yu, X., Banks, S. W., Yang, Y., Zhang, X., ... & Bridgwater, A. V. (2017). Review of physicochemical properties and analytical characterization of lignocellulosic biomass. Renew Sustain Energy Rev;76:309–322. https://doi.org/10.1016/j.rser.2017.03.072.

[9] Czernik, S., & Bridgwater, A. V. (2004). Overview of applications of biomass fast pyrolysis oil. Energy & fuels, 18(2), 590-598. Energy and Fuels 2004. https://doi.org/10.1021/ef034067u.

[10] Bridgwater, A. V. (2012). Review of fast pyrolysis of biomass and product upgrading. Biomass and bioenergy, 38, 68-94. Biomass and Bioenergy. https://doi.org/10.1016/j.biombioe.2011.01.048.

[11] Nanda, S., Dalai, A. K., Berruti, F., & Kozinski, J. A. (2016). Biochar as an exceptional bioresource for energy, agronomy, carbon sequestration, activated carbon and specialty materials. Waste and Biomass Valorization, 7(2), 201-235. https://doi.org/10.1007/s12649-015-9459-z.

[12] Sahoo, K., Bilek, E., Bergman, R., & Mani, S. (2019). Techno-economic analysis of producing solid biofuels and biochar from forest residues using portable systems. Applied Energy, 235, 578-590. https://doi.org/10.1016/j.apenergy

[13] Collard, F. X., & Blin, J. (2014). A review on pyrolysis of biomass constituents: Mechanisms and composition of the products obtained from the conversion of cellulose, hemicelluloses and lignin. Renew Sustain Energy Rev 2016:594–608. https://doi.org/10.1016/j.rser.2014.06.013

[14] Uzoejinwa, B. B., He, X., Wang, S., Abomohra, A. E. F., Hu, Y., & Wang, Q. (2018). Co-pyrolysis of biomass and waste plastics as a thermochemical conversion

technology for high-grade biofuel production: Recent progress and future directions elsewhere worldwide. Energy Convers Manag 2018;163:468–492. https://doi.org/10.1016/j.enconman.2018.02.004.

[15] Kelkar, S., Li, Z., Bovee, J., Thelen, K. D., Kriegel, R. M., & Saffron, C. M. (2014). Pyrolysis of North-American grass species: effect of feedstock composition and taxonomy on pyrolysis products. biomass and bioenergy, 64, 152-161. https://doi.org/10.1016/j.biombioe.2014.03.032.

[16] Mohan, D., Pittman Jr, C. U., & Steele, P. H. (2006). Pyrolysis of wood/biomass for bio-oil: a critical review. Energy & fuels, 20(3), 848-889. https://doi.org/10.1021/ef0502397.

[17] Purohit, P., & Michaelowa, A. (2007). CDM potential of bagasse cogeneration in India. Energy policy, 35(10), 4779-4798. Energy Policy https://doi.org/10.1016/j.enpol.2007.03.029.

[18] Parikh, J. (2011). Hardships and health impacts on women due to traditional cooking fuels: A case study of Himachal Pradesh, India. Energy Policy;39:7587–94. https://doi.org/10.1016/j.enpol.2011.05.055.

[19] Kiplagat, J. K., Wang, R. Z., & Li, T. X. (2011). Renewable energy in Kenya: Resource potential and status of exploitation. Renew Sustain Energy Rev. https://doi.org/10.1016/j.rser.2011.03.023.

[20] Mostafazadeh, A. K., Solomatnikova, O., Drogui, P., & Tyagi, R. D. (2018). A review of recent research and developments in fast pyrolysis and bio-oil upgrading. Biomass Conversion and Biorefinery, 8(3), 739-773..

[21] Imran, A., Bramer, E. A., Seshan, K., & Brem, G. (2016). Catalytic flash pyrolysis of

biomass using different types of zeolite and online vapor fractionation. Energies, 9(3), 187. https://doi.org/10.3390/en9030187.

[22] Savou, V., Grause, G., Kumagai, S., Saito, Y., Kameda, T., & Yoshioka, T. (2019). Pyrolysis of sugarcane bagasse pretreated with sulfuric acid. J Energy Inst, 92(4), 1149-1157. https://doi.org/10.1016/j.joei.2018.06.003.

[23] Zhang, X., Lei, H., Chen, S., & Wu, J. (2016). Catalytic co-pyrolysis of lignocellulosic biomass with polymers: a critical review. Green Chem Green Chemistry, 18(15), 4145-4169. https://doi.org/10.1039/c6gc00911e.

[24] Zhao, S. X., Ta, N., & Wang, X. D. (2017). Effect of temperature on the structural and physicochemical properties of biochar with apple tree branches as feedstock material. Energies, 10(9), 1293. https://doi.org/10.3390/en10091293.

[25] Wang, S., Dai, G., Yang, H., & Luo, Z. (2017). Lignocellulosic biomass pyrolysis mechanism: a state-of-the-art review. Prog Energy Combust Sci, 62, 33-86. https://doi.org/10.1016/j.pecs.2017.05.004.

[26] Isikgor, F. H., & Becer, C. R. (2015). Lignocellulosic biomass: a sustainable platform for the production of bio-based chemicals and polymers. Polymer Chem, 6(25), 4497-4559. https://doi.org/10.1039/c5py00263j.

[27] Zhao, C., Jiang, E., & Chen, A. (2017). Volatile production from pyrolysis of cellulose, hemicellulose and lignin. J Energy Inst, 90(6), 902-913. https://doi.org/10.1016/j.joei.2016.08.004.

[28] Alam, M., Bhavanam, A., Jana, A., & Peela, N. R. (2020). Co-pyrolysis of bamboo sawdust and plastic: Synergistic effects and kinetics. Renewable Energy, 149, 1133-1145. https://doi.org/10.1016/j.renene.2019.10.103.

[29] Chen, X., Liu, L., Zhang, L., Zhao, Y., & Qiu, P. (2019). Pyrolysis Characteristics and Kinetics of Coal–Biomass Blends during Co-Pyrolysis. Energy & Fuels, 33(2), 1267-1278. https://doi.org/10.1021/acs.energyfuels.8b03987.

[30] Chen, J., Liu, C., Wu, S., Liang, J., & Lei, M. (2016). Enhancing the quality of bio-oil from catalytic pyrolysis of kraft black liquor lignin. RSC Adv, 6(109), 107970-107976. 2016. https://doi.org/10.1039/c6ra18923g.

[31] Hemavathy, R. V., Kumar, P. S., Kanmani, K., & Jahnavi, N. (2020). Adsorptive separation of Cu (II) ions from aqueous medium using thermally/chemically treated Cassia fistula based biochar. J Clean Prod , 249, 119390. https://doi.org/10.1016/j.jclepro.2019.119390.

[32] Askeland, M., Clarke, B., & Paz-Ferreiro, J. (2019). Comparative characterization of biochars produced at three selected pyrolysis temperatures from common woody and herbaceous waste streams. PeerJ, 7, e6784. https://doi.org/10.7717/peerj.6784.

[33] Domingues, R. R., Trugilho, P. F., Silva, C. A., Melo, I. C. N. D., Melo, L. C., Magriotis, Z. M., & Sanchez-Monedero, M. A. (2017). Properties of biochar derived from wood and high-nutrient biomasses with the aim of agronomic and environmental benefits. PloS one, 12(5), e0176884. https://doi.org/https://doi.org/10.1371/journal.pone.

[34] Li, F., Shen, K., Long, X., Wen, J., Xie, X., Zeng, X., ... & Zhong, R. (2016). Preparation and characterization of biochars from Eichornia crassipes for cadmium removal in aqueous solutions. PloS one, 11(2), e0148132.. https://doi.org/10.1371/journal.pone.0148132.

[35] Jindo, K., Mizumoto, H., Sawada, Y., Sanchez-Monedero, M. A., & Sonoki, T. (2014).

Physical and chemical characterization of biochars derived from different agricultural residues. Biogeosciences, 11(23), 6613-6621. https://doi.org/10.5194/bg-11-6613-2014.

[36] Wang, Y., Wu, Q., Duan, D., Ruan, R., Liu, Y., Dai, L., ... & Yu, Z. (2018). Ex-situ catalytic upgrading of vapors from fast microwave-assisted co-pyrolysis of Chromolaena odorata and soybean soapstock. Bioresour Technol https://doi.org/10.1016/j.biortech.2018.04.042.

[37] Chen, L., Yu, Z., Liang, J., Liao, Y., & Ma, X. (2018). Co-pyrolysis of chlorella vulgaris and kitchen waste with different additives using TG-FTIR and Py-GC/MS. Energy Convers Manag, 177, 582-591. 2018;177:582–91. https://doi.org/10.1016/j.enconman.2018.10.010.

[38] Shah, S. A. Y., Zeeshan, M., Farooq, M. Z., Ahmed, N., & Iqbal, N. (2019). Co-pyrolysis of cotton stalk and waste tire with a focus on liquid yield quantity and quality. Renewable Energy, 130, 238-244 130:238–44. https://doi.org/10.1016/j.renene.2018.06.045.

[39] Hossain, M. S., Ferdous, J., Islam, M. S., Islam, M. R., Mustafi, N. N., & Haniu, H. (2019). Production of liquid fuel from co-pyrolysis of polythene waste and rice straw. Energy Procedia, 160, 116-122. https://doi.org/10.1016/j.egypro.2019.02.126.

[40] Chen, W., Li, K., Xia, M., Yang, H., Chen, Y., Chen, X., ... & Chen, H. (2018). Catalytic deoxygenation co-pyrolysis of bamboo wastes and microChlorella vulgaris with biochar catalyst. Energy, 157, 472-482. https://doi.org/10.1016/j.energy.2018.05.149.

[41] Wang, X., Zhao, B., & Yang, X. (2016). Co-pyrolysis of microChlorella vulgaris and

sewage sludge: biocrude assessment and char yield prediction. Energy Convers Manag, 117, 326-334. 2016;117:326–34. https://doi.org/10.1016/j.enconman.2016.03.013.

[42] Chen, B., Han, X., Mu, M., & Jiang, X. (2017). Studies of the co-pyrolysis of oil shale and wheat straw. *Energy & Fuels, 31*(7), 6941-6950. https://doi.org/10.1021/acs.energyfuels.7b00871.

[43] Geyer, R., Jambeck, J. R., & Law, K. L. (2017). Production, use, and fate of all plastics ever made. Science advances, 3(7), e1700782.

[44] Tang, Z., Chen, W., Chen, Y., Yang, H., & Chen, H. (2019). Co-pyrolysis of microChlorella vulgaris and plastic: Characteristics and interaction effects. Bioresour Technol,274, 145-152. https://doi.org/10.1016/j.biortech.2018.11.083.

[45] Dewangan, A., Pradhan, D., & Singh, R. K. (2016). Co-pyrolysis of sugarcane bagasse and low-density polyethylene: influence of plastic on pyrolysis product yield. Fuel, 185, 508-516. https://doi.org/10.1016/j.fuel.2016.08.011.

[46] Hassan, H., Hameed, B. H., & Lim, J. K. (2020). Co-pyrolysis of sugarcane bagasse and waste high-density polyethylene: Synergistic effect and product distributions. Energy, 191, 116545. https://doi.org/10.1016/j.energy.2019.116545.

[47] Pinto, F., Duarte, L. C., Carvalheiro, F., Paradela, F., Costa, P., Marques, J., ... & Sampaio, B. (2019). Production of liquid compounds by co-pyrolysis of different pre-treated biomasses mixed with plastic wastes. Chem Eng Trans, 76, 1393-1398. https://doi.org/10.3303/CET1976233.

[48] Izzatie, N. I., Basha, M. H., Uemura, Y., Hashim, M. S. M., Afendi, M., & Mazlan, M. A. F. (2019). Co-pyrolysis of rubberwood sawdust (RWS) and polypropylene (PP) in a

fixed bed pyrolyzer. J Mech Eng Sci, 13(1), 4636-4647. 2https://doi.org/10.15282/jmes.13.1.2019.20.0390.

[49] Ephraim, A., Minh, D. P., Lebonnois, D., Peregrina, C., Sharrock, P., & Nzihou, A. (2018). Co-pyrolysis of wood and plastics: influence of plastic type and content on product yield, gas composition and quality. Fuel, 231, 110-117. https://doi.org/10.1016/j.fuel.2018.04.140.

[50] Matsuzawa, Y., Ayabe, M., & Nishino, J. (2001). Acceleration of cellulose co-pyrolysis with polymer. Polymer degradation and stability, 71(3), 435-444. Mr 2001;71:435–44.

[51] Jeon, M. J., Choi, S. J., Yoo, K. S., Ryu, C., Park, S. H., Lee, J. M., ... & Kim, S. (2011). Copyrolysis of block polypropylene with waste wood chip. Korean J Chem Eng, 28(2), 497-501. https://doi.org/10.1007/s11814-010-0497-8.

[52] Tang, Y., Huang, Q., Sun, K., Chi, Y., & Yan, J. (2018). Co-pyrolysis characteristics and kinetic analysis of organic food waste and plastic. . Bioresour Technol, 249, 16-23. https://doi.org/10.1016/j.biortech.2017.09.210.

[53] Wang, S., Uzoejinwa, B. B., Abomohra, A. E. F., Wang, Q., He, Z., Feng, Y., ... & Hui, C. W. (2018). Characterization and pyrolysis behavior of the green microalga Micractinium conductrix grown in lab-scale tubular photobioreactor using Py-GC/MS and TGA/MS. J Anal Appl Pyrolysis J, 135, 340-349. https://doi.org/10.1016/j.jaap.2018.08.019.

[54] Fekhar, B., Miskolczi, N., Bhaskar, T., Kumar, J., & Dhyani, V. (2018, May). Co-pyrolysis of biomass and plastic wastes: investigation of apparent kinetic parameters and stability of pyrolysis oils. Int Conf Clean Green Energy I (Vol. 154, No. 1, p.

012022). https://doi.org/doi :10.1088/1755-1315/154/1/012022.

[55] Xue, Y., & Bai, X. (2018). Synergistic enhancement of product quality through fast co-pyrolysis of acid pretreated biomass and waste plastic. Energy Convers Manag, 164, 629-638. 2018;164:629–38. https://doi.org/10.1016/j.enconman.2018.03.036.

[56] Zhao, Y., Wang, Y., Duan, D., Ruan, R., Fan, L., Zhou, Y., ... & Liu, Y. (2018). Fast microwave-assisted ex-catalytic co-pyrolysis of bamboo and polypropylene for bio-oil production. Bioresour Technol 49, 69-75.

[57] Shadangi, K. P., & Mohanty, K. (2015). Co-pyrolysis of Karanja and Niger seeds with waste polystyrene to produce liquid fuel. Fuel, 153, 492-498.S. https://doi.org/http://dx.doi/org/1o.10.16j.fuel.2015.03.017.

[58] Izzatie, N. I., Basha, M. H., Uemura, Y., Mazlan, M. A., Hashim, M. S. M., Amin, N. A. M., & Hamid, M. F. (2016,). Co-pyrolysis of rice straw and polypropylene using fixed-bed pyrolyzer. IOP Conf Ser Mater Sci Eng (Vol. 160, No. 1, p. 012033). IOP Publishing. 2016;160:757–899. https://doi.org/10.1088/1757-899X/160/1/012033.

[59] Fonts, I., Gea, G., Azuara, M., Ábrego, J., & Arauzo, J. (2012). Sewage sludge pyrolysis for liquid production: a review. Renew Sustain Energy Rev, 16(5), 2781-2805. https://doi.org/10.1016/j.rser.2012.02.070.

[60] Alvarez, J., Amutio, M., Lopez, G., Barbarias, I., Bilbao, J., & Olazar, M. (2015). Sewage sludge valorization by flash pyrolysis in a conical spouted bed reactor. Chemical Engineering Journal, 273, 173-183. https://doi.org/10.1016/j.cej.2015.03.047.

[61] Syed-Hassan, S. S. A., Wang, Y., Hu, S., Su, S., & Xiang, J. (2017). Thermochemical processing of sewage sludge to energy and fuel: Fundamentals, challenges and

considerations. Renew Sustain Energy Rev, 80, 888-913. https://doi.org/10.1016/j.rser.2017.05.262.

[62] Naqvi, S. R., Hameed, Z., Tariq, R., Taqvi, S. A., Ali, I., Niazi, M. B. K., ... & Shahbaz, M. (2019). Synergistic effect on co-pyrolysis of rice husk and sewage sludge by thermal behavior, kinetics, thermodynamic parameters and artificial neural network., Waste Manag 85, 131-140. https://doi.org/10.1016/j.wasman.2018.12.031.

[63] Huang, H. J., Yang, T., Lai, F. Y., & Wu, G. Q. (2017). Co-pyrolysis of sewage sludge and sawdust/rice straw for the production of biochar. J Anal Appl Pyrolysis 125, 61-68. https://doi.org/10.1016/j.jaap.2017.04.018.

[64] Yang, Y. Q., Cui, M. H., Ren, Y. G., Guo, J. C., Zheng, Z. Y., & Liu, H. (2020). Towards understanding the mechanism of heavy metals immobilization in biochar derived from Co-pyrolysis of sawdust and sewage sludge. Bull Enviromental Contam Toxicol, 1-8.

[65] Alvarez, J., Amutio, M., Lopez, G., Bilbao, J., & Olazar, M. (2015). Fast co-pyrolysis of sewage sludge and lignocellulosic biomass in a conical spouted bed reactor. Fuel, 159, 810-818. Fuel. https://doi.org/10.1016/j.fuel.2015.07.039.

[66] Weber, K., & Quicker, P. (2018). Properties of biochar. Fuel, 217, 240-261. https://doi.org/10.1016/j.fuel.2017.12.054.

[67] Yargicoglu, E. N., Sadasivam, B. Y., Reddy, K. R., & Spokas, K. (2015). Physical and chemical characterization of waste wood derived biochars. Waste management, 36, 256-268. https://doi.org/10.5194/bg-11-6613-2014.

[68] Li, F., Shen, K., Long, X., Wen, J., Xie, X., Zeng, X., ... & Zhong, R. (2016). Preparation and characterization of biochars from Eichornia crassipes for cadmium

removal in aqueous solutions. PloS one, 11(2), e0148132. https://doi.org/10.1371/journal.pone.0148132.

[69] Figueiredo, C., Lopes, H., Coser, T., Vale, A., Busato, J., Aguiar, N., ... & Canellas, L. (2018). Influence of pyrolysis temperature on chemical and physical properties of biochar from sewage sludge. Archives of Agronomy and Soil Science, 64(6), 881-889.. https://doi.org/10.1080/03650340.2017.1407870.

[70] de Figueiredo, C. C., Chagas, J. K. M., da Silva, J., & Paz-Ferreiro, J. (2019). Short-term effects of a sewage sludge biochar amendment on total and available heavy metal content of a tropical soil. Geoderma, 344, 31-39.. https://doi.org/10.1016/j.geoderma.2019.01.052.

[71] Zhang, J., Wu, S., Xu, Z., Wang, M., Man, Y. B., Christie, P., ... & Wong, M. H. (2019). The role of sewage sludge biochar in methylmercury formation and accumulation in rice. Chemosphere, 218, 527-533. https://doi.org/10.1016/j.chemosphere.2018.11.090.

[72] Liu, Y., Ran, C., Siddiqui, A. R., Siyal, A. A., Song, Y., Dai, J., ... & Zhang, T. (2020). Characterization and analysis of sludge char prepared from bench-scale fluidized bed pyrolysis of sewage sludge. Energy, 200, 117398. https://doi.org/10.1016/j.energy.2020.117398.

[73] Yin, Q., Liu, M., & Ren, H. (2019). Biochar produced from the co-pyrolysis of sewage sludge and walnut shell for ammonium and phosphate adsorption from water. J Environ Manage, 249, 109410. 2019;249:109410. https://doi.org/10.1016/j.jenvman.2019.109410.

[74] Huang, H. J., Yang, T., Lai, F. Y., & Wu, G. Q. (2017). Co-pyrolysis of sewage sludge

and sawdust/rice straw for the production of biochar. J Anal Appl Pyrolysis, 125, 61-68. https://doi.org/10.1016/j.jaap.2017.04.018.

[75] Carvalho, W. S., Júnior, J. A. S., de Oliveira, T. J. P., & Ataíde, C. H. (2017). Fast pyrolysis of sweet sorghum bagasse in a fluidized bed reactor: Product characterization and comparison with vapors generated in analytical pyrolysis. Energy, 131, 186-197. C https://doi.org/10.1016/j.energy.2017.05.058.

[76] Biswas B, Pandey N, Bisht Y, Singh R, Kumar J, Bhaskar T. (2017) Pyrolysis of agricultural biomass residues: Comparative study of corn cob, wheat straw, rice straw and rice husk. Bioresour Technol;237:57–63. https://doi.org/10.1016/j.biortech.2017.02.046.

[77] Bordoloi N, Narzari R, Chutia RS, Bhaskar T, Kataki R. (2015) Pyrolysis of Mesua ferrea and Pongamia glabra seed cover: Characterization of bio-oil and its sub-fractions. Bioresour Technol;178:83–9. https://doi.org/10.1016/j.biortech.2014.10.079.

[78] Sohaib Q, Muhammad A, Younas M. (2017)Fast pyrolysis of sugarcane bagasse: Effect of pyrolysis conditions on final product distribution and properties. Energy Sources, Part A Recover Util Environ Eff;39:184–90. https://doi.org/10.1080/15567036.2016.1212292.

[79] Chen D, Li Y, Cen K, Luo M, Li H, Lu B.(2016) Pyrolysis polygeneration of poplar wood: Effect of heating rate and pyrolysis temperature. Bioresour Technol 2016. https://doi.org/10.1016/j.biortech.2016.07.049.

[80] Jin X, Chen Y, Deng-yin Z, Yan-hui G, Qi-min H, Yu-hong X. (2019) Co-pyrolysis of rice straw and water hyacinth : Characterization of products , yields and biomass interaction e ff ect 2019;127. https://doi.org/10.1016/j.biombioe..105281.

[81] Hua M, Li B. (2016) Co-pyrolysis characteristics of the sugarcane bagasse and Enteromorpha prolifera;120:238–46. https://doi.org/10.1016/j.enconman.2016.04.072.

[82] Zhao B, Wang X, Yang X. (2015) Co-pyrolysis characteristics of microChlorella vulgaris Isochrysis and Chlorella : Kinetics , biocrude yield and interaction. Bioresour Technol;198:332–9. https://doi.org/10.1016/j.biortech.2015.09.021.

[83] Xu S, Hu Y, Wang S, He Z, Qian L, Feng Y, (2019) Investigation on the co-pyrolysis mechanism of seaweed and rice husk with multi-method comprehensive study;132:266–77. https://doi.org/10.1016/j.renene.2018.08.002.

[84] Chen L, Yu Z, Xu H, Wan K, Liao Y, Ma X. ()2019 Microwave-assisted co-pyrolysis of Chlorella vulgaris and wood sawdust using different additives 2019;273:34–9. https://doi.org/10.1016/j.biortech.2018.10.086.

[85] Awasthi A, Singh G, Dhyani Vv, Kumar J, Reddy Yenumula S, Adarsh V .P, Puthiyamadam A, Kumar K, Sukumaran Rajeev K, Sabeela Beevi U, Dinabandhu S TB (2019). Co-pyrolysis of phumdi and para grass biomass from Loktak Lake 9;285. https://doi.org/10.1016/j.biortech.2019.03.147.

[86] Martínez, J. D., Veses, A., Mastral, A. M., Murillo, R., Navarro, M. V., Puy, N., ... & García, T. (2014). Co-pyrolysis of biomass with waste tyres: Upgrading of liquid bio-fuel, 119, 263-271. https://doi.org/10.1016/j.fuproc.2013.11.015.

[87] Sanahuja-Parejo, O., Veses, A., Navarro, M. V., López, J. M., Murillo, R., Callén, M. S., & García, T. (2018). Catalytic co-pyrolysis of grape seeds and waste tyres for the production of drop-in biofuels. Energy Convers Manag, 171, 1202-1212. 2018; https://doi.org/10.1016/j.enconman.2018.06.053.

[88] Wang, L., Chai, M., Liu, R., & Cai, J. (2018). Synergetic effects during co-pyrolysis of

biomass and waste tire: a study on product distribution and reaction kinetics. Bioresour Technol, 268, 363-370. https://doi.org/10.1016/j.biortech.2018.07.153.

[89] Yang, Z., Wu, Y., Zhang, Z., Li, H., Li, X., Egorov, R. I., ... & Gao, X. (2019). Recent advances in co-thermochemical conversions of biomass with fossil fuels focusing on the synergistic effects. Renew Sustain Energy Rev, 103, 384-398. https://doi.org/10.1016/j.rser.2018.12.047.

[90] Abnisa, F., & Daud, W. M. A. W. (2014). A review on co-pyrolysis of biomass: an optional technique to obtain a high-grade pyrolysis oil. Energy Convers Manag, 87, 71-85.. https://doi.org/10.1016/j.enconman.2014.07.007.

[91] Chen, X., Chen, Y., Chen, Z., Zhu, D., Yang, H., Liu, P., ... & Chen, H. (2018). Catalytic fast pyrolysis of cellulose to produce furan compounds with SAPO type catalysts. J Anal Appl Pyrolysis 129, 53-60. https://doi.org/10.1016/j.jaap.2017.12.004.

[92] Verma, R., Vinoda, K. S., Papireddy, M., & Gowda, A. N. S. (2016). Toxic pollutants from plastic waste-a review. Procedia Environ Sci, 35, 701-708. 2016;35:701–8. https://doi.org/10.1016/j.proenv..07.069.

[93] Godfrey L. Waste Plastic , the Challenge Facing Developing Countries — Ban It , Change It , Collect It ? 2019:2–7. https://doi.org/10.3390/recycling4010003.

[94] Alam, O., Billah, M., & Yajie, D. (2018). Characteristics of plastic bags and their potential environmental hazards. Resour Conserv Recycl, 132, 121-129.. https://doi.org/10.1016/j.resconrec.2018.01.037.

[95] Bordoloi, S., Gopal, P., Boddu, R., Wang, Q., Cheng, Y. F., Garg, A., & Sreedeep, S. (2019). Soil-biochar-water interactions: role of biochar from Eichhornia crassipes in

influencing crack propagation and suction in unsaturated soils. J Clean Prod, 210, 847-859. https://doi.org/10.1016/j.jclepro.2018.11.051.

[96] Muigai, H. H., Bordoloi, U., Hussain, R., Ravi, K., Moholkar, V. S., & Kalita, P. (2020). A comparative study on synthesis and characterization of biochars derived from lignocellulosic biomass for their candidacy in agronomy and energy applications. Int J Energy Res:1–17. https://doi.org/10.1002/er.6092.

[97] Patel S (2012). Threats, management and envisaged utilizations of aquatic weed Eichhornia crassipes: An overview. Rev Environ Sci Biotechnol;11:249–59. https://doi.org/10.1007/s11157-012-9289-4.

[98] Güereña, D., Neufeldt, H., Berazneva, J., & Duby, S. (2015). Water hyacinth control in Lake Victoria: Transforming an ecological catastrophe into economic, social, and environmental benefits. Sustain Prod Consum, 3, 59-69. https://doi.org/10.1016/j.spc.2015.06.003.

[99] Rezania, S., Ponraj, M., Din, M. F. M., Songip, A. R., Sairan, F. M., & Chelliapan, S. (2015). The diverse applications of water hyacinth with main focus on sustainable energy and production for new era: An overview. Renew Sustain Energy Rev, 41, 943-954. https://doi.org/10.1016/j.rser.2014.09.006.

[100] Heena, S., Shweta, M., Oisik, D., & Sharma, A. K. (2014). Value added properties of water hyacinth: a promising renewable source of energy. Current Trends in Biotechnology and Chemical Research, 4(1), 38-41. .

[101] Basumatary S.(2014). Yellow oleander (Thevetia peruviana) seed oil biodiesel as an alternative and renewable fuel for diesel engines: A review. Int J ChemTech Res 2014;7:2823–2840.

[102] Pavithra GS, Anusha M, Rajyalakshmi M. (2012). Effect of Thevetia peruviana extracts on in-vitro and in-vivo cultures of Parthenium hysterophorus L . J Crop Sci;3:83–86.

[103] ASTM Standard D873-82. Standard test method for bulk density of densified particulate biomass fuels ASTM International, West Conshohocken 2013;82:1–2. https://doi.org/10.1520/E0873-82R13.4.

[104] Disco Y, Mahanta P, Bora U.(2017). Comprehensive characterization of lignocellulosic biomass through proximate , ultimate and compositional analysis for bioenergy production;103:490–500. https://doi.org/10.1016/j.renene.2016.11.039.

[105] Omoniyi TE, A.O Olorunnisola.(2014). Experimental Characterisation of Bagasse Biomass Material for Energy Production. Int J Eng Technol;4:582–589.

[106] Sasmal S, Goud V V., Mohanty K.(2012). Characterization of biomasses available in the region of North-East India for production of biofuels. Biomass and Bioenergy 2012;45:212–220. https://doi.org/10.1016/j.biombioe..06.008.

[107] Abhishek S. Patnaik and Jillian L. Goldfarb. (2016). Continuous activation energy representation of the Arrhenius equation for the pyrolysis of cellulosic materials: Feed corn stover and cocoa shell biomass. Cellul Chem Technol;50:311–320.

[108] Zheng Y, Tao L, Yang X, Huang Y, Liu C, Zheng Z. (2018). Study of the thermal behavior, kinetics, and product characterization of biomass and low-density polyethylene co-pyrolysis by thermogravimetric analysis and pyrolysis-GC/MS. J Anal Appl Pyrolysis;133:185–197. https://doi.org/10.1016/j.jaap.2018.04.001.

[109] Konwar, K., Nath, H. P., Bhuyan, N., Saikia, B. K., Borah, R. C., Kalita, A. C., & Saikia, N. (2019). Effect of biomass addition on the devolatilization kinetics,

mechanisms and thermodynamics of a northeast Indian low rank sub-bituminous coal. Fuel, 256, 115926. https://doi.org/10.1016/j.fuel.2019.115926.

[110] Vyazovkin S. (1997). Advanced Isoconversional Method. J Therm Anal Calorim;49:1493–1499.

[111] Criado J. M. , J. Malek A O. (1989). Applicability of the master plots in Kinetic analysis of Non-Isothermal Data. Thermochim Acta 147:377–385.

[112] Starink M J.(2003). The determination of activation energy from linear heating rate experiments: A comparison of the accuracy of isoconversion methods. Thermochim Acta;404:163–76. https://doi.org/10.1016/S0040-6031(03)00144-148.

[113] Rezania S, Fadhil M, Fatimah S. (2016). Evaluation of water hyacinth (Eichhornia crassipes) as a potential raw material source for briquette production. Energy;111:768–73. https://doi.org/10.1016/j.energy.2016.06.026.

[114] Sohni, S., Norulaini, N. N., Hashim, R., Khan, S. B., Fadhullah, W., & Omar, A. M. (2018). Physicochemical characterization of Malaysian crop and agro-industrial biomass residues as renewable energy resources. Ind Crops Prod, 111, 642-650.. https://doi.org/10.1016/j.indcrop.2017.11.031.

[115] Dash, M., Venkata Dasu, V., & Mohanty, K. (2015). Physico-chemical characterization of Miscanthus, Castor, and Jatropha towards biofuel production. J Renew Sustain Energy, 7(4), 043124. https://doi.org/10.1063/1.4926577.

[116] Saikia, R., Chutia, R. S., Kataki, R., & Pant, K. K. (2015). Perennial grass (Arundo donax L.) as a feedstock for thermo-chemical conversion to energy and materials. Bioresour Technol 188, 265-272. https://doi.org/10.1016/j.biortech.2015.01.089.

[117] Mohammed IY, Abakr YA, Yusup S, Kazi FK. (2017). Valorization of Napier grass via intermediate pyrolysis: Optimization using response surface methodology and pyrolysis products characterization. J Clean Prod;142:1848–66. https://doi.org/10.1016/j.jclepro.2016.11.099.

[118] Wang, Z., McDonald, A. G., Westerhof, R. J., Kersten, S. R., Cuba-Torres, C. M., Ha, S., & Garcia-Perez, M. (2013). Effect of cellulose crystallinity on the formation of a liquid intermediate and on product distribution during pyrolysis. J Anal Appl Pyrolysis, 100, 56-66. https://doi.org/10.1016/j.jaap.2012.11.017.

[119] Wang, S., Dai, G., Yang, H., & Luo, Z. (2017). Lignocellulosic biomass pyrolysis mechanism: a state-of-the-art review. Prog Energy Combust Sci, 62, 33-86.. https://doi.org/10.1016/j.pecs.2017.05.004.

[120] Kim, S. S., Ly, H. V., Chun, B. H., Ko, J. H., & Kim, J. (2016). Thermogravimetric characteristics of α-cellulose and decomposition kinetics in a micro-tubing reactor. Korean J Chem Eng, 33(11), 3128-3133. https://doi.org/10.1007/s11814-016-0143-1.

[121] Wang, X., Hu, M., Hu, W., Chen, Z., Liu, S., Hu, Z., & Xiao, B. (2016). Thermogravimetric kinetic study of agricultural residue biomass pyrolysis based on combined kinetics. Bioresour Technol, 219, 510-520. https://doi.org/10.1016/j.biortech.2016.07.136.

[122] Monkhouse, P. (2011). On-line spectroscopic and spectrometric methods for the determination of metal species in industrial processes. Prog Energy Combust Sci, 37(2), 125-171. 2011;37:125–71. https://doi.org/10.1016/j.pecs.2010.05.002.

[123] Vyazovkin, S., Chrissafis, K., Di Lorenzo, M. L., Koga, N., Pijolat, M., Roduit, B., ... & Suñol, J. J. (2014). ICTAC Kinetics Committee recommendations for collecting

experimental thermal analysis data for kinetic computations. Thermochimica acta, 590, 1-23. https://doi.org/10.1016/j.tca.2014.05.036.

[124] Biney, P. O., Gyamerah, M., Shen, J., & Menezes, B. (2015). Kinetics of the pyrolysis of arundo, sawdust, corn stover and switch grass biomass by thermogravimetric analysis using a multi-stage model. Bioresource technol, 179, 113-122. https://doi.org/10.1016/j.biortech.2014.10.155.

[125] Dhaundiyal, A., Singh, S. B., Hanon, M. M., & Rawat, R. (2018). Determination of kinetic parameters for the thermal decomposition of parthenium hysterophorus. Envviromental Clim Technol, 22(1), 5-21. https://doi.org/10.1515/rtuect-2018-0001.

[126] Alves, J. L. F., da Silva, J. C. G., da Silva Filho, V. F., Alves, R. F., de Araujo Galdino, W. V., & De Sena, R. F. (2019). Kinetics and thermodynamics parameters evaluation of pyrolysis of invasive aquatic macrophytes to determine their bioenergy potentials. Biomass and bioenergy, 121, 28-40. https://doi.org/10.1016/j.biombioe.2018.12.015.

[127] Yuan X, He T, Cao H, Yuan Q. (2017). Cattle manure pyrolysis process : Kinetic and thermodynamic analysis with isoconversional methods. Renew Energy 107:489–96. https://doi.org/10.1016/j.renene.2017.02.026.

[128] Mishra RK, Mohanty K, Wang X. (2020). Pyrolysis kinetic behavior and Py-GC–MS analysis of waste dahlia flowers into renewable fuel and value-added chemicals. Fuel 260:116338. https://doi.org/10.1016/j.fuel.2019.116338.

[129] Mishra RK, Mohanty K. (2020) Kinetic analysis and pyrolysis behaviour of waste biomass towards its bioenergy potential. Bioresour Technol 311:123480. https://doi.org/10.1016/j.biortech.2020.123480.

[130] Sharma P, Pandey OP, Diwan PK. (2019). Non-isothermal kinetics of pseudo-components of waste biomass. Fuel 253:1149–1161. https://doi.org/10.1016/j.fuel.2019.05.093.

[131] Yuan J, Xu R, Zhang H. (2011). The forms of alkalis in the biochar produced from crop residues at different temperatures. Bioresour Technol102:3488–3497. https://doi.org/10.1016/j.biortech.2010.11.018.

[132] ASTM Standard E870-82. Standard Test Methods for Analysis of Wood Fuels ,Charcoal, ASTM International, West Conshohocken 2019;82:2019–20. https://doi.org/10.1520/E0870-82R19.2.

[133] Aller D, Bakshi S, Laird DA. (2017). Modified method for proximate analysis of biochars. J Anal Appl Pyrolysis 124:335–342. https://doi.org/10.1016/j.jaap.2017.01.012.

[134] ASTM Standard D3175-11. Standard Test Method for Moisture in the Analysis Sample of Coal and Coke 2015:9–12. https://doi.org/10.1520/D3173-11.2.

[135] ASTM Standard D3175-11. Standard Test Method for Volatile Matter in the Analysis Sample of Coal and Coke Charcoal, ASTM International, West Conshohocken 2015:1–6. https://doi.org/10.1520/D3175-11.2.

[136] ASTM Standard D3174-12. Standard Test Method for Ash in the Analysis Sample of Coal and Coke from Coal Charcoal, ASTM International, West Conshohocken, 2015:1–6. https://doi.org/10.1520/D3174-12.2.

[137] Liao, W., & Thomas, S. C. (2019). Biochar particle size and post-pyrolysis mechanical processing affect soil pH, water retention capacity, and plant performance. Soil Systems, 3(1), 14. L. https://doi.org/10.3390/soilsystems3010014.

[138] Munera-echeverri J L, Martinsen V, Strand L T, Zivanovic V, Cornelissen G MJ.(2018). Cation exchange capacity of biochar : An urgent method modification. Sci Total Environ 642:190–197. https://doi.org/10.1016/j.scitotenv.2018.06.017.

[139] Behera SK, Chakraborty S, Meikap BC. (2017). Chemical demineralization of high ash Indian coal by using alkali and acid solutions. Fuel 196:102–109. https://doi.org/10.1016/j.fuel.2017.01.088.

[140] Hytönen, J., & Nurmi, J. (2015). Heating value and ash content of intensively managed stands. Wood research, 60(1), 71-82.

[141] Kim D, Yoshikawa K, Park KY. (2015). Characteristics of Biochar Obtained by Hydrothermal Carbonization of Cellulose for Renewable Energy 2015:14040–14048. https://doi.org/10.3390/en81212412.

[142] Han, T. U., Kim, Y. M., Siddiqui, M. Z., Lee, T., Watanabe, A., Teramae, N., ... & Park, Y. K. (2018). Non-isothermal pyrolysis properties of Laminaria japonica. J Anal Appl Pyrolysis, 130, 277-284. https://doi.org/10.1016/j.jaap.2017.12.021.

[143] Zhang F, Wang X, Xionghui J. Efficient arsenate removal by magnetite-modified water hyacinth 2016;216. https://doi.org/10.1016/j.envpol.2016.06.013.

[144] Zhang, F., Wang, X., Xionghui, J., & Ma, L. (2016). Efficient arsenate removal by magnetite-modified water hyacinth biochar. Environmental Pollution, Sci Total Environ 216, 575-583. https://doi.org/10.1016/j.scitotenv.2017.05.203.

[145] Guo X, Liu H, Zhang J. (2020). The role of biochar in organic waste composting and soil improvement : A review. Waste Manag 2020;102:884–899. https://doi.org/10.1016/j.wasman.2019.12.003.

[146] Sun, Y., Gao, B., Yao, Y., Fang, J., Zhang, M., Zhou, Y., ... & Yang, L. (2014). Effects of feedstock type, production method, and pyrolysis temperature on biochar and hydrochar properties. Chem Eng J , 240, 574-578. https://doi.org/10.1016/j.cej.2013.10.081.

[147] Khalid, S., Shahid, M., Murtaza, B., Bibi, I., Naeem, M. A., & Niazi, N. K. (2020). A critical review of different factors governing the fate of pesticides in soil under biochar application. Sci Total Environ, 711, 134645. 2020;711:134645. https://doi.org/10.1016/j.scitotenv.2019.134645.

[148] Chen, Y., Cui, Z., Ding, H., Wan, Y., Tang, Z., & Gao, J. (2018). Cost-effective biochar produced from agricultural residues and its application for preparation of high performance form-stable phase change material via simple method. Intern journal of molecular scies, 19(10), 3055. https://doi.org/10.3390/ijms19103055.

[149] Das, D., Bordoloi, U., Muigai, H. H., & Kalita, P. (2020). A novel form stable PCM based bio composite material for solar thermal energy storage applications. Journal of Energy Storage, 30, 101403. https://doi.org/10.1016/j.est.2020.101403.

[150] Zeidabadi, Z. A., Bakhtiari, S., Abbaslou, H., & Ghanizadeh, A. R. (2018). Synthesis, characterization and evaluation of biochar from agricultural waste biomass for use in building materials. Constr Build Mater, 181, 301-308.. https://doi.org/10.1016/j.conbuildmat.2018.05.271.

[151] Pariyar, P., Kumari, K., Jain, M. K., & Jadhao, P. S. (2020). Evaluation of change in biochar properties derived from different feedstock and pyrolysis temperature for environmental and agricultural application. Sci Total Environ, 713, 136433.P. 2020;713:136433. https://doi.org/10.1016/j.scitotenv.2019.136433.

[152] Chen, H., Ma, J., Wei, J., Gong, X., Yu, X., Guo, H., & Zhao, Y. (2018). Biochar increases plant growth and alters microbial communities via regulating the moisture and temperature of green roof substrates. Sci Total Environ, 635, 333-342.. https://doi.org/10.1016/j.scitotenv.2018.04.127.

[153] Zhou, Y., Zhang, H., Cai, L., Guo, J., Wang, Y., Ji, L., & Song, W. (2018). Preparation and characterization of macroChlorella vulgaris biochar nanomaterials with highly efficient adsorption and photodegradation ability. Materials, 11(9), 1709. https://doi.org/10.3390/ma11091709.

[154] Das O, Sarmah AK, Bhattacharyya D. A novel approach in organic waste utilization through biochar addition in wood / polypropylene composites. Waste Manag 2015;38:132–40. https://doi.org/10.1016/j.wasman.2015.01.015.

[155] Zhao, B., O'Connor, D., Zhang, J., Peng, T., Shen, Z., Tsang, D. C., & Hou, D. (2018). Effect of pyrolysis temperature, heating rate, and residence time on rapeseed stem derived biochar. J Clean Prod, 174, 977-987. https://doi.org/10.1016/j.jclepro.2017.11.013.

[156] Cantrell, K. B., Hunt, P. G., Uchimiya, M., Novak, J. M., & Ro, K. S. (2012). Impact of pyrolysis temperature and manure source on physicochemical characteristics of biochar. Bioresour Technol, 107, 419-428. https://doi.org/10.1016/j.biortech.2011.11.084.

[157] Uchimiya, M., Wartelle, L. H., Klasson, K. T., Fortier, C. A., & Lima, I. M. (2011). Influence of pyrolysis temperature on biochar property and function as a heavy metal sorbent in soil. J Agric Food Chem, 59(6), 2501-2510. https://doi.org/10.1021/jf104206c.

[158] Wilson, F., Tremain, P., & Moghtaderi, B. (2018). Characterization of biochars derived from pyrolysis of biomass and calcium oxide mixtures. Energy & Fuels, 32(4), 4167-4177. Energy & Fuels https://doi.org/10.1021/acs.energyfuels.7b03221.

[159] Yang, X., Igalavithana, A. D., Oh, S. E., Nam, H., Zhang, M., Wang, C. H., ... & Ok, Y. S. (2018). Characterization of bioenergy biochar and its utilization for metal/metalloid immobilization in contaminated soil. Sci Total Environ, 640, 704-713. https://doi.org/10.1016/j.scitotenv.2018.05.298.

[160] Billa, S. F., Angwafo, T. E., & Ngome, A. F. (2019). Agro-environmental characterization of biochar issued from crop wastes in the humid forest zone of Cameroon. Int J Recycl Org Waste Agri, 8(1), 1-13. https://doi.org/10.1007/s40093-018-0223-9.

[161] Kim, S. S., Kang, Y. S., Lee, H. D., Kim, J. K., & Hong, S. C. (2012). Physicochemical properties of chars at different treatment temperatures. Journal of the Air & Waste Management Association, 62(2), 235-241. https:/doi 10.1007/s11356-015-5063-9

[162] Rao Z, Zhang G, Xu T, Hong K.(2018). Solar Energy Materials and Solar Cells Experimental study on a novel form-stable phase change materials based on diatomite for solar energy storage. Sol Energy Mater Sol Cells 182:52–60. https://doi.org/10.1016/j.solmat.2018.03.016.

[163] Gondek, K., Mierzwa-Hersztek, M., Kopeć, M., Sikora, J., Głąb, T., & Szczurowska, K. (2019). Influence of biochar application on reduced acidification of sandy soil, increased cation exchange capacity, and the content of available forms of K, Mg, and P. Pol. J. Environ. Stud, 28(1), 1-9. https://doi.org/10.15244/pjoes/81688.

[164] Aboulkas, A., Hammani, H., El Achaby, M., Bilal, E., & Barakat, A. (2017). Valorization of algal waste via pyrolysis in a fixed-bed reactor: production and characterization of bio-oil and bio-char. Bioresour Technol, 243, 400-408. https://doi.org/10.1016/j.biortech.2017.06.098.

[165] Gunamantha IM, Widana GAB. (2018). Characterization the potential of biochar from cow and pig manure for geoecology application. IOP Conf Ser Earth Environ Sci 2018;131. https://doi.org/10.1088/1755-1315/131/1/012055.

[166] Oh TK, Choi B, Shinogi Y, Chikushi J. (2012). Characterization of biochar derived from three types of biomass. J Fac Agric Kyushu Univ;57:61–76.

[167] Bera T, Patra TJPAK, Datta SC. (2018). Comparative analysis of physicochemical , nutrient , and spectral properties of agricultural residue biochars as influenced by pyrolysis temperatures. J Mater Cycles Waste Manag 20:1115–1127. https://doi.org/10.1007/s10163-017-0675-4.

[168] Dupont C, Campargue M, Ratel G. (2019). Physicochemical Approach To Blend Biomass Franc o 2019. https://doi.org/10.1021/acs.energyfuels.8b04169.

[169] Singh, Y. D. (2019). Comprehensive characterization of indigenous lignocellulosic biomass from Northeast India for biofuel production. SN Applied Sciences, 1(5), 1-12. https://doi.org/10.1007/s42452-019-0453-0

[170] Cai, J., Wu, W., Liu, R., & Huber, G. W. (2013). A distributed activation energy model for the pyrolysis of lignocellulosic biomass. Green Chem, 15(5), 1331-1340. 2013;15:1331–40. https://doi.org/10.1039/c3gc36958g.

[171] Saikia, R., Baruah, B., Kalita, D., Pant, K. K., Gogoi, N., & Kataki, R. (2018). Pyrolysis and kinetic analyses of a perennial grass (Saccharum ravannae L.) from

north-east India: optimization through response surface methodology and product characterization. Bioresour Technol, 253, 304-314.S. 2018;253:304–14. https://doi.org/10.1016/j.biortech.2018.01.054.

[172] Xu D, Chai M, Dong Z, Rahman M, Yu X, Cai J. (2018). Kinetic compensation effect in logistic distributed activation energy model for lignocellulosic biomass pyrolysis;265:139–145. https://doi.org/10.1016/j.biortech.2018.05.092.

[173] A. S. Patnaik and J. L. Goldfarb. (2016). Continuous activation energy representation of the Arrhenius equation for the pyrolysis of cellulosic materials: Feed corn stover and cocoa shell biomass. Cellul Chem Technol;50:311–20.

[174] Mishra G, Bhaskar T.(2014) Non isothermal model free kinetics for pyrolysis of rice straw. Bioresour Technol;169:614–621. https://doi.org/10.1016/j.biortech.2014.07.045.

[175] Mallick, D., Poddar, M. K., Mahanta, P., & Moholkar, V. S. (2018). Discernment of synergism in pyrolysis of biomass blends using thermogravimetric analysis. Bioresour Technol, 261, 294-305.. https://doi.org/10.1016/j.biortech.2018.04.011.

[176] Huang, J., Liu, J., Chen, J., Xie, W., Kuo, J., Lu, X., ... & Evrendilek, F. (2018). Combustion behaviors of spent mushroom substrate using TG-MS and TG-FTIR: thermal conversion, kinetic, thermodynamic and emission analyses. Bioresour Technol. 266, 389-397. https://doi.org/10.1016/j.biortech.2018.06.106.

[177] Bhagavatula A, Shah N, Honaker R. (2016). Estimating the Pyrolysis Kinetic Parameters of Coal , Biomass , and Their Blends : A Comparative Study 2016. https://doi.org/10.1021/acs.energyfuels.5b00692.

[178] Chen, G., He, S., Cheng, Z., Guan, Y., Yan, B., Ma, W., & Leung, D. Y. (2017). Comparison of kinetic analysis methods in thermal decomposition of cattle manure by

themogravimetric analysis. Bioresour Technol. 243, 69-77. . https://doi.org/10.1016/j.biortech.2017.06.007.

[179] Miura K. (1995) A New and Simple Method to Estimate f \ E) and ko (E) in the Distributed Activation Energy Model from Three 302–307. https://doi.org/10.1021/ef00050a014.

[180] Miura K, Maki T. (1998). A Simple Method for Estimating f(E) and k0(E)inthe Distributed Activation Energy Model Kouichi;0:864–9. https://doi.org/10.1021/ef970212q.

[181] J.M.Criado.(1978). Kinetic analysis of DTG data from master curves. Thermochim Acta 24:0–3.

[182] Dhyani, V., & Bhaskar, T. (2018). Kinetic analysis of biomass pyrolysis. In Waste Biorefinery (pp. 39-83). https://doi.org/10.1016/B978-0-444-63992-9.00002-1.

[183] Dhyani, V., Kumar, J., & Bhaskar, T. (2017). Thermal decomposition kinetics of sorghum straw via thermogravimetric analysis. Bioresour Technol 245, 1122-1129. https://doi.org/10.1016/j.biortech.2017.08.189.

[184] Mishra RK, Mohanty K. (2018). Characterization of non-edible lignocellulosic biomass in terms of their candidacy towards alternative renewable fuels:799–812.

[185] Sasmal S, Goud V V., Mohanty K. (2012). Characterization of biomasses available in the region of North-East India for production of biofuels. Biomass and Bioenergy 2012;45:212–20. https://doi.org/10.1016/j.biombioe.06.008.

[186] Salema Arshad Adam, Man Ryan, Ting Wai SYK. Pyrolysis of blend (oil palm biomass and sawdust) biomass using TG-MS. Bioresour Technol 2020;274:439–46.

https://doi.org/10.1016/j.biortech.2018.12.014.

[187] Wang, S., Hu, Y., Uzoejinwa, B. B., Cao, B., He, Z., Wang, Q., & Xu, S. (2017). Pyrolysis mechanisms of typical seaweed polysaccharides. J Anal Appl Pyrolysis 124, 373-383.. https://doi.org/10.1016/j.jaap.2016.12.005.

[188] Huang H, Liu J, Liu H, Evrendilek F, Buyukada M. (2020). Pyrolysis of water hyacinth biomass parts : Bioenergy , gas emissions , and by- products using TG-FTIR and Py-GC / MS analyses. Energy Convers Manag;207:112552. https://doi.org/10.1016/j.enconman.2020.112552.

[189] Wu, K., Liu, J., Wu, Y., Chen, Y., Li, Q., Xiao, X., & Yang, M. (2014). Pyrolysis characteristics and kinetics of aquatic biomass using thermogravimetric analyzer. Bioresour Technol, 163, 18-25. https://doi.org/10.1016/j.biortech.2014.03.162.

[190] Rodilla I, Contreras ML, Bahillo A. (2017). Thermogravimetric and mass spectrometric (TG-MS) analysis of sub- bituminous coal-energy crops blends in N 2 , air and CO 2 / O 2 atmospheres. Fuel 2018;215:506–14. https://doi.org/10.1016/j.fuel.2017.09.102.

[191] Baruah B, Tiwari P, Thakur P, Kataki R.(2018). TGA-FTIR analysis of Upper Assam oil shale, optimization of lab-scale pyrolysis process parameters using RSM. J Anal Appl Pyrolysis 2018;135:397–405. https://doi.org/10.1016/j.jaap.2018.08.005.

[192] Tahir, M. H., Zhao, Z., Ren, J., Rasool, T., & Naqvi, S. R. (2019). Thermo-kinetics and gaseous product analysis of banana peel pyrolysis for its bioenergy potential. Biomass and Bioenergy, 122, 193-201. https://doi.org/10.1016/j.biombioe.2019.01.009.

[193] Ashraf A, Sattar H, Munir S, Husk R. (2019). A comparative applicability study of

model-fitting and model-free kinetic analysis approaches to non-isothermal pyrolysis of coal and agricultural residues. Fuel 2019;240:326–33. https://doi.org/10.1016/j.fuel.2018.11.149.

[194] da Silva, J. C. G., Andersen, S. L. F., Costa, R. L., Moreira, R. D. F. P. M., & José, H. J. (2019). Bioenergetic potential of Ponkan peel waste (Citrus reticulata) pyrolysis by kinetic modelling and product characterization. Biomass and Bioenergy, 131, 105401. https://doi.org/https://doi.org/10.1016/j.biombioe.2019.105401.

[195] Rasam, S., Haghighi, A. M., Azizi, K., Soria-Verdugo, A., & Moraveji, M. K. (2020). Thermal behavior, thermodynamics and kinetics of co-pyrolysis of binary and ternary mixtures of biomass through thermogravimetric analysis. Fuel, 280, 118665. https://doi.org/10.1016/j.fuel.2020.118665.

[196] Luo, L., Guo, X., Zhang, Z., Chai, M., Rahman, M. M., Zhang, X., & Cai, J. (2020). Insight into pyrolysis kinetics of lignocellulosic biomass: isoconversional kinetic analysis by the modified Friedman method. Energy & Fuels, 34(4), 4874-4881.. https://doi.org/10.1021/acs.energyfuels.0c00275.

[197] Zheng C. (2019). Mechanism and kinetics of thermal degradation of insulating materials developed from cellulose fiber and fire retardants. J Therm Anal Calorim 135:3015–27. https://doi.org/10.1007/s10973-018-7564-5.

[198] Ahmad, M. S., Mehmood, M. A., Al Ayed, O. S., Ye, G., Luo, H., Ibrahim, M., ... & Qadir, G. (2017). Kinetic analyses and pyrolytic behavior of Para grass (Urochloa mutica) for its bioenergy potential. 224, 708-713. https://doi.org/10.1016/j.biortech.2016.10.090.

[199] Bezerra, M. A., Santelli, R. E., Oliveira, E. P., Villar, L. S., & Escaleira, L. A. (2008).

Response surface methodology (RSM) as a tool for optimization in analytical chemistry. Talanta, 76(5), 965-977. Talanta https://doi.org/10.1016/j.talanta.2008.05.019.

[200] García, R., Pizarro, C., Lavín, A. G., & Bueno, J. L. (2012). Characterization of Spanish biomass wastes for energy use. Bioresour Technol. 103(1), 249-258. https://doi.org/10.1016/j.biortech.2011.10.004.

[201] Ioelovich, M. (2015). Recent findings and the energetic potential of plant biomass as a renewable source of biofuels–a review. Bioresources, 10(1), 1879-1914.

[202] Mishra RK, Mohanty K. (2018). Characterization of non-edible lignocellulosic biomass in terms of their candidacy towards alternative renewable fuels. Biomass Convers Biorefinery 2018;8:799–812. https://doi.org/10.1007/s13399-018-0332-8.

[203] Muigai, H. H., Choudhury, B. J., Kalita, P., & Moholkar, V. S. (2021). Physico–chemical characterization and pyrolysis kinetics of Eichhornia Crassipes, Thevetia Peruviana, and Saccharum Officinarum. Fuel, 289, 119949.. https://doi.org/10.1016/j.fuel.2020.119949.

[204] Muigai, H. H., Choudhury, B. J., Kalita, P., & Moholkar, V. S. (2020). Co–pyrolysis of biomass blends: Characterization, kinetic and thermodynamic analysis. Biomass and Bioenergy, 143, 105839. https://doi.org/10.1016/j.biombioe.2020.105839.

[205] Singh, R. K., Shrivastava, D. K., Sarkar, A., & Chakraborty, J. P. (2020). Co-pyrolysis of eucalyptus and sodium polyacrylate: optimization and synergistic effect. Fuel, 277, 118115. https://doi.org/10.1016/j.fuel.2020.118115.

[206] Singh, R. K., Chakraborty, J. P., & Sarkar, A. (2020). Optimizing the torrefaction of pigeon pea stalk (cajanus cajan) using response surface methodology (RSM) and

characterization of solid, liquid and gaseous products. Renew Energy, 155, 677-690. https://doi.org/10.1016/j.renene.2020.03.184.

[207] Idris R, Tung C, Asik JA, Nasir F. (2020). Optimization studies of microwave-induced co-pyrolysis of empty fruit bunches / waste truck tire using response surface methodology. J Clean Prod 2020;244:118649. https://doi.org/10.1016/j.jclepro.2019.118649.

[208] Kılıç, M., Pütün, E., & Pütün, A. E. (2014). Optimization of Euphorbia rigida fast pyrolysis conditions by using response surface methodology. J Anal Appl Pyrolysis s, 110, 163-171. 2014;110:163–71. https://doi.org/10.1016/j.jaap.2014.08.018.

[209] Md A. Hossain, P. Ganesan, J. Jewaratnam KC. (2017). Optimization of process parameters for microwave pyrolysis of oil palm fiber (OPF) for hydrogen and biochar production. Energy Convers Manag133:349–62. https://doi.org/10.1016/j.enconman.2016.10.046.

[210] Yargicoglu, E. N., Sadasivam, B. Y., Reddy, K. R., & Spokas, K. (2015). Physical and chemical characterization of waste wood derived biochars. Waste Manag, 36, 256-268. https://doi.org/10.1016/j.wasman.2014.10.029.

[211] Tan, X. F., Liu, S. B., Liu, Y. G., Gu, Y. L., Zeng, G. M., Hu, X. J., ... & Jiang, L. H. (2017). Biochar as potential sustainable precursors for activated carbon production: multiple applications in environmental protection and energy storage. Bioresour Technol, 227, 359-372. https://doi.org/10.1016/j.biortech.2016.12.083.

[212] Gunamantha, I. M., & Widana, G. A. B. (2018, March). Characterization the potential of biochar from cow and pig manure for geoecology application. In IOP Conference Series: Earth and Environmental Science (Vol. 131, No. 1, p. 012055). IOP Publishing.

https://doi :10.1088/1755-1315/131/1/012055.

[213] Filiberto DM, Gaunt JL. (2013). Practicality of Biochar Additions to Enhance Soil and Crop Productivity 2013:715–25. https://doi.org/10.3390/agriculture3040715.

[214] Pickering, C., Rossi, S. D., Hernando, A., & Barros, A. (2018). Current knowledge and future research directions for the monitoring and management of visitors in recreational and protected areas. Environ Int, 21, 10-18. https://doi.org/10.1016/j.envint.2015.10.018.

[215] Drissi, S., Ling, T. C., & Mo, K. H. (2020). Thermal performance of a solar energy storage concrete panel incorporating phase change material aggregates developed for thermal regulation in buildings. Renewable Energy, 160, 817-829. https://doi.org/10.1016/j.renene.2020.06.076

[216] Inaba H, Tu P. (1997). Evaluation of thermophysical characteristics on shape-stabilized paraffin as a solid-liquid phase change material. Heat Mass Transf Und Stoffuebertragung 1997;32:307–12. https://doi.org/10.1007/s002310050126.

[217] Hong Y, Xin-shi G. (2000). Preparation of polyethylene-paraffin compound as a form-stable solid-liquid phase change material. Sol Energy Mater Sol Cells 2000;64:37–44. https://doi.org/10.1016/S0927-0248(00)00041-6.

[218] Wan, Y. C., Chen, Y., Cui, Z. X., Ding, H., Gao, S. F., Han, Z., & Gao, J. K. (2019). A promising form-stable phase change material prepared using cost effective pinecone biochar as the matrix of palmitic acid for thermal energy storage. Sci Rep 9(1), 1-10. https://doi.org/10.1038/s41598-019-47877-z.

[219] Pimenta, A. S., de Oliveira Miranda, N., de Carvalho, M. A. B., da Silva, G. G. C., & Oliveira, E. M. M. (2019). Effects of biochar addition on chemical properties of a

sandy soil from northeast Brazil. Arabian Journal of Geosciences, 12(3), 70.

[220] Mensah AK. (2018). Biochar and / or Compost Applications Improve Soil Properties , Growth , and Yield of Maize Grown in Acidic Rainforest and Coastal Savannah Soils in Ghana

[221] Świątek J, Spitzer T, Grobelak A, Kacprzak M. (2019). Effects of Biochar Addition on Vermicomposting of Food Industry Sewage Sludge 20:36–45.

[222] Pandit R. Naba, Jan Mulder, Hale S. Elizabeth, Vegard Martinsen, Schmidt P. Hans GC (2018). Biochar improves maize growth by alleviation of nutrient stress in a moderately acidic low-input Nepalese soil. Sci Total Environ 2018;625:1380–1389. https://doi.org/10.1016/j.scitotenv.2018.01.022.

[223] Ma, L., Guo, C., Ou, R., Sun, L., Wang, Q., & Li, L. (2018). Preparation and characterization of modified porous wood flour/lauric-myristic acid eutectic mixture as a form-stable phase change material. Energy & Fuels, 32(4), 5453-5461. https://doi.org/10.1021/acs.energyfuels.7b03933.

[224] Belessiotis, G. V., Papadokostaki, K. G., Favvas, E. P., Efthimiadou, E. K., & Karellas, S. (2018). Preparation and investigation of distinct and shape stable paraffin/SiO2 composite PCM nanospheres. Energy Convers Manag, 168, 382-394.. https://doi.org/10.1016/j.enconman.2018.04.059.

[225] Kenisarin MM, Kenisarina KM. (2012). Form-stable phase change materials for thermal energy storage. Renew Sustain Energy Rev 2012;16:1999–2040. https://doi.org/10.1016/j.rser..01.015.

[226] Gurmen Ozcelik T. (2017). Preparation, characterization and thermal properties of paraffin wax - Expanded perlite form-stable composites for latent heat storage. Mater

Sci;23:39–43. https://doi.org/10.5755/j01.ms.23.1.13661.

[227] Yang, X., Yuan, Y., Zhang, N., Cao, X., & Liu, C. (2014). Preparation and properties of myristic–palmitic–stearic acid/expanded graphite composites as phase change materials for energy storage. Solar Energy, 99, 259-266. https://doi.org/10.1016/j.solener.2013.11.021.

[228] Lei H, Fu C, Zou Y, Guo S, Huo J. (2019). A thermal energy storage composite with sensing function and its thermal conductivity and thermal effusivity enhancement. J Mater Chem ;7:6720–6729. https://doi.org/10.1039/c8ta11753e.

[229] Das D, Kalita P, Dewan A, (2019). Tanweer S. Development of a novel thermal model for a PV/T collector and its experimental analysis. Sol Energy 2019;188:631–643. https://doi.org/https://doi.org/10.1016/j.solener. 06.005.

[230] Das D, Bordoloi U, Dilip A, Hihu H, Krishna R, Kalita P. (2021). Performance investigation of a rectangular spiral flow PV / T collector with a novel form-stable composite material. Appl Therm Eng 2021;182:116035. https://doi.org/10.1016/j.applthermaleng.2020.116035.

APPENDICES

Appendix–A: Physico–chemical characterization and kinetics analysis of water hyacinth, *Thevetia peruviana, and sugarcane bagasse*

The theoretical master plots are obtained from Eq. (3.17) using both differential and integral forms of solid–state reaction models outlined in appendix (Table A.1). below

Table – A1 List of commonly used in solid–state reaction models

Reaction mechanism	Model	*f(α)*	*g(α)*
Reaction order models			
First order	F1	$1 - \alpha$	$-\ln(1-\alpha)$
Second order	F2	$(1-\alpha)^2$	$(1\alpha -)^{-1}1$
Third order	F3	$(1-\alpha)^3$	$(½)[(1-\alpha)^{-2} - 1]$
Nucleation models			
Power law	P2	$2\alpha^{1/1}$	$\alpha^{1/1}$
Power law	P3	$3\alpha^{2/3}$	$\alpha^{1/3}$
Power law	P4	$4\alpha^{3/4}$	$\alpha^{1/4}$
Power law	P2/3	$2/3\alpha^{-1/2}$	$\alpha^{3/2}$
Avrami– Erofeev	A2	$2(1-\alpha)[-\ln(1-\alpha)]^{1/2}$	$[-\ln(1-\alpha)]^{1/2}$
Avrami– Erofeev	A3	$3(1-\alpha)[-\ln(1-\alpha)]^{2/3}$	$[-\ln(1-\alpha)]^{1/3}$
Avrami– Erofeev	A4	$4(1-\alpha)[-\ln(1-\alpha)]^{3/4}$	$[-\ln(1-\alpha)]^{1/4}$
Diffusion models			
One –Dimensional diffusion	D1	$1/2\alpha^{-1}$	α^2
Two –Dimensional diffusion	D2	$[-\ln(1-\alpha)]^{-1}$	$-\ln(1-\alpha)^{1/2}$
Three –Dimensional diffusion	D3	$3/2(1-\alpha)^{2/3}[1-(1-\alpha)^{1/3}]^{-1}$	$-\ln(1-\alpha)^{1/3}$
Ginstling –Brounshtein	D4	$1-(2/3)-\alpha(1-\alpha)^{2/3}$	$3[2((1-\alpha)^{-1/3}-1)]^{-1}$
Geometrical contraction models			
Contracting cylinder	R2	$1-(1-\alpha)^{1/2}$	$2(1-\alpha)^{1/2}$
Contracting sphere	R3	$1-(1-\alpha)^{1/3}$	$3(1-\alpha)^{2/3}$

Table – A2 EDX results of (a) raw biomass (WH, TP and SCB) and (b) ash obtained from proximate analysis are summarized in Table A–5

(a) Feedstock					**(b) Ash**				
Element	**Symbol**	**WH**	**TP**	**SCB**	**Element**	**Symbol**	**WH**	**TP**	**SCB**
Calcium	Ca	0.65±0.17	0.70±0.20	0.13±0.05	Aluminium	Al	0.20±0.07	1.13±0.46	0.73±0.28
Carbon	C	54.90±1.11	70.13±1.69	62.55±0.68	Barium	Ba	1.35±0.41	0.15±0.15	0.45±0.26
Chlorine	Cl	2.68±0.74	0.55±0.06	0.00±0.00	Calcium	Ca	20.13±1.41	11.70±1.52	4.95±0.23
Chromium	Cr	0.10±0.07	0.00±0.00	0.25±0.17	Chlorine	Cl	5.05±1.94	18.03±2.25	0.73±0.21
Copper	Cu	0.00±0.00	0.00±0.00	0.13±0.13	Chromium	Cr	0.30±0.16	0.50±0.18	0.00±0.00
Gariaum	Ga	0.00±0.00	0.00±0.00	0.00±0.00	Cobalt	Co	1.00±0.41	0.40±0.23	0.00±0.00
Iron	Fe	0.00±0.00	0.10±0.00	0.43±0.28	Iron	Fe	0.00±0.00	1.43±0.61	0.43±0.33
Lead	Pb	0.55±0.10	0.00±0.00	0.08±0.03	Lead	Pb	0.85±0.46	0.28±0.28	1.23±0.71
Magnesium	Ma	0.38±0.05	0.30±0.11	0.35±0.17	Magnesium	Mg	7.00±1.26	2.28±0.36	1.90±0.11
Manganese	Mn	0.10±0.04	0.23±0.13	34.33±1.41	Manganese	Mn	0.50±0.22	0.93±0.55	2.13±0.83
Oxygen	O	0.10±0.04	26.20±1.12	0.33±0.19	Nitrogen	N	34.18±3.02	25.18±4.13	0.00±0.00
Phosphorous	P	0.68±0.12	0.13±0.03	0.43±0.10	Phosphorous	P	2.23±0.15	4.78±0.60	4.20±0.91
Potassium	K	3.73±0.70	1.50±0.34	0.15±0.06	Potassium	K	23.30±2.33	27.78±3.33	63.28±2.29
Sodium	Na	0.18±0.08	0.00±0.00	0.25±0.19	Silicon	Si	0.55±0.24	2.98±1.27	9.75±1.15
Sulphur	S	0.08±0.05	0.10±0.00	0.15±0.06	Sodium	Na	0.15±0.09	0.88±0.27	1.58±0.43
Titanium	Ti	0.03±0.03	0.03±0.03	0.08±0.05	Sulphur	S	1.78±0.48	0.80±0.19	5.58±1.16
Zinc	Zn	0.00±0.00	0.03±0.03	0.40±0.09	Titanium	Ti	0.48±0.15	0.30±0.15	0.40±0.34
Zirconium	Zr	0.00±0.00	0.03±0.03	0.00±0.00	Zinc	Zn	0.98±0.21	0.50±0.19	1.83±0.40
					Zirconium	Zr	0.00±0.00	0.03±0.03	0.88±0.64

Table A3– Kinetic parameters for WH

α	**KAS**			**OFW**			**Friedman**			**Vyazovkin_AIC**	
	E_a (kJ mol^{-1})	R^2	Relative Error (%)	E_a (kJ mol^{-1})	R^2	Relative Error (%)	E_a (kJ mol^{-1})	R^2	Relative Error (%)	E_a (kJ mol^{-1})	A (s^{-1})
0.05	277.98	0.99	4.92	272.03	0.99	6.95	265.45	0.99	9.20	292.36	4.40×10^{33}
0.10	228.88	0.99	1.73	225.75	0.99	3.08	214.61	0.99	7.86	232.92	6.97×10^{25}
0.15	213.28	0.99	1.62	211.17	0.99	2.59	207.28	0.99	4.39	216.79	2.96×10^{23}
0.20	209.55	0.99	3.27	207.83	0.99	4.07	207.32	0.99	4.30	216.64	8.40×10^{22}
0.25	206.12	0.99	2.22	204.75	0.99	2.87	197.16	0.99	6.48	210.81	7.81×10^{21}
0.30	199.68	0.99	2.07	198.79	0.99	2.51	198.25	0.99	2.78	203.91	7.40×10^{20}
0.35	198.94	0.99	0.88	198.21	0.99	1.24	198.00	0.99	1.35	200.7	1.92×10^{20}
0.40	196.97	0.99	0.61	196.44	0.99	0.88	191.63	0.99	3.31	198.18	6.54×10^{19}
0.45	194.89	0.99	0.25	194.57	0.99	0.41	187.74	0.99	3.91	195.38	2.30×10^{19}
0.50	193.57	0.99	0.75	193.4	0.99	0.67	195.43	0.99	1.72	192.12	7.80×10^{18}
0.55	190.46	0.99	0.07	190.52	0.99	0.04	188.4	0.99	1.15	190.6	4.02×10^{18}
0.60	189.16	0.99	1.54	189.36	0.99	1.43	190.24	0.99	0.97	192.11	2.88×10^{18}
0.65	190.82	0.99	6.19	191.02	0.99	6.09	200.47	0.99	1.45	203.41	4.40×10^{19}
0.70	205.78	0.99	13.55	205.36	0.99	13.72	245.01	0.98	2.94	238.02	1.94×10^{22}
0.75	258.13	0.97	13.84	255.37	0.98	14.77	290.59	0.96	3.01	299.61	1.05×10^{27}
0.80	329.71	0.99	5.83	323.87	0.99	3.95	327.25	0.94	5.04	311.55	7.50×10^{26}

$$* \, \text{Relative Error (\%)} = 100 \text{ x } \frac{\left| E_{AIC} - E_{KAS/FWO/Friedman} \right|}{E_{AIC}}$$

Table –A4 Kinetic parameters for TP

α	KAS			OFW			Friedman			Vyazovkin_AIC	
	E_a (kJ mol^{-1})	R^2	Relative Error (%)	E_a (kJ mol^{-1})	R^2	Relative Error (%)	E_a (kJ mol^{-1})	R^2	Relative Error (%)	E_a (kJ mol^{-1})	A (s^{-1})
0.05	193.48	0.99	1.94	191.77	0.99	2.80	188.47	0.99	4.48	197.3	1.03×10^{23}
0.10	188.80	0.99	3.74	187.64	0.99	4.33	185.06	0.99	5.64	196.13	1.01×10^{22}
0.15	182.95	0.99	4.55	182.28	0.99	4.90	183.30	0.98	4.37	191.67	1.13×10^{21}
0.20	189.43	0.99	6.66	188.61	0.99	7.07	196.19	0.99	3.33	202.95	6.38×10^{21}
0.25	189.54	0.99	4.35	188.86	0.99	4.69	187.29	0.99	5.49	198.16	9.03×10^{20}
0.30	191.66	0.99	3.79	191.03	0.99	4.11	193.77	0.99	2.74	199.22	5.18×10^{20}
0.35	193.73	0.99	5.84	193.14	0.99	6.13	201.17	0.99	2.23	205.75	1.07×10^{21}
0.40	196.41	0.99	6.51	195.83	0.99	6.78	195.60	0.97	6.89	210.08	1.36×10^{21}
0.45	195.92	0.99	6.80	195.49	0.99	7.00	204.25	0.99	2.84	210.21	7.27×10^{20}
0.50	201.70	0.98	5.12	201.10	0.99	5.40	211.19	0.99	0.65	212.58	6.62×10^{20}
0.55	204.94	0.99	5.81	204.30	0.99	6.11	213.25	0.99	1.99	217.59	1.07×10^{21}
0.60	213.79	0.99	5.88	212.84	0.99	6.30	229.09	0.99	0.86	227.14	4.17×10^{21}
0.65	229.45	0.99	8.12	227.88	0.99	8.75	256.40	0.98	2.67	249.74	1.88×10^{23}
0.70	261.83	0.98	9.03	258.89	0.98	10.05	291.36	0.97	1.23	287.82	1.02×10^{26}
0.75	295.00	0.97	3.72	290.77	0.98	5.10	308.25	0.98	0.61	306.39	4.93×10^{26}
0.80	357.47	0.98	3.80	350.62	0.98	5.64	389.24	0.98	4.75	371.58	5.88×10^{30}

Table–A5 Kinetic parameters for SCB

α	KAS			OFW			Friedman			Vyazovkin_AIC	
	E_a (kJ mol^{-1})	R^2	Relative Error (%)	E_a (kJ mol^{-1})	R^2	Relative Error (%)	E_a (kJ mol^{-1})	R^2	Relative Error (%)	E_a (kJ mol^{-1})	A (s^{-1})
0.05	293.49	0.99	19.34	287.18	0.99	16.78	285.12	0.99	15.94	245.92	1.47×10^{27}
0.10	209.86	0.97	0.24	208.05	0.99	0.63	200.67	0.99	4.15	209.36	2.33×10^{22}
0.15	204.32	0.99	1.98	203.01	1.00	2.61	206.55	0.99	0.91	208.45	5.61×10^{21}
0.20	208.04	0.99	3.48	206.70	1.00	4.10	212.32	0.99	1.49	215.53	1.12×10^{22}
0.25	211.22	0.99	5.67	209.86	0.99	6.28	219.68	0.99	1.89	223.92	3.35×10^{22}
0.30	219.11	0.99	5.29	217.49	0.99	5.99	227.68	0.99	1.58	231.34	8.40×10^{22}
0.35	223.73	0.99	4.18	222.00	0.99	4.92	228.82	0.99	2.00	233.49	7.06×10^{22}
0.40	222.51	0.99	2.22	220.94	1.00	2.91	219.77	0.99	3.43	227.57	1.16×10^{22}
0.45	221.00	0.99	1.67	219.60	1.00	1.03	211.73	0.99	2.59	217.36	8.49×10^{20}
0.50	214.73	0.99	3.45	213.73	0.99	2.97	203.15	0.99	2.12	207.56	7.45×10^{19}
0.55	208.94	0.99	4.11	213.73	0.99	6.49	196.56	0.99	2.06	200.70	1.31×10^{19}
0.60	208.94	0.99	6.93	206.50	0.99	5.68	194.18	1.00	0.62	195.40	3.30×10^{18}
0.65	204.59	0.99	5.76	204.30	0.99	5.61	195.10	1.00	0.85	193.45	1.70×10^{18}
0.70	201.00	0.99	3.45	200.95	0.99	3.42	191.33	0.99	1.53	194.30	1.55×10^{18}
0.75	200.00	1.00	2.64	200.07	1.00	2.67	193.75	0.99	0.57	194.86	1.29×10^{18}
0.80	194.93	0.99	1.00	195.35	0.99	0.79	192.54	0.94	2.21	196.90	1.34×10^{18}

Appendix–B: A Comparative study on synthesis and characterization of biochar derived from lignocellulosic biomass for their candidacy in agronomy and energy applications

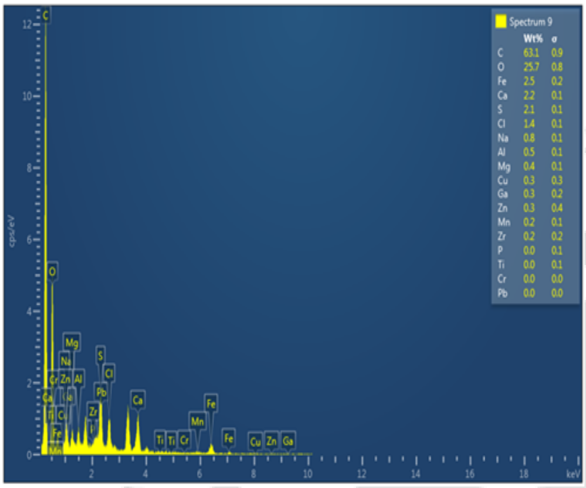

Spectrum 9

	Wt%	σ
C	63.1	0.9
O	25.7	0.8
Fe	2.5	0.2
Ca	2.2	0.1
S	2.1	0.1
Cl	1.4	0.1
Na	0.8	0.1
Al	0.5	0.1
Mg	0.4	0.1
Cu	0.3	0.3
Ga	0.3	0.2
Zn	0.3	0.4
Mn	0.2	0.1
Zr	0.2	0.2
P	0.0	0.1
Ti	0.0	0.1
Cr	0.0	0.0
Pb	0.0	0.0

(a)

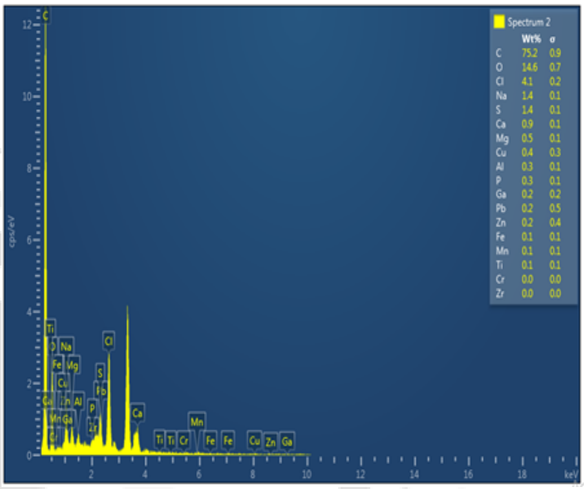

Spectrum 2

	Wt%	σ
C	75.2	0.9
O	14.6	0.7
Cl	4.1	0.2
Na	1.4	0.1
S	1.4	0.1
Ca	0.9	0.1
Mg	0.5	0.1
Cu	0.4	0.3
Al	0.3	0.1
P	0.3	0.1
Ga	0.2	0.2
Pb	0.2	0.5
Zn	0.2	0.4
Fe	0.1	0.1
Mn	0.1	0.1
Ti	0.1	0.1
Cr	0.0	0.0
Zr	0.0	0.0

(b)

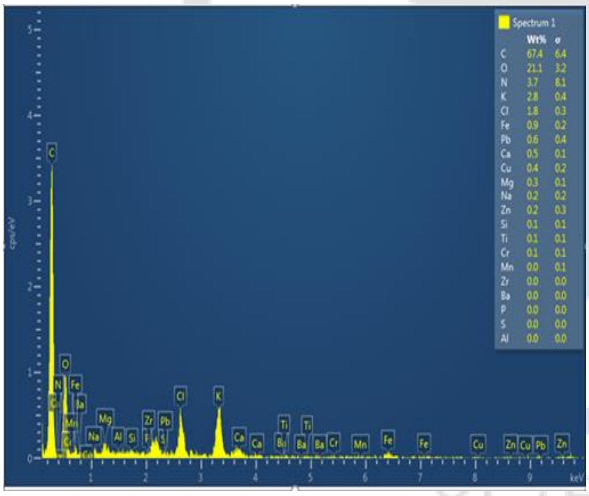

Spectrum 1

	Wt%	σ
C	67.4	6.4
O	21.1	3.2
N	3.7	8.1
K	2.8	0.4
Cl	1.8	0.3
Fe	0.9	0.2
Pb	0.6	0.4
Ca	0.5	0.1
Cu	0.4	0.2
Mg	0.3	0.1
Na	0.2	0.2
Zn	0.2	0.3
Si	0.1	0.1
Ti	0.1	0.1
Cr	0.1	0.1
Mn	0.0	0.1
Zr	0.0	0.0
Ba	0.0	0.0
P	0.0	0.0
S	0.0	0.0
Al	0.0	0.0

(c)

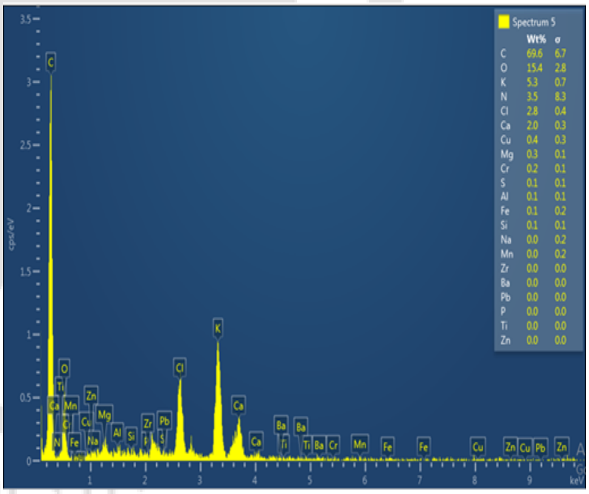

Spectrum 5

	Wt%	σ
C	69.6	6.7
O	15.4	2.8
K	5.3	0.7
N	3.5	8.3
Cl	2.8	0.4
Ca	2.0	0.3
Cu	0.4	0.3
Mg	0.3	0.1
Cr	0.2	0.1
S	0.1	0.1
Al	0.1	0.1
Fe	0.1	0.2
Si	0.1	0.1
Na	0.0	0.2
Mn	0.0	0.2
Zr	0.0	0.0
Ba	0.0	0.0
Pb	0.0	0.0
P	0.0	0.0
Ti	0.0	0.0
Zn	0.0	0.0

(d)

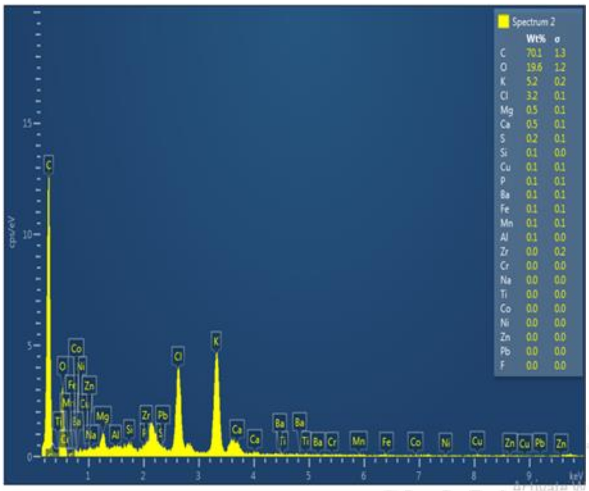

Spectrum 2

	Wt%	σ
C	70.1	1.3
O	19.6	1.2
K	5.2	0.2
Cl	3.2	0.1
Mg	0.5	0.1
Ca	0.5	0.1
S	0.2	0.1
Si	0.1	0.0
Cu	0.1	0.1
P	0.1	0.1
Ba	0.1	0.1
Fe	0.1	0.1
Mn	0.1	0.1
Al	0.1	0.0
Zr	0.0	0.2
Cr	0.0	0.0
Na	0.0	0.0
Ti	0.0	0.0
Co	0.0	0.0
Ni	0.0	0.0
Zn	0.0	0.0
Pb	0.0	0.0
F	0.0	0.0

(e)

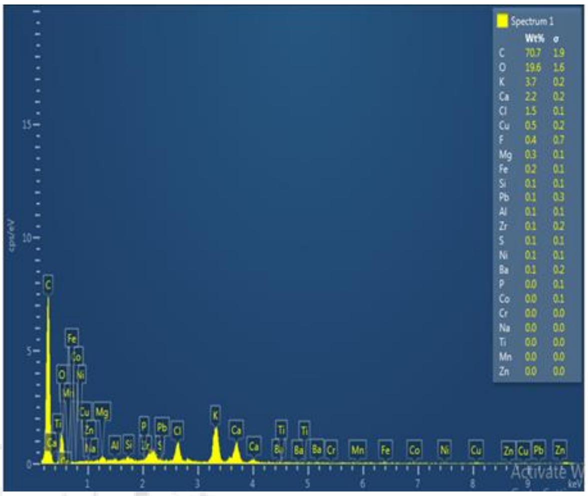

Spectrum 1

	Wt%	σ
C	70.7	1.9
O	19.6	1.6
K	3.7	0.2
Ca	2.2	0.2
Cl	1.5	0.1
Cu	0.5	0.2
F	0.4	0.7
Mg	0.3	0.1
Fe	0.2	0.1
Si	0.1	0.1
Pb	0.1	0.3
Al	0.1	0.1
Zr	0.1	0.2
S	0.1	0.1
Ni	0.1	0.1
Ba	0.1	0.2
P	0.0	0.1
Co	0.0	0.1
Cr	0.0	0.0
Na	0.0	0.0
Ti	0.0	0.0
Mn	0.0	0.0
Zn	0.0	0.0

(f)

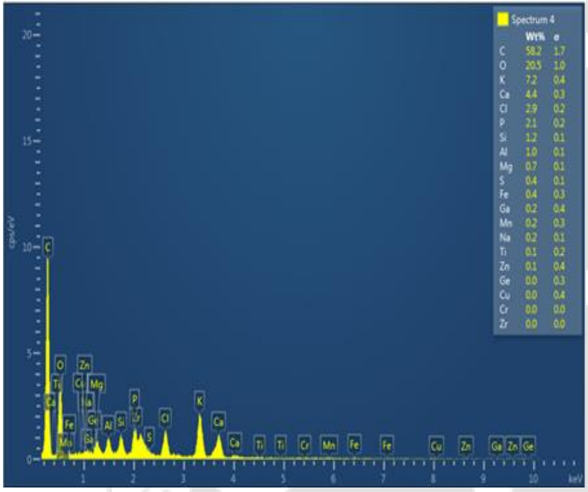

Spectrum 4

	Wt%	σ
C	58.2	1.7
O	20.5	1.0
K	7.2	0.4
Ca	4.4	0.3
Cl	2.9	0.2
P	2.1	0.2
Si	1.2	0.1
Al	1.0	0.1
Mg	0.7	0.1
S	0.4	0.1
Fe	0.4	0.3
Ga	0.2	0.4
Mn	0.2	0.3
Na	0.2	0.1
Ti	0.1	0.2
Zn	0.1	0.4
Ge	0.0	0.3
Cu	0.0	0.4
Cr	0.0	0.0
Zr	0.0	0.0

(g)

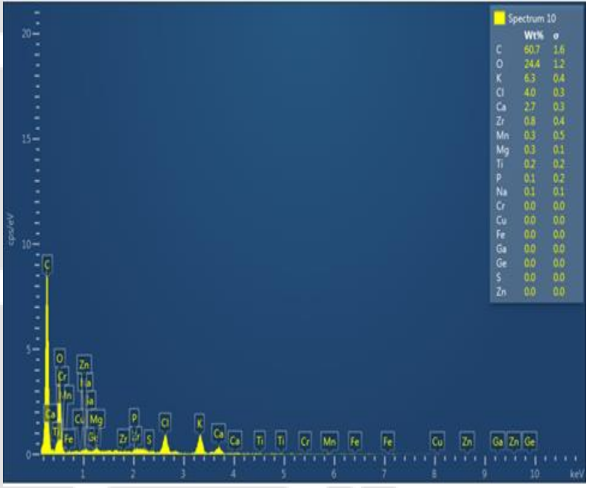

Spectrum 10

	Wt%	σ
C	60.7	1.6
O	24.4	1.2
K	6.3	0.4
Cl	4.0	0.3
Ca	2.7	0.3
Zr	0.8	0.4
Mn	0.3	0.5
Mg	0.3	0.1
Ti	0.2	0.2
P	0.1	0.2
Na	0.1	0.1
Cr	0.0	0.0
Cu	0.0	0.0
Fe	0.0	0.0
Ga	0.0	0.0
Ge	0.0	0.0
S	0.0	0.0
Zn	0.0	0.0

(h)

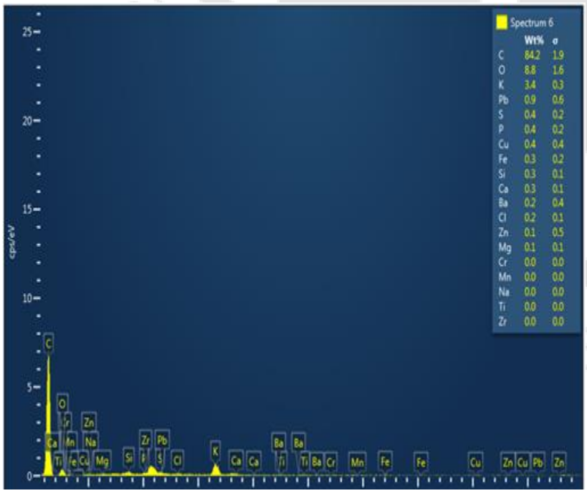

Spectrum 6

	Wt%	σ
C	84.2	1.9
O	8.8	1.6
K	3.4	0.3
Pb	0.9	0.6
S	0.4	0.2
P	0.4	0.2
Cu	0.4	0.4
Fe	0.3	0.2
Si	0.3	0.1
Ca	0.3	0.1
Ba	0.2	0.4
Cl	0.2	0.1
Zn	0.1	0.5
Mg	0.1	0.1
Cr	0.0	0.0
Mn	0.0	0.0
Na	0.0	0.0
Ti	0.0	0.0
Zr	0.0	0.0

(i)

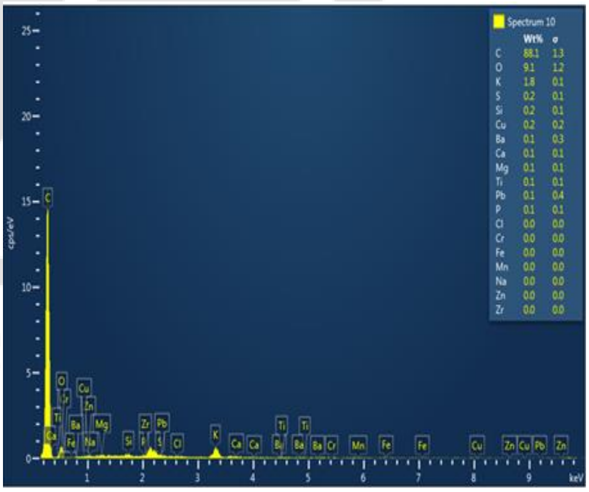

Spectrum 10

	Wt%	σ
C	88.1	1.3
O	9.1	1.2
K	1.8	0.1
S	0.2	0.1
Si	0.2	0.1
Cu	0.2	0.2
Ba	0.1	0.3
Ca	0.1	0.1
Mg	0.1	0.1
Ti	0.1	0.1
Pb	0.1	0.4
P	0.1	0.1
Cl	0.0	0.0
Cr	0.0	0.0
Fe	0.0	0.0
Mn	0.0	0.0
Na	0.0	0.0
Zn	0.0	0.0
Zr	0.0	0.0

(j)

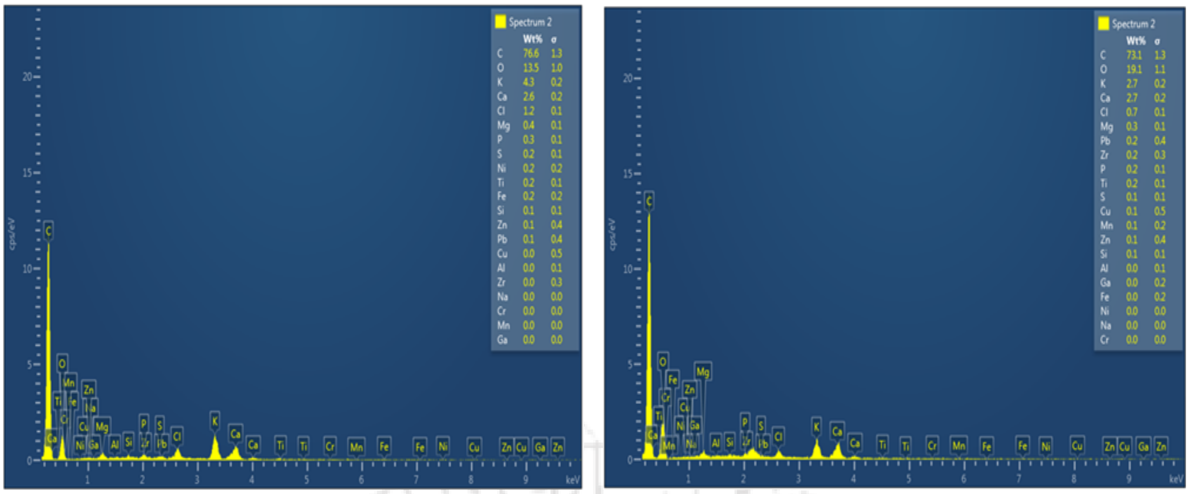

Spectrum 2

	Wt%	σ
C	76.6	1.3
O	13.5	1.0
K	4.3	0.2
Ca	2.6	0.2
Cl	1.2	0.1
Mg	0.4	0.1
P	0.3	0.1
S	0.2	0.1
Ni	0.2	0.2
Ti	0.2	0.1
Fe	0.2	0.2
Si	0.1	0.1
Zn	0.1	0.4
Pb	0.1	0.4
Cu	0.0	0.5
Al	0.0	0.1
Zr	0.0	0.3
Na	0.0	0.0
Cr	0.0	0.0
Mn	0.0	0.0
Ga	0.0	0.0

Spectrum 2

	Wt%	σ
C	73.1	1.3
O	19.1	1.1
K	2.7	0.2
Ca	2.7	0.2
Cl	0.7	0.1
Mg	0.3	0.1
Pb	0.2	0.4
Zr	0.2	0.3
P	0.2	0.1
Ti	0.2	0.1
S	0.1	0.1
Cu	0.1	0.5
Mn	0.1	0.2
Zn	0.1	0.4
Si	0.1	0.1
Al	0.0	0.1
Ga	0.0	0.2
Fe	0.0	0.2
Ni	0.0	0.0
Na	0.0	0.0
Cr	0.0	0.0

(k) **(l)**

Figures B1 EDX Micrographs of biochar: (a) WH R350, (b) WH R550, (c) WH S350, (d) WH S550, (e) WH L350, (f) WH L550, (g) WH 350, (h) WH 550, (i) SCB 350, (j) SCB S550, (k) TP 350, (l) TP 550

Table –B1: EDX Results of biochar

Element	WH350R % wt	WH550R % wt	WHS350 % wt	WHS5550 % wt	WHL350 % wt	WHL550 % wt	WH350 % wt	SCB350 % wt	TP350 % wt	WH550 % wt	SCB550 % wt	TP550 % wt
Aluminium	0.88±0.25	0.72±0.35	0.00±0.00	0.05±0.03	0.08±0.03	0.08±0.02	1.16±1.27	0.	0.04±0.03	1.07±0.107	0.	0.
Calcium	0.90±0.44	0.40±0.46	0.93±0.46	2.78±0.62	0.95±0.21	2.64±0.43	2.36±0.76	0.10±0.04	2.72±0.20	2.66±0.70	0.08±0.02	2.82±0.38
Carbon	62.85±1.07	71.98±3.61	67.45±1.51	70.55±1.52	70.10±1.68	71.84±1.12	58.26±4.75	74.38±0.50	67.72±0.46	60.60±2.26	88.66±0.63	72.08±1.16
Chlorine	1.85±0.66	2.60±1.73	2.83±1.38	3.73±0.32	2.15±0.83	1.42±0.19	5.12±2.07	0.04±0.03	0.98±0.18	3.88±1.12	0.08±0.02	0.68±0.13
Copper	0.08±0.08	0.12±0.08	0.60±0.67	0.23±0.09	0.18±0.03	0.24±0.09	0.04±0.04	0.22±0.04	0.10±0.09	0.08±0.09	0.32±0.11	0.06±0.04
Iron	4.78±2.59	2.22±1.64	1.23±0.78	0.15±0.03	0.15±0.03	0.16±0.07	0.24±0.08	0.06±0.03	0.18±0.05	0.40±0.15	0.	0.22±0.08
Lead	0.13±0.15	0.22±0.13	0.15±0.15	0.23±0.13	0.15±0.15	0.16±0.04	0.12±0.11	0.16±0.8	0.18±0.09	0.14±0.10	0.06±0.04	0.18±0.10
Magnesium	0.43±0.13	0.58±0.16	0.28±0.10	0.43±0.05	0.38±0.06	0.36±0.03	0.32±0.08	0.08±0.04	0.38±0.02	0.52±0.08	0.12±0.04	0.40±0.06
Manganese	0.80±0.45	0.05±0.04	0.08±0.15	0.10±0.07	0.05±0.03	0.10±0.05	0.12±0.11	0.04±0.03	0.06±0.04	0.04±0.03	0.02±0.02	0.08±0.07
Oxygen	24.01±2.14	16.09±3.22	21.40±1.74	14..45±0.90	21.38±1.05	18.32±0.69	20.78±3.01	23.64±0.52	23.28±0.50	18.08±3.15	9.12±1.040	19.72±1.10
Phosphorous	0.15±0.10	0.22±0.07	0.05±0.10	0.05±0.05	0.05±0.03	0.14±0.04	0.44±0.17	0.06±0.03	0.24±0.03	0.80±0.39	0.06±0.03	0.26±0.03
Potassium	0.11±0.26	0.55±0.45	3.90±0.60	6.63±0.55	3.98±0.97	3.78±0.41	7.20±1.88	0.86±0.0.3	3.66±0.30	6.82±01.46	1.12±0.55	2.88±0.38
Silicon	0.	0.06±0.07	0.43±0.17	0.03±0.03	0.23±0.10	0.10±0.04	0.02±0.02	0.14±0.04	0.06±0.03	3.08±3.03	0.08±0.04	0.08±0.02
Sodium	1.18±0.68	1.32±0.70	0.10±0.06	0.08±0.05	0.05±0.03	0.10±0.04	0.88±1.36	0.02±0.02	0.10±0.10	1.08±0.98	0.06±0.03	0.04±0.03
Sulphur	1.60±0.52	1.40±0.35	0.08±0.03	0.25±0.06	0.08±0.05	0.20±0.06	2.50±0.03	0.10±0.04	0.08±0.04	0.22±0.07	0.12±0.05	0.12±0.08
Titanium	0.05±0.06	0.10±0.04	0.23±0.17	0.08±0.05	0.±0.00	0.12±0.07	0.10±0.14	0.04±0.03	0.12±0.07	0.08±0.07	0.02±0.02	0.20±0.16
Zinc	0.23±0.10	0.22±0.19	0.30±0.07	0.03±0.03	0.10±0.07	0.16±0.03	0.06±0.07	0.06±0.04	0.02±0.02	0.06±0.02	0.	0.08±0.07
Zirconium	0.	0.12±0.07	0.	0.10±0.10	0.	0.08±0.09	0.28±0.17	0.	0.08±0.09	0.26±0.06	0.08±0.04	0.08±0.11

Table –C1. Kinetic parameters obtained using DAEM and OFW method for ternary blends

	DAEM							**OFW**					
	WH 111		**WH 211**		**WH 311**			**WH 111**		**WH 211**		**WH 311**	
α	E_a kJ mol^{-1}	R^2	E_a kJ mol^{-1}	R^2	E_a kJ mol^{-1}	R^2	**α**	E_a kJ mol^{-1}	R^2	E_a kJ mol^{-1}	R^2	E_a kJ mol^{-1}	R^2
0.05	119.64	0.83	137.84	0.97	168.70	0.99	0.05	121.65	0.84	139.03	0.98	168.34	0.99
0.10	125.10	0.85	139.62	0.97	147.33	0.99	0.10	127.21	0.87	141.08	0.98	148.40	0.99
0.15	127.95	0.86	138.00	0.97	143.49	0.99	0.15	130.14	0.87	139.76	0.97	144.96	0.99
0.20	127.98	0.86	139.21	0.97	151.46	0.98	0.20	130.36	0.87	148.37	0.97	152.73	0.99
0.25	134.84	0.88	147.42	0.98	156.52	0.98	0.25	137.05	0.89	149.07	0.98	157.73	0.99
0.30	146.36	0.91	155.06	0.99	159.66	0.99	0.30	148.16	0.92	156.49	0.99	160.88	0.99
0.35	158.72	0.93	159.50	0.99	156.13	0.99	0.35	160.06	0.94	160.85	0.99	157.67	0.98
0.40	166.48	0.96	161.64	0.99	150.39	0.99	0.40	167.56	0.96	163.01	0.99	152.32	0.99
0.45	169.70	0.97	160.81	0.99	147.86	0.99	0.45	170.74	0.97	162.33	0.99	150.02	0.99
0.50	173.98	0.99	159.21	0.99	144.32	1.00	0.50	174.90	0.99	160.90	0.99	146.75	1.00
0.55	175.29	0.99	158.67	0.99	137.77	0.99	0.55	176.24	0.99	160.47	0.99	140.61	0.99
0.60	176.55	1.00	157.55	0.99	140.13	1.00	0.60	177.52	1.00	159.47	0.99	142.92	1.00
0.65	180.44	1.00	156.99	0.99	138.52	1.00	0.65	181.30	1.00	159.02	0.99	141.46	1.00
0.70	185.05	0.98	156.36	0.99	138.66	1.00	0.70	185.78	0.99	158.51	0.99	141.69	1.00
0.75	194.31	0.89	171.45	0.95	154.31	0.99	0.75	194.75	0.90	172.99	0.95	156.71	0.99

Table –C2. Kinetic parameters obtained using DAEM and OFW method for binary blends

	DAEM							**OFW**					
	WH SCB		**WH TP**		**TP SCB**			**WH SCB**		**WH TP**		**TP SCB**	
α	E_a kJ mol^{-1}	R^2	E_a kJ mol^{-1}	R^2	E_a kJ mol^{-1}	R^2	**α**	E_a kJ mol^{-1}	R^2	E_a kJ mol^{-1}	R^2	E_a kJ mol^{-1}	R^2
0.05	184.67	0.95	239.63	0.88	122.90	0.97	0.05	183.58	0.95	235.67	0.89	124.80	0.97
0.10	174.03	0.96	206.90	0.95	126.12	0.97	0.10	173.80	0.97	204.95	0.95	128.26	0.98
0.15	173.42	0.96	206.50	0.98	132.29	0.98	0.15	173.44	0.96	204.79	0.98	134.38	0.98
0.20	179.00	0.96	211.19	0.98	141.13	0.98	0.20	178.93	0.96	209.44	0.98	142.98	0.99
0.25	189.84	0.97	222.35	0.98	148.02	0.99	0.25	189.41	0.97	220.23	0.98	149.70	0.99
0.30	197.75	0.99	218.70	0.99	155.80	0.99	0.30	197.09	0.99	216.93	0.99	157.24	0.99
0.35	198.74	0.99	214.79	0.99	163.09	0.99	0.35	198.18	0.99	213.35	0.99	164.32	0.99
0.40	195.38	1.00	212.76	1.00	169.11	0.98	0.40	195.10	1.00	211.56	1.00	170.17	0.98
0.45	190.79	1.00	208.51	1.00	168.76	0.98	0.45	190.84	1.00	207.62	1.00	169.96	0.98
0.50	183.88	1.00	204.43	1.00	169.49	0.97	0.50	184.36	1.00	203.84	1.00	170.76	0.98
0.55	181.62	1.00	200.10	1.00	170.60	0.97	0.55	182.29	1.00	199.81	1.00	171.91	0.97
0.60	180.67	1.00	197.89	1.00	174.43	0.96	0.60	181.46	1.00	197.80	1.00	175.64	0.97
0.65	179.44	1.00	196.29	0.99	181.04	0.96	0.65	180.35	1.00	196.37	0.99	182.01	0.96
0.70	181.15	0.99	203.90	0.99	191.73	0.96	0.70	182.05	1.00	203.72	0.99	192.27	0.97
0.75	189.95	0.99	237.53	0.95	205.63	0.98	0.75	190.51	0.99	235.94	0.96	205.58	0.98

Table –C3. Kinetic parameters obtained for ternary blends using Vyazovkin_AIC

α	**Vyazovkin_AIC**											
	WH 111		**WH 211**		**WH 311**		**WH SCB**		**WH TP**		**TP SCB**	
	E_a kJ mol^{-1}	A (s^{-1})	E_a kJ mol^{-1}	A (s^{-1})	E_a kJ mol^{-1}	A (s^{-1})	E_a kJ mol^{-1}	A (s^{-1})	E_a kJ mol^{-1}	A (s^{-1})	E_a kJ mol^{-1}	A (s^{-1})
0.05	123.40	5.03×10^{14}	144.6	6.43×10^{16}	212.19	1.55×10^{24}	192.40	6.46×10^{21}	247.85	2.41×10^{28}	127.93	1.03×10^{15}
0.10	135.76	2.33×10^{15}	149.87	4.59×10^{16}	187.19	4.15×10^{20}	181.71	7.66×10^{19}	217.04	7.79×10^{23}	136.95	1.84×10^{15}
0.15	134.33	6.52×10^{14}	144.1	4.77×10^{15}	189.72	2.38×10^{20}	186.81	8.34×10^{19}	219.46	3.26×10^{23}	146.4	6.28×10^{15}
0.20	135.96	4.78×10^{14}	151.05	1.12×10^{16}	203.62	2.09×10^{21}	198.34	4.38×10^{20}	232.37	2.06×10^{24}	156.88	3.11×10^{16}
0.25	152.79	1.13×10^{16}	165.02	1.26×10^{17}	210.22	3.38×10^{21}	209.94	2.36×10^{21}	237.12	1.95×10^{24}	166.71	1.40×10^{17}
0.30	168.64	2.00×10^{17}	171.46	2.70×10^{17}	203.77	3.46×10^{20}	213.27	2.14×10^{21}	229.28	1.27×10^{23}	175.74	5.25×10^{17}
0.35	178.00	8.17×10^{17}	170.76	1.29×10^{17}	193.72	1.98×10^{19}	205.53	2.01×10^{20}	221.51	1.03×10^{22}	180.87	8.65×10^{17}
0.40	180.87	8.64×10^{17}	167.35	3.85×10^{16}	184.15	1.49×10^{18}	193.35	8.75×10^{18}	215.13	1.34×10^{21}	180.34	4.48×10^{17}
0.45	180.54	4.99×10^{17}	163.98	1.28×10^{16}	176.93	2.11×10^{17}	184.01	7.93×10^{17}	208.21	1.80×10^{20}	177.49	1.53×10^{17}
0.50	182.10	4.62×10^{17}	161.83	5.86×10^{15}	173.23	6.87×10^{16}	179.40	2.14×10^{17}	203.15	3.97×10^{19}	176.78	8.72×10^{16}
0.55	183.96	4.77×10^{17}	160.54	3.39×10^{15}	171.79	3.76×10^{16}	179.66	1.70×10^{17}	200.83	1.67×10^{19}	180.61	1.32×10^{17}
0.60	188.56	8.76×10^{17}	158.91	1.89×10^{15}	171.79	2.86×10^{16}	182.19	2.19×10^{17}	201.89	1.43×10^{19}	192.18	9.60×10^{17}
0.65	196.25	2.88×10^{18}	157.55	1.13×10^{15}	173.27	2.93×10^{16}	187.24	4.71×10^{17}	205.66	2.07×10^{19}	208.64	1.81×10^{19}
0.70	209.06	2.32×10^{19}	164.64	3.68×10^{15}	182.66	1.39×10^{17}	197.67	2.88×10^{18}	225.39	6.16×10^{20}	225.7	3.59×10^{20}
0.75	246.8	1.89×10^{22}	218.82	1.24×10^{20}	234.5	2.14×10^{21}	232.65	2.04×10^{21}	272.92	1.86×10^{24}	237.76	2.45×10^{21}

Appendix–D: Applications of biochar in agronomy and engineering

Table –E1. The PV/T characteristics

Characteristic	Value
Number of solar cells	36
Open circuit voltage	21.40 V
Short circuit current	06.31 A
Maximum power current	05.56 A
Maximum power voltage	18.00 V
Glass thickness	3 mm
Tube material	Copper
Tube diameter	7.9 mm
Efficiency	14.64 %

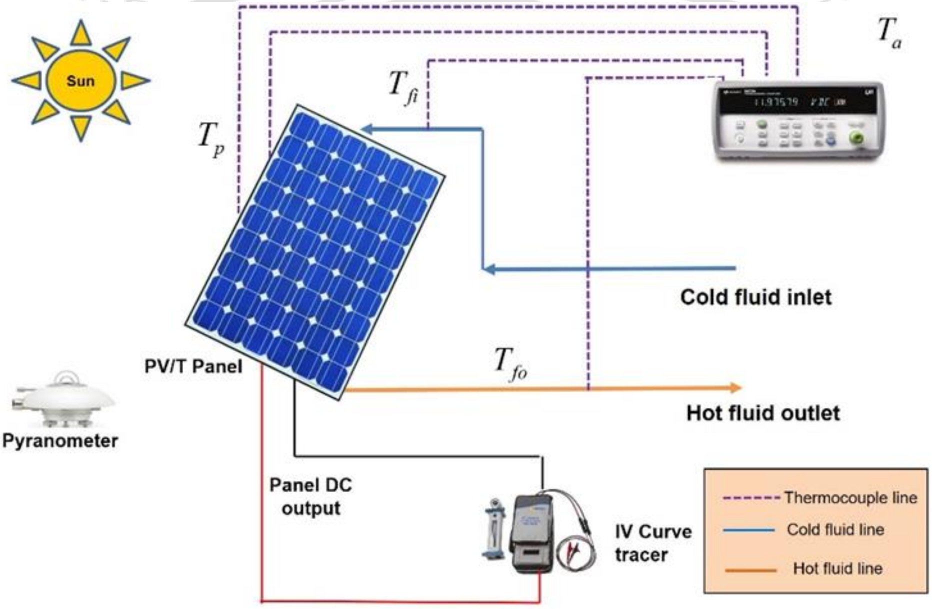

Figure E1 Schematic of the experimental setup for the experimental investigation.

List of publications

Journals

1) **Harrison Hihu Muigai,** Bordoloi, U., Kalita, P., Moholkar, V., Hussain, R., Ravi, K. (2020), A comparative study on synthesis and characterization of biochar derived from lignocellulosic biomass for their candidacy in agronomy and energy applications *International Journal of Energy Research*, https://doi.org/10.1002/er.6092

2) **Harrison Hihu Muigai**, Bhaskar J. Choudhury, Pankaj Kalita, Vijayanand S. Moholkar, (2020), Co–pyrolysis of biomass blends: Characterization, kinetic and thermodynamic analysis, *Biomass Bioenergy*, https://doi.org/10.1016/j.biombioe.105839

3) **Harrison Hihu Muigai**, Bhaskar J. Choudhury, Pankaj Kalita, Vijayanand S. Moholkar, (2020), Physio–chemical characterization and pyrolysis kinetic analyses of Eichhornia Crassipes, Thevetia Peruviana, and Saccharum Officinarum, Fuel https://doi.org/10.1016/j.fuel.2020.119949

4) Das,D. U. Bordoloi, **Harrison Hihu Muigai,** P. Kalita, (2020), A novel form stable PCM based bio composite material for solar thermal energy storage applications, *Energy Storage*, 30 101403, https://doi.org/10.1016/j.est.2020.101403

5) Das, D. Bordoloi, U., **Harrison Hihu Muigai**, Kamble, A.D., Ranjith K.Pai, Kalita, P. (2020), Performance investigation of a rectangular spiral flow PV/T collector with a novel form stable composite material, *Applied Thermal Engineering*, https://doi.org/10.1016/j.applthermaleng. 116035.

6) **Harrison Hihu Muigai,** Moholkar, V., Kalita, P., Co–pyrolysis of ternary biomass blend, optimization using response surface methodology and characterization of biochar. (**under preparation)**

Conferences

1) **Harrison Hihu Muigai,** Pankaj Kalita, Vijayanand S. Moholkar, Valorization of sugarcane baggase for energy production, Interanational conference on future aspects of sustainable technologies (FAST–2019) at CIT Kokrajhar Assam.

2) **Harrison Hihu Muigai,** Pankaj Kalita, Vijayanand S. Moholkar Estimating the Gross calorific value of noxious weeds through proximate and ultimate analysis for energy application. National conference on waste to energy conversion (NCWEC–2018) at NIT Mizoram December 28th –29th 2018.